

**NEW DEVELOPMENTS IN MICRO ELECTRO
MECHANICAL SYSTEMS FOR RADIO FREQUENCY
AND MILLIMETER WAVE APPLICATIONS**

**NOUTĂȚI ÎN DOMENIUL MĂSURĂTORILOR MICRO-
ELECTRO-MECANICE PENTRU APLICAȚII DE RADIO
FRECVENȚĂ ȘI UNDE MILIMETRICE**

**NEW DEVELOPMENTS IN MICRO
ELECTRO MECHANICAL SYSTEMS
FOR RADIO FREQUENCY AND
MILLIMETER WAVE APPLICATIONS**

EDITORS:

**George Konstantinidis, Alexandru Muller,
Dan Dascalu, Robert Plana**



**EDITURA ACADEMIEI ROMÂNE
București, 2009**

Copyright © Editura Academiei Române, 2009.
All rights reserved.

The responsibility for originality and the contents of the
articles lies exclusively with the authors.

Address: EDITURA ACADEMIEI ROMÂNE
Calea 13 Septembrie nr. 13, sector 5,
050 711, București, România,
Tel. 40-21-3188146, 40-21-3188106
Fax: 40-21-3182444
E-mail: edacad@ear.ro
Internet: <http://www.ear.ro>

Peer reviewers: Prof. Adrian Rusu, Prof. Gheorghe Brezeanu

Descrierea CIP a Bibliotecii Naționale a României

New Developments in Micro Electro Mechanical Systems for Radio
Frequency and Millimeter Wave Applications /

editors: George Konstantinidis, Alexandru Muller, Dan Dascalu,
Robert Plana

- București : Editura Academiei Române, 2009
ISBN 978-973-27-1813-1

I. Konstantinidis, George (ed.)

II. Müller, Alexandru (ed)

III. Dascălu, Dan (ed.)

IV. Robert, Plana (ed.)

621.3.049.77

Editorial assistant: Mihaela Marian

Computer operator: Elena Trică

Cover: Elena Trică

Passed for press: 06.2009. Size: 16 / 70 × 100.

Printed sheets: 23.5

D.L.C. for large libraries 621.317:621.38.032

for small libraries 53.08

CONTENTS

FOREWORD	11
HOW TO BUILD A RELIABLE RF MEMS SWITCH <i>Gabriel M. REBEIZ</i>	13
COMBINATION OF 2D AND 3D METHOD OF LINE APPROACH FOR THE ACCURATE LOSS DETERMINATION IN RF MEMS CIRCUITS <i>Larissa VIETZORRECK</i>	19
LOW LOSS PIEZOELECTRIC SPMT RF MEMS SWITCHES <i>David J. CHUNG, Ronald G. POLCAWICH, Daniel JUDY, Jeffrey PULSKAMP, John PAPAPOLYMEROU</i>	27
PAPER-BASED INKJET-PRINTED ANTENNAS AND WIRELESS SENSOR MODULES: THE NEW PARADIGM FOR WEARABLE AND BIOMONITORING ELECTRONICS? <i>M.M. TENTZERIS, R. VYAS, A. RIDA, L. YANG, A. TRAILLE, C. KRUESI</i>	35
CHARGING EFFECT IN RF MEMS SWITCHES WITH DIELECTRIC LESS ACTUATORS <i>D. MARDIVIRIN, A. POTHIER, A. CRUNTEANU, P. BLONDY</i>	45
SIMPLE AND ROBUST AIR GAP-BASED MEMS TECHNOLOGY FOR RF-APPLICATIONS <i>Phillip EKKELS, Xavier ROTTENBERG, Robert PUERS, Harrie A.C. TILMANS</i>	53
INVESTIGATION OF DIELECTRIC CHARGING MECHANISMS IN Al₂O₃ RF-MEMS CAPACITIVE SWITCHES <i>E. PAPANDREOU, A. CRUNTEANU, G. PAPAIOANNOU, P. BLONDY, F. DUMAS-BOUCHIAT, C. CHAMPEAUX, A. CATHERINOT</i>	63
CHARGING EFFECTS AND RELATED EQUIVALENT CIRCUITS FOR OHMIC SERIES AND SHUNT CAPACITIVE RF MEMS SWITCHES <i>George PAPAIOANNU, Romolo MARCELLI, Giancarlo BARTOLUCCI, Simone CATONI, Giorgio De ANGELIS, Andrea LUCIBELLO, Emanuela PROIETTI, Benno MARGESIN, Flavio GIACOMOZZI, François DEBORGIÉS</i>	73
AN EFFICIENT MODELING METHOD FOR SIMULATING TIME-RESPONSE OF RF-MEMS SWITCHES <i>V. LEUS, D. ELATA</i>	81

**NANO-ELECTRO-MECHANICAL-SYSTEMS:
FROM IDEAS TO REALITY CHECK**

Adrian M. IONESCU 89

**SIMPLE NANOELECTROMECHANICAL SYSTEMS
FOR GIGA-APPLICATIONS**

*Mircea DRAGOMAN, George KONSTANTINIDIS, Dana DRAGOMAN,
Dan NECULOIU, Alina CISMARU, Robert PLANA, H. HARNAGEL,
A. KOSTOPOULOS, Raluca BUICULESCU* 97

**GaN MEMBRANE SUPPORTED MSM ULTRAVIOLET
PHOTODETECTOR**

*Alexandru MÜLLER, George KONSTANTINIDIS, Mircea DRAGOMAN,
Dan NECULOIU, Adrian DINESCU, M. ANDROULIDAKI,
M. KAYAMBAKI, A. STAVRINIDIS, Dan VASILACHE,
Cristina BUICULESCU, A. KOSTOPOULOS, Dan DASCALU* 101

SILICON MEMS TUNABLE SUPERCONDUCTING MICROWAVE CIRCUITS

M.J. PREST, Y. WANG, F. HUANG, M.J. LANCASTER 109

CAN MICROMACHINING HELP US TO FILL THE ‘TERAHERTZ GAP’?

Andrew J. GALLANT 117

IN-PLANE RF MEMS RESONATOR SIMULATION

*F. CASSET, C. WELHAM, C. DURAND, E. OLLIER,
J.F. CARPENTIER, P. ANCEY, M. AÏD* 127

**A CAPACITIVE SHUNT RF MEMS SWITCH FOR COPLANAR
WAVEGUIDE TRANSMISSION LINES**

*Bengt HOLTER, Karsten HUSBY, Håkon SAGBERG, Geir U. JENSEN,
Ulrik HANKE, Shimul CHANDRA SAHA, Trond SÆTHER* 135

**HIGH-ISOLATION SHUNT-SERIES MEMS SWITCH FOR
A WIDE FREQUENCY RANGE (6-40GHz)**

M. FERNÁNDEZ-BOLAÑOS, P. DAINESI, A. M. IONESCU 145

**DESIGN AND MANUFACTURING OF A 5-BIT MEMS
PHASE SHIFTER AT K-BAND**

*S. BASTIOLI, F. Di MAGGIO, P. FARINELLI, F. GIACOMOZZI,
B. MARGESIN, A. OCERA, I. POMONA, M. RUSSO, R. SORRENTINO* 155

**RECONFIGURABLE THREE-DIMENSIONAL MICROMACHINED
DIELECTRIC-LOADED CPW PHASE-SHIFTER**

N. SOMJIT, G. STEMME, J. OBERHAMMER 163

**COMPACT REFLECTION-TYPE RF-MEMS PHASE SHIFTER
FOR BEAM-STEERABLE REFLECTARRAYS**

*Tatyana PURTOVA, Till FEGER, Thomas LISEC,
Bernd WAGNER, Hermann SCHUMACHER* 169

LOW-LOSS DMTL PHASE SHIFTER BASED ON FAST MINIATURE RF MEMS SWITCHED CAPACITORS	
<i>B. LACROIX, A. POTHIER, A. CRUNTEANU, P. BLONDY</i>	177
A SINGLE-POLE-DOUBLE-THROW SWITCH BASED ON CAPACITIVE-ANCHORED MEMS	
<i>David GIRBAU, Marco Antonio LLAMAS, Antonio LÁZARO, Lluís PRADELL, Jaume PRADA, Pierre CALMON, Patrick PONS, Robert PLANA</i>	185
SYSTEMS ENGINEERING - A HOLISTIC APPROACH, WHATEVER THE REQUIREMENT?	
<i>Ayman EL-FATATRY, Henne van Heeren</i>	193
FABRICATION OF AN ON-WAFER PACKAGE FOR RF MEMS SWITCHES	
<i>F. BARRIERE, A. CRUNTEANU, A. BESSAUDOU, A. POTHIER, F. COSSET, P. BLONDY</i>	199
GLASS CAP PACKAGED HIGH ISOLATING Ka-BAND RF-MEMS SWITCH	
<i>A. STEHLE, G. GEORGIEV, V. ZIEGLER, B. SCHOENLINNER, U. PRECHTEL, H. SEIDEL, U. SCHMID</i>	205
MILLIMETER-WAVE QUARTER-WAVE PATCH ANTENNA ON BENZOCYCLOBUTENE POLYMER	
<i>Seonho SEOK, Nathalie ROLLAND, Paul-Alain ROLLAND</i>	213
ACOUSTICAL STRUCTURES BASED ON THE THICKENED EDGE LOAD SOLUTION	
<i>Jordi VERDU, Pedro de PACO, Oscar MENENDEZ, Eden CORRALES</i>	221
A NOVEL BULK ACOUSTIC WAVE DUPLEXER BASED ON STACKED CRYSTAL FILTERS FOR WCDMA HANDSET APPLICATIONS	
<i>Oscar MENENDEZ, Pedro de PACO, Eden CORRALES, Jordi VERDU</i>	231
BULK ACOUSTIC WAVE CRF DESIGN	
<i>Eden CORRALES, Pedro de PACO, Oscar MENENDEZ, Jordi VERDU</i>	239
MODELLING AN FABRICATION OF FBARs BASED ON NITRIDES MICROMACHINED MEMBRANES	
<i>Dan NECULOIU, Alexandru MULLER, George KONSTANTINIDIS, C. MOROSANU, Dan VASILACHE, A. KOSTOPOULOS, A. STAVRINIDIS</i>	249
DEVELOPMENT OF A LAMB-WAVE SENSOR FOR BIOLOGICAL APPLICATIONS	
<i>A.K. PANTAZIS, E. GIZELI, A. ADIKIMENAKIS, A. GEORGAKILAS, A. STAVRINIDIS, G. KONSTANTINIDIS</i>	255

**35 GHz ANALOG PHASE SHIFTER BASED ON
PUSH-PULL TOGGLE MEMS VARACTOR**

F. SOLAZZI, P. FARINELLI, B. MARGESIN, R. SORRENTINO 265

**A Ka-BAND TRUE-DELAY-LINE PHASE SHIFTER
USING CAPACITIVE MEMS SWITCHES**

*Themistoklis PRODROMAKIS, Christos PAPAVALASSILOU,
Kostis MICHELAKIS* 273

**ONE SINGLE DMTL-BASED CIRCUIT FOR RF-MEMS
IMPEDANCE TUNERS AND PHASE SHIFTERS**

*Tatyana PURTOVA, Tauno VÄHÄ-HEIKKILÄ, Till FEGER, Thomas LISEC,
Joachim JANES, Bernd WAGNER, Hermann SCHUMACHER* 281

**RECONFIGURABLE RF-MEMS BASED IMPEDANCE MATCHING
NETWORK FOR A CMOS POWER AMPLIFIER**

*J. IANACCI, A. GNUDI, B. MARGESIN, F. GIACOMOZZI,
L. LARCHER, R. BRAMA* 289

**NUMERICAL SIMULATION OF A CATHODE MICRO-UNIT
WITH SILICON FIELD EMITTER**

V.A. FEDIRKO, S.V. POLYAKOV 297

**DIMENSIONING OF THE STOPPERS USED TO REDUCE
THE STICKING EFFECT IN ELECTROSTATIC
CAPACITOR SWITCHES**

*H. ACHKAR, J. RUAN, C. VILLENEUVE, D. PEYROU,
F. PENNEC, M. SARTOR, P. PONS, R. PLANA* 301

**STICTION INDUCED BY DIELECTRIC BREAKDOWN
ON RF-MEMS SWITCHES**

A. TAZZOLI, E. AUTIZI, V. PERETTI, G. MENEGHESSO 311

**INVESTIGATION OF CHARGING PROCESSES IN
DIELECTRICS FOR RF-MEMS CAPACITIVE SWITCHES**

*E. PAPANDREOU, G. PAPAIOANNOU, F. GIACOMOZZI,
M. KOUTSOURELI, B. MARGESIN, S. COLPO* 321

**NANOSCALE INVESTIGATIONS IN DIELECTRICS CHARGING
BY ELECTROSTATIC FORCE MICROSCOPY**

*A. BELARNI, M. LAMHAMDI, P. PONS, L. BOUDOU, J. GUASTAVINO,
Y. SEGUI, G. PAPAIOANNOU, M. DILHAN, R. PLANA* 329

**RF MEMS DIELECTRIC CHARGING EFFECT ESTIMATION
DUE TO HIGH ENERGY ELECTRONS IRRADIATION**

V.G. THEONAS, G.J. PAPAIOANNOU, G. KONSTANTINIDIS 335

**EFFECT OF ENVIRONMENT HUMIDITY ON THE C-V
CHARACTERISTICS OF RF-MEMS CAPACITIVE SWITCH**

Zbigniew OLSZEWSKI, Russell DUANE, Conor O'MAHONY 345

FABRICATION OF RF MEMS COMPONENTS ON CMOS CIRCUITS

*A.G. MUKHERJEE, M.E. KIZIROGLOU, S. VATTI,
C. PAPAVALASSILOU, A.S. HOLMES, E.M. YEATMAN* 353

**ON-WAFER METHOD FOR EXPERIMENTAL CHARACTERIZATION
OF MEMS MATRIX, USING A TWO-PORT VECTOR NETWORK
ANALYZER**

*S. SIMION, R. MARCELLI, G. BARLOLUCCI,
G. SAJIN, F. CRACIUNOIU* 363

**DYNAMICS OF MICROMECHANICAL CAPACITIVE
SHUNT SWITCHES**

*Romolo MARCELLI, Andrea LUCIBELLO, Giorgio De ANGELIS,
Emanuela PROIETTI, Daniele COMASTRI* 371

**ELECTROMAGNETIC AND ELECTROMECHANICAL STUDY
OF A H-SHAPED MILLIMETER MEMS SHUNT SWITCH**

*Federico CASINI, Romain CRUNELLE, Michel FRYZIEL, Natalie ROLLAND,
Paul Alain ROLLAND, Paola FARINELLI, Roberto SORRENTINO* 381

FOREWORD

A lot of effort has been put into RF-MEMS technologies during the past years. In this new technology, the mechanical and electrical functions are combined to improve the performance of existing devices and circuits, to allow on-wafer system integration and the creation of completely new Microsystems. A broad range of components and subsystems have been demonstrated, with functions and performances that are significantly improved over conventional microwave and millimetre (mm)-wave technologies.

To realize the RF microsystem concept, research and collaboration in many different fields including fabrication technology, material science, electromagnetism, micromechanics, thermal and electrical modelling, characterization, packaging and reliability is required.

The main scope of the MEMSWAVE workshop is to bring together scientists from different universities, research institutes, and industrial companies interested in the development of the RF-MEMS field and to create a forum for the knowledge exchange between the RF-MEMS players. The workshop is now technically sponsored by the European Microwave Association (EuMA)

The MEMSWAVE workshop was generated by the European project “Micromachined Circuits for Microwave and Millimeter Wave Applications” <<MEMSWAVE>> (1998-2001) coordinated by IMT-Bucharest. The project was nominated between the ten finalists (from 108 participants) to the Descartes Prize 2002.

The first 2 editions of the MEMSWAVE workshop were organized at Sinaia (Romania) in 1999 and 2001. A special volume in the series Micro and Nanoengineering “Micromachined Microwave Devices and Circuits” was dedicated to the second edition of the workshop and was published in 2002. Starting from 2002, the MEMSWAVE workshops became an itinerant European event. The next editions were held in Heraklion and Toulouse. From 2004 the MEMSWAVE workshop was connected to the European FP6 Network of Excellence in RF MEMS “AMICOM” and was strongly supported by this network. Most of the European teams involved in these

challenging topics were partners in the AMICOM project. The workshop was organized in Uppsala (2004), Lausanne (2005), Orvieto (2006), Barcelona (2007) and became important instruments for knowledge dissemination of the AMICOM network results.

In 2008 took place the first MEMSWAVE following the completion of AMICOM. However, the significant number of contribution has manifested the lasting support of the European RF MST community to this event.

It is now a tradition to publish the extended version of the papers of the Series of Micro and Nanotechnologies of the Romanian Academy Press. Previous volumes may be requested at IMT-Bucharest (print@imt.ro). The present volume contains the papers presented at the 9th edition of the MEMSWAVE workshop organized by the Foundation for Research & Technology Hellas (FORTH) in July 2008, at Fodele, Greece.

Editors

How to Build a Reliable RF MEMS Switch

Gabriel M. REBEIZ

University of California, San Diego, ECE Department, La Jolla, CA 92093, USA

Phone: +1-858-534-8001

Abstract. This paper discusses the successes and pitfalls in building RF MEMS switches. It is the author's opinion, after 11 years in the field of RF MEMS, that factors which are *not* related to microwave engineering have the largest impact on RF MEMS viability. The field may therefore be shifting from one which was traditionally based on microwave engineering to one where chemical, mechanical and manufacturing engineering play a vital role in the success of this endeavor. Also, a realistic view of the role of RF MEMS should be taken, and one should only develop components which have a large chance of grabbing a decent market share. As will be shown in this paper, there are few RF MEMS components or sub-systems which are viable in today's competing technologies.

1. INTRODUCTION

RF MEMS (In this paper, RF MEMS refers to the field of metal-based MEMS, which is used to build switches (both capacitive and metal-contact), tunable capacitors and inductors, and switched-capacitor banks. It does not refer to the silicon-based or the piezo-based RF MEMS which is used to build high-Q ($Q > 1000$) resonators and filters.) has been in an active research area since 1986 with the development of the low-loss MEMS capacitive and metal-contact switches by Raytheon and Rockwell Scientific, respectively. These switches demonstrated state-of-the-art performance up to 50 GHz and ignited a very active research field. To-date, at least two textbooks and hundreds of research papers have been written on RF MEMS, and state-of-the-art components such as low-loss switches from DC-110 GHz, single-pole multiple-throw switches, phase shifters, tunable matching networks, tunable filters, and tunable antennas have been demonstrated from 1 GHz to 100 GHz. In every case, the RF MEMS-based circuit resulted in state-of-the-art performance which exceeded by a large margin the performance of equivalent circuits built using solid-state devices (Schottky diodes, p-i-n diodes,

GaAs transistors, etc.). Many consulting companies have even predicted that by 2007, we will RF MEMS in cell phones with a market share of billions of dollars. But as is well known, RF MEMS is still a niche industry and with very small numbers being actually being sold and used (it is true that there are several start-up companies and groups who are actively trying to build large-scale RF MEMS, but as of this writing, there is no breakthrough yet). So, why, after 12 years, is RF MEMS still not widely developed? This paper will attempt to answer this question using the hardearned author's experience.

2. OVERVIEW OF THE BEST SWITCHES

A look at the RF MEMS field results in just four high reliability switches which are used on a medium scale to build components and sub-systems. These are: 1) Radant MEMS (metal-contact), 2) MIT-Lincoln Labs (capacitive), 3) Raytheon (capacitive) and 4) Omron (metal-contact). All of these switches (except Omron) have been tested to > 100 billion cycles over tens if not hundreds of individual units, and some Radant MEMS switches have completed 1 trillion cycles at 100 mW of RF power (cold-switching) with no failures. The Omron switch is slow and therefore has been tested to only 100 million cycles. The capacitive switches do not operate down to DC frequencies, but on the other hand, are excellent at hot-switching, and both the MIT-LL and the Raytheon switches have been tested at 0.5-1 W hot switching and performed very well to billions of cycles. All test frequencies are around X-band (8-12 GHz). The Radant MEMS, Omron and the MIT-Lincoln Labs designs are built on high-resistivity silicon substrates and packaged using either a glass-frit or anodic-glass bonding technology (Radant, Omron) or using gold-to-gold thermo-compression (MIT-LL). The Raytheon switch can be built on silicon or ceramic substrates and is packaged using a gold-type seal (not released).

There are other switches or switched-capacitors which are being demonstrated and with good reliability: Memtronics (capacitive), XCOM (metal contact), RFMD (metal-contact), Philips NXP (capacitive), Wispry (capacitive), UCSD (capacitive) and the University of Limoges (capacitive). All of these devices have shown operation to hundred of millions or billions of cycles. The Memtronics and the RFMD switches are packaged in-situ using a thin dielectric-cap which has the potential to reduce the manufacturing costs for very large numbers. To the authors' knowledge, Teravicta, ST, Rockwell Scientific, Northrop Grumman, Bosch, HRL have closed or drastically scaled back their RF MEMS effort.

3. RF MEMS FIELDS OF USE

I. Phase Shifters: RF MEMS was first developed to solve a serious problem in phased arrays. To recall, in the late 1990's, GaAs technology was quickly becoming a mature technology with state-of-the-art low noise amplifiers and very

high efficiency power amplifiers. However, the MESFET was still a relatively poor switch with a figure-of-merit “cutoff” frequency of 200-400 GHz, and this resulted in MMIC phase shifters with high loss at mm-wave frequencies (8-14 dB loss for a 4-bit phase shifter at 35 GHz). RF MEMS switches, with their near-ideal performance, promised mm-wave phase shifters with a loss of only 3 dB for a 4-bit design. This drastic increase in performance could pave the way to lower cost phased arrays (from 10 GHz to 94 GHz) and RF MEMS was funded to achieve this performance. It is important to note that RF MEMS did deliver on this promise, and many companies and groups demonstrated extremely low-loss phase shifters from 6 GHz to 100 GHz using capacitive or metal-contact switches, and RF MEMS phased arrays were developed for both commercial (automotive radars, SATCOM) and defense applications. However, it is not GaAs which stopped RF MEMS phase shifters but CMOS and SiGe! It is now possible to build high performance phase shifters to 77 GHz using extremely small CMOS or SiGe phase shifters with a current consumption of only 4 mA from a 1.5-2 V supply. RF MEMS is therefore now only used for truetime delay phase shifters where wideband performance (2-18 GHz, 18-40 GHz) and large delay times are imperative for the operation of the wideband phased array.

II. Switching Networks: The low-loss performance of RF MEMS opened other avenues, mainly the vast area of microwave switching networks used in test instruments, general-purpose reconfigurable test stations, satellite systems, telephone/internet routing networks, and wireless base-stations. In this area, RF MEMS was supposed to replace the ubiquitous relay which is relatively large and heavy. RF MEMS delivered on the size and switching speed, and could achieve much larger reliability numbers than the standard relay (hundreds of millions vs. 1-2 million cycles for the relay), but could not deliver on latching designs or the high power handling. Still, there is a niche market for RF MEMS in this arena. These are: a) low-cost non-latching relays and b) very low-cost, very high volume SPNT switches for cell phone applications. This application is appealing since one can build the RF MEMS directly on-top of the CMOS substrates. However, one must be able to produce tens if not hundreds of millions of units and for very low cost (around 5 cents a throw). This is not for the lighthearted.

III. Reconfigurable Networks: Reconfigurable matching networks, tunable filters and tunable antennas is where RF MEMS has shined in the past 5 years. This is due to a congruence of factors: a) very low insertion loss and high Q, b) very high linearity ($IP_3 > 60$ dBm), c) capability of handling Watts of RF power (0.5-3 W) or large RF voltage swings (10-40 V), d) small size and zero power consumption and e) wide temperature performance (when well designed). None of the available tuning technology available today, such as Schottky diodes, p-i-n diodes, ferrite and ferroelectric tuners can achieve these conditions and this is where RF MEMS shines. For the first time, RF MEMS is not replacing a technology with proven performance, but in this case, it is currently the *only*

technology which can meet these specifications. It is for this reason that many companies and research groups are developing power amplifier tuning networks and tunable antennas based on RF MEMS. The application areas are in high efficiency PA networks and reconfigurable antennas for multi-standard mobile phones or for wideband electronic warfare or countermeasures. Other groups are developing low-loss tunable filters, either for commercial applications (multistandard cell phones) or for defense applications (cognitive radios, etc.). It is clear that the first large scale RF MEMS products will be developed in this area for mobile phones. Still, the path forward is still not crystal clear since SOI CMOS transistor switches have advanced greatly in the past 3 years, and can now nearly meet the five requirements (loss, linearity, voltage/power handling, small size/power consumption, temperature). Also, some companies claim that Ferroelectrics can also meet these 5 requirements. It is clear that RF MEMS can play a vital role here, and in the future, given equal performance for all of these three technologies, the final decision will be based on reliability and costs.

4. WHY IT IS HARD TO BUILD RF MEMS

RF MEMS, which has been pioneered by the microwave community since they saw the need for such an ideal device, is essentially a mechanical device with serious constraints on planarity, contact material, contact and release forces, and dielectric and metal layers. Also, packaging and any contamination added during this process can seriously degrade the RF MEMS device performance. It is for this reason that an RF MEMS development team should have not only the microwave engineer for design and test, but also should have a mechanical engineer, a chemical/surface science engineer, a processing engineer, a packaging engineer and finally a manager who has the background and the patience to lead such a diverse group of people. In fact, RF MEMS are quite easy to model from a microwave circuit perspective and commercial software such as ADS Momentum, Sonnet, HFSS, CST, and IED all do a wonderful job for the full-wave electromagnetic analysis and model extraction of the RF MEMS device. This means that the RF circuit design is one of the easiest aspects of the problem and requires very little microwave design work. It is therefore strange that this area has always been led by the IEEE microwave group and not by the mechanical engineering department.

Where are the problems in RF MEMS? They have very little to do with electrical engineering! They are mostly in actuator design which can withstand large temperatures encountered during packaging (mechanical engineering), stress control of all the layers used (manufacturing), metal contacts and related contamination (chemical engineering/surface physics), in dielectric charging (chemical engineering/surface physics) and in hermetic packaging (mechanical engineering). Some of these problems, such as stress control or dielectric charging,

are poorly understood and cannot be transported from one foundry to the other or even from one deposition machine to the other. Other problems are hard to quantify, such as metal-contact contamination and the exact cause of switch failure, and others are well known but hard to implement well without the adequate funds (such as wafer-scale packaging). The highly reliable RF MEMS switches developed to-date either use robust and mechanically simple designs (Radant MEMS), or intricate features designed to solve several of these issues (Raytheon, MIT-LL). But the most important part is that none developed a reliable and manufacturable RF MEMS switch in 1-2 years. Each took more than 5 years to achieve the high reliability designs, and after countless experiments to understand their processes. This is perhaps one of the main limitations of this technology: Very few have the funding and the patience required to develop a large-scale RF MEMS effort with high yield. But for the ones who do, the pay off can be very high from the commercial and defense perspective.

5. CONCLUSION

This paper discusses some of the aspect for large scale RF MEMS design and manufacturing. It is seen that the microwave/electrical engineering aspect of the project, while important, is not the crucial factor for RF MEMS, but it is the unknowns and the hard-to-quantify which are the main limitations of this technology (stress, contamination, charging, etc.). Still, with experience and a good team, it the author's opinion that one can build a high reliability, high volume RF MEMS switch in 2-3 years.

Acknowledgement. The author wishes to acknowledge the men and women working in the area of RF MEMS for the past 12 years.

Combination of 2D and 3D Method of Line Approach for the Accurate Loss Determination in RF MEMS Circuits

Larissa VIETZORRECK

Institut für Hochfrequenztechnik, TU München, Arcisstr. 21, 80333 München, Germany

E-mail: vietzorreck@tum.de

Abstract. In RF MEMS circuits one crucial point is the accurate determination of loss, caused by lossy substrate or conductors. Substrate loss can play a role if lossy silicon is used as substrate material, conductor loss can be important if thin layers are used as conductors as the underpass or membrane in RF MEMS switches. Existing modeling tools usually underestimate the loss caused by thin conductors, as the used models are not appropriate or the discretization of the metal conductor is not sufficient. This can be a critical point in the design, when for the resulting device a strict requirement regarding insertion loss is given as usually done for RF MEMS switches.

1. INTRODUCTION

The Method of Lines is a fullwave numerical method, based on a finite difference discretization scheme. The difference to commercially used finite difference solvers is that the discretization is only performed in 2 directions of the relevant coordinate systems, whereas in the remaining direction the calculation is analytical. If this direction is chosen to be the propagation direction of the wave in the considered structure, the 2D analysis of the cross-section performed with finite differences gives a set of propagating modes for each homogeneous part of the device. In the second step the related field is propagated to the interfaces of this homogeneous section and matched to the fields of the adjacent section. Thus the scattering parameters are derived by the repeated matching and propagation procedure throughout the structure.

This 3D algorithm [1] is very well suited for the analysis of cascaded devices like distributed loaded line phase shifters, where we have a high number of concatenated sections combined with small lateral dimensions. However, if substrate or conductor loss occurs in the structure, than - as in other methods - a very fine discretization is needed to account for the accurate determination of the

loss. The required fine discretization of the cross-section with sufficient discretization points also within the conductor will enlarge the numerical problem drastically. The resulting computation times will be slow and not any more suited for an optimization process.

The MoL algorithm can also be performed in only two dimensions for longitudinally homogeneous structures like transmission lines [2]. For the 2D problem only a one-dimensional discretization becomes necessary. In an eigenvalue analysis the propagation constants of the various modes of interest can be determined with high accuracy but low numerical effort. However, with this approach the incorporation of discontinuities is not possible.

The idea is now, to combine both approaches in order to get an efficient tool for considering accurately the loss of a 3D structure with comparable low numerical effort. Therefore the analysis of the 3D structure will be performed as usual with the 2D MoL approach and a coarse discretization, which will not fully consider the conductor loss. For the critical sections – e.g. sections containing thin membranes or underpasses, where the loss will be highly contribute – an additional quick analysis of the propagation constant will be performed using the 1D approach. The crucial point in the usual procedure of finding eigenvalues, namely the definition of an appropriate starting value, is easy in this case, as the 2D approach will already give an approximate value, which is close enough to guarantee a fast convergence of the root finding process. The relevant propagation constant of the 2D process will then be updated by the far more accurate result of the 1D calculation. If more modes than the fundamental mode are propagating, this correction can be increased to all propagating modes. A correction of the evanescent modes, which are bound to the discontinuity will not be necessary, also the resulting field distribution needs not to be altered, as the discretized field distributions exhibit only negligible differences between the two mentioned cases.

2. MOL-APPROACHES

A. 3D Approach

For the 3D MoL approach the structure under consideration is divided into longitudinally homogeneous sections. For each section the Helmholtz equation for the potential with two components is established (with the orientation of the components of the potential in transversal direction as the cross-section of the structure). Each section is subjected to a two-dimensional discretization using a finite difference scheme with central differences. A sketch of the cross-section of the structure with the location of field and potential components is shown in Fig. 1.

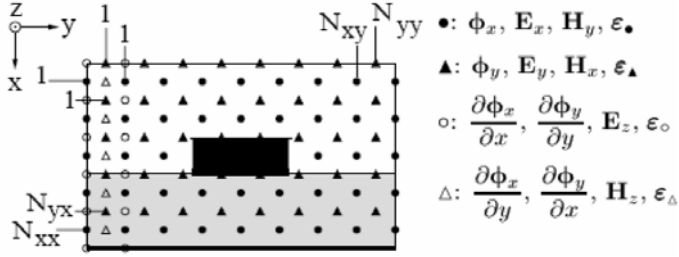


Fig. 1. Discretized cross-section of the structure with all components of fields and potential (discretization lines in propagation (horizontal) direction, 2D discretization).

All analytic derivatives in transversal directions are now replaced by the corresponding numerical difference operators. The remaining discretized set of wave equations exhibits only an analytical dependence in z-direction (propagation direction of the wave within the component). However, the single equations are coupled.

The following steps to solve the wave equation are usual in the method of lines and in detail described in [1].

- The wave equation is transformed to principle axes in order to decouple the set of wave equations. The decoupled equations are solved, each equation giving a mode of the structure with a certain field distribution and a propagation constant γ_i .
- The total field (as a superposition of all modes) is calculated at the interfaces of the sections.
- The tangential field components are matched, given the unknown amplitudes of the different modes.
- By concatenating all sections the scattering matrix of the component can be derived.

This algorithm is very well suited for the investigation of components, consisting of a high number of concatenated sections like filter elements, distributed MEMS transmission lines or phase shifters.

A drawback, as also in other full discretizing methods, is the fact, that the cross-section needs to be discretized. If the cross-section of a structure exhibits tiny features like very thin layers, the used discretization mesh has to be very fine to resolve all these details, thus increasing the number of discretization points as well as the computation time. Unfortunately the same mesh is needed for all sections of the structure in order to perform an accurate matching procedure, even if the discretization in other sections doesn't need to be that fine, as no small details are contained. Therefore the existence of just one thin layer in one of the sections will increase the numerical effort drastically, if accurate results are needed. If the mesh is chosen to be coarse, the total result will be less accurate, as the propagation and

especially attenuation constants in one subsection are not determined correctly.

In Fig. 2 an example of the convergence of the propagation and attenuation constant in one subsection containing a thin and lossy conductor is depicted. The computed results dependent on the number of discretization points is shown. N_x denotes the number of discretization points in vertical direction, N_y the number in horizontal direction of the cross-section. As a nonequidistant discretization scheme is used, the convergence is not smooth. As it can be seen, the attenuation constant is much more sensitive to the used mesh density as the propagation constant.

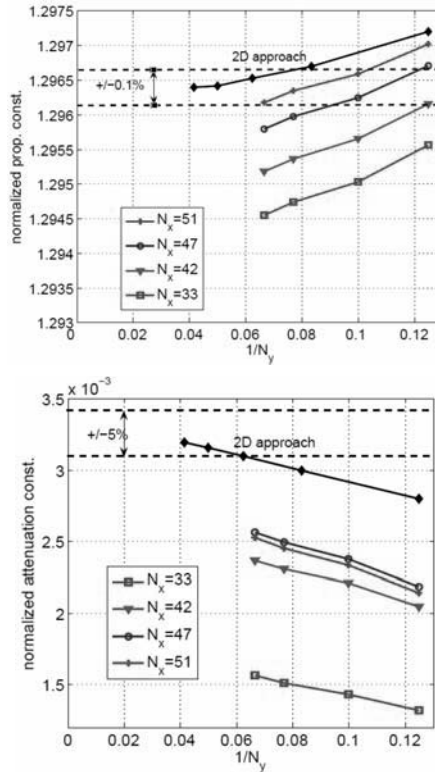


Fig. 2. Convergence of propagation and attenuation constant of thin lossy transmission line.

B. 2D Approach

The Method of lines can also be used for the twodimensional analysis of longitudinally homogeneous components like transmission lines. Here only a onedimensional discretization is required, the discretization lines are chosen in vertical direction and an eigenmode problem has to be solved. A detailed description of this approach can be found in [2]. Here only the essential steps are briefly described.

- The structure is divided now into layers, which have to be homogeneous in vertical direction. The layers are discretized as it can be seen in Fig. 3.

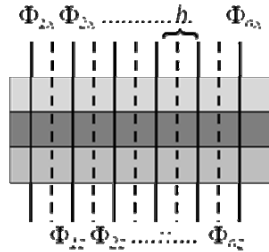


Fig. 3. Discretization Scheme of the 2D approach (discretization lines in vertical direction, 1D discretization).

- Matching the field components at the layer interfaces will yield a matrix system in the transformed domain, where the eigenmodes are the propagation constants of the transmission line. Compared to the eigenmodes calculated with the 3D approach a much higher accuracy is obtained with much less discretization effort, as the necessary discretization is only one-dimensional instead of two-dimensional Fig. 2.

Drawback of this approach is that only longitudinally homogeneous lines can be investigated, even without connection to any input or output lines. For 3D structures that special approach is not applicable.

C. Combination of Methods

As it has been shown in [3, 4], the calculated eigenmodes in the 3D case can be divided into accessible and localized modes Fig. 4. The localized modes are only important for the field matching procedure at the interfaces, whereas the accessible modes propagate through the sections from interface to the other. Those accessible modes will contribute mainly to the overall conductor loss.

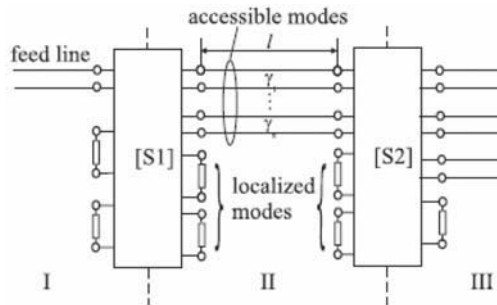


Fig. 4. Network representation of coupling inside section II by accessible modes with complex propagation constant γ_i . Localized modes are bound to one discontinuity.

An accurate computation of the propagation constant in the 3D case is therefore essential. However, instead of refining the mesh size more and more at the cost of severely increased computation times, it is possible to replace the relevant 3D propagation constants by the more accurate values of the 2D computation.

One difficulty of the 2D eigenmode approach is in general that a suitable starting value has to be defined to find the roots of the eigenmode system. Here the already computed values of the 3D approach can be used: they are already close to the desired value such that the root finding is run quickly.

3. RESULTS

The described procedure has been applied to coplanar waveguide, where the middle section is a lossy underpass, as usual in RF MEMS switches. A correction of the evanescent modes, which are bound to the discontinuity will not be necessary, also the resulting field distribution needs not to be altered, as the discretized field distributions exhibit only negligible differences between the two mentioned cases.

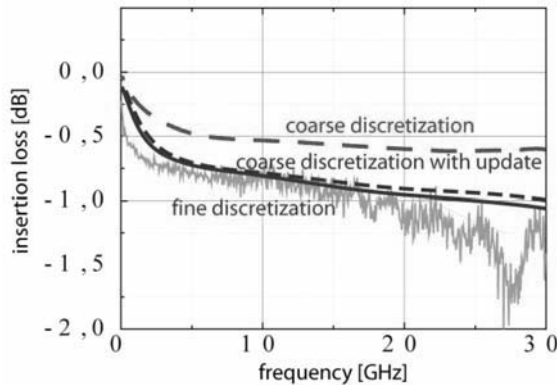


Fig. 5. Comparison of computed insertion loss for conventional 2D algorithm with fine and coarse discretization and new approach for CPW line with lossy underpass. The computation of the new approach is 10 times faster than the fine discretization.

4. CONCLUSION

A new algorithm based on the method of lines (MoL) has been developed, combining the advantages of the existing two and three-dimensional algorithms. Critical sections with high loss are e.g. parts of an RF MEMS switch with underpass oder thin lossy membrane. Here a very dense discretization is needed in order to achieve a precise estimation of the insertion loss in the 3D algorithms. The relevant propagation constants obtained in the 3D approach are updated by the

more accurate results of a 2D approach, which can compute propagation constants of a homogeneous section much faster, as only a one-dimensional discretization is required. With a coarse discretization plus update the same accuracy is obtained as with a dense discretization, The computation time is reduced by a factor of ten.

References

- [1] L. VIETZORRECK, R. PREGLA, *Hybrid Analysis of 3-D MMIC Elements by the Method of Lines*, IEEE Trans.MTT., **44**(12), pp. 2580–2586, December 1996.
- [2] R. PREGLA, W. PASCHER, *The Method of Lines*, in Numerical Techniques for Microwave and Millimeter Wave Passive Structures, T. Itoh, (Ed.), J. Wiley Publ., pp. 381–446, New York, USA, 1989.
- [3] C.J. RAILTON, T. ROZZI, *The rigorous analysis of cascaded step discontinuities in microstrip*, IEEE Trans. Microwave Theory Tech., **MTT-36**(7), pp. 1177–1185, July 1988.
- [4] L. VIETZORRECK, W. PASCHER, *Efficient Analysis of Cascaded Structures by the Method of Lines (MoL)*, in Fields, Networks, Methods, and Systems in Modern Electrodynamics, pp. 95–102, Springer, Berlin, Germany, 2004.

Low Loss Piezoelectric SPMT RF MEMS Switches

David J. CHUNG¹, Ronald G. POLCAWICH², Daniel JUDY²,
Jeffrey PULSKAMP², John PAPAPOLYMEROU¹

¹Georgia Institute of Technology, Electrical and Computer Engineering, Atlanta, GA, USA

²US Army Research Laboratory, AMSRD-ARL-SE-RL,
2800 Powder Mill Rd., Adelphi, MD, USA

Abstract. This paper presents Single Pole Double Throw (SP2T) and Single Pole Four Throw (SP4T) switches using piezoelectric micro-electro-mechanical (MEMS) switches measured from DC to 50 GHz. The overall performance of the switches shows better than 20 dB isolation up to 50 GHz when the MEMS switches are in the off or zero volt state. When the switches are actuated with 7 V, the SP2T shows less than 1.8 dB of insertion loss while the SP4T on average, shows less than 2 dB of insertion loss up to 40 GHz.

1. INTRODUCTION

Over the past decade, rapid technology advances in RF MEMS switches have been promising for phase shifters and phased array antennas used in communication and radar systems. These micro-devices allow low loss, low power consumption, wideband performance, and high isolation, which are all great RF characteristics compared to traditional transistors and diodes [1]. Much of the research has been focused on electrostatic actuation because of the ease of fabrication and being relatively free from restraint of materials. However, electrostatic actuation requires higher voltages than desired with values ranging from 20 to 100 V.

In attempts to lower this actuation voltage while maintaining the same RF performance, piezoelectric actuation has been chosen as a promising choice. Using lead zirconate titanate (PZT) material, RF MEMS switches have been measured to have low actuation voltage with great RF characteristics from DC to 65 GHz [2], [3], [4], [5]. The actuation voltage is as low as 2 V with insertion loss less than 1 dB and isolation greater than 20 dB for frequencies up to 40 GHz.

Using RF MEMS switches, SP4T junctions have been presented in the past for RF applications, such as phase shifters and phased arrays [6]. In order to improve the RF performance of these devices, it is essential to obtain good responses from each of the switching components.

For the first time, this paper presents a SP2T and a SP4T device operated with PZT MEMS switches similar to the one shown in Fig. 1. Similar SP2T and SP4T devices have been tested with electrostatically actuated MEMS. Tang *et al.* [7] reported a SP2T with 12.5 V actuation and 0.9 dB at 20 GHz. Muldavin *et al.* [8] reported a SP4T with 0.26 dB loss but with higher actuation voltage. In this paper, 0.75 dB loss at 20 GHz with an actuation voltage of 7 V for the SP4T is reported. The circuits have been fabricated using surface micromachining technology developed at the Army Research Laboratory (ARL).

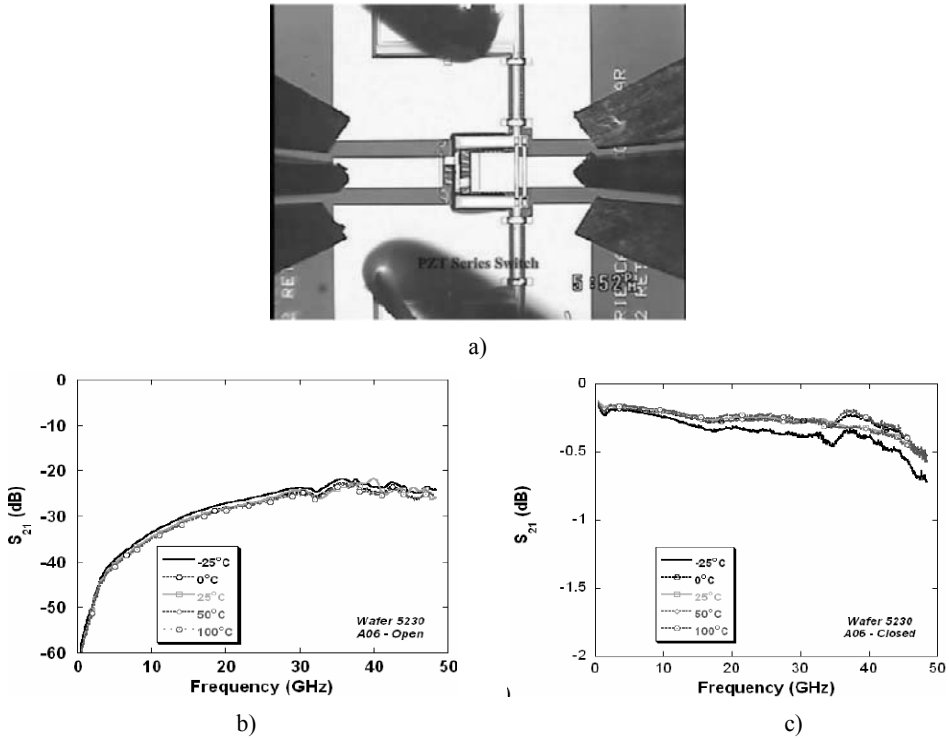


Fig. 1. (a) Fabricated single PZT switch (b) open state (c) closed state at 10 V [5].

2. SWITCH DESIGN

Individual PZT switches have been designed at ARL as shown in Fig. 1. The switches show great RF characteristics of greater than 20 dB isolation and less than

0.5 dB loss up to 50 GHz. These switches are used in the design of a SP2T and a SP4T that have been simulated with ADS Momentum and HFSS. Some.

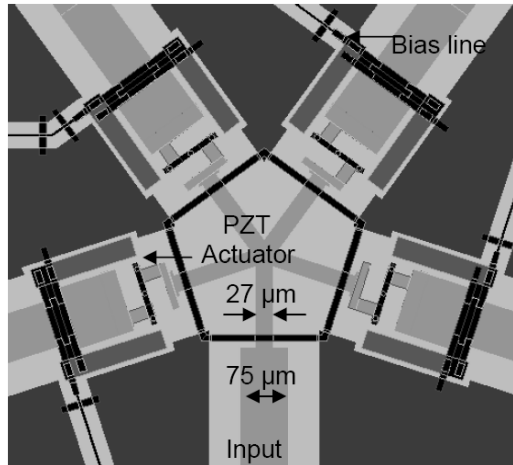


Fig. 2. Layout of the designed SP4T and the PZT MEMS switches.

Some tradeoffs have been taken as the simulations are simplified ideal case versions in order to reduce the simulation time to more manageable levels. The overall size of the final design is $1.6 \text{ mm} \times 2.2 \text{ mm}$ and the individual switches take up about $230 \text{ } \mu\text{m} \times 200 \text{ } \mu\text{m}$. The layout and dimensions are shown in Fig. 2. The signal line width is $75 \text{ } \mu\text{m}$ and the optimal simulated performance came with a spoke width (the line width in the spoke region) of $27 \text{ } \mu\text{m}$. All bends in the circuit have been optimized for the best impedance match ranging from 20 to $25 \text{ } \mu\text{m}$. In addition, there are $15 \text{ } \mu\text{m}$ air bridges across all of the bends and discontinuities in the CPW line, and also along the $5 \text{ } \mu\text{m}$ actuator bias lines. The air bridges are for suppressing extra modes that can rise from the discontinuities as well as connecting the ground planes.

The fabrication was done at the ARL cleanroom facility. Starting with the seed layer of patterned Pt and PZT, next, the structural layer is patterned with ion etching that exposes the silicon for the eventual release etch. The CPW lines are patterned and the contact dimple is made for minimal contact area. Then, the sacrificial layer is patterned followed by the bridge layer. O_2 plasma is used to remove the sacrificial layer and XeF_2 is used to remove the silicon underneath the actuators. The bulk of the fabrication procedure is explained in detail in earlier publications [4, 5]. The only significant change in the fabrication process involves altering the sacrificial photoresist layer to enable a liftoff procedure to pattern the gold used for the air bridge and cantilevers. It should be noted that the open cavities near the switch junctions were created with the same XeF_2 etch step that releases the PZT actuators.

3. RESULTS AND DISCUSSION

Fig. 3a) shows the ADS Momentum simulation result as well as the measured response of the SP2T. Only S_{21} of the SP2T is simulated since the structure is symmetric. The dielectric loss is not included in the simulations as we merely want to optimize the structural dimensions.

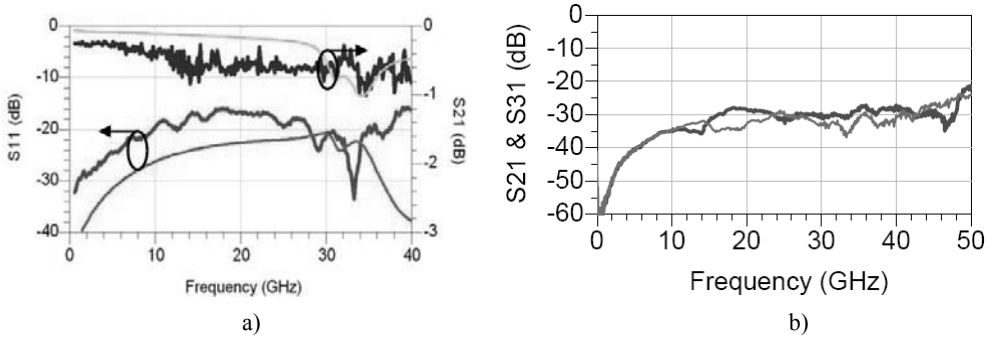


Fig. 3. a) Comparison of the simulated (thin lines) and measured responses (thick lines) of the SP2T, b) isolation.

This accounts for the simulated response having less loss compared to the actual measurements. As stated above, simulating a MEMS switch in a 2.5-D simulation has its limits. The optimal case has been taken in which the down state MEMS switch is replaced by a microstrip line. With the knowledge of the RF characteristics of a single PZT MEMS switch and the simulation results, we can estimate the expected loss of the actual SP2T. The PZT MEMS switch should add about 0.25 dB/switch of loss at 20 GHz and 0.5 dB/switch of loss at 40 GHz. Also, we should add an additional 0.25 dB of loss to include the dielectric loss. The expected actual loss will be 0.7 dB at 20 GHz and 1.2 dB of loss at 40 GHz.

The measurement of the s-parameters was carried out using an Agilent E8361A vector network analyzer from DC to 50 GHz. Looking at the measured response from Fig. 3(a), there is less than 2 dB of loss up to 40 GHz with an actuation voltage of 7 V. Also, the results agree well with the simulated response when accounting for the additional loss not in the simulated response. In Fig. 3(b), we can see that the isolation is greater than 20 dB from DC to 50 GHz for both the S_{21} and S_{31} responses. A DC current of 100mA is sent through the circuit in attempt to break through any residue that can be left on the contact point. The PZT switches have introduced parasitic capacitance and inductance as well as contact resistance that have not been accurately modeled in the initial simulations. Including accurate models of MEMS switches lead to memory problems and time consuming simulations that have been replaced with ideal modeling of the MEMS switches. We can conclude that there remains space for improving the matching of

the SP2T switch, but the overall response reflects the advantage of using PZT switches in this application.

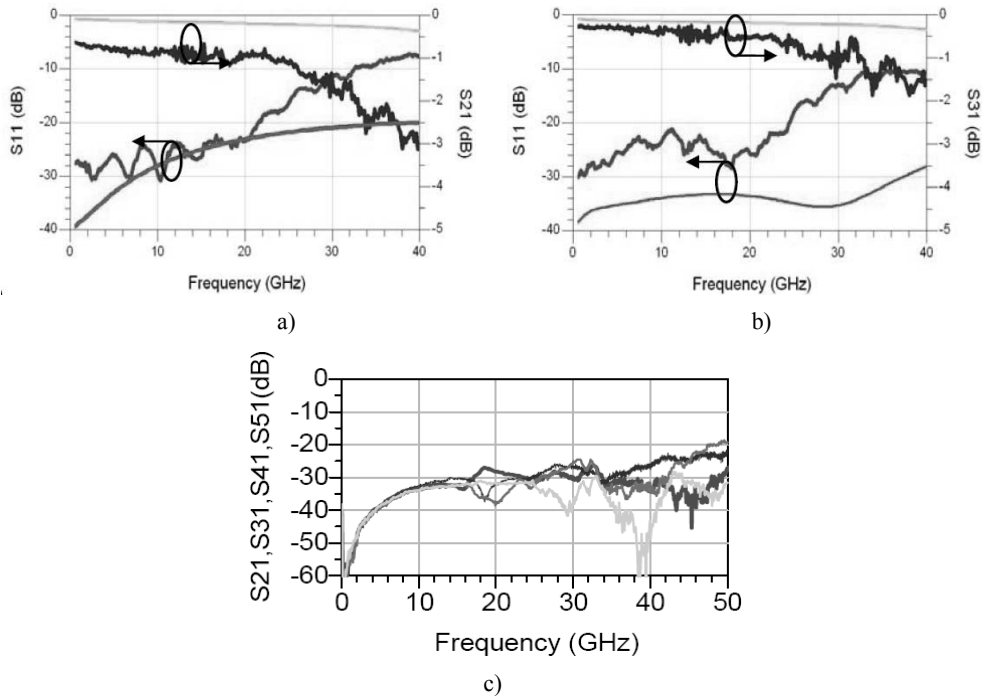


Fig. 4. Comparison of simulated (thin lines) and measured (thick lines) response of a) S_{21} and b) S_{31} and c) is the isolation of all paths.

Fig. 4 shows the comparison of the simulated and measured response of the SP4T. Only the S_{21} and S_{31} of the SP4T are simulated since the structure is symmetric as well. Similar to the estimation of overall loss done for the SP2T, we can estimate the expected loss for the SP4T. Adding the switch loss and dielectric loss, the resulting estimated overall loss of the SP4T should be 0.75 dB at 20 GHz and 1.5 dB at 40 GHz.

From Fig. 4a-b), we can see that on average, the insertion loss is less than 1 dB at 20 GHz and about 2 dB at 40 GHz. The reason for more loss in the S_{21} path is because the bend at the junction is greater than that of the S_{31} path, which makes it harder for the signal to propagate. The return loss is greater than 15 dB up to about 30 GHz. Similar to the SP2T switch, the SP4T does not exhibit a great match at higher frequencies in contrast to the modeling predictions. Looking at Fig. 4c), the isolation is greater than 20 dB up to 50 GHz. Comparing to the simulated and estimate results, we have an additional 0.5 dB of loss to account for.

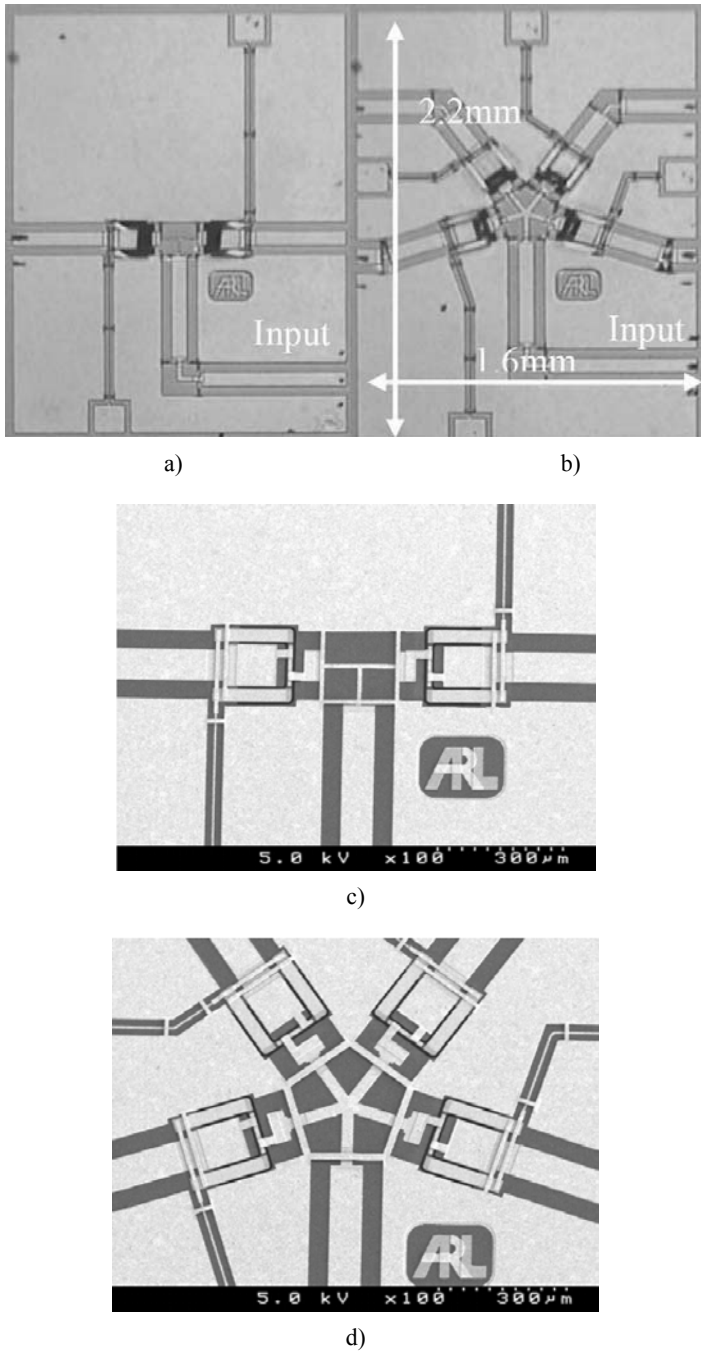


Fig. 5. Fabricated a) SP2T and b) SP4T and SEM pictures of c) SP2T and d) SP4T.

Possible reasons include contact contamination from the fabrication process and discrepancies between the simplified simulation and the actual switch response. The additional loss is not a big deviation from the measured results and the overall response is well estimated with the simulations. The reflection still has room to improve with better modeling of the PZT MEMS switch in the SP4T simulation.

Fabricated devices are shown in Fig. 5. The SP2T in Fig. 5(a) and 5(c) has one input and two PZT MEMS switches leading to the outputs. The SP4T shown in Fig. 5(b) and 5(d) has one input and four PZT MEMS switches leading to outputs. In both cases, any given path will require one PZT MEMS switch to operate. The overall dimension is 2.2 mm by 1.6 mm.

4. CONCLUSION

A SP2T and SP4T switch has been designed, fabricated, and measured taking advantage of the great RF characteristics of PZT MEMS switches. With high isolation and low loss beyond 40 GHz along with a low actuation voltage of 7 V, the SP2T and the SP4T switch show promising use for RF applications, such as phase shifters and phased arrays. The isolation is below -20 dB from DC to 50 GHz and the insertion loss is less than 1.8 dB up to 40 GHz for the SP2T and less than 2 dB up to 40 GHz for the SP4T.

Acknowledgement. The authors wish to acknowledge the assistance and support of Joel Martin and Brian Power of General Technical Services and Richard Piekars from the ARL for their assistance with device fabrication.

References

- [1] G.M. REBEIZ, *RF MEMS Switches: Status of the Technology*, in IEEE Transducers Dig., Boston, MA, pp. 1726–1729, June 2003.
- [2] H.C. LEE, J.Y. PARK, J.U. BU, *Piezoelectrically Actuated RF MEMS DC Contact Switches With Low Voltage Operation*, IEEE Microwave Wireless Comp. Letter, **15** (4), pp. 202–204, 2005.
- [3] H.C. LEE, J.H. PARK, H.J. NAM, J.U. BU, *Design, Fabrication, and RF Performance of Two Different Types of Piezoelectrically Actuated Ohmic MEMS Switches*, J. Micromech. Microeng., **15**, pp. 2098–2104, 2005.
- [4] R.G. POLCAWICH, J.S. PULSKAMP, D. JUDY, P. RANADE, S.T. MCKINSTRY, M. DUBEY, *Surface Micromachined Microelectromechanical Ohmic Series Switch Using Thinfilm Piezoelectric Actuators*, IEEE Transactions Microwave Theory and Techniques, **55**(12), pp. 2642–2654, December 2007.
- [5] R.G. POLCAWICH, D. JUDY, J.S. PULSKAMP, S.T. MCKINSTRY, M. DUBEY, *Advances in Piezoelectrically Actuated RF MEMS Switches and Phase Shifters*, IEEE MTT-S Microwave Symposium, pp. 2083–2086, June 2007.
- [6] G.M. REBEIZ, *RF MEMS: Theory, Design, and Technology*, Wiley, John & Sons, Inc. Jan. 2003.

- [7] M. TANG, A.Q. LIU, A. AGARWA, *A Compact DC–20 GHz SPDT Switch Circuit Using Lateral RF MEMS Switches*, *Asia-Pacific Microwave Conference Proceedings*, **2**, December 2005.
- [8] J. MULDAVIN, C. BOZLER, C. KEAST, *Wafer-Scale Packaged RF-MEMS Switches*, *IEEE MTT-S Microwave Symposium Digest*, June 2006, pp. 267–270.

Paper-Based Inkjet-Printed Antennas and Wireless Sensor Modules: The New Paradigm for Wearable and Biomonitoring Electronics?

M.M. TENTZERIS¹, R. VYAS¹, A. RIDA¹, L. YANG¹,
A. TRAILLE^{1,2}, C. KRUESI¹

¹GEDC/ECE, Georgia Tech, Atlanta, GA 30332-250, USA

²GTRI-SEAL, Georgia Tech, Atlanta, GA, USA

Abstract. In this paper, inkjet-printed flexible antennas fabricated on paper substrates are introduced as a system-level solution for ultra-low-cost mass production of UHF Radio Frequency Identification (RFID) Tags and Wireless Sensor Nodes (WSN) in an approach that could be easily extended to other microwave and wireless applications. The presented material is a review of our group's major reported milestones in this area. First, we discuss the benefits of using paper as a substrate for high-frequency applications, reporting its very good electrical/dielectric performance up to at least 1 GHz. The RF characteristics of the paper-based substrate are studied by using the microstrip ring resonator in order to characterize the dielectric properties (dielectric constant and loss tangent). Then, we give details about the inkjet printing technology, including the characterization of the conductive ink, which consists of nano-silver-particles, while highlighting the importance of this technology as a fast and simple fabrication technique especially on flexible organic (e.g. LCP) or paper-based substrates. A compact inkjet-printed UHF "passive-RFID" antenna using the classic T-match approach and designed to match IC's complex impedance, is presented as a demonstrating prototype for this technology. In addition, the author briefly touches up the state-of-the-art area of fully-integrated wireless sensor modules on paper and show the first ever 2D sensor integration with an RFID tag module on paper, as well as the possibility of a 3D multilayer paper-based RF/microwave structures. The presented approach could potentially set the foundation for the development of low-cost light-weight autonomous nodes for cognitive intelligence applications and for wearable communication and biomonitoring systems.

1. INTRODUCTION

In the last few years, automatic identification requirements have increased tremendously in a multitude of areas, including logistics, Aero-ID, sensing, anti-counterfeiting, supply-chain, space, healthcare and pharmaceutical [i]. This

demand is further enhanced by the need for inexpensive, reliable, and durable wireless RFID-enabled sensor nodes [2]. There are a few major challenges in today's RFID technologies impeding a large-scale practical implementation, the most challenging one being the realization of ultra-low-cost tags. RFID tags for mass production. Another challenge is the variety of applications in different frequency bands around the world, ranging from the UHF band (900 MHz) to RF (2.4 GHz), and up to millimeter wave (60GHz).

The block diagram of Wireless Sensor Network architecture is presented in Fig. 1. Potential solutions for the module-level integration include printing the battery on the top with recharging energy-harvesting mechanisms such as light, pressure or temperature, printable sensors and technologies like flip-chip and TSSOP for the IC integration[3-6].

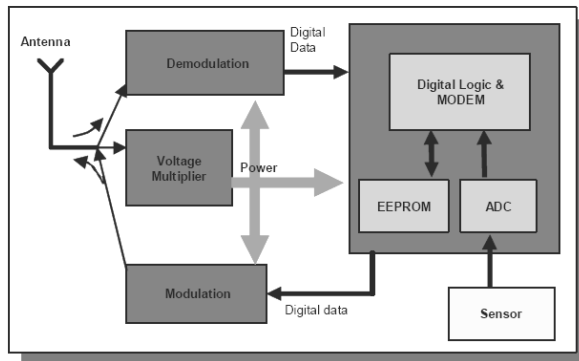


Fig. 1. Wireless Sensor Node Architecture.

Paper has all the attributes to be one of the most appropriate organic-based substrates for UHF and RF applications. Its wide availability, the high demand and the mass production make it the cheapest material ever made. Paper is suited for reel-to-reel processing and, more importantly, it is environmentally friendly. Paper also has low surface profile and, with appropriate coating, it is suitable for fast printing processes such as direct write methodologies instead of the traditional metal etching techniques. A fast process, like inkjet printing, can be used efficiently to print electronics on/in paper substrates. In addition, paper can be made hydrophobic and/or fire-retardant by adding certain textiles to it [7].

However, there are hundreds of different paper materials available on the market, varying in density, coating, thickness, texture, and implicitly, electrical properties and constitutive parameters (dielectric constant, loss tangent, etc.). That makes the RF characterization of paper substrates an essential step before any RF “on-paper” designs.

The dielectric characterization has been achieved by the authors for the UHF frequency range [8]. The results of dielectric constant and dielectric loss tangent have been used in the antenna design sections.

Inkjet-printing is a direct-write technology by which the design pattern is transferred directly to the substrate, and there is no requirement of masks contrary to the traditional etching technique which is widely used [9]. In addition, unlike etching which is a subtractive method by removing unwanted metal from the substrate surface and which also uses chemicals such as the etchants throughout the fabrication process, inkjet-printing jets the single ink droplet from the nozzle to the desired position, therefore no waste is created, resulting in an economical fabrication solution. This aspect, together with the fact that the chemicals necessary for etching are eliminated, makes this approach environmentally friendly also.

Since silver has the highest electrical conductivity of all metals; the inkjet-printing process uses silver nano-particle inks to ensure good metal conductivity. After the silver nano-particle droplet is driven through the nozzle, sintering process is found to be necessary to remove excess solvent and to remove material impurities from the depositions. Sintering process also provides the secondary benefit of increasing the bond of the deposition with the paper substrate [10]. The conductivity of the conductive ink varies from $0.4\sim 2.5\times 10^7$ Siemens/m depending on the curing temperature and duration time. Fig. 2 shows a photograph taken by a fiducial camera of the Dimatix Material Printer DMP-2800 of an edge section (hence showing the substrate to the left of the ink) of the T-match bowtie antenna of section 4. The total view width is 1.628 mm while the total height view is 1.221 mm with resolution of 2.54 microns.

Curing the nano-silver particles has to occur before any operation of the ink as a good conductor. Curing at lower temperature, large gap exists between the particles, resulting in a poor connection. When the temperature is increased, the particles begin to expand and gaps start to diminish. In this paper, the conductivity performance is ensured by a bulk inkjet-printed layer which allows the realization of the right metal thickness. Curing temperature of 100°C and duration time of ten hours is used in the following fabrication to sufficiently cure the nano-particle ink. However, other methods such as UV or photonic curing may be used, which takes up only few seconds. The inkjet printing on-paper approach is very repeatable, allows for features down to $20\mu\text{m}$ and can be easily utilized for other passive functions, such as filters, baluns in single or multilayer (multi-sheet) configurations [9].

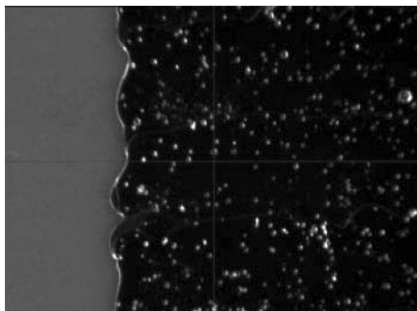


Fig. 2. Photograph of silver ink on paper by fiducial camera with a resolution of 2.54 microns.

As a preliminary demonstration to an all-printed RFID module [10], two passive RFID tags were developed in this section. Passive tags utilize energy from an RFID reader antenna to power up the IC and communicate with the RFID reader antenna through backscatter concept. The main challenge for this application was the miniaturization of the passive tags in the UHF RFID frequency range (at the lower end: 866 MHz to 868 MHz in Europe and the upper limit: 952 MHz to 954 MHz in Japan with US frequency band being 902 MHz to 928 MHz). Another challenge was the matching of passive RFID antennas to the impedance of the IC, which commonly exhibits complex (highly capacitive) behaviour, for optimum range and power flow in/out of the passive tag while communicating with the reader. Last but not least is the challenge of a worldwide operability of a tag antenna or design of an antenna that is capable of replying to different frequencies as set by Gen2 standards to meet all regulations.

The first design of choice was a half-wavelength tapered-width U-shaped antenna, shown in Fig. 3. The two stubs, namely inductive and shorting stubs, shown in Fig. 3 are responsible for the matching of the antenna terminals to the IC impedance of value $16-j350$ Ohms, which is expected to have a flat response over the UHF RFID frequency band. The resistive stub primarily matched the radiating body's total input impedance to the resistive part of the IC while the inductive stub primarily matches it to the reactance part of the IC. The tapered width of the two arms offers an increased bandwidth compared with most of the available passive RFID tags that exhibit about 1-2 % bandwidth only [11]. The dimensions of this antenna are $8.2 \text{ cm} \times 4.5 \text{ cm}$.

This method of introducing stubs is very effective in matching to any arbitrarily IC impedance (Z_{IC}). The target Z_{IC} used in this design was Philips EPC 1.19 Gen2 RFID ASIC IC which exhibits a stable impedance behavior of $16-j350 \Omega$ over the frequency $902 \text{ MHz} \rightarrow 928 \text{ MHz}$.

Return Loss (RL) plot is shown in Fig. 5 with a bandwidth of $905 \text{ MHz} \rightarrow 925 \text{ MHz}$ defined by a value of $RL < -10 \text{ dB}$, with radiation efficiency of 92%, for an excellent read range of the RFID tag. The radiation pattern of the antenna is quite similar to that of a classic dipole as shown in Fig. 6 which is desirable in most RFID applications.

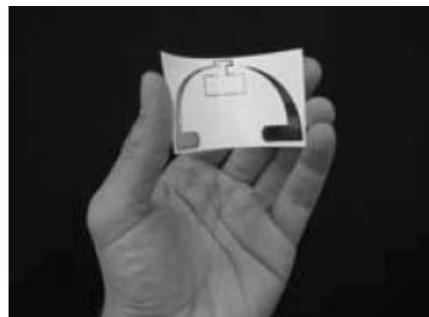


Fig. 3. Photograph of U-shaped Antenna showing flexibility.

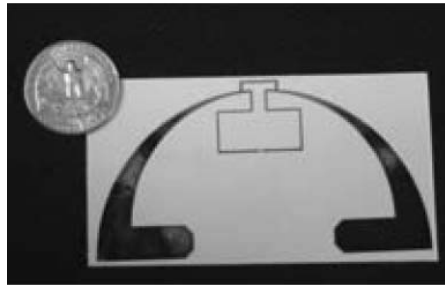


Fig. 4. U-shaped Antenna showing matching stubs.

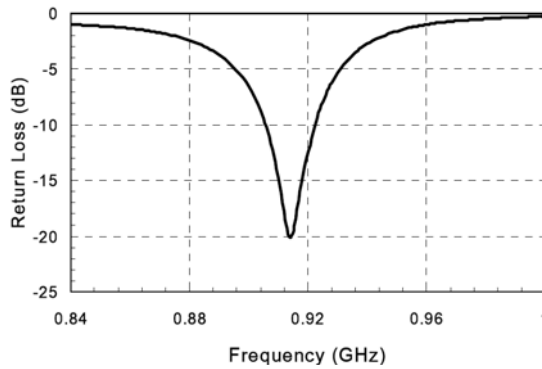


Fig. 5. Return Loss of U-shaped Antenna showing bandwidth.

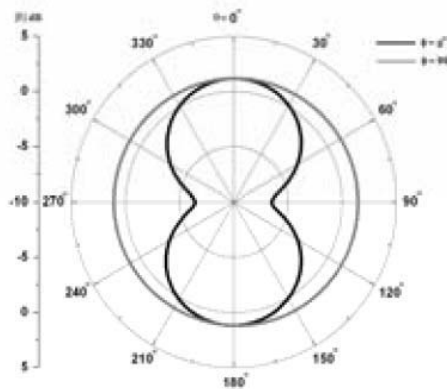


Fig. 6. Radiation Pattern of U-shaped Antenna.

4. RFID-SENSOR INTEGRATION

In addition to the basic RFID automatic Identification capabilities along with the technologies and designs discussed above, the authors have demonstrated the capabilities of inkjet-printing technology in integrated wireless sensors on paper

bridging RFID and sensing technology. The aim is to create a system that is capable of not only tracking, but also monitoring. With this real-time cognition of the status of a certain object will be made possible by a simple function of a sensor integrated in the RFID tag. The ultimate goal is to create a secured “intelligent network of RFID-enabled sensors.” For this effort, the authors have developed the FIRST Sensor-enabled RFID on-paper, that uses Gen2 protocols as means of communication on paper substrate. The authors have also investigated enhanced-functionality RFID’s on organics/paper for automotive applications, specifically for tire-pressure monitoring.

As a first benchmark, a microcontroller-enabled wireless sensor module was realized on a paper-based substrate. The system level design for this wireless transmitter can be seen in Fig. 7. At the heart of the unit was an integrated 8-bit integrated microcontroller unit, that was programmed to sample an analog temperature sensor, perform an analog to digital conversion of the sensed data, bit encode the digital form of the sensed data into full 2 sub carrier cycle Miller bits and finally modulate the power amplifier in the integrated transmitter module in the same sequence as bit-encoded, digital sensor data using Amplitude Shift Keying (ASK) modulation. The transmission frequency of 904.4 MHz was generated by using a crystal oscillator that was tied to the input of the phase lock loop (PLL) unit of the transmitter. The data transmission was to be carried out at the unlicensed UHF frequency around 900 MHz.

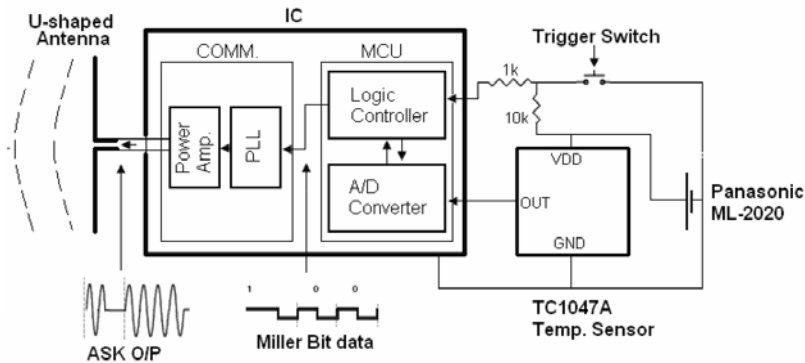


Fig. 7. System-level diagram of a wireless sensor module.

The overall dimensions of the structure shown in Fig. 8 are: $9.5 \times 5 \text{ cm}^2$. The antenna and the traces used for the assembled components including: TC1047 Temperature sensor, TSSOP packaged IC, Inductors, Capacitors, Resistors, Crystal oscillator and Battery. The Return Loss (S_{11}) for the center frequency for the antenna terminals was recorded to be -15.05 dB for the simulated structure using the full wave EM simulator HFSS and -12.45 dB using the ZVA-8 VNA. The normalized radiation pattern, as shown in Fig. 9, was also measured using Satimo’s

Stargate 64 Antenna Chamber measurement system by using the NIST Calibrated SH8000 Horn Antenna as a calibration kit for the measured radiation pattern at 904 MHz. This prototype was tested for wireless transmission using a XR-400 RFID reader antenna interfaced to a Tektronix RSA 3408A Real Time Spectrum Analyzer (RTSA) and the measured power was recorded to be -68 dBm.

This module can be easily extended to a 3D multilayer paper-on-paper RFID/Sensor module by laminating a number of photo-paper sheets (260 μm thickness/sheet). This is expected to decrease the cost of the sensor nodes significantly and eventually realize “ubiquitous computing networks” with a convergent ability to communicate, sense, and even process information.

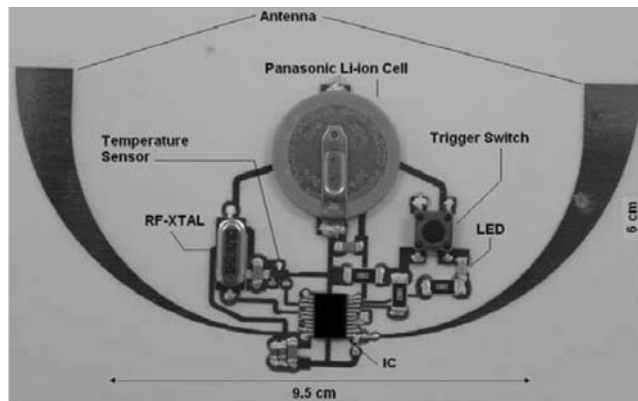


Fig. 8. Wireless Sensor transmitter prototype on paper substrate silver-inkjet printing technology.

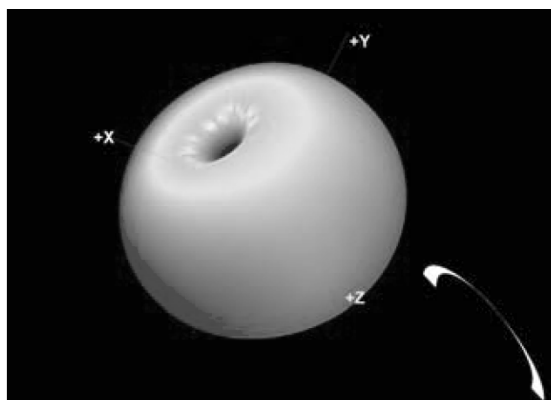


Fig. 9. Measured radiation pattern of U-shaped antenna.

The above prototype is the first step in the deployment of ubiquitous wearable sensors. In the future, this platform could enable the development of flexible hybrid paper/liquid electronics [11] for biomonitoring applications, as well

as it could be realized in 3D “magic-cube” configurations [12] for enhanced-functionality “smart-dust” applications. Further details about these two future paths will be presented at the MEMSWAVE 2008 conference.

5. CONCLUSION

In this paper, the RF characteristics of paper substrates and the utilization of direct-write inkjet-printing technology have been investigated and have enabled the development of a novel ultra-low cost fabrication of antennas on a paper substrate over the UHF frequency range. Two RFID tag prototype modules on paper-based substrates operating in the UHF frequency band were designed and inkjet printed, both featuring excellent performance. These first steps could potentially revolutionize the RF industry and allow for the implementation of large-scale, simple, low-cost fully integrated on paper and multi-band Wireless Sensor Networks.

References

- [1] K. FINKENZELLER, R. HANDBOOK, 2nd ed., Wiley, 2004.
- [2] T. MISHIMA, N. ABE, K. TANAKA, H. TAKI, *Toward Construction of a Mobile System With Long-Range RFID Sensors*, IEEE conference on Cybernetics and Intelligent Systems, **2**, pp. 960–965, 2004.
- [3] A. VIDAL, A. RIDA, S. BASAT, L. YANG, M.M. TENTZERIS, *Integration of Sensors and RFIDs on Ultra-low-cost Paper-based Substrates for Wireless Sensor Networks Applications*, 2nd IEEE Workshop, Wireless Mesh Networks, pp. 126–128, Reston, VA, 2006.
- [4] R. NOHRIA, R.K. KHILLAN, Y. SU, R. DIKSHIT, Y. LVOV, K. VARAHRAMYAN, *Humidity Sensors Based on Polyaniline Film Deposited Using Layer-by-Layer Nano-Assembly*, Sensors and Actuators B, **114**, pp. 218–222, 2006.
- [5] J.N. PALASAGARAM, R. RAMADOSs, *MEMS Capacitive Pressure Sensor Array Fabricated Using Printed Circuit Processing Techniques*, 32nd Annual Conference of IEEE, Industrial Electronics Society, pp. 2357–2362, 2005.
- [6] A. SHAMELI, A. SAFARIAN, A. ROFOUGARAN, M. ROFOUGARAN, F. De FLAVIIS, *Power Harvester Design for Passive UHF RFID Tag Using a Voltage Boosting Technique*, IEEE Transactions on Microwave Theory and Techniques, **55**(6), Part 1, pp. 1089–1097, June 2007.
- [7] M. LESSARD, L. NIFTERIK, M. MASSE, J. PENNEAU, R. GROB, *Thermal Aging Study of Insulating Papers Used in Power Transformers*, Electrical Insulation and Dielectric Phenomena 1996, IEEE Annual Report of the Conference on, **2**, pp. 854–859.
- [8] L. YANG, A. RIDA, R. VYAS, M.M. TENTZERIS, *RFID Tag and RF Structures on a Paper Substrate Using Inkjet-Printing Technologies*, IEEE Transactions on Microwave Theory and Techniques, **55**(12-II), pp. 2894–2901, December 2007.
- [9] A. RIDA, L. YANG, R. VYAS, S. BASAT, S. BHATTACHARYA, M.M. TENTZERIS, *Novel Manufacturing Processes for Ultra-Low-Cost Paper-Based RFID Tags With Enhanced Wireless Intelligence*, Procs. 57th IEEE-ECTC Symposium, Sparks, NV, pp. 773–776, June 2007.

- [10] A. RIDA, L. YANG, M.M. TENTZERIS, *Design and Characterization of Novel Paper-Based Inkjet-Printed UHF Antennas for RFID and Sensing Applications*, Procs. 2007 IEEE-APS Symposium, Honolulu, HI, July 2007, pp. 2749–2752.
- [11] A. TRAILLE, L. YANG, M.M. TENTZERIS, *A Novel Liquid Ionic Antenna for Bio-Signal Monitoring Applications*, IEEE-APS Symposium, San Diego, CA, July 2008.
- [12] C.M. KRUESI, M.M. TENTZERIS, *Magic-Cube, Antenna Configurations for Ultra Compact RFID and Wireless Sensor Nodes*, IEEE-APS Symposium, San Diego, CA, July 2008.

Charging Effect in RF MEMS Switches with Dielectric Less Actuators

D. MARDIVIRIN, A. POTHIER, A. CRUNTEANU, P. BLONDY

XLIM UMR 6172–Université de Limoges/CNRS, 123 Avenue Albert Thomas,
87060 Limoges Cedex, France

Abstract. A major issue in the reliability of electrostatically actuated RF MEMS is dominated to dielectric charging troubles, since it generally induces a quick component failure. By using dielectric less actuator implemented on RF MEMS switches, it has been showed that this phenomenon is strongly attenuated. Also, the lifetime of the switch highly increases and charge trapping becomes residual. In this study, this actuator has been implemented on two kinds of RF MEMS switches: capacitive and ohmic contact. Based on experimental results, the actuator longterm reliability is presented and pull-down pull-up voltage drift behaviors are observed and modeled. Based on Curie–Von Schweidler equation, we demonstrate that the failure of these specific actuators can be predicted with a good accuracy. The projected lifetime of current RF-MEMS dielectric less switches held in the down state is expected to be several months or years, whereas the same switches held in the down state 50% of the time with a 10 Hz square bias voltage will have a lifetime of several tens of months or years.

1. INTRODUCTION

RF-MEMS switches are one of the most promising applications in micro-technologies development for telecommunication thanks to their low loss, low power consumption and small size. However, their integration is currently slowed by reliability problems, especially dielectric charging which is one of the main failure mechanism.

Indeed, using a dielectric layer to protect the bottom electrode from the top moveable electrode, parasitic charge injection phenomenon occurs into this dielectric thin film, due to a large electric field required to actuate the MEMS. As the result, an uncontrollable drift in the MEMS switch $C(V)$ characteristics appears. This phenomenon has been the subject of intensive studies over the past few years [1-4] and several models, based on different conduction mechanisms

have been developed. However, practical solutions proposed up to now to prevent or at least to sufficiently reduce this charge injection effects stay still insufficient to reach the expected component lifetime for industrial applications.

In this work, we have studied a specific electrostatic actuator design without dielectric layer as a solution to improve dramatically the switch reliability. Several structures have been presented in the past few years using this principle with interesting properties [5-7]. This paper is expected to discuss on the reliability benefit of this new generation of actuators. Hence, we present experimental results on charging mechanisms observed on long-term with this actuator implemented indifferently on capacitive or ohmic contact switches. A model of the long-term drift prediction will be introduced with a good agreement with experimental measurement. Some similar studies were already accomplished in [3] and [8].

2. DIELECTRIC LESS ELECTROSTATIC ACTUATOR FOR RF MEMS SWITCHES

This actuator concept has been implemented to design indifferently capacitive or ohmic contact switches as can be shown respectively on Fig. 1 and Fig. 4. Both have been fabricated on a sapphire substrate favored for its low loss characteristic in RF frequency.

To design such actuator, specific mechanical stoppers have been introduced under the switch movable beam, allowing this metallic plan to stop before any contact can occur with its actuation electrodes. In our case, these stoppers are made of the same metal than the switch beam and contact only on the substrate, allowing leaving a small air gap between the top and bottom electrodes. A sketch of the actuator down state is shown on Fig. 3 when the switch is actuated. As shown, charging can not occurs in any dielectric layer thin film. However, the applied bias voltage results in non-negligible electric field between the contact pads and the bottom electrode, especially in the substrate. Indeed, typical distances between electrodes are about 5 μm , with 60 to 80 Volts applied. This level is very comparable to 30-40 Volts applied on a conventional 2 μm high bridge metal switch, where it was shown that dielectric polarization can be large enough to modify the pull-down pull-up voltages of the switch. As the result, in such actuator designs the substrate electrical quality and dielectric loss properties will be an important parameter for the switch reliability.

In the capacitive switch design, a 250 μm long “curled shape” Cr/Au/Cr tri-layer cantilever structure is used, for its thermal stability. Moreover due to its curvature, the available large air gap in the cantilever end (15-20 μm) allows a higher impedance contrast between open and closed states and also results with a moderate actuation voltage in the 50 V range. On the other hand, 6 lines of 5 mechanical stoppers have been patterned to uniformly cover the cantilever surface and to prevent any contact with the bottom electrode during the progressive beam

deflection when the switch actuation occurs. As the result can be seen on Fig. 2, the bottom actuation electrode pattern presents several holes in front of the cantilever mechanical stoppers, which then contact only on the substrate. In this design, the actuation electrode also acts as RF electrode and the contact stopper thickness (0.5 μm) allows controlling the switch down state capacitance. Typical 9 to 10 On/Off impedance ratios are generally reached with such components.

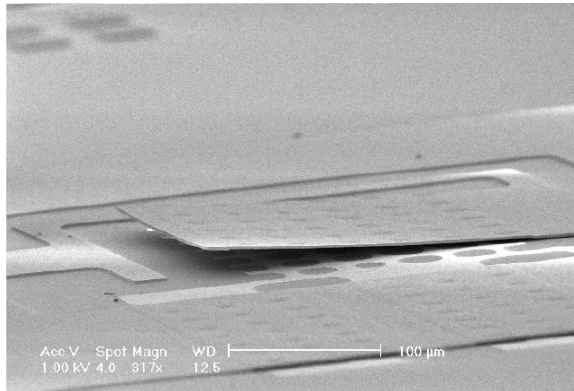


Fig. 1. Dielectric less electrostatic actuator implementation in a RF MEMS capacitive switch.

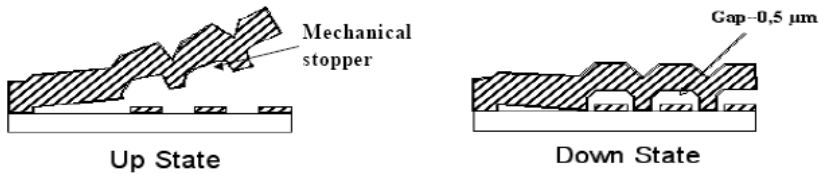


Fig. 2. Dielectric less actuator operating principle on a RF MEMS capacitive switch.

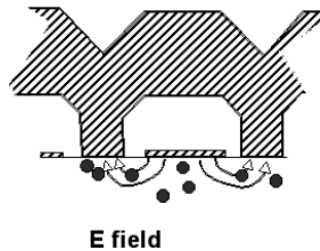


Fig. 3. Sketch of the actuator in the down state.

In case of ohmic contact switch design, only two mechanical stoppers are used in order to keep the maximum contact force allowable at the end of the cantilever structure Fig. 5, in the zone where the metal to metal contact with the RF

electrode occurs. The contact material is pure gold. These two metallic mechanical stoppers, made under the cantilever, have been introduced on the sides of the switch beam. Their location and thickness have been optimized to keep a sufficient actuation electrode surface and contact force on the metal to metal contact areas. In this design, 90 to 130 μm long and low stress gold cantilever structure is considered to generate a sufficient contact force that allows reaching contact resistance in the 1 ohm range per contact. As the result, typical actuation voltages are in the 70-80 V range.

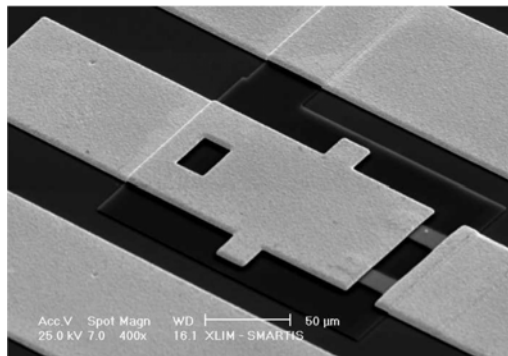


Fig. 4. Dielectric less electrostatic actuator implementation in a RF MEMS ohmic contact switch.

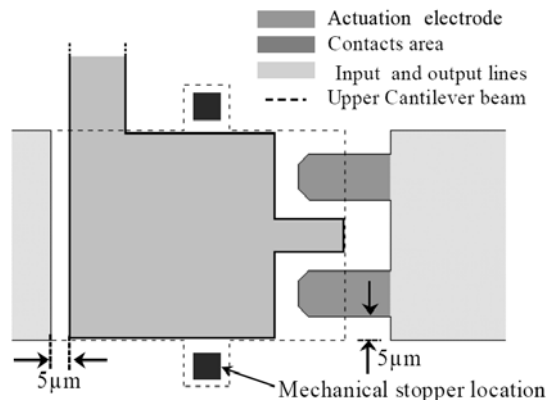


Fig. 5. Top view of the electrostatic actuator layout on a RF MEMS ohmic contact switch.

3. RELIABILITY STUDY

To study specifically the actuator reliability, a dedicated test bench has been used allowing monitoring the evolution of the switch pull-down and pull-up voltages over time, for different stresses, from [6] and [7]. Moreover, although

tested switches are not packaged, all tests were performed under dry nitrogen in a controlled atmosphere chamber.

As shown on Fig. 6, the actuator is biased with a specific periodic actuation waveform. Thanks to a quick (15 ms) positive triangular pulse, the switch C(V) characteristic is recorded. Then, during the remaining 985 ms, a chosen stress is applied. In the case of a continuous positive DC stress, the switch stays 98% of the time actuated which can be considered as a “worst case testing”. Another possible stress is to apply a 10 Hz unipolar square waveform with a user specified duty cycle, as conventionally used cycling waveforms.

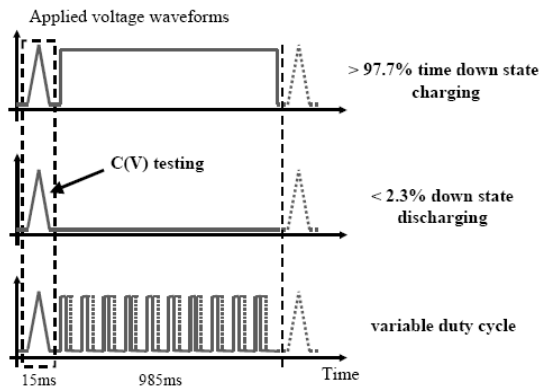


Fig. 6. Typical biasing waveforms used to measure the pull-down and pull-up voltage shifts during the dielectric less switch is stressed or not.

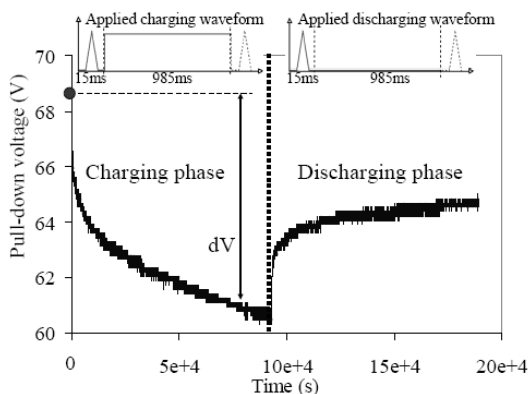


Fig. 7. Typical recording sequence for lifetime testing on Dielectric less actuator switches.

Although the switch is not made with any dielectric layer, we still observe a residual charging, which in fact occurs in the substrate. Nevertheless, when the device is put to a specific stress, the actuation voltage drift is different and presents

a better reliability than the classical behavior usually seen. Fig. 7 shows a charging – discharging measure on this type of actuator. During the charging phase, the switch is put in the down state by a 70 V DC stress applied 97.7% of the time. The actuator pull-down voltage loses only 8 Volts in 25 hours. Furthermore, the observed charging phenomenon is reversible but taking longer time to fully discharge the actuator.

Experimental results, presented on Fig. 8, for a capacitive switch, and Fig. 9, for a ohmic contact switch, with a double logarithm axes plot scale, show that the influence on the pull-down voltage drift characteristic of a periodic square signal as biasing waveform stress follows a Curie - Von Schweidler behavior [9]. In addition, measured voltage drifts are proportional to the applied waveform duty cycle.

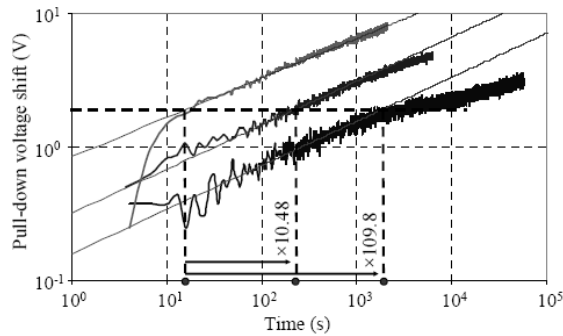


Fig. 8. Double logarithm axes plot of the measured pull-down voltage shift over time on a dielectric less capacitive switch for applied waveform with 97.7~100% duty cycle (green), 50% (brown) and 25% (blue). The Curie Von Schweidler fit is shown for each curve with $n=0.295$ (red).

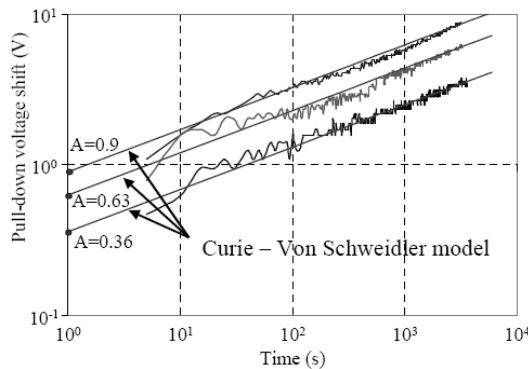


Fig. 9. Measured pull-down voltage shift over time on a dielectric less ohmic contact switch for 97.7%~100% duty cycle (brown), 70% (green) and 40% (blue) and the corresponding modeling fit (red) with $n=0.28$.

Considering that the stored charge in the actuator is proportional to the observed voltage drift dV , the equation of the single model considered is:

$$dV = A \times (\text{Dcy}) \times t^n \quad (1)$$

where dV is the measured voltage drift, t is the stress time, Dcy is the duty cycle and A and n are model-building coefficients (on Fig. 8, $A = 0.88$ and $n = 0.28$, on Fig. 9, $A = 0.9$ and $n = 0.295$).

A simple computation shows that the time taken for a specific duty cycle bias stress to reach the same level of charging than the 100% duty cycle stress is $\text{Dcy}^{-1/n}$. For example on Fig. 8, it takes $(50\%)^{-1/0.295} = 10.48$ times more with 50% duty cycle; for the 25% curve, it would be $(25\%)^{-1/0.295} = 109.8$ times longer. This explains why this phenomenon is not easily seen under a cycling stress. Furthermore, it allows predicting the switch lifetime from a quick test at 100% duty cycle.

For further validation, a capacitive switch has been held in the down state for one month. The pull-down voltage shift recording is shown on Fig. 10. After one month, the measured shift is 20 volts, and the Curie–Von Schweidler model follows very well the measured evolution in the first 10^6 seconds.

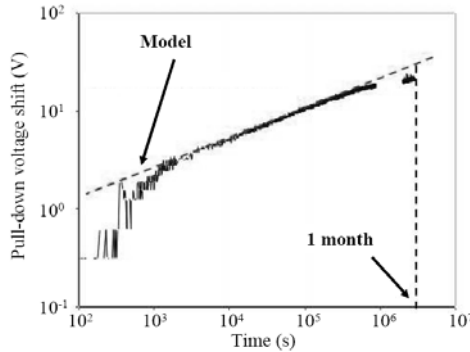


Fig. 10. Measured pull-down voltage drift of a dielectric less capacitive switch held in the down state for 1 month (blue) and Curie-Von Schweidler fit (red).

4. CONCLUSION

Residual charging in dielectric less electrostatic actuators for RF-MEMS switches has been studied and the benefits on lifetime have been demonstrated. This type of actuator strongly extends the lifetime of these devices. We have seen that the observed drift in pull-down or pull-up voltages under various stresses can easily be modeled using a simple Curie-Von Schweidler equation with good accuracy. It allows predicting the long-term behavior of such actuator, based on an only short period of test (less than one hour). It has been shown that hold down periods longer than one month without failure of the switch actuator are today feasible, without applying any special bias waveform. It is also shown that

reducing the duty cycle of the bias signal from 100% to 50% results in 10 times lifetime improvement of the electrostatic actuator.

Acknowledgments. This work has been led in the frame of the European SMARTIS project and the authors wish to acknowledge the French MoD for its support and founding for this study.

Reference

- [1] M.W.M. van SPENGEN, R. PUERS, I. De WOLF, *The Prediction of Stiction Failures in MEMS*, Device and Materials Reliability, IEEE Transactions on **3**(4), pp. 167–172, December 2003.
- [2] Y. XIAOBIN, J.C.M. HWANG, D. FOREHAND, C.L. GOLDSMITH, *Modeling and Characterization of Dielectric-Charging Effects in RF MEMS Capacitive Switches*, Microwave Symposium Digest, IEEE MTT-S International 12-17 June 2005.
- [3] G.J. PAPAIOANNOU, G. WANG, D. BESSAS, J. PAPAPOLYMEROU, *Contactless Dielectric Charging Mechanisms in RF-MEMS Capacitive Switches*, Microwave Conference, 36th European, pp. 1739–1742, September 2006.
- [4] S. MELLE, *et al*, *Reliability modeling of capacitive RF MEMS*, Microwave Theory and Techniques, IEEE Transactions, **53**(11), pp. 3482–3488, November 2005.
- [5] P. BLONDY, A. CRUNTEANU, C. CHAMPEAUX, A. CATHERINOT, P. TRISTANT, O. VENDIER, J.L. CAZAUX, L. MARCHAND, *Dielectric Less Capacitive MEMS Switches*, 2004 IEEE MTT-S Int. Microwave Symp. Dig., **2**, pp. 573–576, June 2004.
- [6] D. MARDIVIRIN, D. BOUYGE, A. CRUNTEANU, A. POTHIER, P. BLONDY, *Study of Residual Charging in Dielectric Less Capacitive MEMS Switches*, IEEE MTT-S Digest Atlanta, June 2008.
- [7] D. MARDIVIRIN, A. POTHIER, M. EL KHATIB, A. CRUNTEANU, O. VENDIER, P. BLONDY, *Reliability of Dielectric Less Electrostatic Actuators in RF-MEMS Ohmic Switches*, 38th European Microwave Conference, Amsterdam, October 2008.
- [8] R.W. HERFST, *et al*, *Time and Voltage Dependence of Dielectric Charging in RF MEMS Capacitive Switches?*, IEEE 45th Annual International Reliability Physics Symposium, pp. 417–421, Phoenix, 2007.
- [9] A.K. JONSCHER, *Dielectric Relaxation in Solids*, J. Physics D: Applied Physics **32**, 1990.

Simple and Robust Air Gap-Based MEMS Technology for RF-Applications

Phillip EKKELS^{1,2}, Xavier ROTTENBERG^{1,2}, Robert PUERS^{1,2},
Harrie A.C. TILMANS¹

¹IMEC, Kapeldreef 75, 3001 Heverlee, Belgium

²K.U.Leuven, Kasteelpark Arenberg 10, 3001 Heverlee, Belgium

Abstract. The reliability of RF-MEMS switching devices becomes more and more important. The lifetime of capacitive switches is mainly limited by dielectric charging. By realizing a capacitive switch without dielectric its lifetime can be significantly improved. This paper presents a technology to fabricate capacitive RF-MEMS switching devices without dielectric. It consists of a thick membrane that defines an airgap capacitor with 2 different states. It is shown how these switched capacitors, even though having a low capacitance ratio, can still form adequate switching devices and RF-circuits by proper design and combining these devices with high-Q inductors and transmission lines. Lifetimes of more than 1×10^8 cycles with unipolar actuation are observed.

1. INTRODUCTION

In this paper we present a simple process that allows the realization of reliable RF-MEMS circuits with a high functionality and a long lifetime. Due to its simplicity it is also relatively easy to integrate with other technologies. The main failure mechanisms in RF-MEMS switching technologies are related to either dielectric charging for capacitive switches or contact degradation for ohmic switches [1]. To overcome these problems an increasing demand on the packaging and on the process complexity can be observed. By removing the dielectric from the active area of capacitive switches, many of the original failure mechanisms are removed. Substrate charging may still remain an issue, as demonstrated in [2]. However, at the same time, replacing the typically thin high-k dielectric from the capacitive device reduces the capacitance ratio, which is an important figure of merit of an RF-MEMS capacitive switch. Nevertheless several groups have demonstrated capacitive switching devices without dielectric that show a high

performance [3] [4]. Furthermore, through proper design, even low capacitance ratio technologies combined with high-Q inductors and transmission lines still offer the possibility to design adequate switching devices as well as Rfcircuits [5]. The device presented here is an example of the latter.

2. BASIC PRINCIPLE

The switchable capacitor we propose consists of an electrostatically actuated bridge structure that switches an airgap capacitor. Dimples on the bottom side of the bridge define this airgap in the down state (after pull-in) as illustrated in Fig. 1. The capacitance ratio is defined by the two different gap heights; $d0$ in the up-state (defined by the sacrificial layer thickness) and $d1$ in the down-state (defined by the dimples). The bridge consists of a $300 \times 600 \mu\text{m}$, $10 \mu\text{m}$ thick membrane which is suspended with four $30 \mu\text{m}$ wide and $400 \mu\text{m}$ long springs as shown in Fig. 2, as a result the membrane has a much higher (bending) stiffness than the springs. This high stiffness together with strategically placed dimples in the membrane prevents it to collapse on the bottom electrode in the down-state.

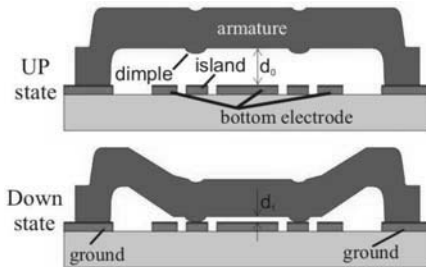


Fig. 1. Sketch of basic working principle of the switchable capacitor.

The $10 \mu\text{m}$ diameter and 500 nm high dimples land after pull-in on $15 \mu\text{m}$ diameter circular electrically isolated islands within the bottom electrode. Fig. 3 shows several distributions of the islands in the bottom electrode that have been studied. It was found that a layout with only 6 islands in the bottom electrode (design 5) is sufficient to prevent the membrane to collapse on the bottom electrode after pull-in.

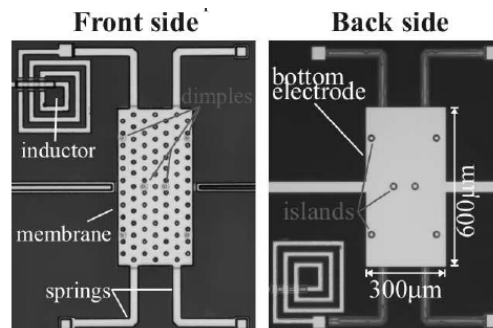


Fig. 2. microphotograph of an airgap switch seen from front side and back side.

Since the capacitance of a parallel plate capacitor is directly related to the distance between the plates, the capacitance ratio $C_{\text{down}}/C_{\text{up}}$ is defined by the ratio of the gap height in the up-state and in down-state d_0/d_1 . The capacitance ratio can be improved by either increasing d_0 , which would result in a higher pull-in voltage, or reducing d_1 , by decreasing the height of the dimples. The scaling of both parameters is limited by the electric field in the airgap which should remain below the breakdown field of the gas in which the switch operates. Actuation of the switch results to a minimum electric field of $E_{\text{min}}=V_{\text{pull-in}}/d_1$. The current design of the springs gives a pull-in voltage of around 50 Volt, which with a gap of 500 nm, would result in an electric field close to $\sim 10^8 \text{V/m}$.

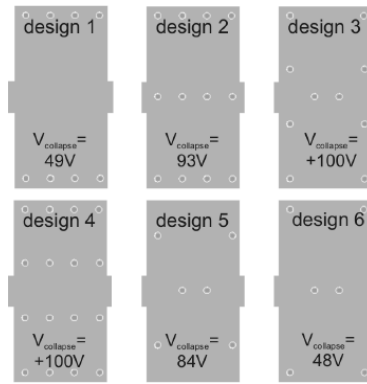


Fig. 3. Illustration of the investigated distributions of islands in the $300 \mu\text{m} \times 600 \mu\text{m}$ bottom electrode and the observed collapse voltages for 500 nm high dimples.

3. FABRICATION PROCESS

The process consists of 4 lithographic steps and is intended to be very robust and reproducible. Fig. 4 shows how the process starts with patterning a $1 \mu\text{m}$ thick aluminum alloy ($\text{AlCu}_{0.5\%}$) bottom metallization on a 200 mm quartz wafer (1). On top of this layer a $3 \mu\text{m}$ thick PW-1530 polyimide sacrificial layer is spin coated and photolithographically patterned. After the 250°C crosslink bake, 500 nm deep dimples are dry etched in the polyimide (2).

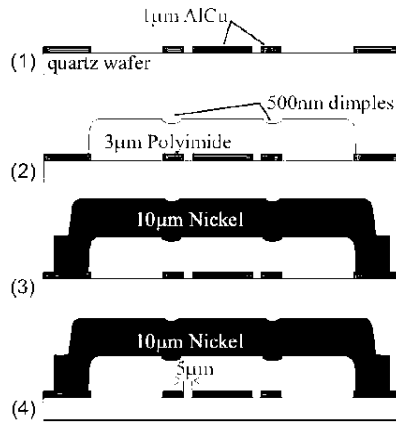


Fig. 4. Sketch of fabrication process.

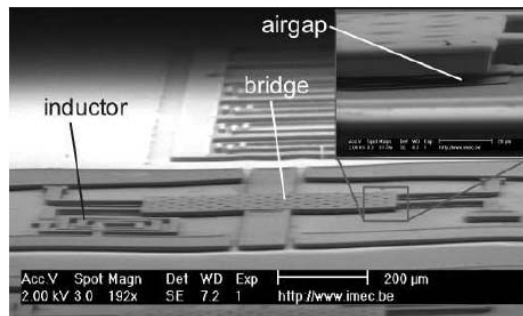


Fig. 5. SEM image of topview of the device.

Next a 10 μm thick nickel film is electroplated through a photoresist mold. This layer serves both as the armature material and as signal line metallization (3). Finally, the sacrificial layer is removed in an O₂-plasma (4). Alternatively a wet release in microstrip followed by a critical point drying step can be used. Fig. 5 shows that both the height of the dimples and of the airgap are relatively small compared to the thickness of the Ni membrane.

The dimples of the membrane land on islands fabricated in the same bottom metallization as the electrode as depicted in Fig. 6. Since the slots between the electrode and the islands are only 5 μm wide, the polyimide shows a good planarization of these slots. The thickness of the polyimide at the dimple-location before the etching of the dimple in the polyimide is therefore the same as the thickness of the polyimide above the electrode. This allows a good definition of the dimple height in relation to the membrane itself. The dimple etching is done with in a O₂ plasma through a metal hardmask in a Matrix bobcat downflow reactor. Only a small number of openings in the mask are defined, which results in a low loading during the plasma etching. This gives a high uniformity in the depth of the etched

dimples (etch depth difference of $\sim 2\%$). The resulting dimples, shown in Fig. 7, have a low roughness and smooth sidewalls.

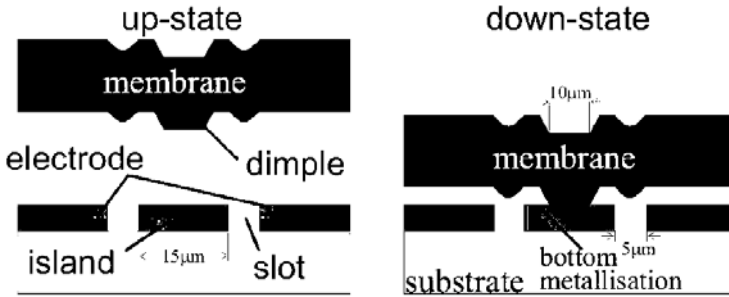


Fig. 6. sketch of membrane at the location of the dimples.

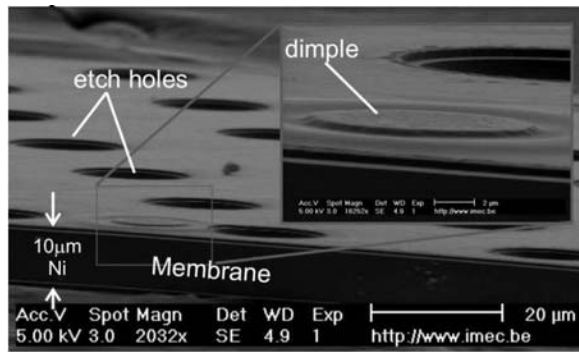


Fig. 7. SEM image of the membrane backside.

The armature is realized by electroplating nickel through a photoresist mold with a Ti(30 nm)/Cu(500 nm) seed layer. The relatively thick seedlayer guarantees a good step coverage at the edges of the sacrificial layer, which is important to achieve a good distribution of the plating current over the wafer. A high density of nickel structures further helps to increase the plating uniformity. Nevertheless a variation in thickness of 3% within a structure and of $\sim 6\text{-}8\%$ within a 200 mm wafer is observed. The stress of the nickel film after plating is ~ 50 MPa compressive, but after a 180°C anneal step the stress becomes 150-200 MPa tensile. The bend in the springs is intended to reduce the dependence of the performance of the switch on the stress in the bridge.

4. MEASUREMENTS & DISCUSSION

The low stiffness of the springs compared to the membrane results in a device that pulls in at 45 V with a capacitance ratio close to 1:1.8 with $C_{\text{down}}/C_{\text{up}} = 3.25$ pF/1.83pF. The C-V measurement in Fig. 8 shows not the sharp pull-in as

commonly observed with capacitive switches but an initially more graduate change in capacitance. The RF-characteristics of the switchable capacitor in shunt configuration are shown in Fig. 9.

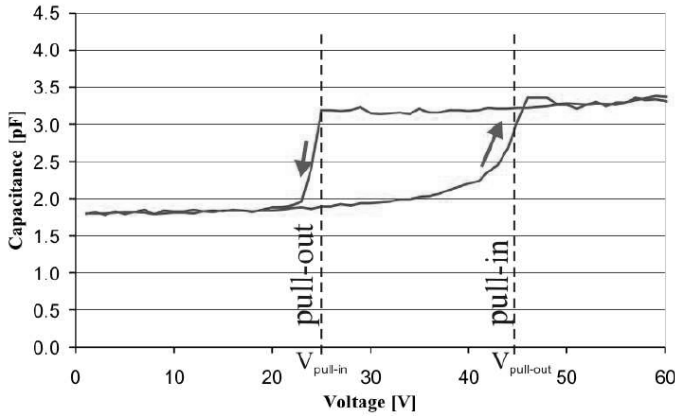


Fig. 8. CV-measurement of the switchable capacitor.

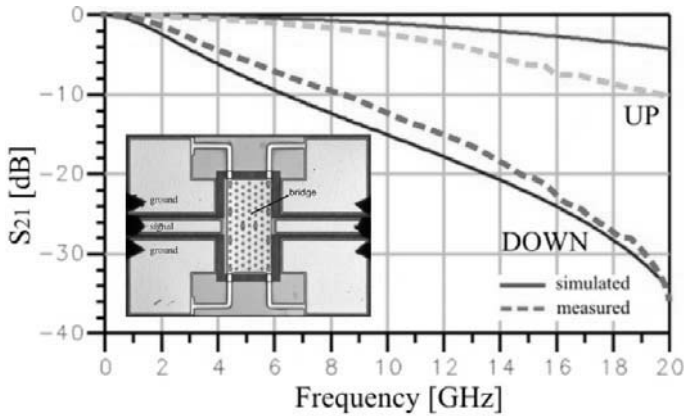


Fig. 9. RF-measurements and simulation results for an airgap switchable capacitor in shunt configuration.

With a device with these basic characteristics several RF-circuits can be realized. In this paper we present two examples: an RF-switch that functions as a tunable notch band filter as shown in Fig. 10 and an enhanced tunable notch band filter as shown in Fig. 13.

For the RF-switch the signal transmission in the upstate, characterized by the S_{12} parameter, is optimized by matching the up-capacitance of the switchable capacitor and the inductive feeding lines. In the down-state, S_{12} is strongly influenced by the resonance of the lumped LC circuit between the MEMS and the

ground. The thick Ni layer allows defining high-Q inductors (L_{series}) that in turn make it possible to define compact low frequency LC tanks of which the circuit representation is shown in Fig. 11. The comparison between measurement and simulation results for a device with a 4 μm gap in up state and a 1 μm gap in down state, shown in Fig. 12, shows only a small deviation.

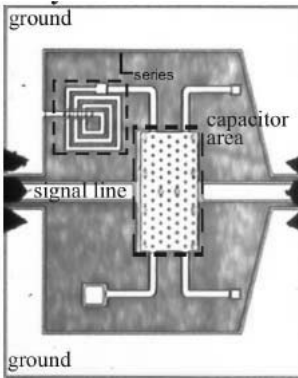


Fig. 10. Microphotograph Picture of an RF-switch.

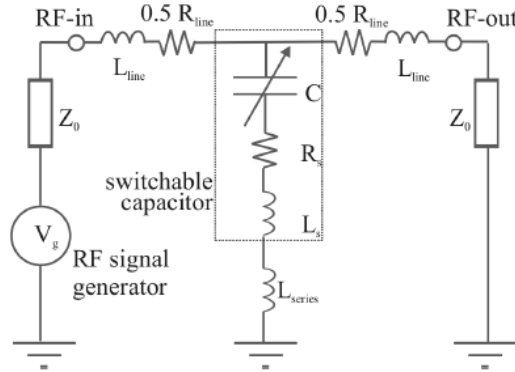


Fig. 11. Circuit representation of an RF-switch forming a tunable notch band filter.

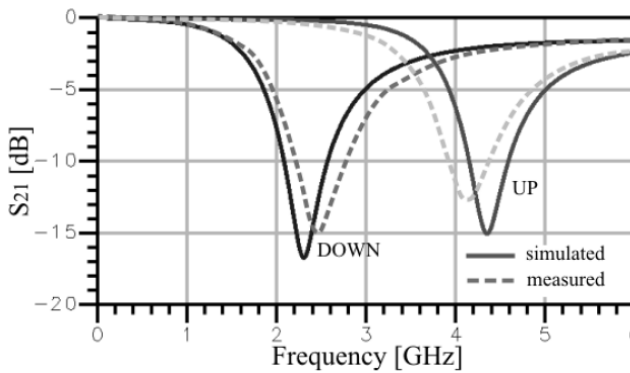


Fig. 12. Simulation results and measured characteristics of the RF-switch of Fig. 10.

We can further improve the switching characteristics of this circuit by implementing a more complex 2-stage circuit shown in Fig. 13 and Fig. 14. Here 2 RF switches in shunt configuration are coupled by an inductor (L_{couple}). This way an enhanced tunable notch band filter is defined with a steep cut off and a wide rejection band as shown in Fig. 15. The measurements resemble the simulation results for a device with a 4 μm gap in up state and a 1 μm gap in down state.

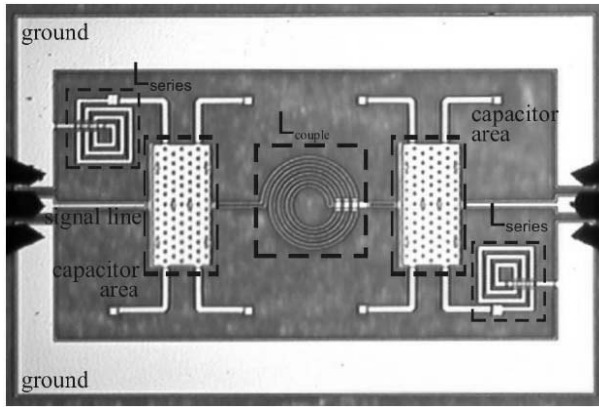


Fig. 13. Microphotograph picture of an enhanced tunable notch band filter.

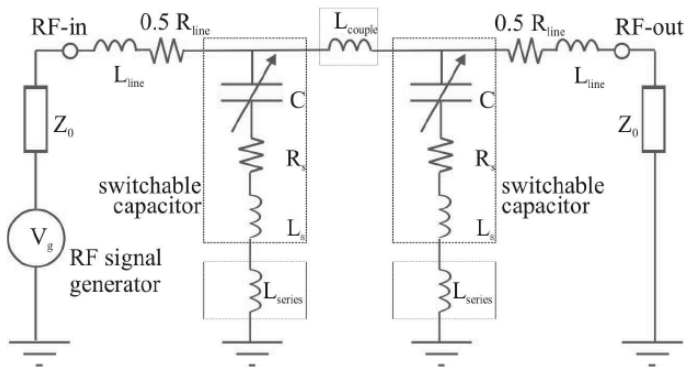


Fig. 14. Circuit representation of the enhanced notch band filter.

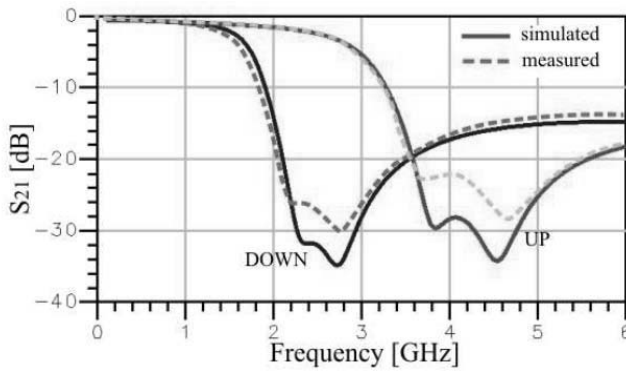


Fig. 15. Simulation results and measured characteristics of the enhanced notch band filter of Fig. 13.

For capacitive switching devices stiction due to interposer dielectric charging is the main cause of failure. Since there is no interposer dielectric in the device presented here, the only remaining source of charging is substrate charging. Lifetime measurements with 50V unipolar actuation, 100 Hz and 50% duty cycle in N₂ were done as depicted in Fig. 16. During 1×10⁸ cycles no failure was observed. The only significant shifts in the up and down capacitance are the result of thermal drift in the equipment during the measurement.

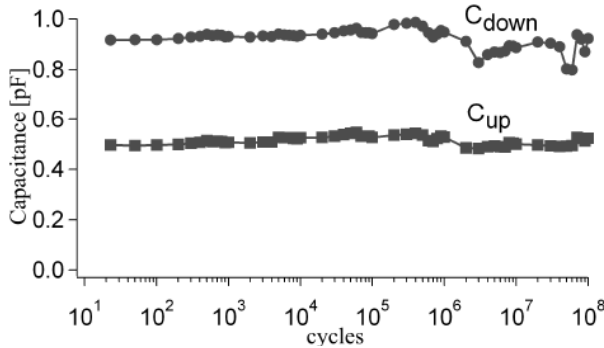


Fig. 16. Lifetime of airgap switch using 50 V unipolar actuation, 100 Hz and 50% duty cycle in N₂ environment.

In order to obtain more information on the charging behavior also the pull-in and pull-out voltage were monitored during the lifetime measurements as shown in Fig. 17. The pull-out voltage initially shows a rapid decrease but stabilizes after ~2×10⁷ cycles. This is most likely due to saturation of the substrate charges. After 1×10⁸ cycles the measurement was stopped since no further drift was observed. After the lifetime measurement was stopped the pull-out voltage gradually increased in time.

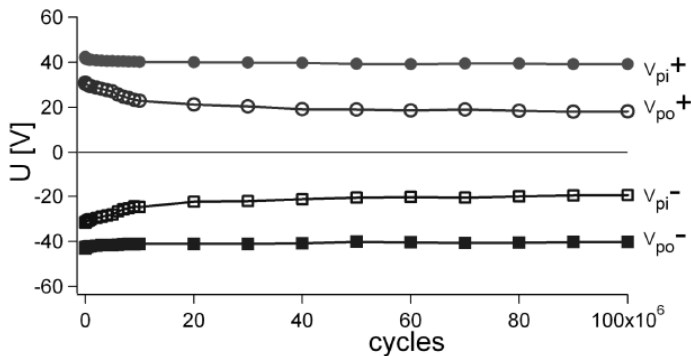


Fig. 17. Monitored pull-in and pull-out voltages of airgap switch using 50V unipolar actuation, 100 Hz and 50% duty cycle in N₂ environment.

This indicates that the substrate charges disappear after the stressing of the device is finished. We therefore believe that the substrate charging is not a failure mechanism that limits the lifetime of these devices and extremely long lifetimes can be realized. It should be noted that the high pull-out voltage is one of the conditions that allows the long lifetime of the device. This should be taken into account in the design of this kind of devices.

6. CONCLUSION

In this paper we present a simple and robust technology for realization of RF circuits with a high functionality and long lifetimes. The technology consists of a 4 lithographic steps process which is used to create a MEMS switchable capacitor. It consists of a 10 μm thick membrane which is used to switch the height of an airgap dielectric. Even though the resulting capacitance ratio is relatively small the thick metallization can be used to create compact low frequency LC-tanks which allows the creation of several interesting circuits. Due to the absence of an interposer dielectric the only source of charging is substrate charging of the quartz substrate. Stable lifetimes of at least 1×10^8 cycles with unipolar actuation have been observed but a much longer lifetime is expected.

Acknowledgement. The authors wish to thank Piotr Czarnecki for his help with, and evaluation of the lifetime measurements.

References

- [1] G.M. REBEIZ, *RF MEMS in Theory, Design and Technology*, Hoboken, NJ, USA, Wiley, 2003.
- [2] X. ROTTENBERG *et al*, *Electrostatic Fringing-Field Actuator (EFFA): Application Towards a Low-Complexity RF-MEMS Technology*, proceedings of MEMS, pp. 203–206, 2007.
- [3] Qin SHEN, N. Scott BARKER, *Distributed MEMS Tunable Matching Network Using Minimal-Contact RF-MEMS Varactors*, IEEE transactions on microwave theory and techniques, **54**(6), pp. 2646–2658, 2006.
- [4] P. BLONDY *et al*, *Dielectric Less Capacitive MEMS Switches*, MTT-S Microwave Symposium Digest, **2**, pp. 573–576, June 2004.
- [5] P. CZARNECKI *et al*, *Influence of the Substrate on the Lifetime of Capacitive RF MEMS Switches*, proceedings of MEMS, pp. 172–175, 2008.

Investigation of Dielectric Charging Mechanisms in Al₂O₃ RF-MEMS Capacitive Switches

E. PAPANDREOU¹, A. CRUNTEANU², G. PAPAIOANNOU¹,
P. BLONDY², F. DUMAS-BOUCHIAT³, C. CHAMPEAUX³,
A. CATHERINOT³

¹University of Athens, Solid State Physics Section, Athens 15784, Greece
Phone: +302107276817

²XLIM Research Institute, 123 Avenue Albert Thomas, Limoges 87060 Cedex, France
Phone: +33555457731

³SPCTS-CNRS, University of Limoges, Department, Street, Limoges 87060 Cedex,
France Phone: +33555457200

Abstract. The dielectric charging processes have been investigated in RF MEMS capacitive switches with Al₂O₃ dielectric. The investigation has been performed by employing both MIM capacitors and MEMS switches.

1. INTRODUCTION

The dielectric charging in RF-MEMS capacitive switches is still the most significant reliability issue that inhibits the commercialization of these devices [1]. In order to overcome this problem several insulating materials, with lower or higher dielectric constant, have been investigated [2-7]. Among those, the most promising ones were found to be based on either silicon or aluminum oxides and nitrides. The silicon based dielectrics are presently intensively investigated although the ones based on aluminum exhibit promising features. More specifically, aluminum oxide is a dielectric material that has been used for FET gate insulator [8] and/or SOI buried insulator layer [9] and Metal-Insulator-Metal capacitors/electronic tunneling junctions [10]. In the case of RF-MEMS there are a few reports on the reliability of devices with Al₂O₃ dielectric [11, 12].

The aim of the present work is to investigate the electrical properties and charging processes in Al₂O₃ based RF-MEMS capacitive switches. The investigation has been performed using MIM (Metal-Insulator-Metal)

capacitors and MEMS switches. The electrical properties were investigated by means of current voltage characteristics and Thermally Stimulated Depolarization Current methods in MIM capacitors. These allowed the determination of temperature dependence of material conductivity and the dependence of stored charge on the applied bias polarity and material deposition method.

2. EXPERIMENTAL DETAILS

The basic structure of our MEMS capacitive switch implemented on a coplanar microwave waveguide (CPW) consists of a gold metal bridge anchored on the two sides to the RF-grounded electrodes and overlapping an RF transmission line. The bridge moves down and contacts a dielectric layer (alumina, Al_2O_3) covering the signal line. The alumina layers were deposited either by Pulsed laser Deposition- PLD or Plasma Enhanced Chemical Vapor Deposition- PECVD methods. Finally, this dielectric was chosen because it can stand high breakdown voltage for relatively thin layers (~600 nm), show less charging effects and they can be deposited at low temperature (even at room temperature) without losing its main properties.

The investigation has been performed using MIM (Metal-Insulator-Metal) capacitors and MEMS switches. The electrical properties of alumina films were investigated by means of current voltage characteristics and Thermally Stimulated Depolarization Current (TSDC) methods in MIM capacitors. These allowed the determination of temperature dependence of material conductivity and stored charge on the applied bias polarity and material deposition method.

The charging process was investigated through the capacitance-voltage characteristic and the switch-ON transient response. Finally, it must be pointed out that in all cases the applied bias polarity applies to the top electrode/bridge with reference to the bottom one, i.e the coplanar waveguide in the case of MEMS switches.

3. RESULTS AND DISCUSSION

A. Current-Voltage characteristics

The importance of Al_2O_3 as insulating dielectric is due to its large band gap, excellent stability and its amorphicity – Al_2O_3 is a good glass former. Experiments have shown that $\alpha\text{-Al}_2\text{O}_3$ is a wide-gap insulator with a direct energy gap of about 8.3 eV [13]. In contrast to SiO_2 and Si_3N_4 , the O–Al bonds in the compound exhibit highly ionic nature and theoretical calculations have shown that the valence band is well separated into two parts, with the lower part consisting of O 2s states and the upper part being dominated by O 2p states. The lower part of the conduction band is in general believed to be

dominated by Al 3s states. Regarding the electrical properties and charging behavior the dc behavior of alumina has been little investigated. The **experimental I(t) curves have shown that the ‘quasi’ steady-state current** is reached for time ranging from 10^4 to 10^5 s [14]. The transient current was reported to consist of two parts, the first one that arises mainly from the polarization of dipoles in the dielectric which dominate at short time, whereas the second part was found to correspond to the carriers transport mechanism. Moreover the conduction mechanism in the high field regime was reported to obey the space charge limited current law.

In order to investigate the electrical conduction of the deposited films we obtained current voltage characteristics in the temperature range of 300K to 450K and under low electric field conditions. The Arrhenius plot of the calculated conductance, presented in Figure 1, reveals the presence of two thermally activated mechanisms.

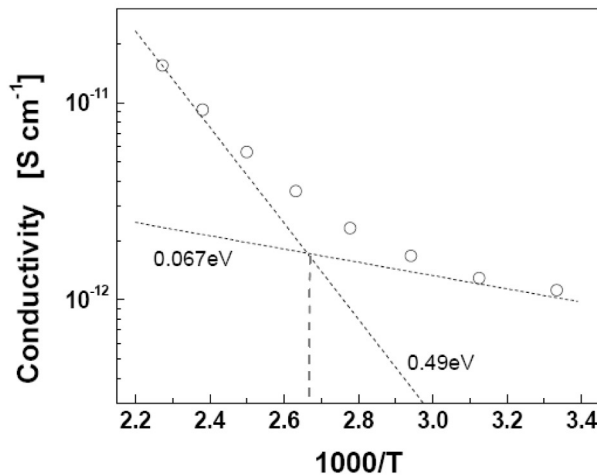


Fig. 1. Temperature dependence of Al_2O_3 film conductivity and activation energies in high and low temperature regimes.

The activation energy of the high temperature conduction mechanism ($T > 375K$) was found to be about 0.49eV. At low temperatures ($T < 375K$) the activation energy was found to be 0.067eV. This clearly indicates that the transport at high temperatures is dominated by carriers emitted from deep traps and at low temperatures by carriers emitted from discrete shallow traps or transport in the b and tails. The calculated energies are close to the ones of about 0.44eV, and 0.082eV determined from TSDC assessment where the charging was performed under low electric fields (4kV) [15]. Here it must be pointed out that the characteristics of the charge traps introduced during deposition depend strongly on the deposition conditions [15].

B. TSDC Assessment

Under working temperatures, these experimental measurements clearly show that space charge takes place in alumina. Consequently, experimental investigations have to be performed to find the relationship between space charge built up and dielectric strength of alumina.

In insulators, the time and temperature dependence of polarization and depolarization processes are determined by the competition, between the orienting action of the electric field and the randomizing action of thermal motion. Thus, the decay of polarization after removal of electric field is given by an exponential function of time (Debye relaxation):

$$P(t) = P_p \cdot \exp\left(-\frac{t}{\tau}\right) \quad (1)$$

where P_p is the steady state polarization. In the case of a MIM capacitor, the depolarization process induces a short circuit discharge current transient. The current density produced by the progressive decrease in polarization in the course of TSDC experiment, where time and temperature are simultaneously varied, is approximated by [16]:

$$J_D(T) \approx \frac{P_s(T_p)}{\tau_0} \cdot \exp\left(-\frac{E_A}{kT}\right) \cdot \exp\left[-\frac{1}{\beta\tau_0} \cdot \frac{kT}{E_A} \exp\left(-\frac{E_A}{kT}\right)\right] \quad (2)$$

where β is the heating rate (K/sec), E_A the depolarization mechanism activation energy, $P_s(T_p)$ is the equilibrium polarization at the polarizing temperature T_p and τ_0 the corresponding infinite temperature relaxation time. At temperatures where the ratio E_A/kT is large enough, the above equation can be simplified and used to determine the activation energy of the leading depolarization mechanism from an Arrhenius plot of $\ln(J_D)$ vs $1/T$.

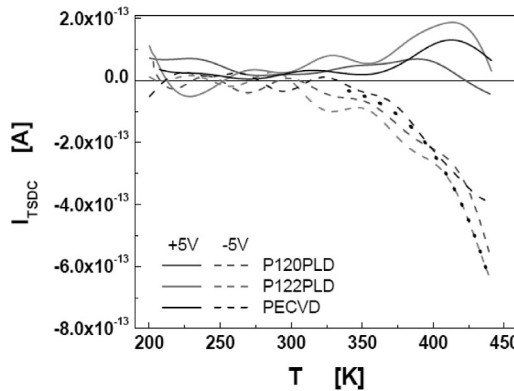


Fig. 2. TSDC spectra of MIM capacitors with different Al_2O_3 films.

The TSDC spectra were obtained after polarization of the dielectric film with a positive or negative bias that has been applied to the top electrode. Fig. 2 shows the spectra that have a complex structure, consisting of several contributions, and that are asymmetrical. Particularly, the collected charge seems to be larger, when the top electrode is negative, than the one obtained when the top electrode is positive. This behavior clearly shows that the dominant charging mechanism arises from charge injection. The charging from dipole orientation would lead to symmetrical TSDC spectra since it would be determined by the magnitude of the applied electric field and not from the nature of the contacting electrodes and the presence of asymmetric interfaces.

The TSDCS spectra show a low current at temperatures below 320 K. Since the polarization/charging process took place at 450 K this clearly denotes that the spectra arise from the contribution of several deep traps. Among those the one that contributes at temperatures above 380 K shows activation energy of 0.39 eV, shown with a dotted line in Fig. 2 and which lies close to the one reported in [15]. The TSDC spectra reveal that the trapped charge by this trap is large. Therefore the lifetime of Al_2O_3 based MEMS switches is expected to be strongly affected by the presence of this trap and the nature and concentration of this defect need both further attention and control. The traps that contribute at lower temperatures are characterized by lower activation energies.

C. MEMS Capacitance-Voltage Characteristic

In MEMS capacitive switches the bias that corresponds to capacitance voltage characteristic minimum is determined by the dielectric film macroscopic polarization P , which is the average surface charge density [14].

$$V_{min} = -\frac{z_1 P}{\epsilon_0} \quad (3)$$

where z_1 is the dielectric film thickness. If the capacitance voltage characteristic is restricted in below pull-in region, V_{min} allows the calculation of residual charging while if the characteristic is extended beyond pull-in, V_{min} provides information on the dielectric charging during down-state, which occurs under high electric field. Finally, the capacitance for zero bias gives information on the presence of opposite polarity charges [17]. So, in the up-state and zero bias the switch bridge displacement, hence capacitance will be proportional to the electrostatic force.

The capacitance-voltage characteristics were obtained by progressively increasing the bias sweep range from below to above pull-in. The aim of this procedure was to determine the shift of the C-V minimum and from this to

determine the corresponding polarization/surface charge. Here it must be pointed out that the shift of C-V minimum is very small when the characteristic is obtained below pull-in since it arises from induced charging and in principle the electric field intensity is low. When the pull-in voltage is exceeded charge injection occurs and the dielectric polarization increases significantly. The charging effect is asymmetric, as shown in Fig. 3 since the capacitance minima have different magnitudes a fact that indicated that the electric field at the minimum of the descending characteristic is larger than in the case of the ascending one.

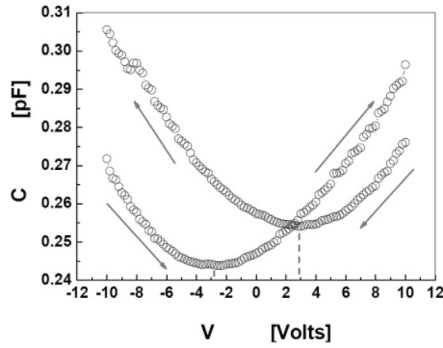


Fig. 3. Capacitance-voltage obtained below pull-in.

The shift of C-V minimum can be used to determine the charging mechanism, i.e. if it arises from Trap-Assisted-Tunneling (TAT) or Poole-Frenkel effect since in the second case the resulting polarization, which is the total trapped charge, is expected to be determined from the contribution of all trapping centers across the material energy gap and the dielectric film thickness [18]:

$$P \propto F \int_{\chi=0}^{\infty} \int_{E=0}^{\chi} \exp \left[-\frac{q}{kT} \left(\Phi - \sqrt{\frac{qE}{\pi \epsilon_{opt}}} \right) \cdot n(\chi, E) dE \right] \quad (4)$$

where F is the electric field intensity, Φ the trapped charge barrier and the other symbols have the usual meaning.

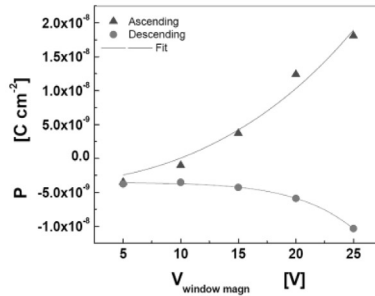


Fig. 4. Dependence of dielectric polarization on C-V window magnitude.

The dependence of calculated polarization vs C-V bias window magnitude is presented in Fig. 4 for the ascending and descending characteristics. As expected for the ascending characteristic the C-V characteristic attains minimum at the same bias with the starting one, i.e. positive for the descending and negative for the ascending. This is because the electric field in the gap is minimized when the bridge and the dielectric film surface have the same average charge. The results in Fig. 4 reveal the presence of a residual polarization/charge density of about $-3 \times 10^{-9} \text{ Ccm}^{-2}$ and that the ascending and descending induced polarizations are asymmetrical. This result agrees with the ones obtained from the TSDC spectra (Fig. 2). The fitting results further revealed differences in the trap barrier and the dielectric constant a fact that has been reported that may arise from a TAT contribution that resembles the Poole-Frenkel effect [19].

D. MEMS Capacitance Transient Response

The MEMS pull-down transient response can be used to extract information on the charging process. It has been previously shown that the pull-down transient arises from the decrease of the electric field in the region between the dielectric free surface and bridge to charge injection, hence the decrease of the electrostatic force and that the transient response obeys the stretched exponential law [20]:

$$\Delta C(t) = \Delta C_0 \cdot \exp \left[- \left(\frac{t}{\tau} \right)^\beta \right] \quad (5)$$

where the τ is the charging process characteristic time constant and β the stretch factor. The pull-down transient and the fitted stretched exponential law are presented in Fig. 5. The calculated time constant was found to be thermally activated only in the high temperature range. The same behavior was revealed when the bias was switched from negative to positive pull-down

conditions. There, it must be pointed, the effect is more complex since it involves simultaneous discharging and charging processes.

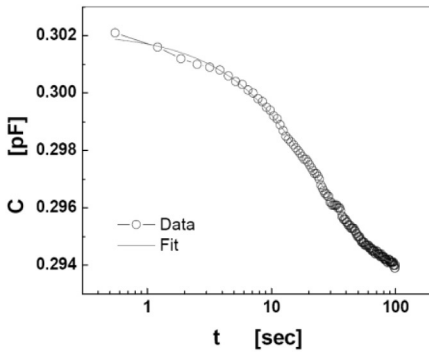


Fig. 5. Pull-down transient response.

4. CONCLUSION

In conclusion, the charging processes have been investigated in Al_2O_3 based MEMS switch. The charging process was found to be asymmetric, being larger when the top electrode is negative. Finally, the dominant charging process was found to arise from both Poole-Frenkel and TAT effect. A deep trap, which needs further investigation, was found to contribute the dielectric charging.

References

- [1] G.M. REBEIZ, *RF MEMS. Theory, Design and Technology*, pp. 185–192, Hoboken, New Jersey: J. Wiley & Sons, 2003.
- [2] Z. PENG, X. YUAN, J.C. M. HWANG, D.I. FOREHAND and C.L. GOLDSMITH, *Superposition Model for Dielectric Charging of RF MEMS Capacitive Switches Under Bipolar Control-Voltage Waveforms*, IEEE Trans. on Microwave Theory and Techniques, **55**, pp. 2911–2918, 2007.
- [3] C. CALAZA, B. MARGESIN, F. GIACOMOZZI, K. RANGRA and V. MULLONI, *Electromechanical Characterization of Low Actuation Voltage RF MEMS Capacitive Switches Based on DC CV Measurements*, Microelectronic Engineering, **84**, pp. 1358–1362, 2007.
- [4] G. PAPAIOANNOU, M. EXARCHOS, V. THEONAS, G. WANG and J. PAPAPOLYMEROU, *Temperature Study of the Dielectric Polarization Effects of Capacitive RF MEMS Switches*, IEEE Trans. on Microwave Theory and Techniques, **53**, pp. 3467–3473, 2005.
- [5] G.J. PAPAIOANNOU and T. LISEC, *Dielectric Charging Process in AlN RF-MEMS Capacitive Switches*, Proceedings of the 2nd European Microwave Integrated Circuits Conference, pp. 540–543, 2007.
- [6] P. BLONDY, A. CRUNTEANU, A. POTHIER, P. TRISTANT, A. CATHERINOT and C. CHAMPEAUX, *Effects of Atmosphere on the Reliability of RF-MEMS Capacitive Switches*, European Microwave Integrated Circuits Conference, EuMW, pp. 548–551, 2007.

- [7] H.AC TILMANS, W. Dd RAEDT, E. BEYNE, *MEMS for wireless communications from RF-MEMS components to RF-MEMS-SiP*, J. of Micromechanics and Microenginee-ring, **13**, pp. S139–S163, 2003.
- [8] C-C CHENG, C-H CHIEN, G-L LUO, C-C CHANG, C-C KEI, C-H YANG, C-N HSIAO, T-P PERNG and C-Y CHANG, *Electrical and Material Characterization of Atomic-Layer-Deposited Al_2O_3 Ggate Dielectric on Ammonium Sulfide Treated GaAs Substrates*, J. of Physics: Conference Series, **100**, pp. 042002 1–4, 2008.
- [9] N. BRESSON, S. CRISTOLOVEANU, C. MAZURÉ, F. LETERTRE and H. IWAI, *Integration of Buried Insulators With High Thermal Conductivity in SOI MOSFETs: Thermal Properties and Short Channel Effects*, Solid State Electronics, **49**, pp. 1522–1528, 2005.
- [10] A. KREIMER and A. FRYDMAN, *The Effect of Lithography Processing on the I –V Characteristics of Al– Al_2O_3 –Ag Junctions*”, J. of Applied Physics, **97**, pp. 124502 1–4, 2005.
- [11] A. CRUNTEANUA, A. POTHIER, P. BLONDY, F. DUMAS-BOUCHIAT, C. CHAMPEAUX, A. CATHERINOT, P. TRISTANT, O. VENDIER, C. DREVON, J.L. CAZAUX, L. MARCHAND, *Gamma Radiation Effects on RF MEMS Capacitive Switches*, Microelectronics Reliability, **46**, pp. 1741–1746, 2006.
- [12] P. BLONDY, A. CRUNTEANU, A. POTHIER, P. TRISTANT, A. CATHERINOT and C. CHAMPEAUX, *Effects of Atmosphere on the Reliability of RF-MEMS Capacitive Switches*, Proceedings of the 2nd European Microwave Integrated Circuits Conference, pp. 548–551, 2007.
- [13] C.M. FANG and R.A. De GROOT, *The Nature of Electron States in AlN and $\square-Al_2O_3$* , J. Phys.: Condens. Matter, **19**, pp. 386223 1–6, 2007.
- [14] F. TALBI, F. LALAM and D. MALEC, *DC Conduction of Al_2O_3 Under High Electric Field*, J. Phys. D, Appl. Physics, **40**, pp. 3803–3806, 2007.
- [15] Cheng Rong LI, Li Jian DING, Jin Zhuang LV, You Ping TU and Yang Chun CHENG, *The Relation of Trap Distribution of Alumina with Surface Flashover Performance in Vacuum*, IEEE Trans. on Dielectrics and Electrical Insulation, **13**, pp. 79–84, 2006.
- [16] J. VANDERSHUEREN and J CASIOT, *Thermally Stimulated Relaxation in Solids*, Braunlich P (Ed.) Topics in Applied Physics, **37**, ch. 4, pp. 135, Springer-Verlag, Berlin, 1979.
- [17] G. PAPAIOANNOU, J. PAPAPOLYMEROU, P. PONS and R. PLANA, *Dielectric Charging in Radio Frequency Microelectro-Mechanical System Capacitive Switches: A Study of Material Properties and Device Performance*”, Appl. Phys. Letters, **90**, pp. 233507 1–3, 2007.
- [18] R. RAMPRASAD, *Phenomenological Theory to Model Leakage Currents in Metal–Insulator–Metal Capacitor Systems*, Phys. Stat. Solidi (b), **239**, pp 59–70, 2003.
- [19] S.P. LAU, J.M. SHANNON and B.J. SEALY, *Changes in the Poole–Frenkel Coefficient With Current Induced Defect Band Conductivity of Hydrogenated Amorphous Silicon Nitride*, Journal of Non-Crystalline Solids, **277–230**, pp.533–537, 1998.
- [20] G. PAPAIOANNOU, M. EXARCHOS, V. THEONAS, G. WANG, and J. PAPAPOLYMEROU, *Temperature Study of the Dielectric Polarization Effects of Capacitive RF MEMS Switches*, IEEE Trans. on Microwave Theory and Techniques, **53**, pp. 3467–3473, 2005.

Charging Effects and Related Equivalent Circuits for Ohmic Series and Shunt Capacitive RF MEMS Switches

George PAPAIOANNU¹, Romolo MARCELLI², Giancarlo BARTOLUCCI³, Simone CATONI², Giorgio De ANGELIS², Andrea LUCIBELLO², Emanuela PROIETTI², Benno MARGESIN⁴, Flavio GIACOMOZZI⁴, François DEBORGIES⁵

¹University of Athens, Solid State Physics Section, Panepistimiopolis Zografos, Greece

²CNR-IMM Roma, Via del Fosso del Cavaliere 100, 00133 Roma, Italy

Phone +39 06 4993 4536

³University of Roma “Tor Vergata”, Roma, Italy

Phone +39 06 72597350

⁴FBK-irst, Povo (TN), Italy,

Phone +39 0461 314490

⁵ESA-ESTEC, Noordwijk, The Netherlands

Abstract. Charging effects in dielectrics are currently considered as the major limiting factor for the reliability of RF MEMS switches. In this paper, an ohmic series switch and a shunt capacitive one are studied for modeling the charging contributions due to the actuation pads used for the electrostatic actuation of the device. For simulation purposes, a lumped circuit based on equivalent capacitances can be defined.

1. SUMMARY

RF MEMS switches are micro-mechanical devices utilizing, a DC bias voltage for controlling the collapse of metallized beams [1].

Magnetic [2], thermal [3] and piezoelectric [4] actuations have been also evaluated, but the electrostatic one seems to be until now preferred for no current flowing, i.e. a virtual zero power consumption, less complicated manufacturing processes and more promising reliable devices [5]. During the last few years, several research activities started to release the feasibility of RF MEMS switches

also for Space Applications [6], [7]. The electrostatic actuation of clamped-clamped bridges or cantilevers determines the ON and OFF states depending on the chosen configuration. As well established, RF MEMS switches are widely investigated for providing low insertion loss [1], no or negligible distortion [8], [9] and somehow power handling [10], [11] capabilities for a huge number of structures. On the other hand, the reliability of this technology has been not yet fully assessed, because of the limitations introduced by: (i) the mechanical response of the single switches [12], (ii) the necessary optimization of the packaging [13], and (iii) the charging mechanisms.

In particular, the charging effect is due to the presence of both the dielectric material used for the realization of lateral actuation pads, used to control the collapse of bridges and cantilevers far from the RF path, and the dielectric used for the capacitance in the case of shunt connected microstrip and coplanar configurations. Presently, there is a wide literature about the onset of the mechanism [14], [15], [16] and its control by means of uni-polar and bi-polar actuation voltage schemes. [17], [18].

Some results give evidence also for the substrate contribution to charging effects [19]. Specifically, electromagnetic radiation is a serious issue for space applications [20], [21].

Specific aging schemes based on the temperature are also proposed for long term evaluation of the devices [22].

In this paper, it will be presented the characterization of two configurations of RF MEMS switches, to demonstrate how the actuation voltage is modified by using a uni-polar bias voltage and how it is under control and stable if an inversion in the bias voltage is provided. In particular, the measurements recorded for an ohmic series and for a shunt capacitive configuration will be presented and discussed, considering the main source of charging for both devices.

On the time scale of interest to the RF-MEMS capacitive switches response (i.e. greater than 1 μ sec) an electric field can interact with the dielectric film in two primary ways. These are the re-orientation of defects having an electric dipole moment, such as complex defects, and the translational motion of charge carriers, which usually involve simple defects such as vacancies, ionic interstitials and defect electronic species. These processes give rise to the dipolar (P_D) and the intrinsic space charge (P_{SC-i}) polarization mechanisms, respectively. Moreover, when the dielectric is in contact with conducting electrodes charges are injected through the trap assisted tunneling and/or the Poole-Frenkel effect [23] giving rise to extrinsic space charge polarization (P_{SC-e}) whose polarity is opposite with respect to the other two cases. In RF-MEMS capacitive switches during the actuation all the polarization mechanisms occur simultaneously and the macroscopic polarization is given by

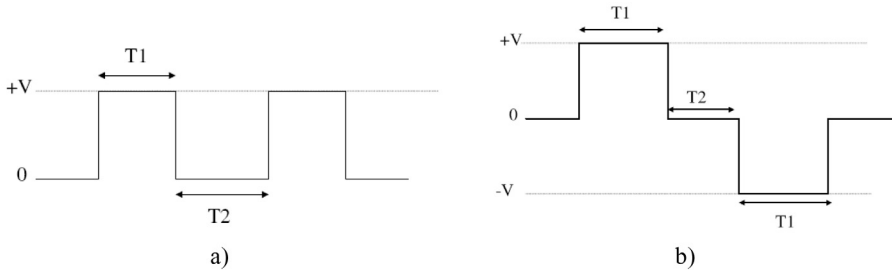


Fig. 1. Shape of the pulse trains used for the experiments on the charging effects. (a) is the uni-polar scheme, while (b) is the bi-polar one.

$$P_{tot} = P_D + P_{SC-i} - P_{SC-e} \tag{1}$$

Now, from elementary physics it is known that the electric displacement, D , defined as the total charge density on the electrodes, will be given by $D = \epsilon_0 E + P$, where E is the applied field and P the dielectric material polarization. The resulting polarization P may be further divided into two parts according to the time constant response [24]:

a) An almost instantaneous polarization due to the displacement of the electrons with respect to the nuclei. The time constant of the process is about 10-16 sec and defines the high frequency dielectric constant that is related to the refractive index.

b) A delayed time dependent polarization $P(t)$, which determines the dielectric charging in MEMS, starting from zero at $t=0$, due to the orientation of dipoles and the distribution of free charges in the dielectric, respectively.

Moreover the growth of these polarization components may be described in the form of $P_j(t) = P_{j0} [1 - f_j(t)]$

The index j refers to each polarization mechanisms and $f_j(t)$ are exponential decay functions of the form $\exp\left[-\left(\frac{t}{\tau}\right)^\beta\right]$ Here τ is the process time and β the stretch

factor. If $\beta=1$ the charging/discharging process is governed by the Debye law. In disordered systems like the amorphous oxides, which possess a degree of disorder, $\beta < 1$ and the charging/discharging process is described by the stretched exponential law.

In the case of a MEMS switch that operates under the waveforms in Fig. 1, the dielectric is subjected to charging when the bridge is in the DOWN position and discharging in the UP position, independently of the ON or OFF functionality of the device.

More specifically, when a uni-polar pulse train is applied (Fig. 1 a)) then the device is subjected to contact-less charging below pull-in and pull-out. Above pull-in and pull-out the device is subjected to contact charging.

If we assume that at room temperature the density of free charges in LTO SiO₂ is very low we can re-write Eq. (1) as:

$$P = P_D - P_{SC} \quad (2)$$

where PSC is the space charge polarization of extrinsic origin. When we apply a pulse train the following will occur:

- during the contact-less charging the electric field increases the dipolar polarization and assists to redistribution and dissipation of injected charges;
- during the contact charging the high electric field causes a further increase of the dipolar polarization, and through the charge injection contributes to the build-up of space charge polarization. Due to the dielectric film polarization the pull-in and pull-out voltages will be determined by

$$V_{pi} = \sqrt{\frac{8kz^3}{27\epsilon_0 A}} - \frac{z_1 P_{pi}}{\epsilon_0} \quad \text{and} \quad V_{p0} = \sqrt{\frac{2kz_1^2(z-z_1)}{\epsilon_0 A}} - \frac{z_1 P_{p0}}{\epsilon_0} \quad (3)$$

In the Si₃N₄ dielectric it has been shown that, at room temperature, the space charge polarization induced by the charge injection is the dominant mechanism [25], [26]. If we assume that the same effect holds for SiO₂ we are led to the conclusion that the pull-out voltage will increase with time when a uni-polar pulse train is applied.

In Fig. 2 and in Fig. 3 the dependence of the actuation and deactuation voltages on the number of cycles was fitted for the exploited devices S1 and CL by assuming that the charging process follows the stretched exponential law. The fitting on the number of cycles (N) can be performed since each cycle maintains a constant shape and represents a certain effective ON and OFF time. The differences in the effective ON and OFF times will reflect in the number of cycles (N*) that corresponds to the process time τ . According to Eq. (3), and in agreement with the above discussed growth for the polarization, we can apply the following equation to describe the evolution of the pull-in and pull-out voltages as a function of time/number of cycles.

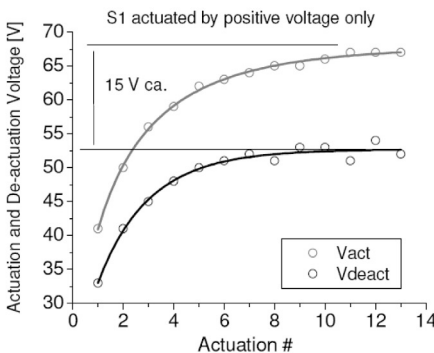
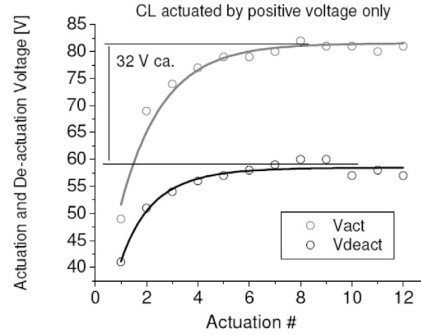


Fig. 2. Fitted actuation and deactuation voltages for the S1 device following an exponential trend.

Fig. 3. Fitted actuation and deactuation voltages for the CL device following an exponential



$$V_j(N) = V_{0,j} - \frac{z_l P_j}{\epsilon_0} \cdot \left\{ 1 - \exp \left[-\frac{N}{N_j^*} \right]^\beta \right\} \quad (4)$$

where z_l is the dielectric thickness, j an index that stands for actuation (pi) and deactuation (po) while $V_{0,j}$ represents the pull-in and pull-out voltages that are determined by the electromechanical model. The fitting results show excellent agreement with the experimental data and the fitting parameters are listed in Table 1.

Here it must be pointed out that:

$$\Delta V = -\frac{z_l P_j}{\epsilon_0} = -\frac{z_l (P_{D,j} - P_{SC,j})}{\epsilon_0} \quad (5)$$

Table 1. Fitted values for the exponential trend of the actuation (Act) and deactuation (Deact) of both S1 and CL devices by using Eq. (4) and Eq. (5).

		V_0	ΔV	β	N^*
Fig. 2	Act	13.5	54.4	0.69	1.67
	Deact	29.5	33.2	0.96	1.96
Fig. 3	Act	27.0	54.5	1	1.67
	Deact	36.8	22.4	0.83	2.5

The fitting results reveal that the dominant mechanism is the space charge polarization ($P_j < 0$). Moreover, it is worth noting that the actuation voltage increases faster than the deactuation one. Such a behavior can result from a faster increase of space charge polarization or decrease of dipolar polarization when the bridge is non-actuated. Such a case could occur if the dipolar polarization process would be faster than the space charge one. Another possible situation could be the charging between the actuation pads and the ground plane of CPW across the substrate dielectric [27]. This charging process gives rise to a longitudinal

polarization across the substrate oxide that behaves like the dipolar polarization. The values of N^* for actuation and deactuation agree with the presence of both mechanisms, which is a slower build-up of space charge polarization and competition from a longitudinal polarization across substrate.

Applying a bipolar bias scheme we observe that both actuation and deactuation voltages do not vary significantly with time. This can be easily attributed to the field induced charging/discharging processes. A significant difference that arises from the bipolar actuation is the reversal of magnitude of actuation and deactuation voltages.

For electrical simulation purposes, an equivalent circuit which accounts for the capacitive effect, intuitively related to such a physical mechanism, can be adopted. A resistive effect has also to be included because of dielectric and ohmic losses. Actually, the energy involved in the charging effect will cause an increase in the actuation voltage as given in Eq. (5), and such an increase is clearly related to the accumulated charge. As a consequence, dependently on the applied voltage scheme (i.e. uni-polar or bi-polar) the equivalent lumped describing this effect can be obtained by assuming the presence of a capacitor in parallel with the resistive contribution coming from the bulk of the dielectric used for the pads under the bridge. For both the exploited devices, pads as wide as $120 \times 120 \mu\text{m}^2$ for the CL configuration, and $120 \times 140 \mu\text{m}^2$ for S1, symmetric with respect to the central conductor of the CPW have to be considered. Lumped components including those MIM capacitors can be obtained by defining the quantities $C_a = \epsilon_0 \epsilon_r A/d$ and $R_a = \rho d/A$, where A is the area of the capacitor, d the thickness and ρ the bulk resistivity of the dielectric. During the actuation, additional elements have to be included in the equivalent circuit, due to the feeding lines in polysilicon material to be used for imposing the actuation voltage. Successively, such a contribution has to be not considered when the de-actuation occurs. In this case, the characteristic time needed for restoring the initial conditions will be $\tau_a = R_a C_a$. For the two measured configurations, by using the following values: $\epsilon_r \approx 4$ for SiO_2 , $d \approx 300 \text{ nm}$ as the dielectric and, as an order of magnitude, $\rho \approx 10^{13} \Omega\text{m}$, we get $C_a(\text{CL}) \approx 1.7 \text{ pF}$ and $R_a(\text{CL}) \approx 2 \times 10^{16} \Omega$, while $C_a(\text{S1}) \approx 2 \text{ pF}$ and $R_a(\text{S1}) \approx 1.8 \times 10^{16} \Omega$, from where $\tau_a(\text{CL}) = 3.4 \times 10^4 \text{ s}$ and $\tau_a(\text{S1}) = 3.6 \times 10^4 \text{ s}$, i.e. almost equal between them and in the order of few hours. Actually, the characteristic times needed by both configurations for having a natural restoring of the initial value for the actuation voltage are so long that it is impossible to re-obtain the initial conditions after continuous actuations. For the above reason, in the previously plotted curves there was no evidence for a decay of the induced charge during the measurement.

Acknowledgement. The authors wish to acknowledge the funding from the Contract ESA/ESTEC AO 1-5288/06/NL/GLC: High Reliability MEMS Redundancy Switch.

References

- [1] G.M. REBEIZ, *RF MEMS Theory, Design, and Technology*, John Wiley and Sons, Hoboken, 2003.
- [2] J. JOUNG, J. SHEN, P. GRODZINSKI, *Micropumps Based on Alternating High-Gradient Magnetic Fields*, *IEEE Trans. on Magn.*, **36**(4), pp. 2012–2014, 2000.
- [3] D. YAN, *Mechanical Design and Modeling of MEMS Thermal Actuators for RF Applications*, thesis on Master of Applied Science in Mechanical Engineering, Waterloo, Ontario, 2002, http://resonance.uwaterloo.ca/students/dyan/thesis_winter_master.pdf
- [4] H.-C. LEE, J.-Y. PARK AND J.-UK BU, *Piezoelectrically Actuated RF MEMS DC Contact Switches With Low Voltage Operation*, *IEEE Microwave and Wireless Components Lett.*, **15**(4), pp. 202–204, 2005.
- [5] H. De LOS SANTOS, G. FISCHER, H.A.C. TILMANS, and J.T.M. van BEEK, *RF MEMS for Ubiquitous Wireless Connectivity Part 1-Fabrication and Part 2-Application*, *IEEE Microwave Magazine*, **5**(4), pp. 36–65, 2004.
- [6] ESA/ESTEC PROJECT No. 14628/NL/CK-MEM Switch on: MICROWAVE ELECTROSTATIC MICROMACHINED DEVICES FOR ON-BOARD APPLICATIONS.
- [7] ESA-ESTEC Project MEDINA No. 14627/00/NL/WK.
- [8] [8] L. Dussopt, G. M. Rebeiz, “Intermodulation distortion and power handling in RF MEMS switches, varactors, and **tunable filters**”, *IEEE Trans. on Microwave Theory Techn.*, Vol. 51, No. 4, Part 1, April 2003 pp.1247 – 1256, 2003.
- [9] D. GIRBAU, N. OTEGI and L. PRADELL, *Study of Intermodulation in RF MEMS Variable Capacitors*, *IEEE Trans. On Microwave Theory Tech.*, **54**(3), pp. 1120–1130, 2006.
- [10] D. MERCIER, P. BLONDY, D. BARATAUD, D. CROS, P. GUILLON, C. CHAMPEAUX, P. TRISTANT, A. CATHERINOT, *Model for MEMS Switches Power Handling and Phase Noise*, *Proceed. of the 32nd European Microwave Conference*, pp. 1–4, 2002.
- [11] D. PEROULIS, S.P. PACHECO, and L.P.B. KATEHI, *RF MEMS Switches With Enhanced Power-Handling Capabilities*, *IEEE Trans. Microwave Theory Tech.*, **52**(1), pp. 50–68, 2004.
- [12] L. ZHOU, *RF MEMS DC Contact Switches for Reconfigurable Antennas*, thesis on Master of Science in Electrical Engineering, San Diego State University, 2006, http://digitaladdis.com/sk/Lei_Zhou_Thesis_RF_MEMS.pdf
- [13] W.P. KORNRUMPF, N.N. KARABUDAK, AND W.J. TAFT, *RF MEMS Packaging for Space Applications*, *Proceed. of 22nd AIAA International Communications Satellite Systems Conference & Exhibit*, pp. AIAA 2004–31069, 12 May, Monterey, California, 2004.
- [14] C. GOLDSMITH, J. EHMKE, A. MALCZEWSKI, B. PILLANS, S. ESHELMAN, Z. YAO, J. BRANK, and M. EBERLY, *Lifetime Characterization of Capacitive RF MEMS Switches*, in *IEEE MTT-S Dig.*, pp. 227–230, 2001.
- [15] X. YUAN, S.V. CHEREPKO, J.C.M. HWANG, C.L. GOLDSMITH, C. NORDQUIST, *Dielectric-Charging Effects on RF MEMS Capacitive Switches*, in *IEEE MTT-S Dig.*, pp. 1943–1946, 2004.
- [16] W.M. van SPENGEN, R. PUERS, R. MERTENS, and I. De WOLF, *A Comprehensive Model to Predict the Charging and Reliability of Capacitive RF MEMS Switches*, *J. Micromech. Microeng.* **14**, pp. 514–521, 2004.
- [17] S.T. PATTON, and J.S. ZABINSKI, *Effects of Dielectric Charging on Fundamental Forces and Reliability in Capacitive Microelectromechanical Systems Radio Frequency Switch Contacts*, *J. Appl. Phys.*, **99**, pp. 94910–91, 2007.
- [18] Z. PENG, X. YUAN, J.C. M. HWANG, D.I. FOREHAND, and C.L. GOLDSMITH, *Superposition Model for Dielectric Charging of RF MEMS Capacitive Switches Under Bipolar Control-Voltage Waveforms*, *IEEE Trans. on Microwave Theory Tech.*, **55**(12), pp. 2911–2918, 2007.
- [19] G. Wang, *RF MEMS Switches with Novel Materials and Micromachining Techniques for SOC/SOP RF Front Ends*, thesis on School of Electrical and Computer Engineering of the Georgia Institute of Technology, 2006, <http://smartech.gatech.edu/handle/1853/14112>
- [20] V.G. THEONAS, M. EXARCHOS, G. KONSTANTINIDIS and G.J. PAPAIOANNOU, *RF MEMS Sensitivity to Electromagnetic Radiation*, *Second Conference on Microelectronics, Microsystems and Nanotechnology, Journal of Physics: Conference Series 10*, pp. 313–316, 2005.
- [21] E. PAPANDREOU, M. LAMHAMDI, C.M. SKOULIKIDOU, P. PONS, G. PAPAIOANNOU, and R. PLANA, *Structure Dependent Charging Process in RF MEMS Capacitive Switches*, *Microelectronics Reliability*, **47** pp. 1812–1817, 2007.

- [22] X. YUAN, Z. PENG, J.C. M. HWANG, D. FOREHAND, and C.L. GOLDSMITH, *Acceleration of Dielectric Charging in RF MEMS Capacitive Switches*, IEEE Trans. on Device and Materials Reliability, **6**(4), pp. 556–563, 2006.
- [23] S. MELLE, D. DE CONTO, L. MAZENQ, D. DUBUC, B. POUSSARD, C. BORDAS, K. GRENIER, L. BARY, O. VENDIER, J.L. MURARO, J.L. CAZAUX, R. PLANA, *Failure Predictive Model of Capacitive RF-MEMS*, Microelectronics Reliability, **45**, pp. 1770–5.
- [24] J. VANDERSHUEREN and J. CASIOT, *Thermally Stimulated Relaxation in Solids*, Braunlich P (Ed.) Topics in Applied Physics, **37**, ch.4, pp. 135–223, Springer-Verlag, Berlin, 1979.
- [25] G. PAPAIOANNOU, J. PAPAPOLYMEROU, P. PONS and R. PLANA, Appl. Phys. Letters, **90**, pp. 233507, 2007.
- [26] G. PAPAIOANNOU, F. GIACOMOZZI, E. PAPANDREOU and B. MARGESIN, *Charging Processes in RF-MEMS Capacitive Switches with SiO₂ Dielectric*, Proceedings of the 2007 MEMSWAVE Workshop, 8th International Symposium on RF MEMS and RF Microsystems, 26-29 June, Barcelona, Spain, 2007.
- [27] P. CZARNECKI, X. ROTTENBERG, P. SOUSSAN, P. EKKELS, P. MULLER, P. NOLMANS, W. De RAEDT, H.A.C. TILMANS, R. PUERS, L. MARCHAN, and I. De WOLF, *Influence of the Substrate on the Lifetime of Capacitive RF MEMS Switches*, accepted for presentation in MEMS-2008.

An Efficient Modeling Method for Simulating Time-Response of RF-MEMS Switches

V. LEUS, D. ELATA

Technion – Israel Institute of Technology, Haifa 32000, Israel

Phone: +9724292617

Abstract. A novel efficient method for simulating the undamped time-response of RF-MEMS switches is presented. Computation of only four static states enables to reconstruct the entire dynamic response for any applied voltage, avoiding explicit time-integration of the momentum equations. Furthermore, the dynamic pull-in voltage of the switch can be easily extracted with no additional computational effort.

1. INTRODUCTION

In some applications of RF MEMS switches, such as phased-array antennas and radars, a short switching time is essential for performance [1]. Therefore, optimal design is crucially important to predict the time required to achieve switching. However, the transient dynamic analysis of the electro-structural coupled system is extremely time-consuming, especially when a 3D model is considered. In this case the extraction of the timeresponse of a specific switch subjected to a specific driving voltage, may take from several hours to several days of computation. This makes parametric design of switches very cumbersome. Efficient modeling tools are required to simplify the procedure of time-response simulation.

The new modeling method proposed here is capable of simulating the dynamic response of actuators with general geometry, including non-linear effects such as stress stiffening and residual stresses. The method is extremely efficient relative to transient dynamic analysis, because instead of time integration of a set of momentum equations (an equation for each node), the problem is reduced to a single scalar momentum equation based on the deformation of only four *static* states of the system.

2. THE MODELING PRINCIPLE

As a model problem of an electrostatic switch, the clamped-clamped beam actuator is considered (Fig. 1).

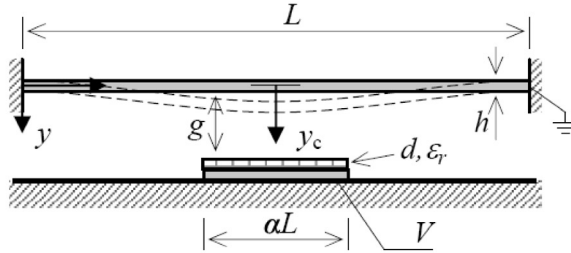


Fig. 1. Clamped-clamped beam actuator ($L=240\mu\text{m}$, $W=240\mu\text{m}$, $g=2\mu\text{m}$, $h=1\mu\text{m}$, $d=0.1\mu\text{m}$ and $\alpha=0.5$; $E=70\text{GPa}$, $\nu=0.35$, $\rho=2700\text{ kg/m}^3$, $\epsilon_r=4$)

This system is actuated by a step-function voltage applied to the fixed bottom electrode, while the beam is grounded. The bottom electrode is coated with a thin dielectric layer. When the applied step-function voltage is lower than the dynamic pull-in voltage the beam oscillates around a steady state deformation [2]. If, however, the applied voltage is higher than the dynamic pull-in voltage the beam collapses into contact with the bottom electrode.

In the proposed modeling approach, all the deformed states during the dynamic response are assumed to have a deformation which is identical to that of a static state. To uniquely identify any dynamic state with a related static state, we consider a single scalar measure of the deformed state. In the case of the clamped-clamped beam actuator this scalar measure is the deflection of the beam center.

Assuming negligible damping in the system, at any given point in time, the energy of the system is given by its Hamiltonian

$$H(t) = E_k + E_m + E_e \quad (1)$$

In the right hand side of (1), E_k is the kinetic energy, E_m is the elastic mechanical potential due to bending and stretching of the beam, and E_e is the total electrostatic potential energy of the system (i.e. the sum of the potential energies of the deformable capacitor and of the voltage source). For this system, the electrostatic potential energy is given by $E_e = 1/2CV^2$, where C is the capacitance of the deformable capacitor at any given state, and V is the applied voltage.

For the initial state at $t=0$ the velocity and the deflection of the beam are zero, and therefore the Hamiltonian is equal to the electrostatic potential energy of the system $H_0 = -1/2CV^2$. For negligible damping, once the voltage is applied at $t=0$, the Hamiltonian is unchanged. This yields an energy constraint that relates

sequential states of the system, where each specific static state (equilibrium deflection) is denoted by a superscript 'j'

$$E_k^j = \frac{1}{2} \Delta C^j V^2 - E_m^j \quad (2)$$

were $\Delta C^j = C^j_{(y(x,z))} - C^j_{(0)}$

The kinetic energy of the beam is defined by

$$E_k = \int_0^L \int_0^W \frac{\gamma}{2} \left(\frac{dy(x,z)}{dt} \right)^2 dx dz \quad (3)$$

Here y is the deflection, x is the coordinate along the beam length, z is the coordinate along the beam width, $\gamma = \rho h$ is the mass of the beam per unit area, where ρ is the density of the material and h is the beam thickness.

For a specific static deflection j , the kinetic energy defined in (3) can be written in the following way

$$\begin{aligned} E_k^j &= \frac{\gamma}{2} \int_0^L \int_0^W \left(\frac{\Delta y(x,z)}{\Delta t^j} \right)^2 dx dz \\ &= \frac{\gamma}{2} \int_0^L \int_0^W \left(\frac{\Delta y^j(x,z)}{\Delta y_c^j} \cdot \frac{\Delta y_c^j}{\Delta t^j} \right)^2 dx dz \end{aligned} \quad (4)$$

where $(\Delta y^j(x,z) = y^{j+1}(x,z) - y^j(x,z))$ is the incremental deflection between two adjacent static states of the beam during the time interval Δt^j , and Δy_c^j is the incremental deflection of the beam-center between the two adjacent static states. By considering the limit case $\Delta t \rightarrow 0$, the velocity of the beam center is given by $\dot{y}_c^j = \Delta y_c^j / \Delta t^j$, and we define

$$\beta^j \equiv \frac{\gamma}{2} \int_0^L \int_0^W \left(\frac{\Delta y^j(x,z)}{\Delta y_c^j} \right)^2 dx dz \quad (5)$$

Now equation (4) can be rewritten as

$$E_k^j = \dot{y}_c^j \beta^j \quad (6)$$

From equations (2) and (5) the velocity of the beam center can be extracted

$$\dot{y}_c^j = \pm \sqrt{\frac{\frac{1}{2} \Delta \mathbf{C}^j V^2 - E_m^j}{\beta_j}} \quad (7)$$

Considering only positive velocities, the time required for transition between two adjacent static states can be calculated as

$$\Delta t^j = \frac{\Delta y_c^j}{\sqrt{\frac{\frac{1}{2} \Delta \mathbf{C}^j V^2 - E_m^j}{\beta_j}}} \quad (8)$$

Consequently, if N is the number of the equilibrium states considered from initial state to contact, then the time required for the beam center to achieve contact (switching time) is found to be

$$t_c = \sum_{j=1}^N \frac{\Delta y_c^j}{\sqrt{\frac{\frac{1}{2} \Delta \mathbf{C}^j V^2 - E_m^j}{\beta_j}}} \quad (9)$$

In order to reconstruct the switching response for any applied step-function voltage V (above the dynamic pullin voltage), we have to know the elastic potential and capacitance at several static deflections throughout the gap. The accuracy of the summation in (9) can be expected to increase if more static states are considered. In the following section we show that the elastic energy, capacitance, and parameter β may be interpolated such that only a few static states (four in this case) must be computed.

2. ALGORITHM IMPLEMENTATION

The response of the clamped-clamped beam actuator was analyzed by a 3D model using the ANSYS finite elements software. Material properties of the beam are: Young modulus $E = 70\text{GPa}$, **Poisson's ratio** $\nu = 0.35$, the density $\rho = 2700\text{ kg/m}^3$, the relative permittivity of the dielectric $\epsilon_r = 4$. The geometrical parameters are: beam length $L = 240\mu\text{m}$, beam width $W = 40\mu\text{m}$, initial gap $g = 2\mu\text{m}$, the beam thickness $h = 1\mu\text{m}$, dielectric thickness $d = 0.1\mu\text{m}$, and $\alpha = 0.5$. The equilibrium deflections of the beam were obtained using the DIPIE algorithm [3] implemented in ANSYS. Accordingly, four equilibrium deflections of the beam were extracted by static electrostructural analysis, corresponding to four center node deflections: 0.2, 0.4, 0.6, and 0.8 of the nominal gap g (Fig. 2). For each state, the electrostatic

and elastic potentials are derived, and the bottom surface nodes of the beam are also extracted for further calculation of the parameter β .

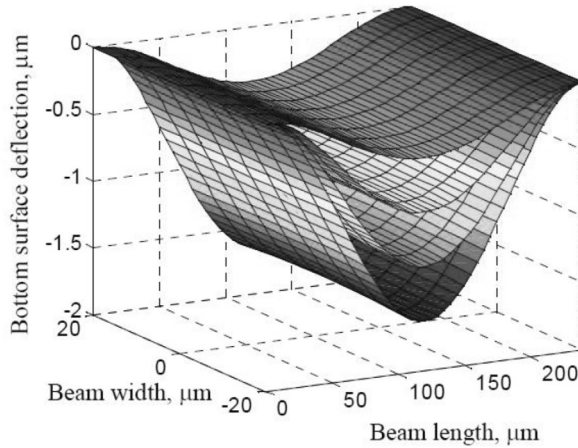


Fig. 2. Four equally spaced equilibrium deflections of the bottom surface of the beam as extracted by ANSYS.

The above finite elements results are a basis for further algorithm implementation which is performed in Matlab. The elastic and electrostatic potentials of the beam throughout the whole air gap are approximated by specific approximation functions using least-square methods. By exploiting the analogy with the parallelplates actuator the elastic energy can be well-described by a third-order polynomial which is optimally fitted by the least square method (Fig. 3).

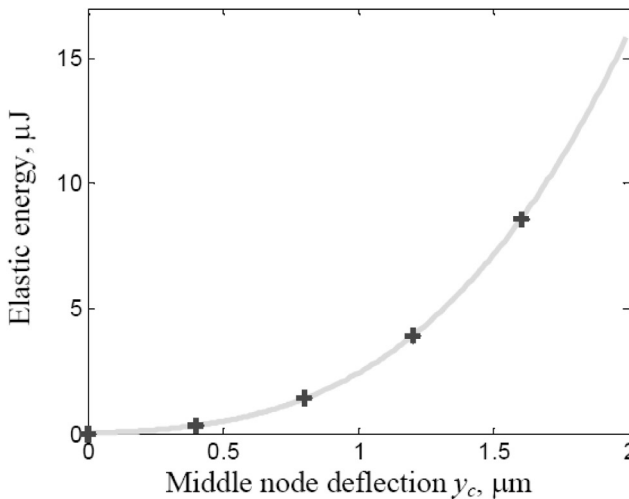


Fig. 3. Elastic energy of the beam as function of the middle node deflection (the '+' markers represent the extracted values from ANSYS, solid line represents the polynomial fit).

Based on the same analogy, the capacitance associated with the beam center is well approximated by the following formula

$$\Delta C = \frac{a \varepsilon_0 A y_c}{(g + d / \varepsilon_r)(g + d / \varepsilon_r - b y_c)} \quad (10)$$

where the coefficients a and b are optimally fitted by the least square method (Fig. 4)

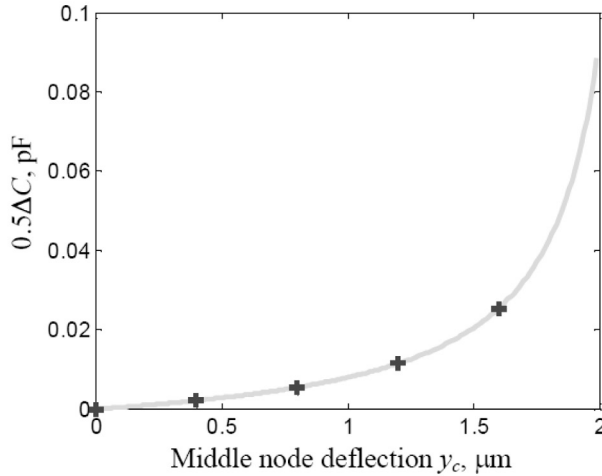


Fig. 4. Relative electrostatic energy per unit voltage-squared as function of the middle node deflection (the '+' markers represent the extracted values from ANSYS, the solid line represents the least square fit).

To find the parameter β (equation (5)), the bottom surface deflections of the beam were interpolated throughout the whole air gap, based on the four simulated static deflections.

3. RESULTS AND COMPARISON

The time-responses of the clamped-clamped beam actuator were calculated by summing the time steps as defined in equation (8), for four different applied voltages (solid lines in Fig. 5). The overall time required to extract these four time trajectories is ten minutes. Most of this computation time is required to simulate the four static deflections in ANSYS, and implemented of the new algorithm in Matlab takes several seconds only.

The performance of the proposed method is compared with full time-integration transient analysis using ANSYS. To this end, the same finite element model that is used to simulate the four static states is used to simulate the dynamic response by performing a transient analysis (full time-integration of the momentum equations). In the transient analysis the time step should be validated to be sufficiently small to insure accuracy of the numerical computation. This requires performing the timeintegration in several iterations, where extraction of each time-response for a specific applied voltage takes at least one and a half hours (depending on what voltage is applied). Consequently, extraction of four time-responses for four different applied voltages took around seven hours of computation (dotted lines in Fig. 5).

It can be seen from Fig. 5, that excellent agreement of the results is obtained (the relative errors are within 1%), but the considerable difference in computation time is evident (Table 1).

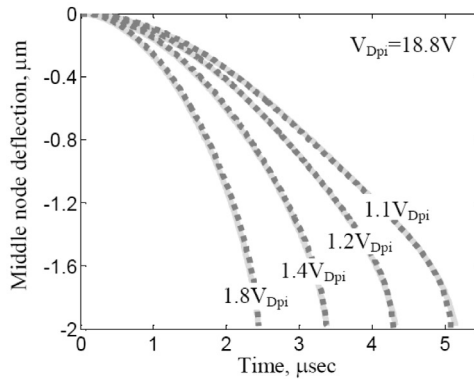


Fig. 5. Time-trajectories of the clamped-clamped beam actuator for four different applied voltages. For each applied voltage the time response is simulated using finite element timeintegration (dotted lines: computation time is around seven hours) and also using the novel algorithm (solid lines: computation time is ten minutes).

Table 1. Comparison of two methods

	Time-investigation method	New method
Time-trajectori extraction for four different applied voltages (computation time)	≈ 7 hours	10 min
Dynamic pull-in voltage extraction (computation time)	≈ 10 hours	< 1 sec
Relative error		< 1 %

Once the switching time for the four applied voltages is extracted, the dynamic pull-in voltage of the actuator can be easily extracted. Using the linear relation between the extracted switching times and the measure of the applied

voltage [4] the dynamic pull-in voltage can be extracted with negligible computation effort. The dynamic pull-in voltage extracted from the switching times is 18.8V (the computation time is less than a second), whereas the dynamic pull-in voltage extracted from the accurate transient analysis is 18.9V (the computation time is around ten hours).

4. CONCLUSION

The new algorithm for simulating the dynamic response of RF-MEMS switches was presented. The method enables to reconstruct the time-response of the switch for any applied voltage based on four static states (equilibrium deflections) only. It is shown that the proposed technique is extremely time-efficient (several minutes of computation) relative to ordinary timeintegration method (several hours of computation), while demonstrating high accuracy of the results. It is also shown that the dynamic pull-in voltage of the switch can be effortlessly extracted based on previously extracted switching times. Consequently, the proposed method may be a very useful tool for parametric design of RF-MEMS switches.

Acknowledgement. The authors wish to acknowledge the assistance and support of the AMICOM Network of Excellence on RFMEMS and RF Microsystems funded by the Sixth Framework Program of the European Commission, and of Scott and Isabelle Black from the New England region of the American Technion Society.

References

- [1] J.J. YAO, *RF MEMS from a Device Perspective*, Journal of Micromechanics and Microengineering, **10**, pp. R9–R38, 2000.
- [2] V. LEUS and D. ELATA, *On the Dynamic Responses of Electrostatic MEMS Switches*," Journal of Microelectromechanical Systems, **17**, pp. 236–243, 2008.
- [3] O. BOCHOBZA-DEGANI, D. ELATA, and Y. NEMIROVSKY, *An Efficient DIPIE Algorithm for CAD of Electrostatically Actuated MEMS Devices*, Journal of Microelectromechanical Systems, **11**, pp. 612–620, 2002.
- [4] V. LEUS and D. ELATA, *Predicting the Switching Time of Electrostatic Actuators*, IEEE-MEMS conference, Tucson, Arizona, January 2008.

Nano-Electro-Mechanical-Systems: from Ideas to Reality Check

Adrian M. IONESCU

Nanolab, École Polytechnique Fédérale Lausanne, Switzerland

Abstract. This paper is addressing some of the opportunities and challenges related to the unique features of Nano-Electro-Mechanical-Systems (NEMS) and their potential for future applications. NEMS have generated a large spectrum of original new device ideas motivated by their intrinsic characteristics, with potential applications in ultimate sensing, analog and radio frequency. However, the path from the simple proof of concept of new NEMS device concepts to the full achievement of the specifications needed for real-life applications faces difficult obstacles that need substantial supplementary efforts and smart engineering for success. Beyond the fabrication, modeling, simulation and design challenges of NEMS, integrated interfaces for local signal processing are critically needed in many applications. The paper is illustrated with some concrete examples of hybrid NEM-semiconductor devices that can hold promise for future low power applications of NEMS.

1. NEMS OPPORTUNITIES, CHALLENGES AND FUTURE APPLICATIONS

Nano-Electro-Mechanical-Systems are expected to introduce a revolution into future signal processing and system architectures by exploiting some of the unique features of ultra-small movable objects that can be operate at unrivalled low levels of power [1]. Today, electro-mechanical signal processing is envisioned as a key technical area of the More-than-Moore research domain of nanoelectronics. Particularly, More-than-Moore is dealing with future electronic systems taking benefits from a large variety of devices and technologies (not limited to pure solid-state electronic devices) and their heterogeneous co-integration, where the Moore's law is not the main driving force (see Fig. 1). In this perspective, MEMS and NEMS unique characteristics that complement today's advances CMOS technology nodes are the new functionality and performance opportunities in sensing and analog/RF. On the other hand, one should realistically consider the benefits and challenges of scaling of MEMS into NEMS and address the generic

problems of NEMS interfacing (Fig. 2) with the real world and their integration in functional system that should be able to exploit their particular features: poor signal-tonoise ratio, extremely low levels of signal, surrounding parasitics, detection of nano-displacements, variability, etc. This paper is briefly addressing some of the identified major challenges and opportunities of NEMS, by confronting academic research ideas with the reality check; the final goal being to bridge the scientific discovery and the engineering of real and useful micro/nano-systems.

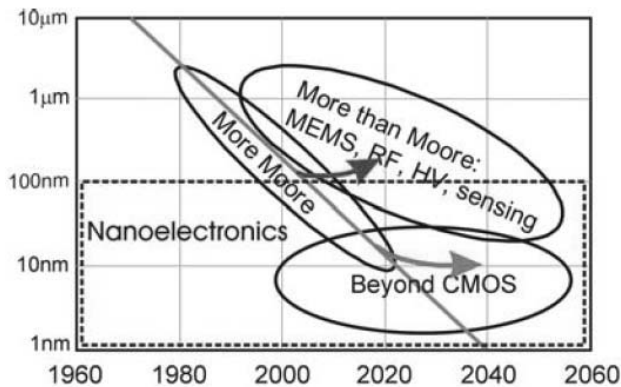


Fig. 1. More Moore, More-than-Moore and Beyond CMOS domains of nanoelectronics in size versus time diagram.

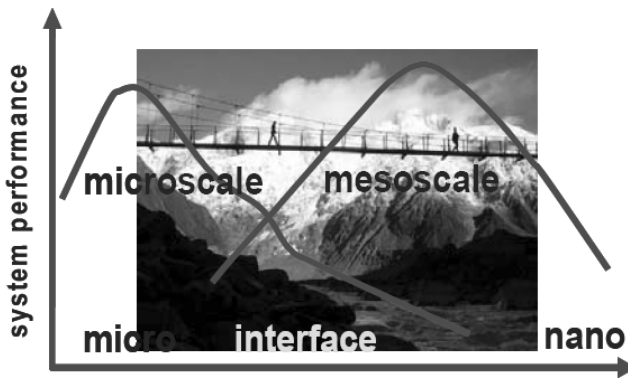


Fig. 2. Illustration of the needs of in terms of bridging micro and meso-scale object properties in complex systems, to achieve high system performance and useful applications.

First, it is worth noting that NEMS have demonstrate new features for signal processing that cannot be mimicked by silicon CMOS. Among their unique characteristics one can cite: (i) extremely low power nano-computation [2] (nanorelays with zero I_{off} currents and zero subthreshold swing for static logic

blocks, (ii) fundamental resonance frequencies ranging from 10's of MHz up to 10's of GHz, featuring very high (tens of thousands) mechanical quality factors [1] and (iii) mass sensitivities at the level of individual molecules (10^{-21} g) [1]. In general these type of performances are naturally accompanied by extreme miniaturization and compatibility of their fabrication processes with silicon CMOS, which enables the monolithic integration of their functions with modern ICs.

Presently, the fabrication of NEMS is possible by both *top-down* and *bottom-up* approaches, by a large variety of processes and materials. The top-down fabrication has the clear advantage of using established silicon toolbox and define the device structures and dimensions by micron and sub-micron optical lithography, e-beam lithography, focused ion beam, stencil (shadow-mask) and nano-imprint. The etching techniques are inspired by the ones used by the microelectronic industry and their control and variability are similar to the ones corresponding to modern transistor fabrication. Scaling-down beyond the lithographic limits in NEMS fabrication [3] becomes possible thanks to bottom-up fabrication techniques such as chemical self-assembly, man-made synthesis (e.g. carbon nanotubes) or biological synthesis (DNA, proteins), Atomic Force Microscopy (AFM) or Scanning Tunneling Microscopy (STM). Top-down and bottom up have specific advantages and disadvantages and their choice is highly dependent on the characteristics of the NEM device, the choice of the material (electro-mechanical properties) and the needed level of integration: it is very probable that in the future top-down and bottom-up techniques should be combined for optimized performance and costs.

Today, silicon nanowires (SiNWs) and carbon nanotubes (CNTs) are the main components used for NEMS fabrication, whatever is the type of device (relay, resonator, sensor). Silicon nanowires fabricated on top-down silicon platform combining traditional lithography with smart processing (spacer technology, isotropic etching and sacrificial oxidation) resulting in diameters controlled in the range of tens of nm's and with the smallest diameter of the cross section of the order of 5nm, have been recently demonstrated, Fig. 3 (a) and (b) [4]. The advantages of such fabrication approach are: the excellent control of the SiNW doping, the precise placement of the devices, excellent contacts, availability of methods for control of the surface properties and roughness and, finally, the possibility to co-integrate the NEM devices with silicon CMOS IC's. Moreover, top-down fabricated SiNWs enable a fast reality check of many new MEMS/NEMS principles and of their performances.

Recently, the MEMS/NEMS field, once exclusively based on silicon, has been broadened by the use of more and more different materials. Among them carbon nanotubes are very promising candidates for designing and developing NEMS. The extraordinary mechanical and electrical properties of carbon nanotubes (CNTs) make them ideal candidates as building blocks of nanoelectromechanical systems. Their length and diameter can, to a certain extend, be adjusted. They are light, have

a very high Young's moduli (on the order of 1TPa, better than Carbon fibers and similar to diamond), can be elastically deformed without breaking. They can be metallic or semiconducting depending on their chirality. The high conductivity of single-wall (SWNT) metallic nanotubes or multi-wall nanotubes (MWNT) allow for designing simple sensing and actuation systems based on the direct electrostatic coupling with metallic gates. Together, these properties make them particularly suitable for operation at high frequency in the GHz range; Fig. 4 (a) and (b) show some first attempts to build RF NEMS devices based on vertical and lateral arrays of CNTs. Compatibility with CMOS is still an issue.

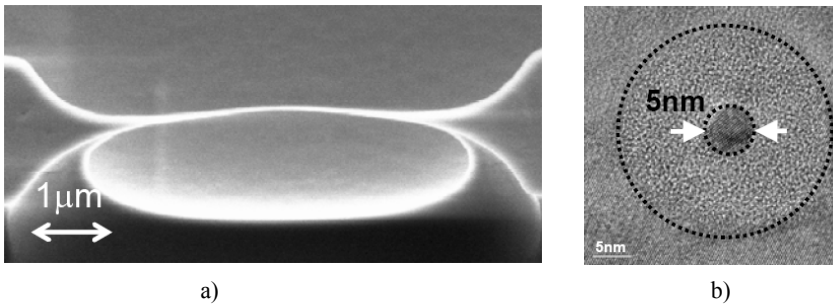


Fig. 3. (a) Suspended silicon nanowire with built-in tensile strain, fabricated by top-down approach, (b) 5nm cross-section in a suspended silicon nanowire; here the wire is oxidized and a polysilicon gate is formed all-around to create a transistor-in-a-wire.

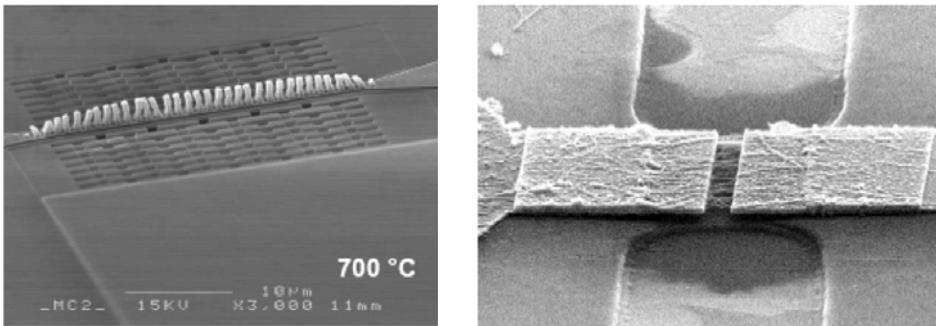


Fig. 4. (a) High temperature growth of brush-like vertical CNTs using Fe catalyst on metal lines for CNT capacitors (courtesy of University of Chalmers and University of Goteborg), (b) CNT array assembled by dielectrophoresis for RF mixer application (courtesy of LEM-CEA).

The success of any new technology is conditioned by the design, modeling and simulation progress; all depend on the deep understanding of mechanics and electrostatics at nanoscale. Exploring and understanding nanoscale material properties, surface effects and defects, quantum mechanical electrostatics and some specific nanoscale effects such as van der Waals and Casimir forces, is

fundamental for the success of NEMS. The experimental validation of theoretical models and the calibration of simulators are of high importance.

Furthermore the use of NEMS critically needs a specific local signal process in order to improve their relatively poor S/N and translate nm displacements into electrical parameter variations that are measurable and/or can be exploited by standard IC interfaces. More specifically, signal processing in NEMS sensor arrays raises great challenges for the hybridization and co-integration with silicon CMOS. Finally, NEMS inherit all the MEMS issues in terms of packaging and reliability; fortunately, protective packages techniques at wafer level with control of parasitics, ensuring inert ambient or local vacuumed cavities are today available.

3. HYBRID NEM-FET

A Micro- or Nano-Electro-Mechanical Field Effect Transistor (MEM- or NEM-FET) combines features of a pure NEM relay and a MOSFET, Fig. 5a) [6, 6]: it has a movable part and a solid-state semiconductor part that operate to *couple the mechanical movement with the formation of the inversion/accumulation channel at the gate-insulator/semiconductor interface*. The movable part determines the state of the gate capacitance C_{gg} (either *low* or *high*), which determines V_{th} ; thus the NEM-FET is a dynamic threshold device, with a high V_{th} in the off state and a low V_{th} in the on state. In [6] abrupt transitions between off and on-states with swings as low as 2 mV/decade, have been reported when the gate voltage is increased beyond the point when an imbalance between the electrostatic and mechanical spring-restoring forces is reached so that “pull-in” (to the high- C_{gg}) occurs. A similarly abrupt transition from the low- V_{th} state to the high- V_{th} state occurs as the gate voltage is decreased, so that “pull-out” occurs and gives rise to a hysteresis in the ID-VG characteristics (Fig 5b). Note that for switching applications, pull-in should occur at a gate voltage less than the (high) off-state V_{th} , to achieve substantial subthreshold leakage power savings for a given on-state current (I_{on}) specification. If pull-out occurs at a gate voltage less than 0 V, the NEM-FET can be used for memory applications. Comprehensive simulation and analytical modeling to enable NEM-FET circuit simulations has been proposed in [7]. Fig. 6a) shows the principle of a recent Double Gate Movable Body MEMFET fabricated on a SOI with a silicon film thickness of 1.25 μm [8, 9]. The great advantage of the proposed resonating-body transistor is demonstrated in Fig. 6b), which compares the S21 transmission parameter of the same MB-MEMFET device at resonance, operated in capacitive two-port configuration (output=gate) and MOSFET detection (output=drain). The power transmitted at resonance to the output port using the MOSFET detection is increased by more than +30dB. This corresponds to a reduction of the impedance at resonance from approximately 20k Ω down to 250 Ω .

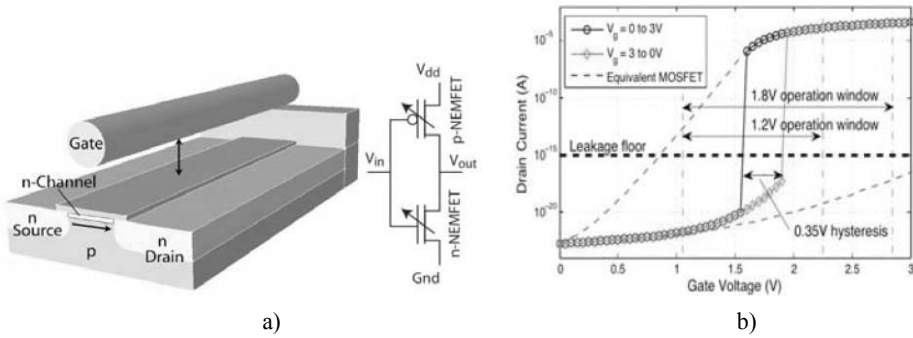


Fig. 5 (a) Movable gate MEM-FET hybrid device and complementary electro-mechanical hybrid inverter, (b) simulated characteristics of NEM-FET switch under the specifications of the 90nm CMOS node (abrupt transition between off and on states and I_{off} limited only by the junction leakage recommend him as a power management switch).

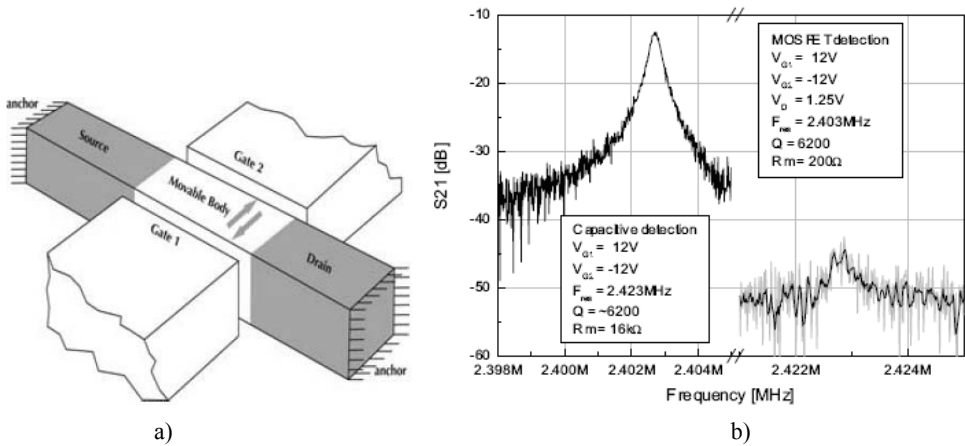


Fig. 6. (a) Illustration of movable body MEM-FET resonator, (b) experimental proof of the +30dB signal gain obtained by the MOSFET detection in a laterally vibration movable body transistor compared with the capacitive detection.

4. CONCLUSION AND ROADMAP FOR NEMS

Fig. 7 [10] summarizes many applications of MEMS and NEMS as well as the benefits of their co-integration with IC technology. MEMS and NEMS devices have enabled new applications in sensing and actuating and their role it is expected to increase in the future in systems where the low power, analog, RF and sensing performance is extremely critical. Products with very high level of MEM device integration, such as the digital micromirror device (DMD) developed by Texas Instruments for projection displays and the photonic switching systems developed by OMM for communication networks, have been recently commercialized. Additionally, the success of Radio-Frequency MEMS (RF-MEMS) [11] such as

tunable micromachined capacitors, integrated high-Q inductors, micromachined low-loss microwave and millimeter-wave filters, low-loss micromechanical switches, microscale vibrating mechanical resonators with Q's in the tens of thousands, and miniature antennas for millimeter-wave applications, have offered miniaturization, MEMS-CMOS co-integration and unique performance enhancement of existing and future wireless transceivers.

There is a clear empty space at the bottom-right of Fig. 7, where the NEMS can play a significant role; today it appears that the key driver for future systems based on thousands to millions of NEMS is the ultra-low power, whatever is the application domain: logic or analog signal processing, RF or sensing. In conclusion, NEMS is expected to be one of the key future technology featuring combined new functionality and low power operation.

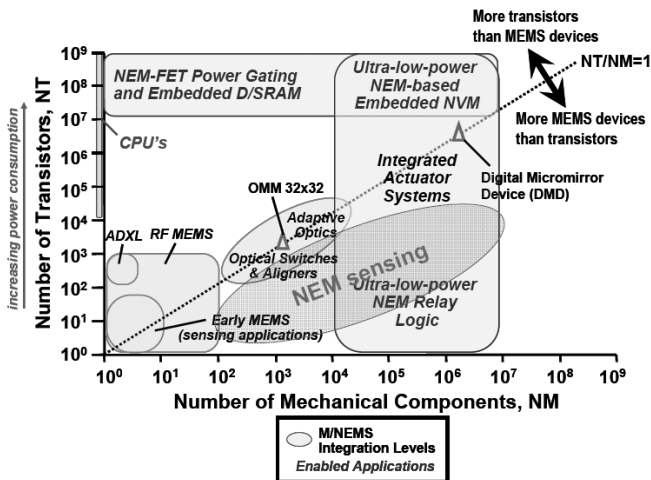


Fig. 7. MEMS/NEMS application roadmap, after [10]. With the increase of the number of NEM components, the average power per function decreases and the functionality of the chip increase.

References

- [1] M.L. ROUKES, *Nanoelectromechanical Systems: Potential, Progress & Projections*, in Proc. IEEE MEMS, pp. 93–94, 2007.
- [2] K. AKARVARDAR, D. ELATA, R. PARSA, G.C. WAN, K. YOO, J. PROVINI, P. PEUMANS, R.T. HOWE, H.-S.P. WONG, *Design Considerations for Complementary Nanoelectromechanical Logic Gates*, IEEE International Electron Devices Meeting Technical Digest, pp. 299–302, 2007.
- [3] Z. CUI, C. GU, *Nanofabrication Challenges for NEMS*, Proceedings of the 1st IEEE International Conference on Nano/Micro Engineered and Molecular Systems, January 18-21, Zhuhai, China, 2006.

- [4] K.E. MOSELUND, D. BOUVET, L. TSCHUOR, V. POTT, P. DAINESI, C. EGGIMANN, N. Le THOMAS, R. HOUDRÉ, A.M. IONESCU, *Cointegration Of Gate-All-Around Mosfets and Local Silicon-on-Insulator Optical Waveguides on Bulk Silicon*, IEEE Transactions on Nanotechnology, **6**, pp. 118–125, 2007.
- [5] H.C. NATHANSON, W.E. NEWELL, R.A. WICKSTROM, and J.R. DAVIS, Jr., *The Resonant Gate Transistor*, IEEE Trans. Electron Devices, **14**, pp. 117–133, 1967.
- [6] N. ABELE, R. FRITSCHI, K. BOUCART, F. CASSET, P. ANCEY, and A. M. IONESCU, *Suspended-Gate MOSFET: Bringing New MEMS Functionality Into Solid-State MOS Transistor*, in IEDM Tech. Dig., pp. 479–481, 2005.
- [7] K. AKARVARDAR, C. EGGIMANN, D. TSAMADOS, Y. CHAUHAN, G.C. WAN, A.M. IONESCU, R.T. HOWE, H.-S.P. WONG, *Analytical Modeling of the Suspended-Gate FET and Design Insights for Low-Power Logic*, IEEE Transactions on Electron Devices, **55**(1), pp. 48–59, 2008.
- [8] D. GROGG, D. TSAMADOS, N.D. BADILA, and A.M. IONESCU, *Integration of MOSFET Transistors in MEMS Resonators for Improved Output Detection*, in Proc. TRANSDUCERS, pp. 1709–1712, 2007.
- [9] D. GROGG, H.C. TEKIN, N.D. BADILA-CIRESSAN, M. MAZZA, D. TSAMADOS, A.M. IONESCU, *Laterally Vibrating-Body Double Gate MOSFET With Improved Signal Detection*, DRC 2008.
- [10] D. TSAMADOS, A.M. IONESCU, K. AKARVARDAR, H.-S. PHILIP WONG, E. ALON, T.-J. KING LIU, *Nano-Electro-Mechanical Switches*, Nano-Electro-Mechanical Switches, White Paper ITRS, 2008.
- [11] C.T.C. NGUYEN, *MEMS Technology for Timing and Frequency Control*, IEEE Trans. Ultrasonics, Ferroelectrics and Frequency Control, **54**, pp. 251–270, 2007.

Simple Nanoelectromechanical Systems for Giga-Applications

M. DRAGOMAN¹, G. KONSTANTINIDIS², D. DRAGOMAN³,
D. NECULOIU⁴, A. CISMARU¹, R. PLANA⁵, H. HARNAGEL⁶,
A. KOSTOPOULOS², R. BUICULESCU⁷

¹National Research and Development Institute in Microtechnology,
Str. Erou Iancu Nicolae 32B, 077190 Bucharest, Romania

²FORTH-IESL-MRG PO Box 1527, Heraklion, Crete, Greece

³Univ. Bucharest, Physics Dept., P.O. Box MG-11, 077125 Bucharest, Romania

⁴Politehnica University of Bucharest, Electronics Department.,
1-3 Iuliu Maniu Av., 061071 Bucharest, Romania

⁵LAAS CNRS, 7 Avenue du Colonel Roche, 31077 Toulouse Cedex 4, France

⁶Institut für Hochfrequenz Technik, Technische Universität Darmstadt,
Merckstrasse 25, 64283 Darmstadt, Germany

⁷University of Crete, Dept. of Chemistry, Vassilika Vouton, Heraklion, Crete, Greece

Nanoelectromechanical systems (NEMS) are simple mechanical systems such cantilevers, and double-clamped beams having at least one dimension of the order of few nanometers and which are electrostatically actuated by an external electrode [1]. NEMS displays mechanical resonance frequencies in the range 100 MHz-5 GHz, so coinciding with the electromagnetic microwave spectrum [1-2]. NEMS have also very high mechanical quality factors of 10² – 10³ at room temperature, in the GHz range.

The correspondence between the electromagnetic GHz spectrum and NEMS mechanical frequency oscillations can be used for new innovative devices in the area of high frequency NEMS [3]. Further, we will demonstrate that simple NEMS configurations based on carbon nanotubes (CNTs) have important applications for signal processing in the GHz range. Two examples will be presented.

In the first example, we show that when microwave signal frequencies are tuned near the mechanical resonant frequency of an array of metallic cantilevered carbon nanotubes (CNTs) sandwiched between two coplanar waveguide (CPW) lines (see Fig. 1a), the CNTs array displays a notch in the microwave transmission

coefficient due to a metal-dielectric transition of the carbon nanotube array at the mechanical resonant frequency of the cantilever. Thus, the CNTs array acts like a resonator. We have used a CNT array having 10^9 CNTs/cm². The measured quality factor of such an array of millions of CNTs cantilevers has a quality factor of 800 at room temperature at the fundamental resonance frequency of 1.4 GHz (see Fig. 1b) [4].

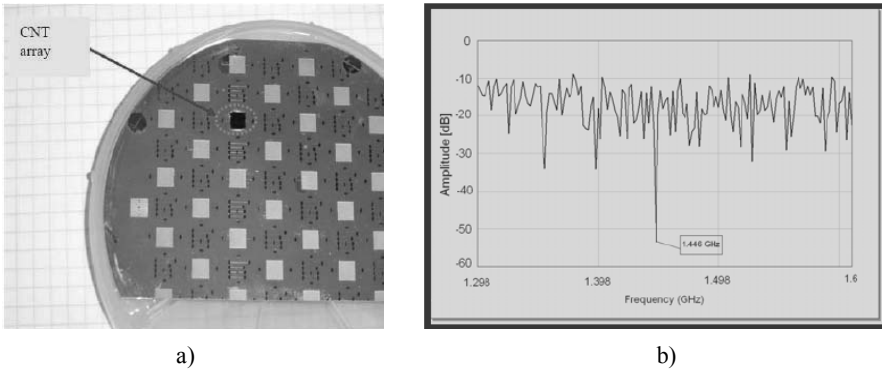


Fig. 1. The CNT resonator (a) The CNT array on the wafer (b) |S21| dependence on frequency.

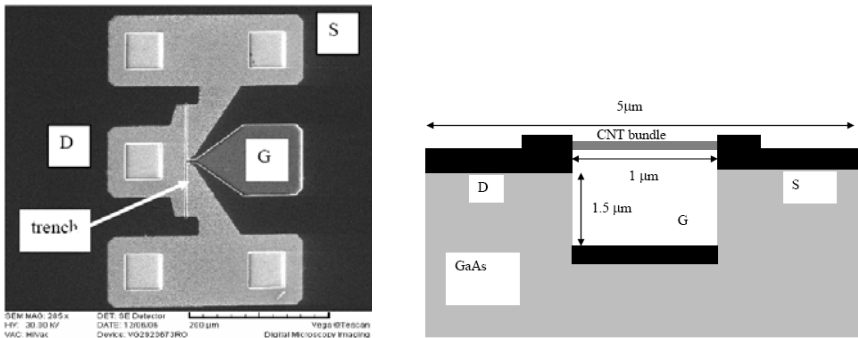


Fig. 2. The double clamped CNT bundle FET-like device.

In the second example, we present a double-clamped CNT bundle suspended over a metallized trench which is 1 μm wide and micromachined in GaAs substrate. In this configuration, this NEMS is behaving as FET-like device (see Fig. 2, and 3). The drain and source contacts are made on the each side of the trench, while the gate is the metallized electrode of the gate located at 1.5 μm below the CNT bundle. The device is biased as FET transistor and low V_G is acting as variable resistor controlled by gate as any FET, but at certain gate voltage in the range 15-18 V, this structure displays a S shaped negative –differential resistance (NDR) (see Fig. 4). Further, applying equal V_{DS} steps of 0.2 V the NDR is displaying multiple branches, which are parallel between them. In this way, the

entire structure is working as a high speed switch with multiple levels which are very useful for multi-valued logic applications. Measurement performed in microwaves demonstrates that this device is amplifying up to 3 GHz, although the device has no matching circuits and the parasitic elements were not minimized (see Fig. 5). These unusual behaviors are due to CNT transport properties and the tunneling of the carriers in the various CNTs forming the bundle. Also, the unscreening properties of CNTs semiconductors allows gate control of carriers between drain and source, although between gate and CNT bundle there is no dielectric except the air.

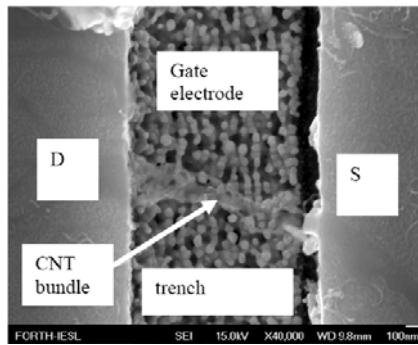


Fig. 3. The detail of the above device to evidence the CNT bundle.

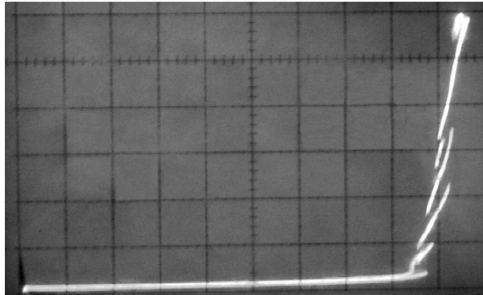


Fig. 4. Multiple NDR of the device ($G V = 14 \text{ V}$; $D I = 500 \mu\text{A}/\text{div}$ and $D V = 2 \text{ V}/\text{div}$).

References

- [1] K.L. EKINCI and M.L. ROUKES, *Nanoelectromechanical Systems*, Rev. Sci. Instr., **76**, pp. 061101/1–4, 2005.
- [2] M. DRAGOMAN and D. DRAGOMAN, *Nanoelectronics: Principles and Devices*, Boston, USA: Artech House, 2006.
- [3] H.B. PENG, C.W. CHANG, S. ALONI, T.D. YUZVINSKY, and A. ZETTL, *Ultrahigh Frequency Nanotube Resonators*, Phys. Rev. Lett., **97**, pp. 087203/1–4, 2006.
- [4] M. DRAGOMAN, D. NECULOIU, A. CISMARU, K. GRENIER, S. PACCHINI, L. MASENQ, and R. PLANA, *High Quality Nanoelectromechanical Microwave Resonator Based on a Carbon Nanotube Array*, Appl. Phys. Lett., **92**, pp. 063118/1–3, 2008.

GaN Membrane Supported MSM Ultraviolet Photodetector

A. MÜLLER¹, G. KONSTANTINIDIS², M. DRAGOMAN¹,
D. NECULOIU¹, A. DINESCU¹, M. ANDROULIDAKI³,
M. KAYAMBAKI², A. STAVRINIDIS², D. VASILACHE¹,
C. BUICULESCU¹, A. KOSTOPOULOS², D. DASCALU¹

¹IMT-Bucharest, 32B Erou Iancu Nicolae Street, 077190 Bucharest, Romania

²FORTH-IESL-MRG- Heraklion, PO Box 1527, Greece

1. INTRODUCTION

In recent years, a lot of research has been focused on semiconductor-based ultraviolet UV detectors. These devices have an important commercial and scientific interest for engine control, astronomy, lithography aligners, solar UV monitoring, space-to-space communications, detection of missiles [1]. Most of these applications fit in the optical spectrum range 200–365 nm covered by nitrides, in particular by GaN and AlGa_N family. Most used photo detectors devices are based on metal-semiconductor-metal (MSM) structures due to their simplicity [2-6]. The MSM configuration consists in two interdigitated Schottky electrodes deposited on a non-intentionally doped or compensated semiconductor material. Recently our group has reported for the first time the manufacturing of an UV detector based on a thin GaN membrane [7].

We present now the experimental results obtained for two different runs of UV photodetectors manufactured on thin GaN membranes using nanolithographic techniques.

2. EXPERIMENTS

The MSM interdigitated structure is symmetrical having a length of 100 μm and a width of 20 μm. Cross section of the MSM UV detector structure is presented in Fig.1.

The first step in UV detector structure manufacturing was the measurements pads patterning and deposition. For this, conventional photolithography, e-beam metallization (Ni/Au 20 nm / 200 nm) and lift-off technique have been used. Due

to sub-micrometer digits/interdigits dimensions for the MSM structure, a direct writing, process using an Electron Beam Lithography (EBL) was selected. The design transfer on the wafer was performed using a Scanning Electron Microscope (Vega from Tescan), equipped with an EBL (Elphy Plus from Raith) by direct writing. Ni/Au metallization for the MSM structure was performed using lift off techniques. Then the samples were mounted face-down on special glass plates and the Si substrate was thinned down to 150 μm by chemo-mechanical lapping. For the membrane formation the substrate was selectively removed using back side patterning and SF6 plasma RIE. We have obtained good MSM UV detector structures in 2 different runs.

The first run was manufactured on $\langle 111 \rangle$ oriented silicon wafer having a 2.2 μm thin GaN layer grown by MOCVD (provided by Azzuro Ltd. Magdeburg). Fingers and interdigits 1 μm wide have been manufactured. Patterning was performed using a Vega SEM and an Elphy Plus EBL. NiAu (30/100 nm) has been evaporated for the Schottky MSM interdigitated structure and lift-off techniques have been used for the metallization. The thickness of the PMMA resist was 200 nm. The active area of the membrane detectors was about 1000 μm^2 (50% of the total detector area). The schematic cross section of the MSM structure is presented in Fig 1.

The SEM photo of the structure is presented in Fig. 2, the dark current measurements are presented in Fig. 3 and the responsivity in Fig. 4.

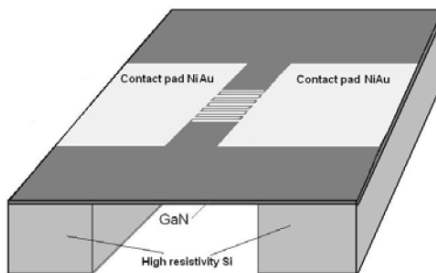


Fig. 1. Schematic cross section of the membrane MSM UV detector structure.

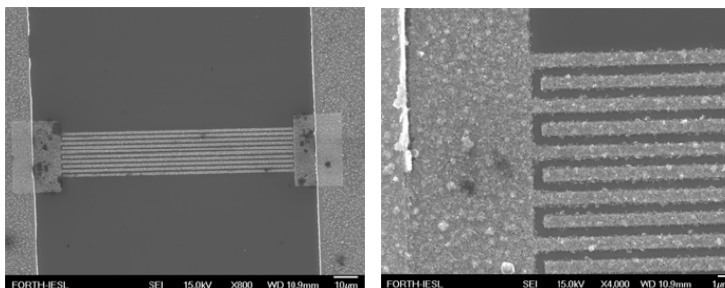


Fig. 2. SEM photo (left) and detail (right) for the 1 μm wide finger/interdigit detector structure manufactured on a 2.2 μm thin GaN membrane.

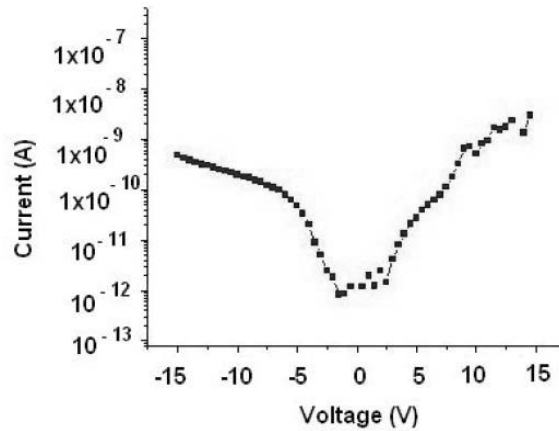


Fig. 3. Dark current for the 1 μm wide finger/interdigit detector structure manufactured on a 2.2 μm thin GaN membrane.

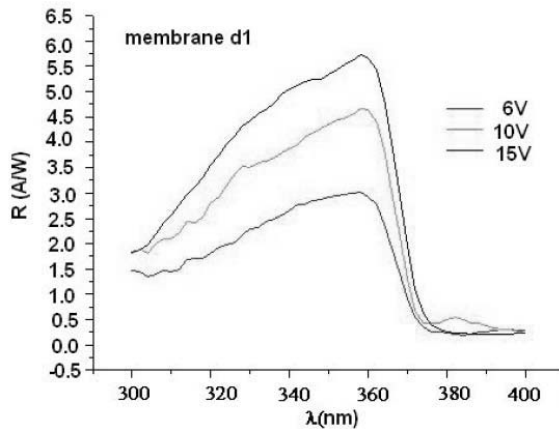


Fig. 4. Responsivity vs wavelength for the 1 μm wide finger/interdigit detector structure manufactured on a 2.2 μm thin GaN membrane.

The second run was manufactured on a 0.78 μm thin membrane starting from a GaN/Si wafer produced by NTT AT Japan using also MOCVD techniques. Fingers and interdigits of about 0.45-0.5 μm have been obtained. At this run semitransparent Ni/Au (5/10 nm) Schottky contacts have been manufactured using a 40nm thick PMMA resist. The total area of the MSM structure was identical with those in the first run but estimating a 50% transparency of the contact [8], the active area was about 1500 μm^2 . SEM photos of the structures are presented in Fig 5.

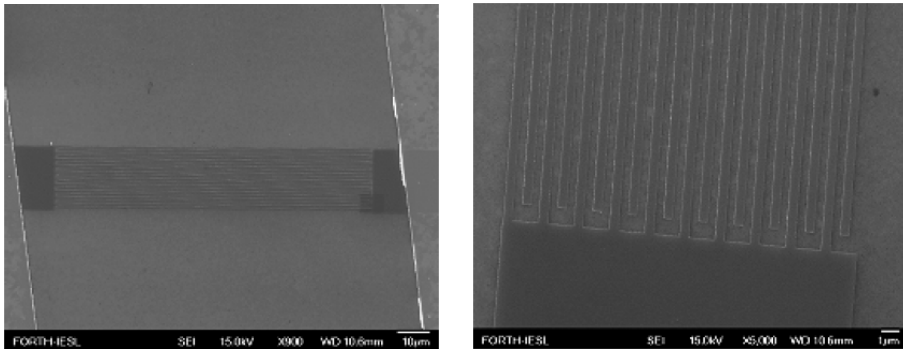


Fig. 5. SEM photo (left) and detail (right) for the 0.5 μm wide finger/ interdigit detector structure manufactured on a 0.78 μm thin GaN membrane.

The dark current and the responsivity were measured on before membrane formation (Fig. 6 the dark current for two structures and Fig. 7 the responsivity measurements as a function of wavelength at various voltages up to 15 V). The dark current after membrane formation is presented in Fig. 8 for two devices and the responsivity is presented in Fig. 9.

We also tried to obtain detector structures with finger interdigit dimensions 300 nm/300 nm and 150 nm/150 nm but without success, most probably due to the difficulties in nanolithographic process in GaN [5].

The responsivity vs photon energy was measured using Ozone free 150 W Xe-lamp UV light source from Hamamatsu. We have used low noise amplifiers to measure all the spectra.

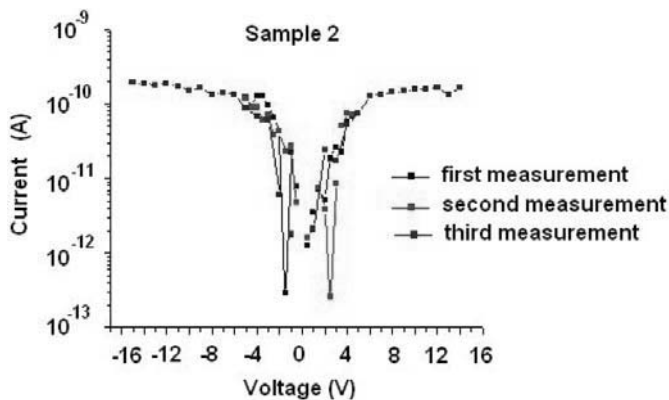


Fig. 6. Dark current for the 0.5 μm finger / interdigit for the UV detector structure **before** the silicon substrate removal (thickness of the GaN layer 0.78 μm).

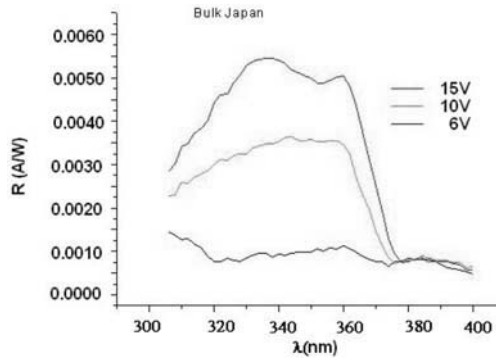


Fig. 7. Responsivity vs wavelength for the 0.5µm finger / interdigit for the UV detector structure-before the silicon substrate removal (thickness of the GAN layer 0.78µm).

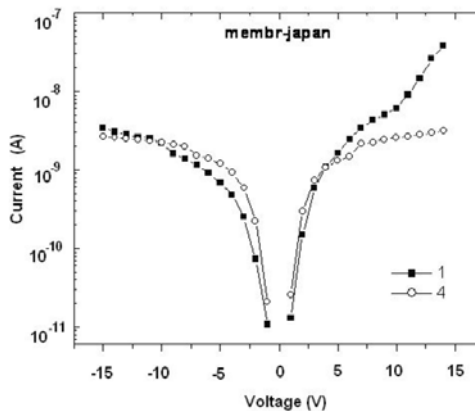


Fig. 8. Dark current for the 0.5µm finger / interdigit for two UV termed “1” and “4” detector structures manufactured on 0.78 µm thin GAN membrane.

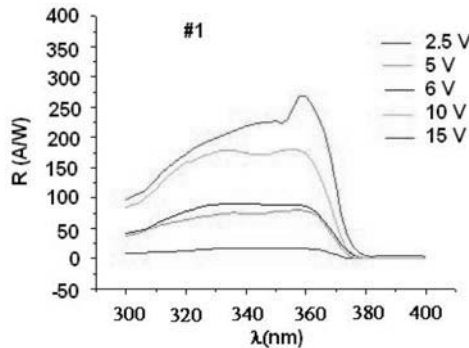


Fig. 9. Responsivity vs wavelength for the 0.5µm finger / interdigit for two UV detector structures- manufactured on 0.78µm thin GAN membrane.

RESULTS AND DISCUSSIONS

Very low dark currents (1-10 pA) at moderate voltages have been obtained for all structures. The values for the responsivity at 362 nm for the first run (2.5A/W at 6V and 4.5A/W for 10 V) were excellent compared with results reported in the literature. The finger /interdigit for these devices was 1 μm . Responsivity measured on the same type of detectors manufactured bulk material [7] was about 2 mA/W.

The second run, which was manufactured on a thinner membrane (0.78 μm), having a MSM structure with fingers and interdigits of 0.5 μm , give unexpected high values for the responsivity (values of 50-100 A/W for a bias in the range 6-10 V). These values are 3 orders of magnitude higher than those obtained for GaN on bulk silicon. The low values obtained for the responsivity for similar GaN detectors on bulk silicon (values of 1-5 mA/W for voltages in the range 6-15V) seems to confirm that responsivity measurements are correct. If we start from this assumption, it seems that we can have a major advantage using micromachining technologies to manufacture UV GaN detectors on thin membranes. As a comparison, for a 0.5 -1 μm finger/interdigit detectors manufactured on GaN /sapphire a maximum responsivity of 0.3-0.5 A /W [4, 9] have been reported. The MSM structure has a gain, and the membrane can stimulate the gain. Carriers are confined in the thin suspended membrane and can have reflections on the top and bottom of the membrane. This can be an explanation for the major influence of the micromachining on the increasing of the responsivity. It must be also noticed that we believe that the material used for the manufacturing of run 2 has a very high quality with less interface and volume defects. This can also have an influence on increasing the responsivity performances of the detectors. Results have to be confirmed on other structures with similar and smaller dimensions for the digit/interdigit width and better yield.

Acknowledgements. The Romanian team work was supported by the Romanian Ministry of Education Research and Youth trough the CEEX projects Nanoscale –Conv (No 6111/2005-CALIST) and ACOMEMS (No 29/INFOSOC).

References

- [1] E. MONROY, F. OMNES and F. CALLE, *Wide-Bandgap Semiconductor Ultraviolet Photodetectors*, Semicond. Sci. technol, **18**, pp. R33–R51, 2003.
- [2] E. MONROY, F CALLE, F MUNOZ, F OMNES, *Algan Metal-Semiconductor-Metal Photodiodes*, Appl. Phys. Lett., **74**, p. 3401, 1999.
- [3] J.C. CARRANO, T LI, P.A GRUDOVSKY., C.J EITING., R.D DUPUIS. AND J.C. CAMPBELL, J. Appl. Phys., **83**, p. 6148, 1998.
- [4] T. PALACIOS, E. MONROY, F CALLE, F OMNES, *High-Responsivity Submicron Metal-Semiconductor-Metal Ultraviolet Detectors*, Appl. Phys. Lett., **81**, pp. 1902–1904, 2002.
- [5] T. PALACIOS, F CALLE, E. MONROY, F MUNOZ, *Submicron Technology For III-Nitride Semiconductors*, J. Vac. Sci. technol. **B 20**, p. 2071, 2002.

- [6] R.W. CHUANG, S.P. CHUANG and S.J. CHUANG, *Gallium Nitride Metal-Semiconductor-Metal Photodetectors Prepared on Silicon Substrates*, J. Appl. Phys., **102**, p. 073110, 2007.
- [7] A. MÜLLER, G. KONSTANTINIDIS, M. DRAGOMAN, D. NECULOIU, A. KOSTOPOULOS, M. ANDROULIDAKI, M. KAYAMBAKI AND D. VASILACHE, *Gan Membrane MSM Ultraviolet Photodetector*, Appl. Opt., **47**, pp. 1453–1456, 2008.
- [8] P.C. CHANG, C.H. CHEN, S.J. CHANG, Y.K. SU, C.L. YU, P.C. CHEN, C.H. WANG, *Algan/Gan MSM Photodetectors With Photo-CVD Annealed Ni/Au Semitransparent Contacts*, Semicond. Sci. Technol., **19**(12), pp. 1354–1357, 2004.
- [9] B.P. M.T. TODARO, M.C. FRASSANITO, A. POMARICO, A. PASSASEO, M. LOMASCOLO, R. CINGOLANI and M. De VITTORIO, *High Responsivity Gan-Based UV Detectors*, Electronics Lett, **39**, November 2003.

Silicon MEMS Tunable Superconducting Microwave Circuits

M.J. PREST, Y. WANG, F. HUANG and M.J. LANCASTER

University of Birmingham, Electrical, Electronic and Computer Engineering, Birmingham, B15 2TT, UK.

Abstract. Tuning of a superconducting microwave resonator, operating at 77 K, is demonstrated using a silicon micro-machined comb-drive actuator. Thermal expansion coefficient differences between the silicon actuator and the MgO substrate are accommodated by the use of compliant springs and a stress-buffering rigid frame. A tuning range of about 3 % is demonstrated for a microwave resonator with a frequency close to 6 GHz. Measurements of Young's modulus show that the value at 77 K is within 1.5 % of the room temperature value.

1. INTRODUCTION

High-temperature superconducting (HTS) circuits are used for microwave radio frequency (RF) applications where there is a demand for ultra low insertion loss and/or extreme sharp edged filters. There has been interest in methods to tune these passive circuits [1] and one possibility is through the introduction of microelectromechanical systems (MEMS).

There is little previous work on superconducting RF MEMS. In 2003 Hijazi *et al.* demonstrated a superconducting RF MEMS switch [2], these devices use an electrostatically actuated, thin film gold membrane to form the switch. Their devices switch between passive components to achieve tuning between discrete values. In our work we vary capacitance using a silicon MEMS comb-drive actuator in order to produce a continuously variable adjustment of frequency.

An appeal of our approach is that it can be achieved using a novel actuator design, standard silicon MEMS processing and standard HTS thin film processing, with only a flip-chip bonding step to combine the two technologies.

2. TUNING PRINCIPLE

The HTS resonator consists of an interdigital capacitor and an inductance (as shown in Fig. 1); the structure resonates at approximately 6.3 GHz, as shown in

Fig. 2. The tuning probe, shown in Fig. 3 is fabricated from high resistivity silicon and has ridges that initially lie directly above the fingers of the HTS capacitor as shown in Fig. 4. The comb-drive voltage controls the probe position, so that the probe ridges cover either the capacitor fingers, the gaps, or partway between. The tuning probe ridge and trench widths are $40\ \mu\text{m}$ and the trenches are $20\ \mu\text{m}$ deep. The vertical gap between the tuning probe and the HTS resonator is nominally $1\ \mu\text{m}$.

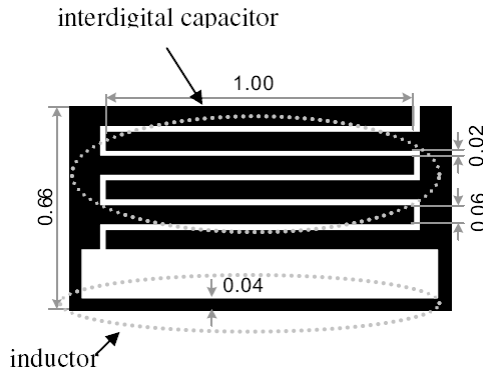


Fig. 1. HTS resonator close-up showing interdigital capacitor and inductor in a parallel circuit. Dimensions are in mm.

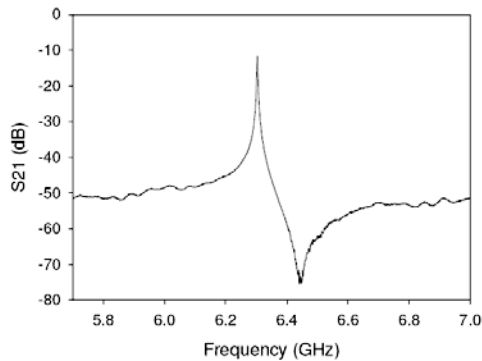


Fig. 2. S21 measurement of superconducting resonator at 77 K without the presence of the tuning probe. The unloaded quality factor is over 3500.

The tuning range depends on the variation in capacitance as the tuning probe moves, and this is maximised by making the gap between the resonator and tuning probe as small as possible. The trade-off, however, is that reducing the gap also lowers the microwave quality factor (Q) of the resonator. High resistivity silicon for the tuning probe is essential to maintain the high Q of the superconducting resonator. The silicon resistivity is the limiting factor in the microwave performance of the device.

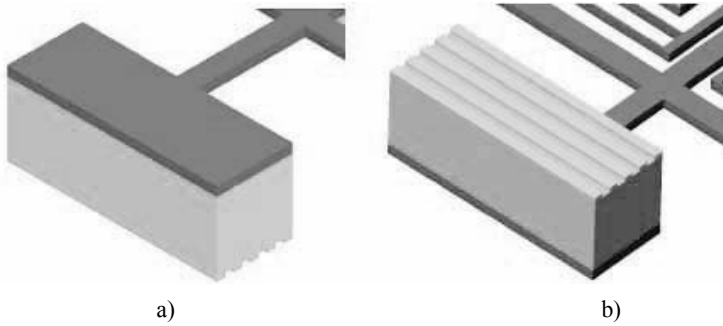


Fig. 3. Close-up of the tuning probe, seen from a) above and b) below.

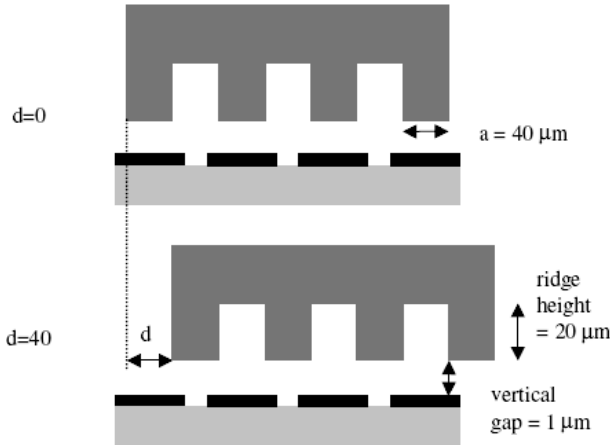


Fig. 4. A cross-section of the silicon tuning probe and HTS resonator. Shows probe displacement (d) and silicon ridge width (a). The vertical height of the silicon ridges was $20 \mu\text{m}$.

3. DESIGN AND FABRICATION

Because of the difference in thermal expansion coefficients (Fig. 5) and the high Young's modulus of both materials, any silicon structure attached to an MgO substrate would be subjected to large forces during cooling. We have therefore adopted the use of compliant mounting springs [3] and a stress-buffering frame to isolate the comb-drive from thermally induced strain, as shown in Fig. 6. The silicon MEMS device was fabricated at Chalmers University, Sweden. The HTS processing and flip-chip bonding were carried out using facilities at the University of Birmingham. The silicon MEMS device was fabricated from a 100 mm diameter silicon on insulator wafer, and the HTS device was fabricated from a 50 mm diameter MgO wafer with an YBCO superconducting thin film.

The comb-drive design, including consideration of spring constants, number of comb fingers and resistance to sideways latching was carried out according to earlier work by Zhou and Dowd [6]. The comb-drive provides a movement of approximately 40 μm for an applied bias of 70 V.

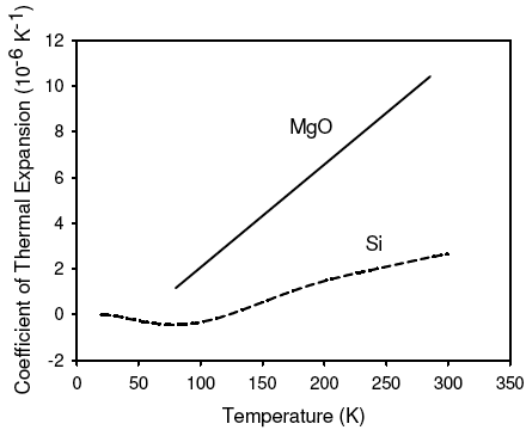


Fig. 5. Coefficients of thermal expansion for silicon and MgO versus temperature. Plots using data from ref.s [4] and [5].

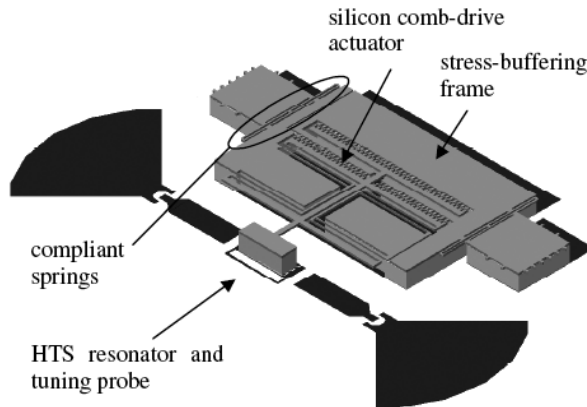


Fig. 6. Diagram of HTS circuit with silicon comb-drive actuator for tuning.

4. YOUNG'S MODULUS MEASUREMENTS

There are few publications on the operation of silicon MEMS at low-temperature; a paper by Gysin *et al.* [7] extracts values for Young's modulus from cantilever measurements. We have performed similar measurements on a comb-drive mechanical resonator structure. Our measurements demonstrate reliable

operation at low temperature and determine the variation in Young's Modulus between 77 K and room temperature. The measurements were performed with incident light to minimise the silicon resistivity (Photon generated chargecarriers reduce the silicon resistivity). Fig. 7 shows the layout of the silicon comb-drive mechanical resonator. The device has drive and sense combs and a central shuttle supported by folded flexure springs. The resonant frequency was found to be 4.27 kHz at room temperature and rose to 4.30 kHz at 77 K. The resonant angular frequency, ω varies as $\sqrt{k/m}$. We assumed that the mass m does not vary and that the variation in ω results from an increase in the spring constant k , as the Young's Modulus increases with falling temperature.

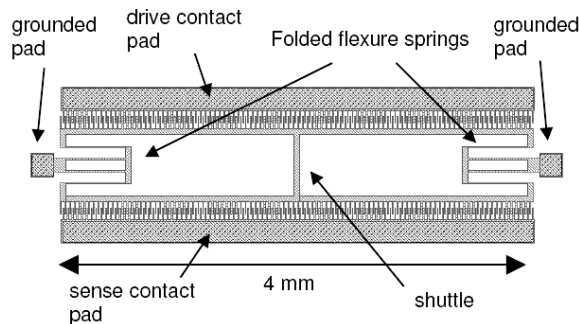


Fig. 7. Silicon mechanical resonator used for measurement of Young's modulus versus temperature. The areas with black dotted shading are fixed to the substrate, the central shuttle, combs and springs are free to move.

We measured the resonant frequency of the device in vacuum using a cryogenic probe station. A DC bias of 200 V was applied between the spring and drive contact pads to pull the shuttle towards the drive pad. The DC bias was then stepped to 0 V and the device allowed to 'ring' at its natural frequency. The damped oscillation lasted for a second or so before fading away. A charge amplifier (with an input biased to 7.5 V) was used to amplify the resonance signal measured at the sense contact pad. The signal was captured using a digital storage oscilloscope. The frequency was determined from the period of oscillation, and several periods were averaged to improve accuracy.

The Young's Modulus E_x was calculated from the measured values of resonance frequency, f using equation 1 [8] and plotted in Fig. 8. Theoretical values of Young's Modulus E_w were also fitted to the data using Wachtmann's formula [9], equation 2. The fitting parameters are given in Table 1. A reasonable fit was obtained, but there are uncertainties in the masses and the device dimensions. Dimensions will shrink with temperature, but this variation is assumed to be small enough to be neglected. The masses were calculated from device dimensions of the

mask using the density of silicon as 2330 kg m^{-3} . The spring thickness was $10 \text{ }\mu\text{m}$ on the mask, but using this value gives a low E_x from equation 1. Mask features are often reduced during lithography and undercutting of the mask occurs during deep reactive ion etching, so we feel that it is fair to reduce this value. The value of E_x is very sensitive to the spring width W , and the value was adjusted to give a low temperature Young's modulus, E_0 of 158.5 GPa . This was a compromise between the thinnest likely spring value and a value for E_x that was felt to be not too low compared to published values. Values of B and T_0 were chosen to give a reasonable fit to the experimental curve with rising temperature.

$$E_x = \frac{(2\pi f)^2 (M_p + 0.3714M)L^3}{2tW^3} \quad (1)$$

$$E_w = E_0 - \left(BT \exp\left(-\frac{T_0}{T}\right) \right) \quad (2)$$

Table 1. Fitting parameters for equations 1 and 2.

Shuttle mass	M_p (kg)	
Spring mass	M (kg)	
Spring length	L (m)	
Spring width	W (m)	
Spring thickness	t (m)	
Young's Modulus at 0K	E_0 (GPa)	
Constant	B (MPa K ⁻¹)	
Constant	T_0 (K)	

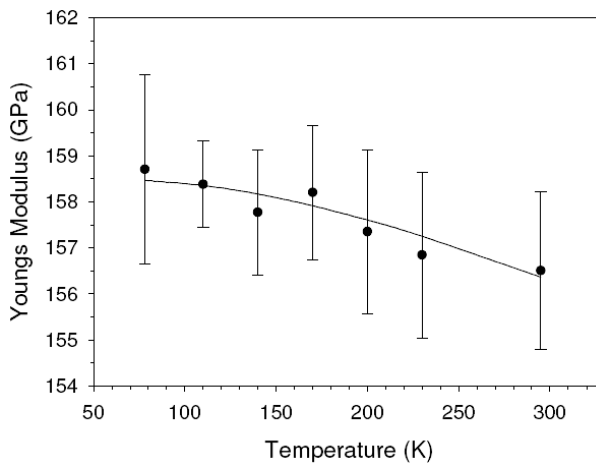


Fig. 8. Young's Modulus of silicon versus temperature. Black circles—experimental data, with E_x determined from equation 1. Error bars indicate the standard deviation of the frequency measurements. Black line—theoretical fit to the data using equation 2 and the fitting parameters in Table 1.

Although the absolute value of E_0 is uncertain, the results demonstrate that the variation in E_0 ($< 1.5\%$ over the measured temperature range) is small, but slightly larger than the measurement accuracy. We can therefore assume that stiffening of silicon structures at low temperature will not cause a dramatic increase in actuation voltages.

5. SUPERCONDUCTING TUNABLE RESONATOR MEASUREMENTS

The MEMS tunable resonator shown in Fig. 6 was cooled to 77 K using a Desert Scientific cryogenic probe station and S21 measurements were performed using an Agilent 8722ES network analyser. For microwave measurements it was important to measure the device with no incident light, otherwise photon generated charge-carriers would have reduced the silicon resistivity. During actuator movements, however, when bias was increased, light was shone on the device to aid charging of the comb-drive actuator.

Fig. 9 shows that as the comb-drive actuation voltage was increased, the tuning probe moved causing the centre frequency of the resonator to shift to higher frequencies. The tuning range was approximately 3%.

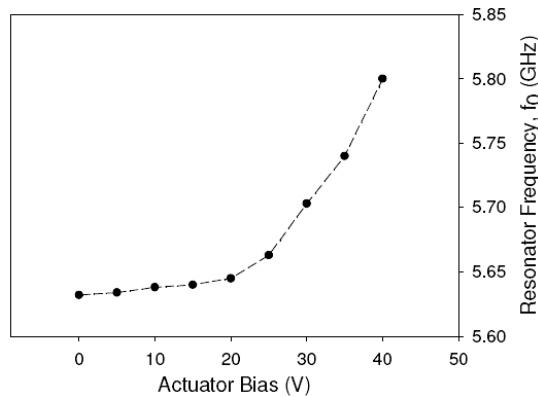


Fig. 9. Tuning of resonant frequency with increasing actuator DC bias at 77 K.

The device was subjected to several thermal cycles between 77 K and room temperature. There was no sign of damage to the device after these cycles, thereby demonstrating that the stress-relieving springs effectively protect the device from the effects of thermal expansion and contraction.

6. CONCLUSIONS

Fabrication of this device presented some demanding requirements particularly in bonding of materials with different coefficients of thermal expansion

and achieving a small gap between the tuning probe and the superconducting resonator. The operation at cryogenic temperatures is a significant challenge. These requirements have been met and tuning of the superconducting device at low-temperature has been demonstrated.

Measurements of Young's Modulus versus temperature demonstrate that the variation is small and that actuation voltages at low temperature should be similar to those at room temperature.

To the authors knowledge, this is the first time that silicon MEMS have been shown to have application for tuning of superconducting RF circuits, this work constitutes a novel technological achievement in the combination of these two technologies.

Acknowledgement. The MEMS structures were fabricated using facilities at the MC2 cleanroom at Chalmers University of Technology in Göteborg, Sweden. The access to this facility was funded by a Framework 6 European grant: 'Research Infrastructures Action'. The authors thank the staff of the nanofabrication laboratory at Chalmers University, particularly Ulf Södervall, Johan Andersson and Göran Petersson, for their support, advice and assistance with the silicon MEMS processing.

References

- [1] G.L. MATTAEI, *Narrow-Band, Fixed-Tuned, and Tunable Bandpass Filters With Zig-Zg Hairpin-Comb Resonators*, IEEE Trans. on Microwave Theory and Techniques, **51**(4), pp. 1214–1219, 2003.
- [2] Y.S. HIJAZI, D. HANNA, D. FAIRWEATHER, Y.A. VLASOV and G.L. LARKINS, *Fabrication of a Superconducting MEM Shunt Switch for RF Applications*, IEEE Trans. on Applied Superconductivity, **13**(2), pp. 700–703, 2003.
- [3] E.F. FAHEEM and Y.C. LEE, *Tether- and Post-Enabled Flipchip Assembly for Manufacturable RF-MEMS*, Sensors and Actuators A, **114**, pp. 486–495, 2004.
- [4] G.K. White, *Thermal Expansion of Reference Materials: Copper, Silica and Silicon*, J. Phys. D: Appl. Phys., **6**, p. 2070, 1973.
- [5] D.K. SMITH and H.R. LEIDER, *Low-Temperature Thermal Expansion of LiH, MgO and CaO*, J. Appl. Cryst., **1**, p. 246, 1968.
- [6] G. ZHOU and P. DOWD, *Tilted Folded-Beam Suspension for Extending the Stable Travel Range of Comb-Drive Actuators*, J. Micromech. Microeng., **13**, p. 178, 2003.
- [7] U. GYSIN, S. RAST, P. RUFF, E. MEYER, D.W. LEE, P. VETTIGER and C. GERBER, *Temperature Dependence of the Force Sensitivity of Silicon Cantilevers*, Physical Review B, **69**, p. 045403, 2004.
- [8] W.C. TANG, T.H. NGUYEN and R.T. HOWE, *Laterally Driven Polysilicon Resonant Microstructures*, Proc. IEEE Micro Electro Mechanical Systems, pp. 53–59, February 1989.
- [9] J.B. WACHTMAN, W.E. TEFFT, D.G. LAM and C.S. APSTEIN, *Exponential Dependence of Young's Modulus for Several Oxides*, Phys. Rev., **122**, p. 1753, 1961.

Can Micromachining Help us to Fill the ‘Terahertz Gap’?

Andrew J. GALLANT

School of Engineering, Durham University, South Road, Durham, UK, DH1 3LE

Phone: +44 191 334 2525

Abstract. The terahertz region of the electromagnetic spectrum has received considerable attention in recent years but has been largely overlooked by the microsystems community. This paper shows how high aspect ratio micromachining can be used to fabricate terahertz based devices. It also identifies the areas where micromachining can provide a valuable contribution to help fill the so-called ‘terahertz gap’.

1. INTRODUCTION

A decade ago, Lubecke *et al* [1] published a paper entitled ‘Micromachining for terahertz applications’. It focused on the use of micromachining to produce antennas, waveguides and transmission lines for the THz regime. However, this coincided with the boom in the telecommunications industry and the emergence of radio frequency microelectromechanical systems, RF MEMS [2]. Therefore the majority of the microsystems attention was devoted to the low GHz region and its corresponding applications. Consequently, the terahertz band (0.3 to 3 THz) which sits between optical and radio has remained largely untouched by micromachining technology.

The universe is full of terahertz radiation left over from the Big Bang. However, the controlled generation and detection of this radiation has been proved to be more problematic. It is too high a frequency for many electronic solutions, yet too low for optical approaches. This ‘terahertz gap’ has lacked powerful sources, sensitive detectors as well as many basic components such as tunable filters and low loss lenses.

The terahertz band has attracted considerable attention and funding in recent years due to its potential applications in the security sector. It promised to produce safe, non-ionising, body scanners which could see through clothing and, perhaps

more excitingly, directly identify dangerous explosives and drugs by their terahertz spectroscopic fingerprint [3].

However, the emerging applications are more diverse than the security headlines suggest. The energy associated with terahertz radiation is in the order of meV which corresponds directly to that of many biological processes. There is significant interest in non-invasive identification of biological material. This includes markerless DNA [4] and protein spectroscopy [5].

Commercially available terahertz products are appearing outside of the well established astronomy sector. Teraview (Cambridge, UK) sells a spectroscopy system which is targeted at the pharmaceutical industry. It is capable of studying the integrity of the complex multilayer pill coatings which are required for controlled drug release. During 2007, Picometrix (Ann Arbor, USA) introduced a benchtop, portable, spectroscopy system. At the same time, M2 lasers (Glasgow, UK) began marketing a, shoebox sized, tunable THz laser which is based on optical parametric oscillator technology developed at St. Andrews University, UK. Quantum cascade lasers have also been developed which reach deep into the terahertz band [6].

2. THZ TIME DOMAIN SPECTROSCOPY

Broadband terahertz time domain spectroscopy (TDS) has become a commonly used laboratory technique. Fig. 1 shows a standard equipment configuration.

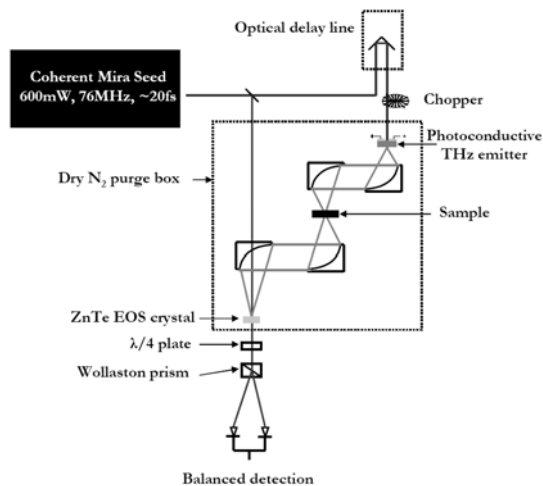


Fig. 1. THz time domain spectroscopy schematic.

TDS [7] is capable of simultaneously measuring the electric field and phase associated with a THz pulse. In the Durham setup, a Ti: sapphire laser produces a 600 mW, near infrared (NIR) pulse of 20 fs duration with a repetition rate of

76 MHz. This is separated into THz-generating and detector-gating beams with a 70:30 beam splitter. The NIR generating beam is focused onto an LTGaAs photoconductive strip-line emitter which is debiased to 250V. Parabolic mirrors are used to focus the THz signal onto the sample. The gating and the THz beam are focused onto a 1 mm thick ZnTe electro-optic crystal. This, in conjunction with a balanced detector, is used to detect the THz radiation transmitted through the structure. A delay line on the NIR generation beam allows the electric field of the THz pulse to be scanned in the time domain. A fast Fourier transform is then used to obtain a frequency spectrum. This system provides a useable bandwidth of approximately 3 THz. Typical terahertz power is in the microwatt region.

For relative transmission measurements, the sample scan is divided by a free space scan in the frequency domain. This effectively deconvolves any reflected signals associated with the measurement setup.

3. ARTIFICIAL MATERIALS

Artificial materials are engineered surfaces or objects which exhibit properties that are difficult to find or control in nature. The typical scales associated with artificial materials depend on the incident wavelength. Therefore RF materials can use printed circuit board and conventional drilling technology. Whereas, optical materials require nanoscale processing such as e-beam writing or nanoimprint lithography. With 1 THz equivalent to a wavelength of 300 μm , this corresponds to the dimensions readily achievable with micromachining techniques.

A. Micromachined Filters

By fabricating arrays of microscale metal rods we can produce diluted metal structures which have an effective plasma frequency in the terahertz region [8]. This ‘toothbrush’ type of structure is difficult and expensive to fabricate using manual techniques. However, it can be readily produced with high aspect ratio polymer lithography. There are a number of applications for this type of structure which range from filtering to negative refraction based lenses.

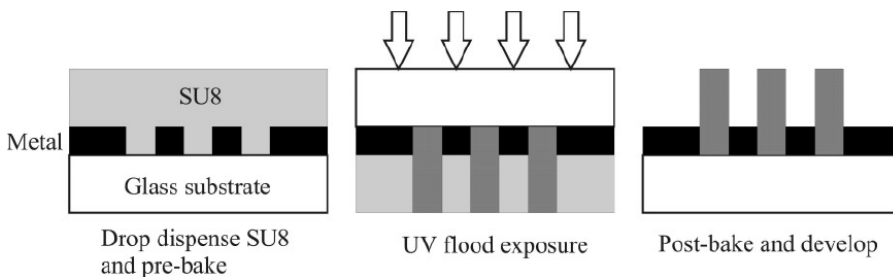


Fig. 2. Backside SU8 processing for the fabrication of high aspect ratio arrays of microscale rods.

Fig. 2 shows an overview of the process flow used to fabricate arrays of microrods. The backside UV exposure of SU8-50 can produce structures with diameters as small as 30 μm and heights in excess of 1.5 mm. The SU8 is fairly transparent to THz radiation; therefore the rods have to be sputter coated with gold in order to form the diluted metal structure.

By carefully aligning these structures in the TDS system, described previously, we can measure their transmission characteristics. Fig. 3 shows the relative transmission for arrays with various rod diameters but a fixed period of 200 μm . The simulated transmission characteristics are also shown [9]. The devices show a clear band structure with peak relative transmission of up to 97% and near zero transmission in the stop bands. As the diameter, and hence the fill-factor, is increased the bands move to higher frequencies.

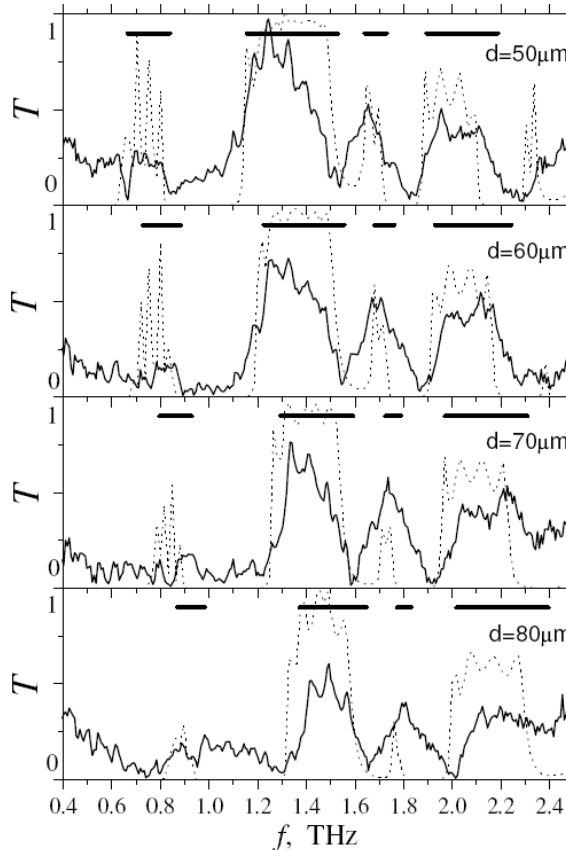


Fig. 3. Transmission of various rod arrays. The pass bands, deduced from complex photonic band theory, are shown as dark horizontal lines. The dotted lines are based on finite difference time domain simulations from [9].

The peak transmission of these devices is sufficiently high to consider fabricating compound filters. This is when two arrays of rods, each with slightly differing fill factors, are placed back to back as shown in Fig 4 (a). With the photolithographic approach it is very easy to precisely align the arrays. Fig. 4 (b) shows an electron micrograph of a fabricated compound filter.

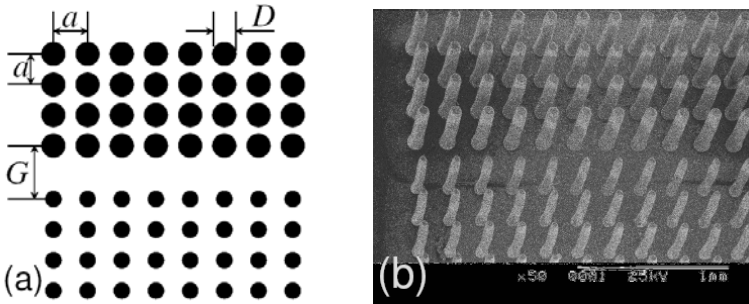


Fig. 4. (a) Schematic view of a compound filter made by combining two 2D square-lattice photonic crystals formed by metallic pillars. (b) SEM image of the structure from [10].

Fig. 5 shows the transmission characteristics of a compound filter. The complex band structure is reduced in the compound filter to a single, well-defined pass band at a frequency which is determined by the fill factor. By varying the fill factor along the array it is possible to produce a mechanically tunable device [11].

The THz beam in the TDS systems can be focused down to approximately 1 mm diameter in free space. The z thickness achievable with thick SU8 processing is therefore ideal in order to confine the beam.

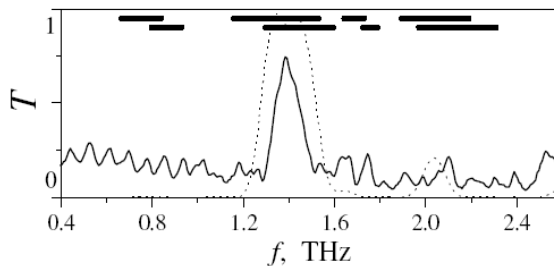


Fig. 5. Transmission spectra for a compound filter formed by two pillar arrays with period 200 μm , containing metal rods with diameter $D = 50 \mu\text{m}$ and $D = 70 \mu\text{m}$ respectively, separated by a gap $G = 250 \mu\text{m}$. The vertical length of the pillar is 1 mm. The experimental spectrum is shown by the solid line and the numerical modelling results by the dotted line. The horizontal bars show the positions of the pass-bands for infinite periodic crystals with rod diameter $D = 50 \mu\text{m}$ (upper bars) and $D = 70 \mu\text{m}$ (lower bars) from [10].

In the future, microsystems based approaches open up the possibility to actuate the arrays and introduce electrical tuning. This type of device is important for terahertz spectroscopy because it enables a broadband source to be filtered and

tuned to specific frequencies. It is therefore possible to excite individual chemical or biological processes.

B. Negative Refraction

Negative refraction materials (NRM) can be divided into two classes. The first class uses split ring resonator structures to exhibit a negative value of permittivity and permeability for a particular frequency [12]. The second class uses a photonic crystal approach. By reconfiguring the rod array, presented in the previous section, into prism arrangement then it is possible to exploit negative refraction effects.

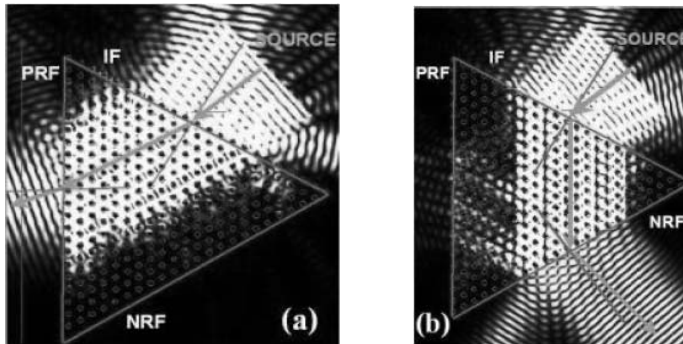


Fig. 6. Simulation of electric field when plane wave is incident on prism. (a) For frequency $f=1.136$ THz positive refraction occurs, while in (b) with $f=1.344$ THz negative refraction occurs. [13].

NRMs are interesting because they will form the basis of new types of terahertz lenses and ultraselective filters [13]. Fig. 6 shows a FDTD simulation of a terahertz prism formed using an array of metallic rods. Depending on the frequency of the incident radiation, the prism behaves as though it has either a positive or negative refractive index.

The Durham THz group has recently experimentally measured the negative refraction effect using a quantum cascade laser which is, by its nature, at a single frequency [14]. However, measurements using a broadband system are significantly more challenging and, in fact, highlight the continued presence of the ‘terahertz gap’.

In order to obtain angular measurements, in a broadband TDS system, it is necessary to move either the emitter or the detector. This correspondingly requires movement of the NIR beam, typically using a fibre-fed approach, which has the side effect of reducing the useful bandwidth of the system. The second problem is that the microwatt power achieved with the photoconductive emitters is insufficient to produce a measurable signal out of the prism. In this case the technology exists to fabricate the structures but the measurement systems still lag behind.

It is worth noting that recently launched EU FP7 project OPTHER (Optically driven THz amplifiers) has the aim of producing amplification systems to address the low power issues with existing sources.

4. EMERGING APPLICATIONS

The development of a true terahertz microscope is an important future application for this technology. High resolution and ability to image in ‘wet’ biological media constitute the main design targets of such a system. The microscope could be used to identify individual cells without requiring markers.

Water represents a significant barrier to terahertz propagation. At best, usually as a vapour, it shows spectral features in terahertz region. However, as a bulk liquid it just attenuates the transmitted radiation. This attenuation is actually a benefit for security applications because it provides excellent contrast against the skin. Furthermore, this sensitivity to water has been used to identify cancerous tumours [15].

For the biological imaging of live samples, water poses a real problem. This year, George *et al* [16] reported the use of microfluidic structures to minimise attenuation. By using techniques such as microfluidics to overcome water attenuation and also to deliver biological media to the terahertz beam it is a significant step forward for the biological applications of this radiation.

For sub-wavelength imaging, one of the common methods is via the use of a waveguide tip. The waveguide is used to direct the THz radiation onto a sample in the near field. After interaction with the sample, the radiation can be detected by a measurement of the transmitted signal. Keilmann [17] reported that by inserting a small diameter wire through the waveguide, he could dramatically increase the output transmission due to the wire acting as a transmitting antenna.

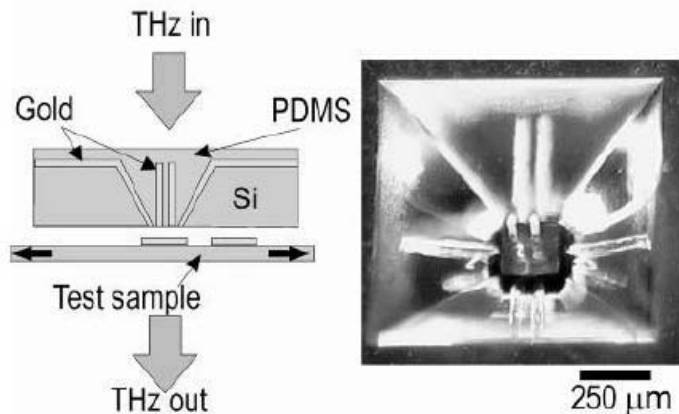


Fig. 7. (left) Schematic of the waveguide (right) A photograph of a fabricated waveguide structure with 40 mm diameter rods (and their reflections).

As with the rod arrays, assembling these structures by hand is both time consuming and expensive. A micromachined approach overcomes these problems. First, KOH-based bulk micromachining is used to etch pyramidal cavities through (100) oriented silicon wafers. Second, we fabricate the high aspect ratio pillars on a glass substrate and sputter coat this with gold. Then the aperture and pillar substrates are aligned, brought into hard contact and Sylgard 184 polydimethylsiloxane, PDMS is poured into the apertures and left at room temperature to cure for 12 hrs. Finally, the substrates are separated, causing the pillars to detached from the glass and remain in the PDMS. This completes the structure. Fig. 7 shows a fabricated waveguide.

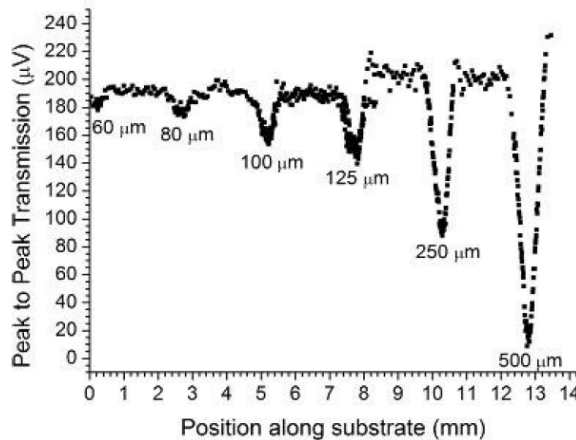


Fig. 8. Variation of the peak to peak THz time domain Efield signal as the test features (width as indicated) are scanned under the waveguide aperture.

The effect on the electric field signal of moving a test sample under the aperture is shown in Fig. 8. Subwavelength lines are clearly visible. This type of micromachined structure is ideally suited for combining with microfluidics and work is underway at Durham to fabricate integrated systems.

5. CONCLUSIONS

In recent years, the terahertz part of the electromagnetic spectrum has been largely overlooked by the microsystems community in favour of RF MEMS. However, hopefully this paper has highlighted that microsystems techniques can produce devices which are likely to play an important role in the next generation of terahertz based systems. Micromachining can indeed help to fill the terahertz gap.

However, this has to be in conjunction with developments in high power terahertz sources.

Acknowledgement. The author wishes to acknowledge the support of the Terahertz and Microsystems groups at Durham University. This work has been funded by Engineering and Physical Science Research Council of the United Kingdom. The LT-GaAs used in the broadband TDS system has been kindly donated by Leeds University.

References

- [1] V.M. LUBECKE, K. MIZUNO, G.M. REBEIZ, *Micromachining for Terahertz Applications*, IEEE Trans. Microwave Theory and Techniques, **46**(11), pp. 1821–1831, 1998.
- [2] J.J. YAO, *RF MEMS from a Device Perspective*, J. Micromech. Microeng., **10**, pp. R9–R38, 2000.
- [3] J.F. FEDERICI, B. SCHULKIN, *THz Imaging and Sensing for Security Applications - Explosives, Weapons and Drugs*, Semicond. Sci. Technol., **20**(7), pp. S266–S280, 2005.
- [4] M. NAGEL, *et al*, *Integrated THz Technology for Label-Free Genetic Diagnostics*, Appl. Phys. Lett., **80**, p. 154, 2002.
- [5] J. XU, K.W. PLAXCO, and S.J. ALLEN, *Probing the Collective Vibrational Dynamics of a Protein in Liquid Water by Terahertz Absorption Spectroscopy*, Prot. Sci., **15**, pp. 1175–1181, 2006.
- [6] R. KOHLER, A. TREDICUCCI, *et al*, *Terahertz Semiconductorheterostructure Laser*, Nature, **417**, p. 156, 2002.
- [7] P.C.M. PLANKEN, C.E.W.M. van RIJMENAM and R.N. SCHOUTEN, *Opto-Electronic Pulsed THz Systems*, Semicond. Sci. Technol., **20**, pp. S121–S127, 2005.
- [8] S. BRAND, R.A. ABRAM and M.A. KALITEEVSKI, *Complex Photonic Band Structure and Effective Plasma Frequency of a Two-Dimensional Array of Metal Rods*, Phys. Rev. B **75**, p. 035102, 2007.
- [9] A.J. GALLANT, *et al*, *Terahertz Frequency Passband Filters*, J. Appl. Phys., **102**, p. 023102, 2007.
- [10] A.J. GALLANT, *et al*, *Passband Filters for Terahertz Radiation Based on Dual Metallic Photonic Structures*, Appl. Phys. Lett., **91**, pp. 161115, 2007.
- [11] A.J. GALLANT, G.P. SWIFT, D. DAI, M. KALITEEVSKI, D.A. ZEZE, D. WOOD, M.C. PETTY, S. BRAND, R.A. ABRAM, J.M. CHAMBERLAIN, *Micromachining for Terahertz Artificial Materials*, Mater. Res. Soc. Symp. Proc, **1016**, pp. 1016–CC05–07, 2007.
- [12] V.G. VESELAGO, *The Electrodynamics of Substances With Simultaneously Negative Values of ϵ and μ* , Sov. Phys. Usp., **10**, pp. 509–514, 1968.
- [13] M.A. KALITEEVSKI, S. BRAND, J. GARVIE-COOK, R.A. ABRAM and J.M. CHAMBERLAIN, *Terahertz Filter Based on Refractive Properties of Metallic Photonic Crystal*, Optics Express, **16**(10), pp. 7330–7335, 2008.
- [14] G.P. SWIFT, *et al*, *Negative Refracting Materials at THz Frequencies*, 33rd International Conference on Infrared, Millimeter, and Terahertz Waves, Pasadena, CA, September 2008.
- [15] A.J. FITZGERALD *et al*, *Terahertz Pulsed Imaging of Human Breast Tumours*, Radiology, **239**(2), pp. 533–540, 2006.
- [16] P.A. GEORGE, *et al*, *Microfluidic Devices for Terahertz Spectroscopy of Biomolecules*, Optics Express, **16**(3), pp. 1577–1582, 2008.
- [17] F. KEILMAN, *FIR Microscopy*, Infrared Phys. and Tech., **36**(1), pp. 217–224, 1995.

In-Plane RF MEMS Resonator Simulation

F. CASSET¹, C. WELHAM², C. DURAND^{1,3,4}, E. OLLIER¹,
J.F. CARPENTIER⁴, P. ANCEY⁴, M. AÏD¹

¹CEA-LETI MINATEC, 17 rue des Martyrs, 38054 Grenoble, France
Phone : +33476927016

²Coventor, 3 Av. Du Québec, ZI Courtaboeuf, Villebon-Sur-Yvette, France

³IEMN CNRS UMR 8520, Cité Scientifique, Av. Poincaré,
59652 Villeneuve d'Asq, France

⁴STMicroelectronics, 850 rue Jean Monnet, 38926 Crolles, France

Abstract. This paper presents an electromechanical system model of a MEMS flexural beam resonator constructed with a new side-electrode component. Simulated results and RF transmission measurements are in good agreement for a 95MHz Silicon-on-Nothing resonator. With the system model, we can predict the MEMS resonator behavior together with pure electrical components, thus enabling the design of a MEMS based oscillator for industrial perspectives.

1. INTRODUCTION

The development of wireless devices, always smaller and more competitive, has driven research into high performance CMOS compatible components. MEMS resonators are good candidates to allow off-chip function integration, such as oscillators. Many references deal with MEMS resonators presenting impressive performance [1, 2, 3]. Nevertheless, the MEMS design is still a key point for industrial production. In this paper we compare RF measurements of a 95 MHz resonator with a CoventorWare ARCHITECT3D™ system model. Using ARCHITECT3D™ allows us to describe the electromechanical behavior of our resonator in its electrical environment, thus enabling the future design of a MEMS based oscillator.

2. MEMS RESONATOR ELECTRICAL EQUIVALENT CIRCUIT AND RF MEASUREMENT

An electromechanical resonator can be modeled using the electrical equivalent circuit shown in Fig. 1. The mechanical resonance is described by a

series RLC circuit (R_m , L_m and C_m) which is in parallel with a parasitic capacitance C_0 , forming an anti-resonant peak in the response. R_1 and R_2 are the line resistances.

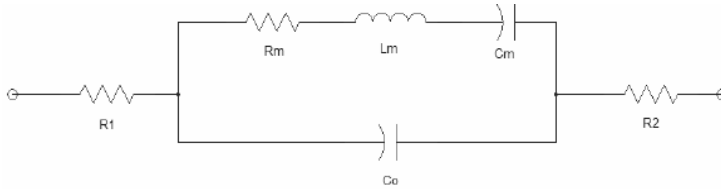


Fig. 1. MEMS electromechanical resonator electrical equivalent circuit.

Figure 2 shows the RF characterization of the in-plane flexural clamped-clamped (CC) beam resonator described in [4]. The resonant frequency is measured to be 95.1MHz and the quality factor (Q) 2630.

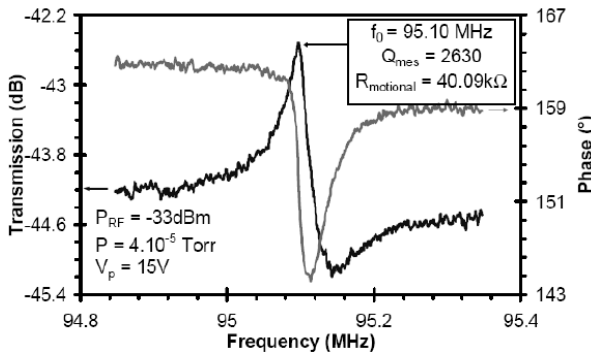


Fig. 2. RF transmission plot of a $4.9 \times 0.26 \mu\text{m}$ beam resonator (thickness=0.4 μm , gap=95 nm) and equivalent circuit.

The values of the different elements of the electrical model were defined from the measurement transmission response, using ADS. The extracted values were then used in the electrical equivalent model, as explained in [4]. Table 1 lists the extracted values for the equivalent circuit.

Table 1. ADS electrical equivalent model values

Parameter	ADS value
R_m	40.1 kOhm
L_m	0.16 H
C_m	16 aF
$R_1=R_2$	140 Ohm
C_0	102 fF

3 ARCHITECT3D™ MODEL

The resonator is modeled in CoventorWare ARCHITECT3D™. ARCHITECT3D™ uses the Synopsis SABER™ circuit simulation tool as the core solving engine. The SABER™ simulator is capable of multi-domain simulation, using models written in C, MAST or VHDL-AMS. The multi-domain capability enables the simulation of micromechanical elements alongside interface electronics, allowing the performance of the complete system to be investigated.

Figure 3 shows the schematic of the resonator, comprising new beam side-electrode models, flexible beams [5], anchors, line resistances and parasitic capacitance. The schematic is equivalent to the electrical model shown in Fig. 1, except the electrical equivalent series RLC components are replaced by exact electromechanical models.

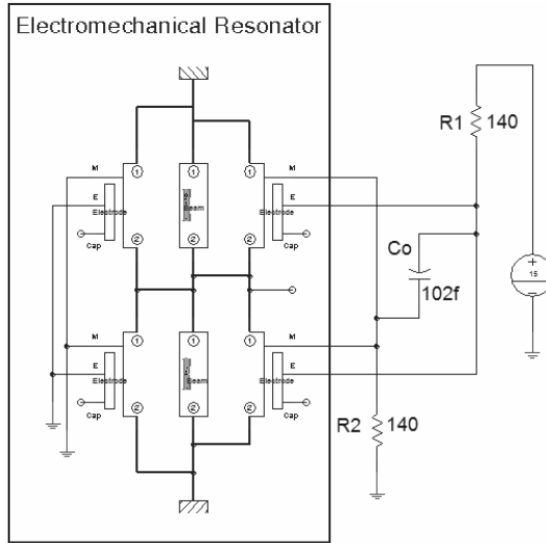


Fig. 3. ARCHITECT3D™ Resonator schematic.

In the schematic, the side-electrode model computes the electrostatic force acting on the faces of a flexible beam and has two mechanical interfaces that connect to moveable beam ends. Electrical pins, *M* and *E*, define the voltages applied to the beam and the electrode, respectively, see Fig. 4a. Capacitance and electrostatic force fields between the beam and electrode are calculated using a 1D-Gaussian integral along the length of the electrode. The more integration points used, the better the approximation, but at the cost of a longer simulation.

Contributions at each integration point are evaluated using 2-D fields, see Fig. 4b. The 2-D fields are created and evaluated using conformal mapping techniques [6, 7]. The actual shape and scaling of the 2-D fields depend on the

specified cross-section geometry (which could be trapezoidal) and the position of the movable beam.

To accurately capture the deformed shape two single segment non-linear beams, connected in series, are used. Each is connected to a side electrode, as shown in Fig. 3. The mathematical description of a single beam segment is based on Bernoulli beam theory, which gives accurate results for long and slender beams [8].

In this model Thermo-Elastic Damping (TED) can be simulated. However, energy loss through the anchors can only be modeled indirectly by adding a material damping factor in the beam so that measured and simulation Q factors match.

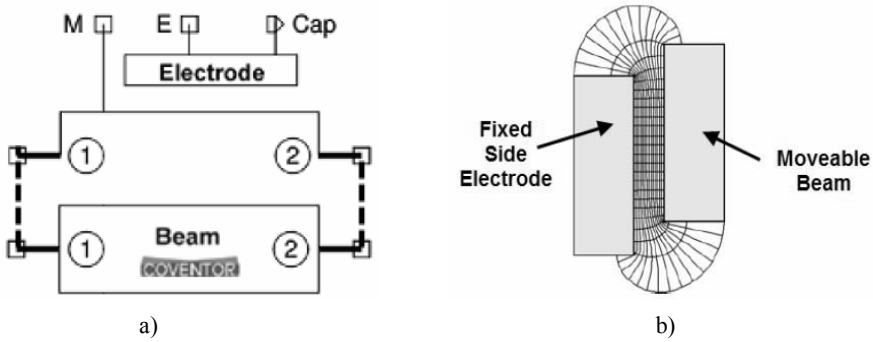


Fig. 4. (a) Side electrode model connected to 6 DOF Bernoulli beam and (b) electrostatic 2D-field

4. SIMULATION RESULTS AND DISCUSSION

Using ARCHITECT3DTM we simulate the first in-plane resonant mode, as shown in Fig. 5.

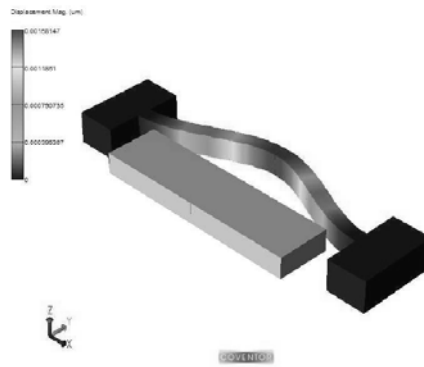


Fig. 5. Beam resonator deformation in its first in plane resonant vibration mode. For clarity, the right-hand electrode is hidden and the beam displacement scaled by 500 in Y.

Under zero bias, the mechanical Q-factor due to TED is predicted by TED models in the beam segments to be 5000, higher than the measured value of 2630. Additional energy loss is likely through the anchor. Figure 6 shows the Quality factor variation with the material damping factor b (no additional TED). A Quality factor of 2630, in good agreement with RF measurement, is obtained with a damping factor of 587 femto.

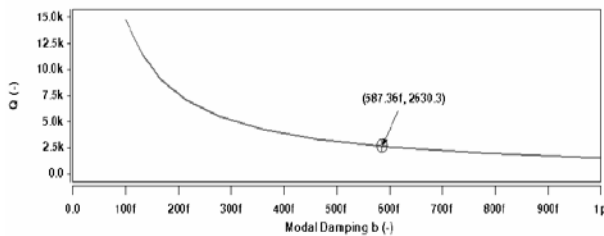


Fig. 6. Quality factor evolution versus damping factor variation. Resonator damping factor definition.

Figure 7 shows the simulated response from ARCHITECT3DTM and the equivalent circuit model extracted from measurement. The results are in good agreement. Equivalent circuit model values are defined in Table 1. the ARCHITECT3D™ electromechanical component models use physical data, i.e. beam width, beam length, beam thickness, resonator to electrode gap, Young modulus and Poisson ratio. Stress is known to be very low and not set.

The beam width is adjusted slightly from the designed value of 260 nm to 267.5 nm to fit the frequency. This small adjustment will always be necessary due to the error between measured nanoscale dimensions (which are difficult to measure exactly) and actual values.

The gap is also adjusted (from 95 nm to 47 nm) to increase the electromechanical coupling so that the simulated output signal and measurement results match well. The lower gap value used in the simulation and needed to fit to measurement, implies a higher level of electromechanical coupling in the fabricated device. The reason for this is yet to be investigated. We assume that the measured Q-factor used to describe our mechanical device in the analytical simulation is probably not correct. The measured Q-factor is from the whole component, i.e. the mechanical resonator and electrical components (pads and lines). The Q-factor used in the simulation is defined for the mechanical resonator only. This latter Q value is probably higher than the measured one and could explain the gap adjustment. Nevertheless, the simulation of a higher Q factor doesn't predict the correct signal curve. The use of a higher Q induces a higher level of electromechanical coupling, as expected, though equally thins down the peak width.

Moreover, the out of plane fringing capacitance (from the topside and underside of the beam) is not taken into account in the Architect simulation. This fringing capacitance along the beam might contribute to the electromechanical coupling. An additional study will be undertaken.

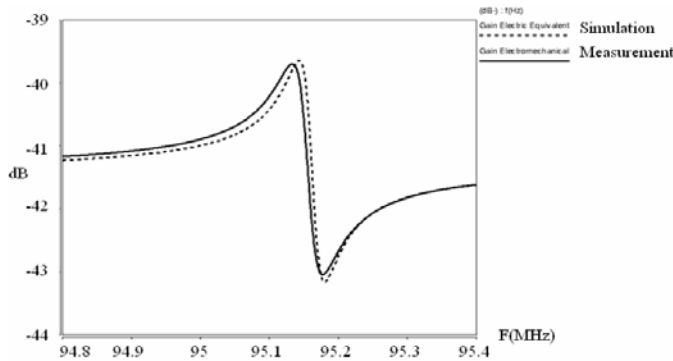


Fig. 7. Simulated and measured gain for CC beam resonator.

One of the major characteristic of a MEMS electromechanical resonator is a resonant frequency that is dependant of the polarization bias variation. The electrostatic force acting on the vibrating beam induces a negative stiffness on the resonator, and so resonant frequency decreases with increasing bias. This phenomenon is illustrated in Fig. 8 [4] which shows RF transmission measurements on a 67 MHz beam resonator ($L=5 \mu\text{m}$, $w=0.19 \mu\text{m}$, $\text{gap}=0.11 \mu\text{m}$) with varying polarization biases of 13 V, 15 V, 17 V and 19 V respectively.

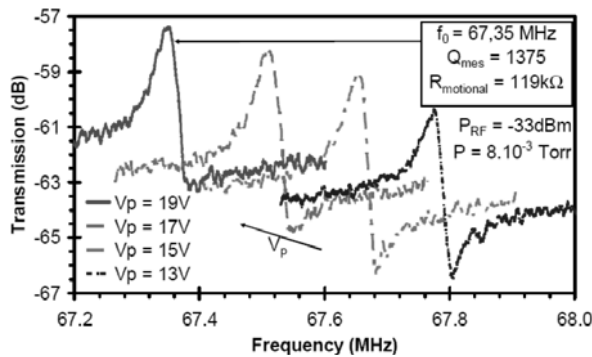


Fig. 8. Measured resonant frequency evolution versus bias variation for a 67 MHz beam resonator ($L=5 \mu\text{m}$, $w=0.19 \mu\text{m}$, $\text{gap}=0.11 \mu\text{m}$)

Using the ARCHITECT3D™ resonator schematic shown in Fig. 3 we simulate the frequency shift induced by bias voltage variation. Figure 9 shows the evolution of the resonator output signal when the bias voltage is ranging from 13 V

to 19 V. The width of the beam is adjusted, from 190 nm to 191.75 nm to match the frequency at 13 V (exactly). Table 2 compares simulation and measured results, which have been reported previously [4].

Table. 2. Resonant frequency variation versus bias voltage – Simulation and measurement results comparison

Bias voltage (V)	Simulation Resonant frequency (MHz)	Measurement Resonant frequency (MHz)
19	67.23	67.35
17	67.46	67.52
15	67.63	67.66
13	67.77	67.77

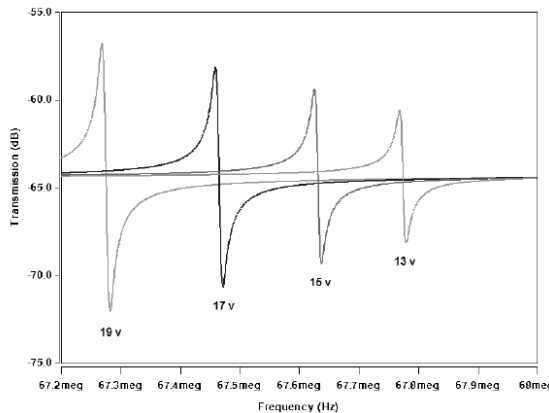


Fig. 9. Simulated resonant frequency evolution versus bias variation for a 67 MHz beam resonator (L=5 μm , w=0.19 μm , gap=0.11 μm)

We note a good match between the simulated and measured frequency shift with bias voltage.

We also note that the simulated output signal away from resonance changes little with bias (the output signals are merged and remain stable around -64dB). This is compared to the measured output signal level which decreases when the bias voltage decreases. This might be due to the static capacitance (C_0) variation induced by the bias voltage variation.

This effect is simulated by the ARCHITECT3D™ simulation, as shown in Fig. 10, where the beam sideelectrode capacitance is plotted over a range of bias voltages from 0 to 20 V. Nevertheless, the static capacitance change in this voltage range is very small (0.4 aF) and can't explain the output signal level variation. Thus an additional parasitic phenomenon must be taken into account such as substrate losses or lines coupling.

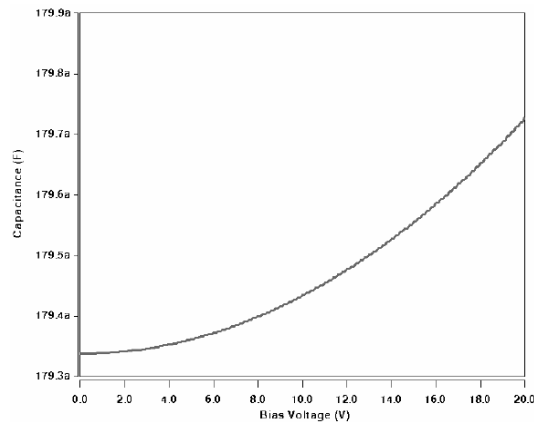


Fig. 10. Simulated static capacitance (C_0) variation induces by the bias voltage variation from 0 to 20 V.

5. CONCLUSION

The ARCHITECT3DTM beam side electrode model enables the system level modeling of the flexural CC beam resonator and thus its behavior in its electrical environment to be investigated. Further work is underway to understand and improve the match between the simulated results and the measured results. We also aim to simulate a complete MEMS based function, such as oscillator, in the near future.

References

- [1] Y.W. LIN, S. LEE, S.S. LI, Y. XIE, Z. REN and C.T.C. NGUYEN, *60-MHz Wine-Glass Micromechanical-Disk Reference Oscillator*, Digest of Technical Paper, IEEE Int. Solid-State Circuits Conference (ISSCC), pp. 322–323, San Francisco, California, Feb. 15-19, 2004
- [2] J.V. KAAJAKARI, T. MATTILA, A. OJA, J. KIIHAMÄKI and H. SEPPÄ, *Square-Extentional Mode Single-Crystal Silicon Micromechanical Resonator for Low Phase Noise Oscillator Applications*, IEEE Electron Device Letters, **25**(4), pp. 173–175, April 2004.
- [3] K. SUNDARESAN, G.K. HO, S. POURKAMALI and F. AYAZI, *Electronically Temperature Compensated Silicon Bulk Acoustic Resonator Reference Oscillators*, IEEE Journal of Solid-State Circuits, **42**(6), June 2007.
- [4] C. DURAND, F. CASSET, B. LEGRAND, M. FAUCHER, P. RENAUX, D. MERCIER, D. RENAUD, D. DUTARTRE, E. OLLIER, P. ANCEY AND L. BUCHAILLOT, *Characterization of in-IC Integrable Inplane Nanometer Scale Resonators Fabricated by a Silicon on Nothing Advanced CMOS Technology*, MEMS, pp. 1016–1019, Tucson, USA, January 13-17, 2008.
- [5] G. LORENZ, Proc 2.Conf. on Modeling and Simulation of Microsystems, MSM, pp. 233–238, Santa Clara, April 1998,
- [6] Steven G. KRANTZ, Handbook of Complex Variables
- [7] P.K. KYTHE, Computational Conformal Mapping, Birkhäuser, 1998.
- [8] CoventorWare 2008 ARCHITECTTM Reference Manual.

A Capacitive Shunt RF MEMS Switch for Coplanar Waveguide Transmission Lines

Bengt HOLTER¹, Karsten HUSBY¹, Håkon SAGBERG², Geir U. JENSEN²,
Ulrik HANKE³, Shimul CHANDRA SAHA⁴, Trond SÆTHER⁴

¹SINTEF ICT, Communication Systems, O.S. Bragstads plass 2C, Trondheim, Norway
Phone: +47 73593000

²SINTEF ICT, Microsystems and Nanotechnology, Gaustadalleen 23, 0373 Oslo, Norway
Phone: +47 22067300

³Vestfold University College, Microsystem Technology, 3103 Tønsberg, Norway
Phone: +47 33031000

⁴Norwegian University of Science and Technology, 7491 Trondheim, Norway
Phone: +47 73595000

Abstract. In this paper, performance results are presented for the first RF MEMS switch ever to be produced in Norway. It is a shunt capacitive switch integrated in a coplanar waveguide configuration. The switch uses a bipolar (square wave) bias voltage for both actuation and holddown, and is designed to operate in the frequency range 10-32GHz. The fabrication process has been developed and performed at the Micro and Nano Laboratory at SINTEF, which has the only independent complete silicon processing line in Norway. In the targeted frequency range (10-32GHz), the measured insertion loss is between -0.17 and -0.4dB, the return loss between -23 and -12dB, and the isolation is between 7.5 and 20dB. The achieved capacitance ratio of the switch is 25. Some stiction problems have been observed for either a too high pull-in voltage or a too high hold-down voltage.

1. INTRODUCTION

RF MEMS (Radio Frequency Micro-ElectroMechanical Systems) technology is currently regarded as a key enabling technology for future development of wireless communication systems due to superior performance and flexibility compared to existing technologies. In particular, RF MEMS components may be applied in future cognitive radio systems to enable reconfigurable RF front-ends such as flexible filtering, adaptive matching networks, and more efficient antenna designs. For the last four years, SINTEF has conducted research within a project

entitled *Integrated reconfigurable radio front-end technologies (IRRFT)*, to gain experience in using RF MEMS components and devices in reconfigurable RF front-ends. One of the main objectives was to develop knowledge and experience to design and process an in-house RF MEMS switch, where the focus was on optimizing the probability of processing success rather than achieving ambitious electrical specifications. In this paper, the fabrication process and some selected performance results of the developed switch are presented. It is the first RF MEMS switch ever to be produced in Norway, and it has been fabricated at the Micro and Nano Laboratory at SINTEF.

The switch is a coplanar waveguide (CPW) capacitive shunt switch, where the suspended MEMS bridge is actuated by applying a bipolar square wave bias voltage between the bridge and the center conductor of the CPW transmission line (t-line). A scanning electron microscope (SEM) image of the fabricated switch is depicted in Fig. 1 (top view). When the bias voltage is applied, an electrostatic force causes the bridge to bend down onto a thin dielectric layer that covers the t-line beneath the bridge. In this down-state position, the bridge connects the t-line to ground (through a capacitance), realizing an RF short for microwave frequencies. When the bias voltage is removed, the electrostatic force is relaxed, causing the bridge to return to its original up-state position. In the literature, detailed analysis on modeling and design of CPW shunt switches are given in [1]-[3].

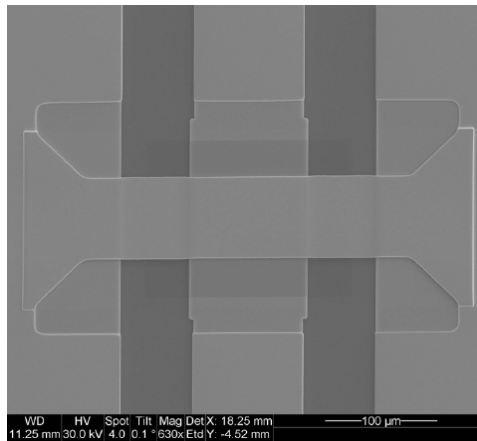


Fig. 1. The SINTEF RF MEMS switch

2. FABRICATION PROCESS

The switches are fabricated on high-resistivity (4-8 k Ω cm) Si with 500nm of thermal silicon dioxide. The switch bridge measures (80 \times 300) μ m, and is made of sputtered gold (Au) on top of a 2.5 μ m thick sacrificial photoresist layer. The 1.2 μ m thick Au bridge has a relatively low tensile stress (30-60 MPa), and ‘climbs’ the sloping sidewalls of the patterned photoresist. Below the bridge, the

bottom electrode is made of sputtered tungsten (W) covered by a 200 nm thick plasma-enhanced chemical vapour deposited (PECVD) silicon nitride layer (Si_3N_4). Only four photomask levels were used, defining (1) The W for electrode and CPW bottom layer (2) The Si_3N_4 layer covering the bottom electrode (3) The patch of sacrificial photoresist that creates the bridge-to-dielectric gap, and (4) The Au bridge and CPW upper layer. An additional layer of metal (Au) is often included for strengthening the bridge anchors and improving the t-line RF properties. Such a layer would probably have had a noticeable influence on the pull-in voltage, at least, but the SINTEF switch operates remarkably well without that layer. For implementation of circuits based on these switches, an additional step/mask for polysilicon bias lines is used.

A. Bottom Electrode

The bottom electrode consists of a 100 μm wide and 500 nm thick stripe of sputter-deposited W with a 12-15 nm Ti adhesion layer. Patterning is done by reactive ion etching (RIE). A refractory metal, W withstands the subsequent high-temperature processing without forming hillocks as, for instance, aluminium would do. A smooth electrode surface is essential for a high down-state capacitance. Unlike e.g., Al, W has no hillock formation.

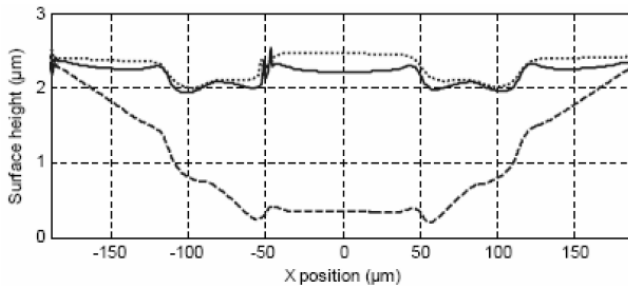


Fig. 2. Surface profile of the bridge in three states: *Prerelease* (dotted curve), *post-release* (solid curve), and *actuated* (dashed curve).

The heights are relative to the top of the WNiCr-Au stack. Pre-release data were obtained with optical profilometry on surfaces partially covered with photoresist, and the profile has been scaled and offset to obtain a good fit to the post-release data.

Since the W electrode also serves as a section of the tline, a sufficiently thick electrode is needed for transmission quality. However, two other effects call for a thin electrode layer: First, the subsequent deposition steps (nitride deposition, sacrificial resist and Au sputter) are (at least partly) conformal, so the edges of the electrode will create steps in the Au bridge, as illustrated in Fig. 2, which also shows the shape of the resulting bridge before and after release. Second, sputtered

W has a large internal compressive stress (~1GPa); thus a thick W layer would produce wafer curvature and also adhesion problems (peeling). As such, the selected thickness of 500 nm for the bottom electrode is a compromise.

B. Dielectric Layer

A 200 nm thick layer of Si_3N_4 serves as the dielectric layer in the capacitive switch. The Si_3N_4 is deposited using PECVD at 300°C, and a (180×140)μm patch is patterned by RIE. The relative permittivity of the Si_3N_4 is around 8, but the surface roughness of the Si_3N_4 as well as that of the underside of the Au bridge results in a lower 'effective' permittivity.

C. Sacrificial Photoresist

While achieving vertical photoresist sidewalls is the goal of many high-resolution photoprocesses, the switch requires a process resulting in roughly 45° sloping sidewalls so that the Au slope/wall remains thick enough for good mechanical as well as electrical properties. The correct sloping sidewalls were achieved with a combination of proximity exposure and careful finetuning of hard baking parameters (temperature and time). We used a standard DNQ-novolac positive photoresist (HIPR 6517), which is spin coated at 2000 rpm and exposed at a gap of 25 μm. The optimum hotplate hardbake conditions were found to be 115°C for 300 s [4]. The temperature during subsequent processing steps must be kept well below the hard baking temperature, in order to prevent excessive baking of the photoresist.

D. Bridge

A 1.2 μm Au layer, with an adhesion layer of 10 nm NiCr, is deposited using low-power sputtering at relatively high pressure (20 mTorr). The NiCr/Au is deposited partly on W (CPW lines), and partly on photoresist (bridges). A low sputtering power ensures that the sacrificial photoresist is not much affected, and the sputtering pressure was tuned to achieve a low tensile stress in the Au film. The resulting biaxial stress of the suspended Au bridge was characterized to lie in the range 30-60 MPa using test structures such as Guckel rings.

The Au film was patterned using standard photolithography and a potassium iodide (KI) solution. The sacrificial photoresist was removed using O₂ plasma and Shipley 1165 microposit remover, and then the NiCr layer underneath the Au in the bridge was etched. Finally, the switches were dried with supercritical CO₂ drying to avoid stiction. Images of the device are shown in Fig. 3.



Fig. 3. SEM images of the fabricated switch in its idle (top) and actuated (bottom) states.

E. Mechanical Properties and Switch Operation

A bias voltage applied between the bottom electrode and the bridge will cause the latter to move towards the former. The spring constant is often calculated under the assumptions of a fixed-fixed bridge and that there are no steps in the bridge. These assumptions do not apply in our case. When released, the bridge contracts and the parts close to the anchors deform slightly. This creates a sag or curvature of the released bridge, as seen in Fig. 2. Also, the bridge steps on each side of the bottom electrode result in local curvature changes and a softening of the bridge. A several μm thick additional top metal layer would reduce the first sag, but some electrode induced sag will always be present. However, the SINTEF switch exhibits an overall good performance. The measured pullin voltage is 30 V, and the down-state and up-state capacitance are 1.2 pF and 49 fF, respectively.

3. RF PERFORMANCE

The SINTEF RF MEMS switch has been characterized by observing static S-parameters during steady state operation, and by observing settling dynamics during transient operation. The measurements have been performed directly on wafer by the use of a probe station according to the measurement set up displayed in Fig. 4.

The use of a bipolar bias voltage was selected in order to reduce the possibility of dielectric charging commonly observed in capacitive switches [3]. According to [3], the dielectric will not charge if the bipolar signal has a period that is shorter than the charging time of the dielectric. Since the electrostatic force of the bias signal is proportional to the square of the voltage, it will represent a constant attractive force to the bridge even if the polarity changes. This force will however go to zero in the transition between the two bipolar levels, but as long as this transition phase is fast enough (20-100 ns [3]), the bridge will not have time to react to the change. Based on these facts and the results reported in [Sec. 7.2, 3], a

square wave bipolar bias voltage has been selected for both the actuation and hold-down cycle of the switch presented in this paper.

In our case, the bias/control voltage is generated by a high voltage arbitrary bipolar pulse generator, which is isolated from the sensitive measurement equipment by tees and attenuators. Due to the flexibility of this generator, it is possible to address mechanical switch dynamics and to identify a bias voltage for fast and careful excitation. The selected bias tee in Fig. 4 represents a capacitive loading of the pulse generator. However, the generator still managed to deliver up to 60V pulses at a slew rate of 600V/ μ s. In Fig. 5, a magnified view of the probe tip ready for touch down on the RF MEMS switch is shown.

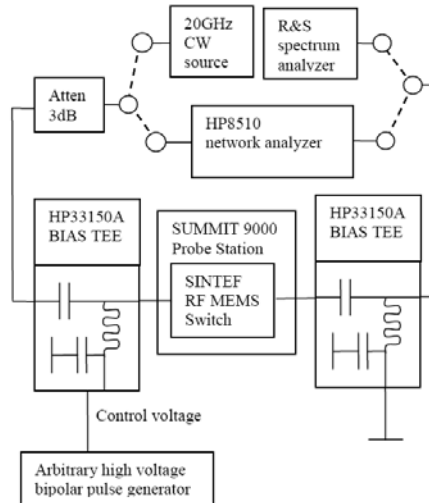


Fig. 4. Measurement set up for either S-parameters with network analyzer or for dynamic transient response with a high speed synchronized spectrum analyzer.

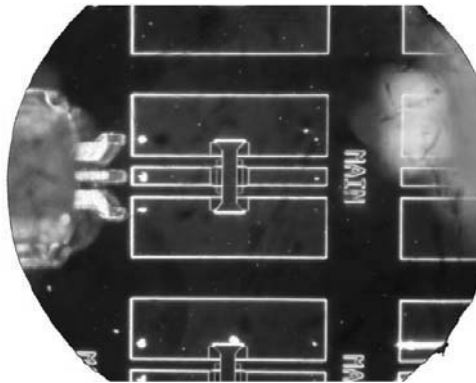


Fig. 5. The probe tip (GSG 200) ready for touch down on the SINTEF RF MEMS switch denoted MAIN.

A. S-parameters

For the S-parameter measurements, the bias voltage was selected to be a rectangular bipolar signal at 10 kHz slightly above the pull-in voltage, hence using a hold-in voltage that is identical to the pull-in voltage. The switch was released after 10 s by setting the bias voltage to zero. Under these conditions, none of the tested samples returned to their initial up state position. However, as shown in Section III B, the switches did release when the bias voltage was quickly and gracefully reduced after pull-in to a lower hold-in voltage.

The measured S-parameters of the SINTEF switch are presented in Fig. 6 and Fig. 7. In Fig. 6, insertion and reflection loss are presented for the open switch (up-state) whereas in Fig. 7, similar results are presented for the closed switch (down-state). All the measured results are compared to a modelled result based on the lumped RLC model shown in Fig. 8.

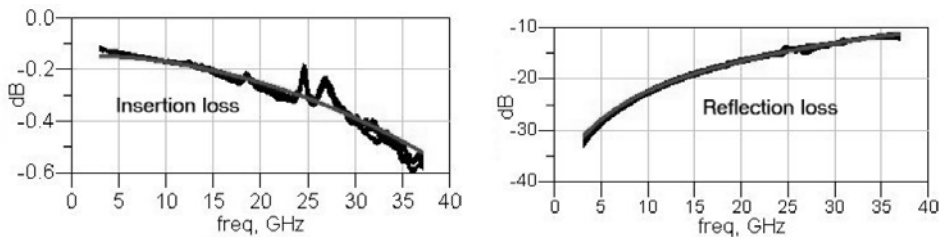


Fig. 6. Insertion and reflection loss for the open switch (black) together with the modeled result (red) for the T-model with $C=49\text{fF}$, $R=0.82$ and $L=15\text{pH}$.

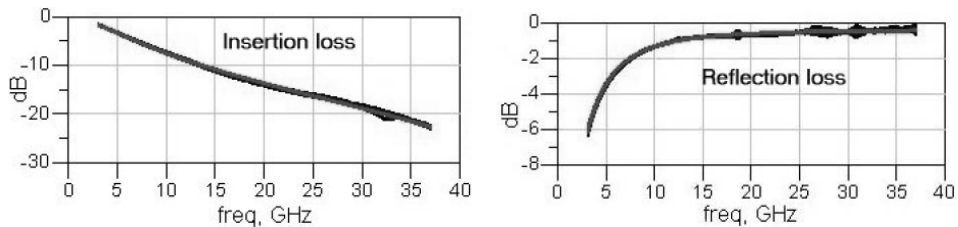


Fig. 7. Insertion and reflection loss for the closed switch (black) together with the modeled result (red) for the T-model with $C=1.24\text{pF}$, $R=1.0$ and $L=6.5\text{pH}$.

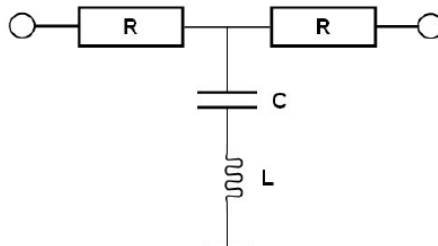


Fig. 8. Lumped T-model of a capacitive shunt switch.

The impedance of the switch as a single port device with the output port left open is $Z = Z_0[(1+\Gamma e^{j\phi})/(1-\Gamma e^{j\phi})]$, where Z_0 is the characteristic impedance of the t-line, and Γ is the magnitude of the reflection coefficient. The highest Q -factor is found at the phase angle $\phi = \pm \frac{\pi}{2}$, where the total reflection coefficient is pure imaginary. From the measured S-parameters, the down-state Q -factor of the switch has been estimated to about 20-30 according to the equation $Q = \frac{|\text{im}(z)|}{|\text{re}(z)|} \approx \frac{1}{1-\Gamma}$.

B. Settling Dynamics

The bias voltage level affects the settling time of the switch, so fast operation is possible if the bias voltage is increased. However, it has been observed that fast operation also introduces a mechanical bounce in the switch. Due to this, the settling speed was aimed to about 100 μs . In Fig. 9, the RF attenuation through the switch is depicted as measured by a Rohde & Schwarz spectrum analyzer. The switch is operated with the bipolar bias voltage and a 30 V pull-in voltage, which is gracefully reduced to a hold-in voltage of approximately 12 V. After 360 μs , the bias voltage goes from -12V to zero and the bridge starts to return to its original up-state position.

The switches have been turned on and off at a rate of 250 Hz to provoke for any failure. After some time, a stiction tendency was observed. The delayed rise up movement is possibly caused by a stiction mechanism not yet identified. Charge buildup, mechanical failure and viscous tension from contamination are some candidate explanations for this behavior.

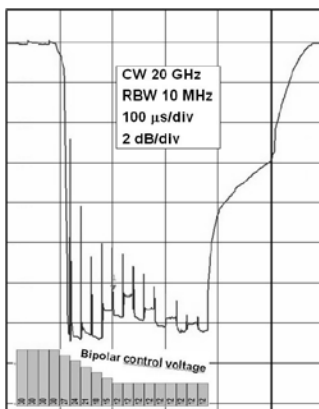


Fig. 9. Dynamic on/off response of the RF MEMS switch at 20 GHz after one million cycles with a spectrum analyzer in zero span mode.

4. CONCLUSION

This paper has presented Norway's first RF MEMS switch, a capacitive shunt switch produced at SINTEF. Between 10-32 GHz, the measured insertion loss is

between -0.17 and -0.4dB, the return loss is between -23 and -12dB, and the isolation is between 7.5 and 20dB. The achieved capacitance ratio of the switch is 25.

Acknowledgement. This work has been funded by the Norwegian Research Council through the IRRFT (159259/I40) and SMIDA (159559/130) projects. The authors would like to thank Prof. Gabriel Rebeiz of the University of California at San Diego for his valuable comments to the process development of the switch.

References

- [1] J.B. MULDAVIN and G.M. REBEIZ, *High Isolation CPW MEMS Shunt Switches - Part 1: Modeling*, IEEE Transactions on Microwave Theory and Techniques, **48**(6), pp. 1045–1052, June 2000.
- [2] J.B. MULDAVIN and G.M. REBEIZ, *High Isolation CPW MEMS Shunt Switches - Part 2: Design*, IEEE Transactions on Microwave Theory and Techniques, **48**(6), pp. 1053–1056, June 2000.
- [3] G.M. REBEIZ, *RF MEMS: Theory, Design, and Technology*, John Wiley & Sons, 2003.
- [4] S.C. SAHA, H. SAGBERG, E. POPPE, G.U. JENSEN, T.A. FJELDLY, and T. SÆTHER, *Tuning of Resist Slope With Hardbaking Parameters and Release Methods of Extra Hard Photoresist for RF MEMS Switches*, Journal of Sensor and Actuators A: Phys., **142**(2), pp. 452–461, 2008.

High-Isolation Shunt-Series MEMS Switch for a Wide Frequency Range (6-40GHz)

M. FERNÁNDEZ-BOLAÑOS, P. DAINESI, A.M. IONESCU

École Polytechnique Fédérale de Lausanne (EPFL), Nanolab, 1015 Lausanne, Switzerland

Phone: +41 21 693 46 07

Abstract. This paper reports on a capacitive shunt and an ohmic series RF MEMS switches behaving with high performances in a wide range of frequencies (6 to 40 GHz). The shunt switch produces an insertion loss of 1.1dB and an isolation better than 30dB at 40GHz. On the other hand, the series switch has a measured isolation and return loss better than 25dB and less than -15dB respectively, for the entire range. A cascade configuration of both devices suggests that a very high isolation is achievable (better than -40dB over the frequency range of 6 to 40GHz), while keeping low the insertion (-1.1dB) and return losses (better than -17dB).

1. INTRODUCTION

RF switches are widely used in wireless communication systems, such as switched-line phase shifters in phase array antennas or transmit/receive switches for reconfigurable front-end radios [1]. For these applications are required switches with low insertion loss and very high isolation for a wide range of frequencies.

RF MEMS shunt capacitive switches performances are limited by a low-medium capacitive ratio (Cr). Even if theoretically a 100 on/off Cr is feasible, due to the roughness and planarization of the bottom and suspended electrodes, the fabricated Cr rarely is bigger than 50 and commonly is around 10 [2]. A poor on/off capacitance ratio commonly results in poor matching and/or poor isolation. RF MEMS series ohmic switches are generally suited for low frequency applications. The isolation is limited by the up capacitance at high frequencies ($S_{21} > -20dB$)[3].

In order to achieve a very high isolation a solution is to design the shunt capacitive switch to resonate at the frequency of interest [4]. However, the high isolation performance is only possible in a narrow frequency bandwidth. Overcoming these limitations is possible by combining multiple devices (ohmic

and capacitive) in parallel or series to achieve the desired characteristics [5] at the expense of a slightly increase of the insertion loss.

Thus, the aim of the paper is to propose a very high isolation solution over a wider range of frequency by cascading a series ohmic cantilever with a shunt capacitive switch (Fig. 1). As a result the reflection coefficient of the shunt switch in the up state position (standard limited parameter) is reduced improving the matching for the conductive ON state (series ohmic in down and shunt capacitive in up state) as well as increasing the isolation in the isolation OFF state (applying the contrary states).

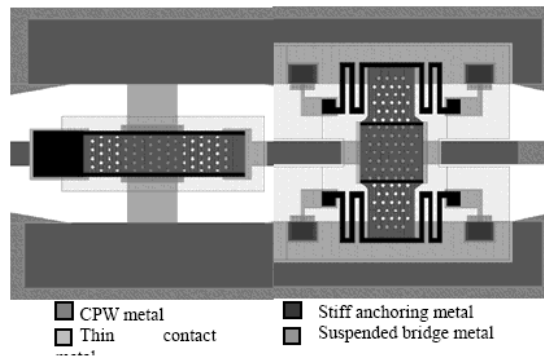


Fig. 1. Layout of the series-shunt switch cascade configuration.

This paper focuses on the design, modeling, 3D finite-element and circuit parameter electromagnetic (EM) simulations and on the implementation of a capacitive shunt switch, an ohmic series cantilever and the result of cascading both devices suitable for 6 to 40 GHz very high-isolation applications. The fabrication of these devices have been done and fully characterized individually. The cascaded solution is in process and simulations of the expected results are presented.

2. DESCRIPTION OF THE DEVICES

Both ohmic and capacitive switches have been fabricated by ISIT-FHG within a multi project wafer run on a 508 μm high resistivity silicon substrate ($>3 \text{ k}\Omega\cdot\text{cm}$). The silicon substrate is isolated with a thick 2 μm thermal oxide insulator to avoid the effect of free charge carriers in the substrate interface. The RF MEMS switches are loaded on a 78Ω -high impedance CPW line consisting of 2.5 μm gold conductor, except under the MEMS bridges or cantilever where a thin layer of a sandwich of metals (Ti/Pt/Au/Pt) is used instead. The thin metal signal line is covered in the actuation region by 300 nm of AlN, which dielectric constant is 9.8. The total CPW width is 300 μm with G/W/G of 125/50/125 μm .

The suspended membrane is 900 nm thick consisting of a AuNiAu multi-layer. In Fig. 2 it can be observed the profilometer optic images of the finish

devices and a FIB cross section of the capacitive switch where the measured air gap is $1\ \mu\text{m}$. However, the expected air gap was supposed to be bigger and RF performances comparing with 3D EM Ansoft's HFSS simulations confirm that the real air gap is around $2\text{-}2.5\ \mu\text{m}$. The reason is that a partial self-actuation of the suspended beam is produced when doing the FIB cross section due to the high ion current needed for milling the structure.

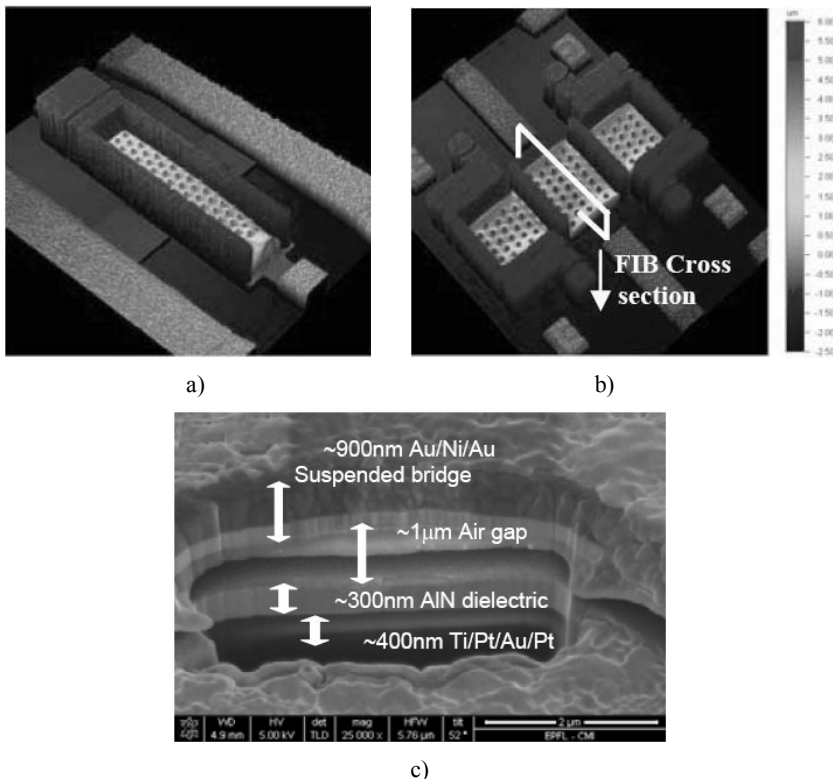


Fig. 2. a) and b) Profilometer optic images of the finish devices;
c) Focused Ion Beam (FIB) cross section of the released shunt capacitive switch.

3. CAPACITANCE SHUNT SWITCH

A $13\ \text{V}$ low actuation RF MEMS shunt capacitive switch is designed using meander-type anchoring with a spring constant of $k=9\ \text{N/m}$. The shunt switch is modeled by an equivalent T-model circuit as shown in Fig. 3. Device characterization from 6 to $40\ \text{GHz}$ is carried out on E8361A Vector Network Analyzer and the calibration is done using an external SOLT commercial kit. Fig. 4 illustrates the S parameter measurements and a SEM image of the shunt switch which provides good RF performances with an isolation better than $30\ \text{dB}$, $1.1\ \text{dB}$

of insertion loss and 15 dB of return loss at 40 GHz. The extracted circuit parameters are shown in Table 1. ADS equivalent circuit simulation of the extracted values is plotted in Fig. 5.a. as well as 3D EM finite-element HFSS simulation of the capacitive switch is depicted in Fig. 5.b. Both simulations are in good agreement with the measurements validating the extracting parameter method and the HFSS model.

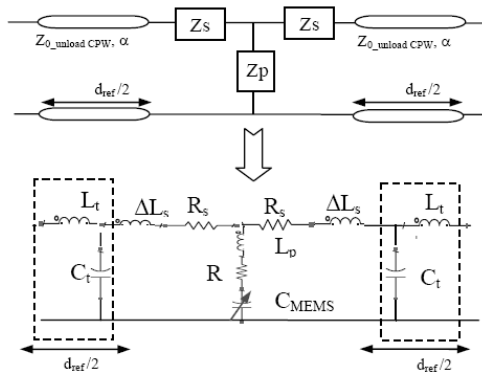
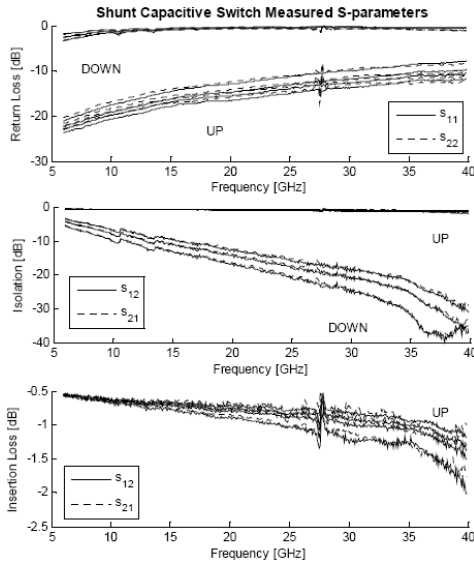
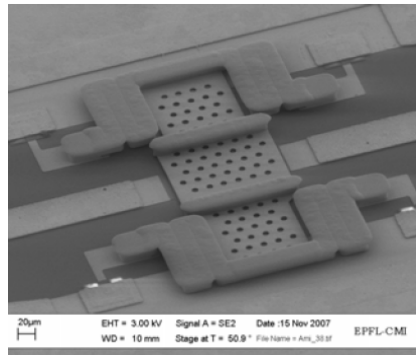


Fig. 3. Equivalent T-model used to extract the circuit parameters of the RF MEMS capacitive shunt switch from Sparameters measurements.



a)



b)

Fig. 4. a) Measured S-parameters of capacitive shunt switch in the up-state and the down-state, b) SEM of the fabricated capacitive shunt switch.

Table 1. T-Model Circuit Parameter Extraction from S-Parameters Measurements

Parameter @ 6-40GHz		Capacitive Shunt Switch						
		Up				Down		
Voltage		0V	8V	10V	12V	13V	20V	40V
Parallel Zp	Cp	40 fF	44.5 fF	48.5 fF	59 fF	1.11 pF	1.28 pF	1.55 pF
	Rp	---	---	---	---	0.25Ω		
	Lp	---	---	---	---	12pH		
Series Zs	Δ Ls	-10pH				-10pH		
	Rs	2.64Ω				0.54Ω		
CPW line	Lt	170pH						
	Ct	45fF						
Natural frequency		---	---	---	---	43.6 GHz	40.6 GHz	36.9 GHz

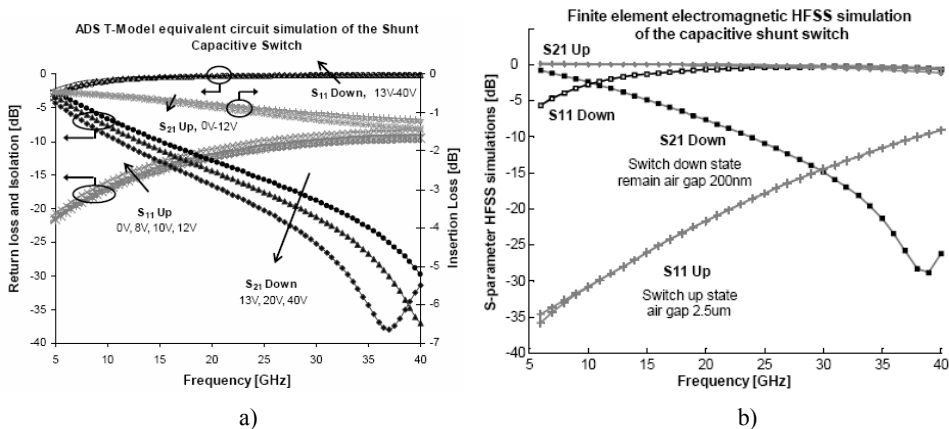


Fig. 5. a) ADS T-model circuit simulation of the extracted values from the capacitive shunt switch S-parameters measurements in the up-state and the down-states from 0V to 40V. b) HFSS S-parameter simulation of the 3D finite element electromagnetic model of the fabricated capacitance switch.

4. OHMIC SERIES CANTILEVER

The RF MEMS series ohmic cantilever is modeled by an equivalent PI-model circuit as shown in Fig. 6. The model includes the influence of the external actuation by means of Rbias and Cbias. The actuation voltage is higher than expected due to an induced stress on the cantilever while fabrication. Device characterization is performed by the same way as the capacitive switch. Figure 7 depicts the ohmic cantilever as well as the Sparameters measurements.

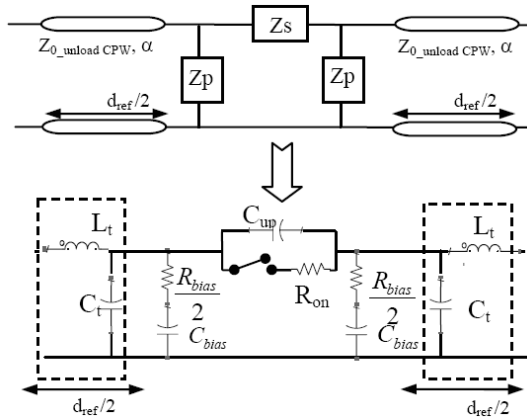
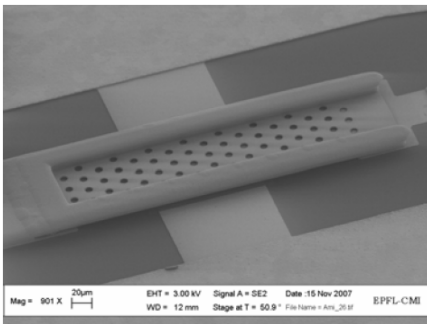
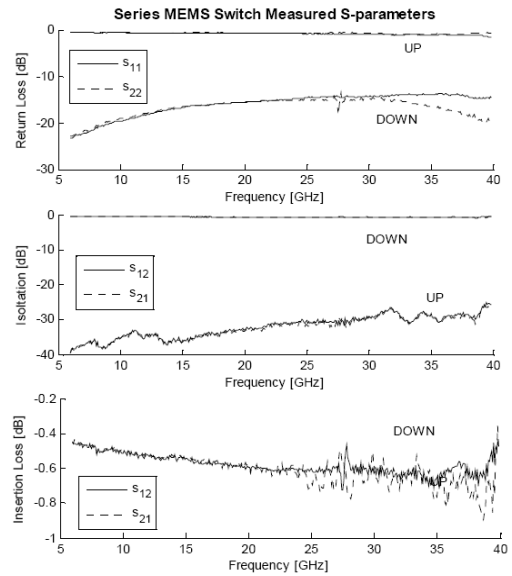


Fig. 6. Equivalent PI-model used to extract the circuit parameters of the RF MEMS ohmic series cantilever from Sparameters measurements.



a)

Fig. 7. a) SEM of the fabricated novel metal membrane ohmic series switch.



b)

b) Measured S-parameters of the MEMS series switch in the up-state and the down-state.

The ohmic switch provides an insertion loss of 0.6dB, an isolation better than 25dB and a return loss less than -15dB for the entire frequency range. The extracted circuit parameters are shown in Table 2. ADS equivalent circuit simulation is plotted in Fig. 8 being in concordance with measurements.

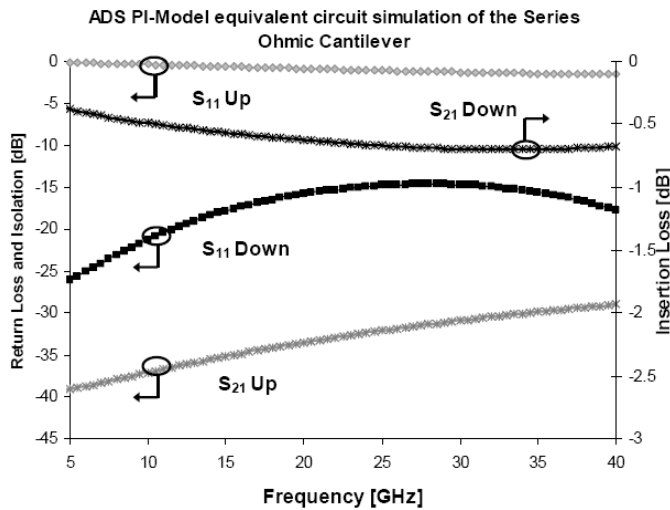


Fig. 8. ADS PI-model circuit parameter simulation of the ohmic series switch S-parameters in the up-state and the down-states.

Table 2. Pi-Model Circuit Parameter Extraction from S-Parameters Measurements

Parameter @ 6-40GHz		Ohmic Series Cantilever	
		<i>Up</i>	<i>Down</i>
Voltage		0V	> 80V
Series Z _s	C _{up}	2fF	-----
	R _{on}	>10kΩ	3Ω
Parallel Z _p	C _{bia_s}	33.46fF	33.46fF
	R _{bia_s}	400Ω	1.2kΩ
CPW line	L _t	170pH	
	C _t	33fF	
Cutoff frequency		20 THz	

5. SERIES AND SHUNT CASCADED SIMULATIONS

The ohmic series and capacitive shunt switches can be cascaded to produce a very high isolation over a wide range (6-40 GHz) when the series switch is in the up-state and the shunt switch is in the down-state and very good matching (low return loss) on the contrary situation. Figure 9 illustrates the result of simulating the cascade of individual S-parameters simulations.

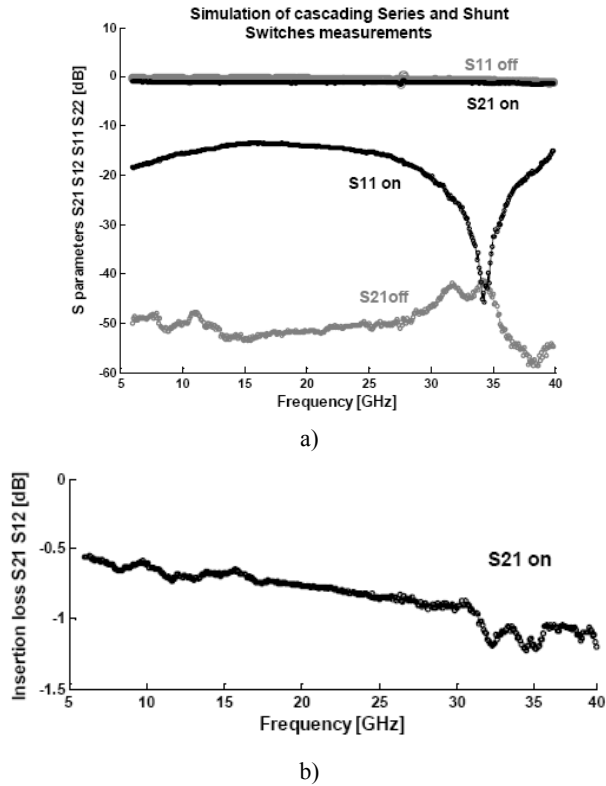


Fig. 9. Simulated S-parameters for the cascaded series-shunt switch: a) In the isolation state (S21 off, series up and shunt down) and in the conduction state (S11 on, series down and shunt up) and b) the insertion loss in the conduction state. The simulation is done using individual series and shunt switch S-parameters measurements and cascading the ABCD matrixes.

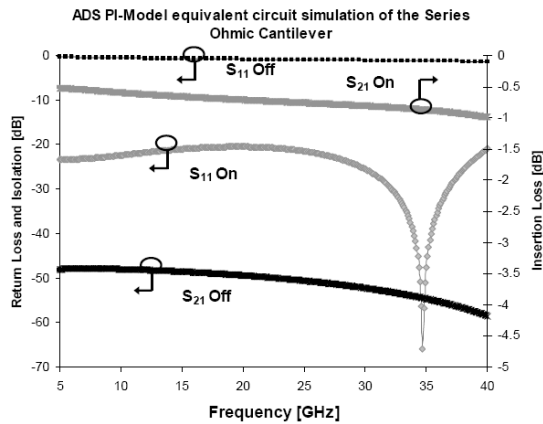


Fig. 10. Circuit parameter simulation of the cascade ADS T-model and PI-model of the series-shunt switch configuration.

On the other hand, Fig. 10 depicts the result of cascading the ADS circuit parameters shunt switch Tmodel and ohmic cantilever PI-model. Both approaches provide very promising results for very high isolation wide-frequency-band applications.

5. CONCLUSION

This article suggests that very high isolation in a wide range of frequency is possible cascading ohmic series and capacitive shunt switches. Such configuration provides an isolation better than -40dB over the extended frequency range from 6 to 40GHz, while keeping low insertion losses (-1.1dB) and acceptable return losses (-17dB).

The RF MEMS capacitive shunt switch and the RF MEMS ohmic series cantilever have been characterized. A full 3D electromagnetic and circuit parameter model has been developed and validated by comparison with S-parameters measurements.

Acknowledgement. The authors would like to acknowledge the assistance and fabrication support of Thomas Lisec within the multi-project of AMICOM at Fraunhofer Institute. This work was supported by the European Commission, FP6 IST Integrated Project e-CUBES.

References

- [1] G.E. PONCHAK, *et al.*, *Finite Ground Coplanar Waveguide Shunt MEMS Switches for Switched Line Phase Shifters*, 30th European Microwave Conference, pp. 1–4, Oct. 2000.
- [2] S.P. PACHECO, *et al.*, *Design of Low Actuation Voltage RF MEMS Switch*, Microwave Symposium Digest., 2000 IEEE MTT-S International, **1**, pp. 165–168, 2000.
- [3] R.G. POLCAWICH, *et al.*, *Surface Micromachined Microelectromechanical Ohmic Series Switch Using Thin-Film Piezoelectric Actuators*, Microwave Theory and Techniques, IEEE Transactions, **55**(12), pp. 2642–2654, Dec. 2007.
- [4] J.B. MULDAVIN, *et al.*, *High-Isolation Inductively-Tuned X-band MEMS Shunt Switches*, IEEE MTT-International Microwave Symposium Digest, **1**, pp. 169–172, 2000.
- [5] J.B. MULDAVIN, *et al.*, *Novel Series and Shunt MEMS Switch Geometries for X-Band Applications*, 30th European Microwave Conference, **1**, pp.1–4, France, Oct. 2000.

Design and Manufacturing of a 5-bit MEMS Phase Shifter at K-band

S. BASTIOLI¹, F. Di MAGGIO², P. FARINELLI¹, F. GIACOMOZZI³,
B. MARGESIN³, A. OCERA¹, I. POMONA², M. RUSSO²,
R. SORRENTINO¹

¹University of Perugia, Dept. of Electronic and Information Engineering,
Via G. Duranti, 93, 06125, Italy

²Selex Communications Spa, Via Sidney Sonnino, 6 - 95045 Misterbianco (CT), Italy

³MEMS Group, FBK-irst, Via Sommarive 14, 38050 Trento, Italy

Abstract. This work presents the design, and manufacturing of a novel K-band 5-bit MEMS phase shifter for applications in reconfigurable antenna systems. A hybrid architecture based on both switched line and loaded line topologies has been adopted. The device has been manufactured in microstrip technology on 200 μm thick high resistivity silicon substrate by using the 8-masks FBK MEMS process. The phase shifter full wave simulations show excellent performance in the frequency band of interest 20.2-21.2 GHz. Return loss and insertion loss better than 17 dB and 2 dB and phase error minor than 2 degrees are obtained for all the 2^5 phase shifter states. The on-wafer measurements of the single bits confirmed such high performance, showing a phase error minor than 2.5 degrees and a return loss better than 20 dB for all bits. The losses are dominated by the MEMS switch contact resistance, which is about 1.8 Ohm for every MEMS clamped-clamped beam ohmic switch. A low cost plastic package has been designed and manufactured as well. The on-wafer measurements of the complete 5-bit phase shifter are in progress as well as the packaged device.

1. INTRODUCTION

Microwave phase shifters are basic components used in a large variety of communication and radar systems, microwave instrumentation, and industrial applications [1-4]. As commercial and military systems increasingly move towards smaller and high performance antenna systems, MEMS technology can be applied to develop electronically reprogrammable phase shifters with low-power consumption, low loss, and excellent linearity.

This paper presents the design and manufacturing of a compact 5-bit K-band MEMS phase shifter to be used in reconfigurable telecommunication systems. The phase shifter is being manufactured on 200 μm thick high resistivity silicon substrate by using the well-established FBK MEMS process [5]. The electromagnetic design of the 5-bit phase shifter is shown in Section 2. Section 3 presents the device manufacturing and preliminary experimental results. The design of the low cost plastic package developed is described in Section 4.

2. PHASE SHIFTER DESIGN

The 5-bit MEMS phase shifter has been developed with a hybrid architecture to operate in the bandwidth 20.2-21.2 GHz. For the first four bits (180° , 90° , 45° , 22.5°) a switched line topology has been chosen since in the frequency band of interest it results to be the best trade-off among large phase shift, low loss and reduced space occupation. The fifth bit (11.25°) is based on a loaded line topology, which is convenient for the less significant bit where a small phase shift is required. The whole device has been designed on 200 μm thick HR Silicon substrate in microstrip technology. The total space occupation of the device is $11.35 \times 3.2 \text{ mm}^2$, a photo being shown in Fig. 1.

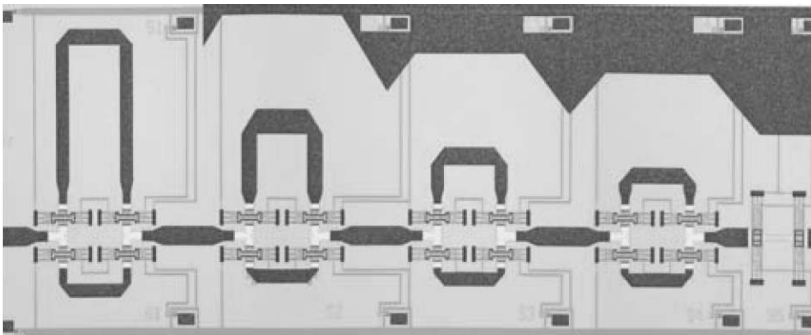


Fig. 1. Photo of the 5-bit MEMS phase shifter.

The first 4 bits utilizes ohmic clamped-clamped beam MEMS switches as building blocks in order to drive the signal into the desired path. Such switches have been previously developed and tested as presented in [6]. Excellent performance was measured for the single switch, with an on-state contact resistance below 2 Ohm and isolation better than 20 dB in the 0-30 GHz frequency band.

On the other hand, shunt capacitive switches were used as tunable capacitive loads for the realization of the fifth bit (11.25°). These capacitive switches show a similar mechanical structure with respect to the ohmic ones but lower loss since they are placed in shunt configuration.

Each bit of the phase shifter was designed by using the full wave simulator ADS Momentum [7]. Afterwards the simulations of the single bits were circuitally cascaded in order to predict the performance of the whole structure. The results are presented in Fig. 2 for all the 2^5 states.

Simulated results show a return loss and an insertion loss better than 17 dB and 2 dB respectively for all the phase shifter states. The losses are expected to be higher than simulated since the MEMS switch contact resistance was not taken into account in the simulations. Phase error is minor than 2 degrees in the 20.2-21.2 GHz frequency band.

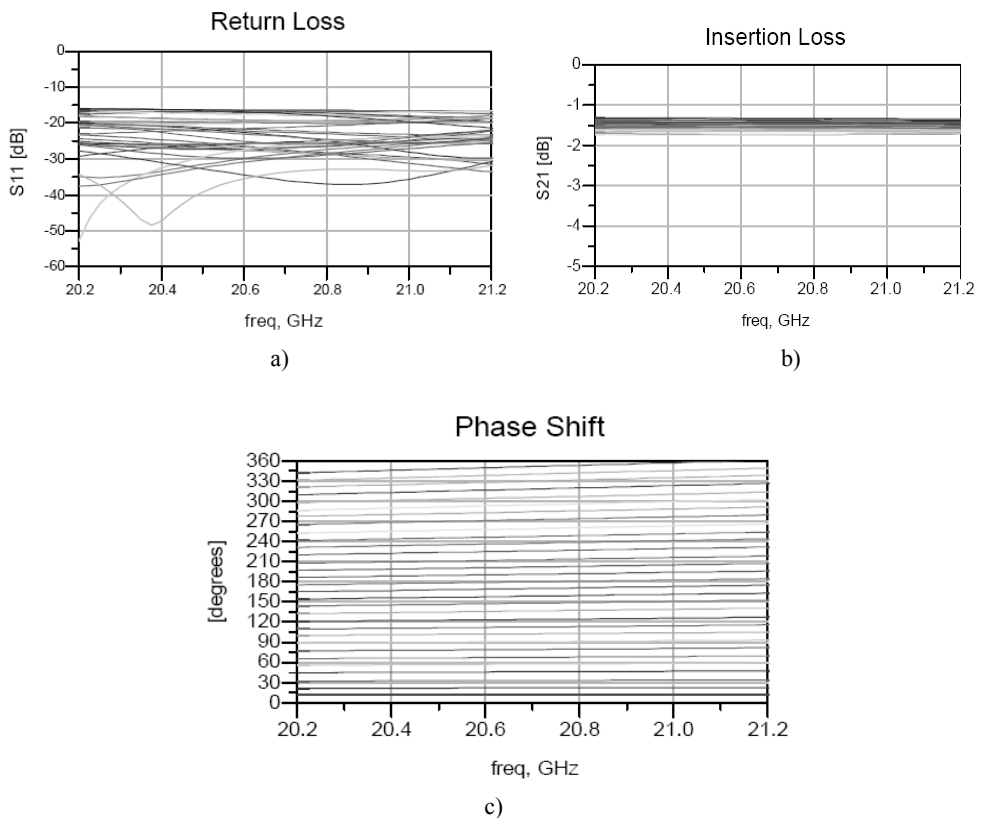


Fig. 2. Simulated S-Parameters of the phase shifter for all the states: Return loss (a), Insertion Loss (b), Phase Shift (c).

2. MANUFACTURING & EXPERIMENTAL RESULTS

The MEMS phase shifter has been fabricated at Fondazione Bruno Kessler Laboratories, employing the well-established eight-mask surface micro-machining process. The process allows the electrodeposition of two gold layers of different

thicknesses for highly complex movable bridges and microstrip lines. The air bridges are realized without the need of any planarization step by using photoresist as sacrificial layer. The bridge release is done with a modified plasma ashing process in order to avoid sticking problems. The bias network is realized by depositing a high resistive poly-silicon layer covered with silicon oxide for isolating the DC from the RF lines. The process allows the monolithic manufacturing of both ohmic and capacitive switches. Low Temperature Oxide is used as dielectric for capacitive switches as well as MIM capacitors. On the other hand, a third gold layer is deposited for the realization of low resistance metal-to-metal electro-mechanic contacts for ohmic switches.

The SPST switches and the single bits constituting the phase shifter have been realized in the same wafer in order to be able to look at the performance and the phase error introduced by every single part of the circuit. Via-less coplanar to microstrip transitions have been realized enabling on-wafer probe tests (Fig. 3). A TRL calibration kit has been then thus realized on the same wafer in order to remove the contribution of such transitions during the measurements.

As an example, the layout and the measured performance of the most significant bit (Bit 1) are presented in Figs. 3-4. Return loss better than 20 dB and insertion loss better than 1.3 dB were measured for both signal paths (reference and 180° phase shift lines) in the entire frequency band of interest 20.2-21.2 GHz. The loss is dominated by the switch contact resistance, which is about 0.9 Ohm for every contact point (1.8 Ohm for every SPST switch)

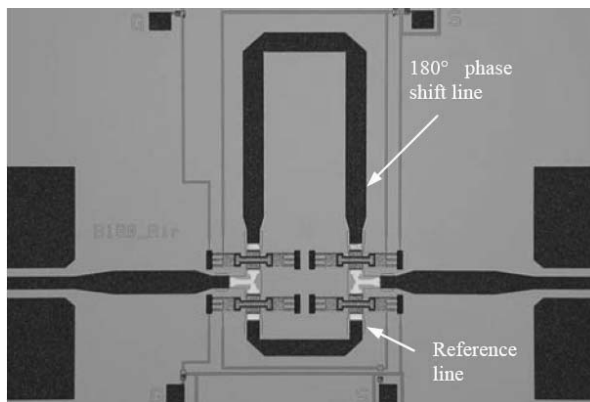


Fig. 3. Photo of Bit1 coplanar- microstrip transition for on-wafer probe measurements.

All 5 bits showed excellent performance and a very good agreement with the full-wave simulations. Return loss better than 20 dB and insertion loss better than 1.3 dB have been measured for all bits in the frequency band of interest 20.2-21.2 GHz. As expected for such a phase shifter topology, the phase shift of every single bit is extremely linear over a very wide frequency band (Fig. 5).

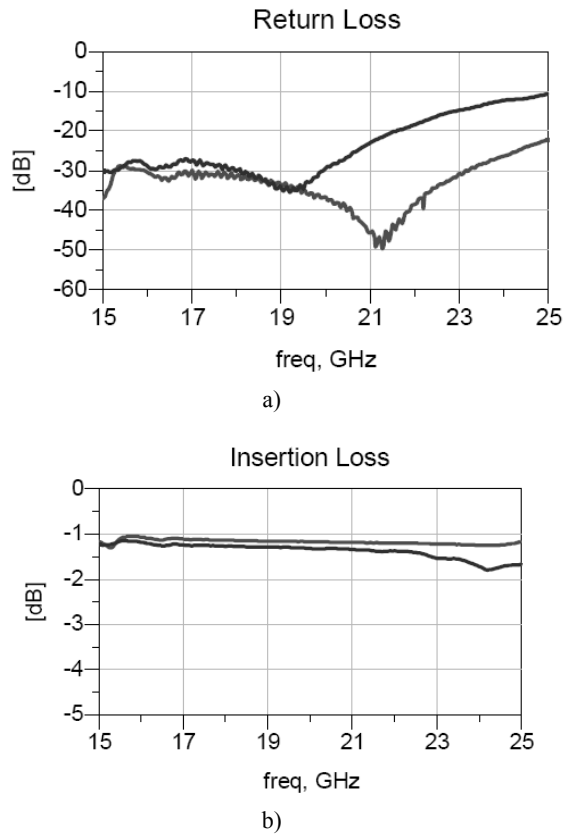


Fig. 4. Measured Return Loss (a) and Insertion Loss (b) of Bit1 in the 15-25 GHz frequency band. Red curve refers to the reference signal line, blue curve to the 180° phase shift path.

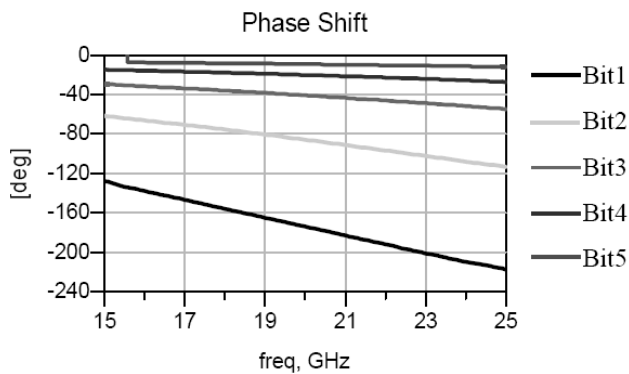


Fig. 5. Measured Phase Shift for all the phase shifter single bits.

The performance of all five bits is summarized in Table 1. Note that Bit 5 is extremely low loss with respect to the others since it does not utilize series ohmic

switches. It is indeed based on loaded line topology and the desired phase shift is provided by the activation of two shunt capacitive switches.

Table 1. Single bit performance @ 20.7 GHz

	Theoretical Phase Shift [degrees]	Measured Phase Shift	Phase Error	Measured Insertion Loss [dB]	Measured Return Loss [dB]
Bit1	180	180,17	0,17	1,18	41,72
Bit2	90	89,52	-0,48	0,95	24,25
Bit3	44,5	42,58	-2,42	1,08	30,62
Bit4	22,25	20,97	-1,53	1,01	23,56
Bit5	11,125	9,56	-1,69	0,15	32,45

2. PACKAGE DESIGN

The 5 bit MEMS phase shifter has been packaged by using a low cost package manufactured at Optoi [8] on Laminate RT Duroid 5880 substrate [9]. Five layers of laminate, 254 μm thick each, have been used to realize the 1-level plastic package. The RF interconnections between the microstrip on the silicon die and the package are made by using 3 parallel wire bondings (25 μm in diameter). L-C matching sections have been designed and patterned in the silicon die as well as in the package side in order to obtain a good matching in a very wide frequency band.

The via-holes transitions needed to bring the RF signal from the intermediate laminate layer into the external bottom surface have been optimized as well. In this way it has been possible to carry all signals, both RF and DC, on the package bottom side allowing for automatic surface mounting.

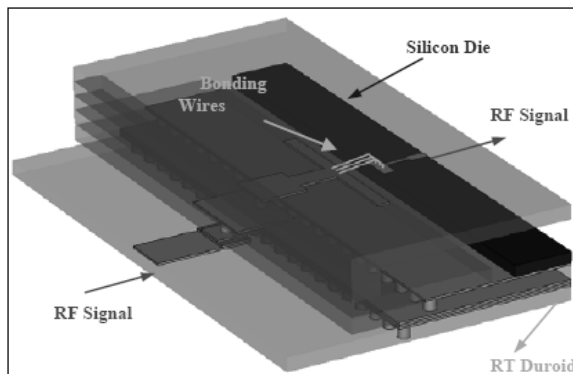


Fig. 6. 3D-Layout of the 1-level plastic package transition.

The 3D layout of the transition is shown in Fig. 6 whereas Fig. 7 presents the corresponding simulated parameters. The simulations were obtained by using the 3D simulator CST Studio [10]. Simulated results show an insertion loss and a return loss better than 0.5 dB and 25 dB, respectively, from DC up to 25 GHz.

The total space occupation of the packaged phase shifter is $16.95 \times 8.40 \times 1.27 \text{ mm}^3$.

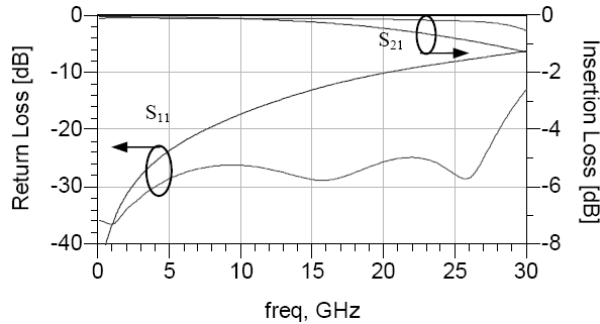


Fig. 7. CST Studio simulations of the package transition. Row transition in blue and compensated one in red.

3. CONCLUSIONS

The design and manufacturing of a novel K-band 5-bit MEMS phase shifter has been presented. The phase shifter has been manufactured on 200 μm thick high resistivity silicon substrate by using the well-established FBK process. The single bits constituting the device have been manufactured and tested in the same wafer. The measurements are in a very good agreement with the full-wave simulations showing high performance in a wide frequency band. All bits are very well matched and the phase error is below 2.5 degrees for all devices. The design of a low cost packaging solution has also been shown. Particular attention was focused on the optimization of the die-package transition in order to preserve the extremely high performance of the device. The on-wafer measurements of the complete 5-bit phase shifter are in progress as well as the testing of the packaged device.

Acknowledgments. The authors would like to acknowledge Optoi [8] who took care of the package manufacturing.

References

- [1] M. KIM, J.B. HACKER, R.E. MIHAILOVICH, and J.F. DeNATALE, *A DC-To-40 Ghz Four-Bit RF MEMS True-Time Delay Network*, IEEE Microwave and Wireless Components Lett., **11**(2), pp. 56–58, Feb. 2001.
- [2] G.L. TAN, R.E. MIHAILOVICH, J.B. HACKER, J.F. DeNATALE, and G.M. REBEIZ, *A Very-Low-Loss 2-Bit X-Band RF MEMS Phase Shifter*, presented at the 2002 IEEE Int. Microwave Symp., Seattle, WA.

- [3] PILLANS, S. ESHELMAN, A. MALCZEWSKI, J. EHMKE, and C. GOLDSMITH, *Ka-Band RF MEMS Phase Shifters*, IEEE Microwave Guided Wave Lett., **9**, pp. 520–522, Dec. 1999.
- [4] J.S. HAYDEN, A. MALCZEWSKI, J. KLEBER, C.L. GOLDSMITH, G.M. REBEIZ, *2 and 4-Bit DC-18 GHz Microstrip MEMS Distributed Phase Shifters*, 2001 IEEE.
- [5] A. OCERA, P. FARINELLI, F. CHERUBINI, P. MEZZANOTTE, R. SORRENTINO, B. MARGESIN, F. GIACOMOZZI, *A MEMS-Reconfigurable Power Divider on High Resistivity Silicon Substrate*, IEEE MTT-S International Microwave Symposium, Honolulu, 3-8 June 2007
- [6] P. FARINELLI, B. MARGESIN, F. GIACOMOZZI, G. MANNOCCHI, S. CATONI, R. MARCELLI, P. MEZZANOTTE, L. VIETZORRECK, F. VITULLI, R. SORRENTINO, F. DEBORGIES, *A Low Contact-Resistance Winged-Bridge RF-MEMS Series Switch for Wide-Band Applications*, Proceedings of the European Microwave Association, **3**, pp: 268–278, Sept. 2007.
- [7] ADS Agilent Momentum www.agilent.com
- [8] xxx www.optoi.com
- [9] Rogers Corporation www.rogerscorporation.com/mwu/pdf/5000data.pdf
- [10] CST Studio www.cst.com

Reconfigurable Three-Dimensional Micromachined Dielectric-Loaded CPW Phase-Shifter

N. SOMJIT, G. STEMME, J. OBERHAMMER

Royal Institute of Technology, Microsystem Technology, Osquldas väg 10, 10044
Stockholm, Sweden

E-mail: {nutapong.somjit, goran.stemme,
joachim.oberhammer}@ee.kth.se

Abstract. In this paper three variations of wideband single-state digital microwave MEMS dielectric-loaded phase shifter based on 3dimensional micromachined coplanar waveguide (CPW) are introduced. By vertically moving a $\lambda/2$ -long dielectric block above CPW with electrostatic actuation, relative phase shift between up and down state is determined. Periodically etched pattern of the dielectric block with three different sizes is introduced for tuning the effective dielectric constant resulting in relative phase shift of 45° , 30° and 15° . The devices are fabricated monolithically using an in-house bulk and surface micromachining process on a high-resistivity silicon substrate (HRSS). Measurement results show that the first prototype of this phase shifter has return and insertion loss better than -10 dB and -1.5 dB, respectively, for frequency range of 10 to 100 GHz with decent linear phase.

1. INTRODUCTION

RF MEMS phase shifters have advantages over the other types of phase shifter such as solid-state and ferrite because of their linear phase, less DC power consumption and suitability for millimeter wave applications. At W-band frequencies distributed MEMS transmission-line (DMTL) phase shifter in [1] have an excellent performance in terms of return and insertion loss. The drawback of this concept is that it is limited to low-power RF signals since high RF power quickly leads to the critical current density in the thin metallic membranes which results in the destruction of the switches [2].

This paper introduces a novel digital high-frequency phase shifter which by its nature has a high power handling capability since no moving metallic membrane is employed resulting in no current density induced during the pull-down

mechanism. The power handling limitation depends; therefore, only on the CPW which can be increased by fabricating thicker t-line.

2. DIELECTRIC-LOADED PHASE SHIFTER

A MEMS electrostatic actuator, vertically moving a $\lambda/2$ -long dielectric block above a 3dimensional micromachined CPW, tunes the propagation constant of the RF signal, resulting in a relative phase shift between the up and down-state shown in Fig. 1.

A trailer-made high-resistivity silicon block is suspended over a 3d micromachined CPW connected to the anchor by four serpentine flexures. The HRSS silicon wafers are use to minimize substrate loss of microwave signal. Length of the dielectric block is selected to be half-wavelength. In this case the reflected electromagnetic (EM) waves from both discontinuous sides of the block are out of phase (180° different) and, thus, cancel each other.

Relative phase shift is obtained by moving the dielectric block over the high-impedance CPW ($>50 \Omega$) resulting in different characteristic impedance of the t-line and propagation constant of the EM waves propagating along the t-line between up and down state. For an example, relative phase shift of 45° is accomplished by vertically moving the dielectric block of $5\text{-}\mu\text{m}$. Periodically etched pattern of the dielectric block with three different sizes is introduced for tuning the effective dielectric constant resulting in relative phase shift of 45° , 30° and 15° . The short circuit of DC-actuation voltage between the dielectric block and the CPW can be prevented by patterning an array of small silicon nitride (Si_3N_4) bumps on the CPW.

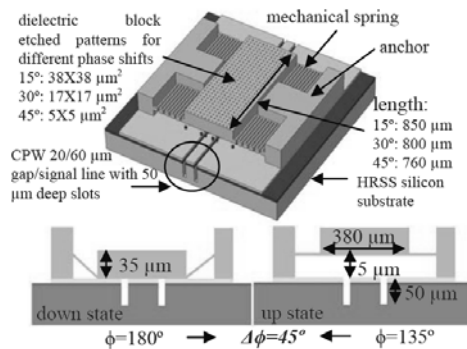


Fig. 1. Single stage phase shifter: cross-section and schematically functional drawing.

3. FABRICATION PROCESS

The process flow for fabricating the dielectric-loaded phase shifter is shown in Fig. 2.

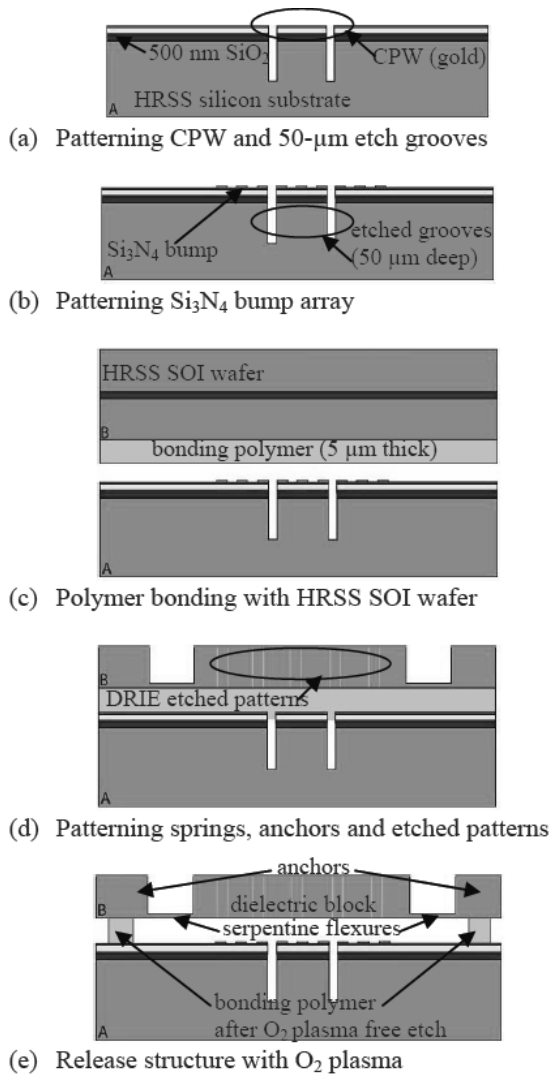


Fig. 2. Process flow.

Fabrication starts with patterning the CPW of 1- μm gold layer with thin adhesive Ti-layer on the high resistivity silicon substrate. Additionally, the gaps of the CPW are etched into the substrate for more sensitivity of the wave propagation to the dielectric block. The small Si_3N_4 bumps are patterned. Subsequently, the patterned silicon wafer is bonded to a high resistivity silicon-on-insulator (SOI) wafer by adhesive polymer bonding. Deep reactive-ion etching (DRIE) steps are performed to create the mechanical springs and dielectric block. The structure is released by standard O_2 plasma process. The phase shift in a single stage can be

determined by artificially tuning the dielectric constant of the silicon block by varying the size of the etch-holes, Fig. 3.

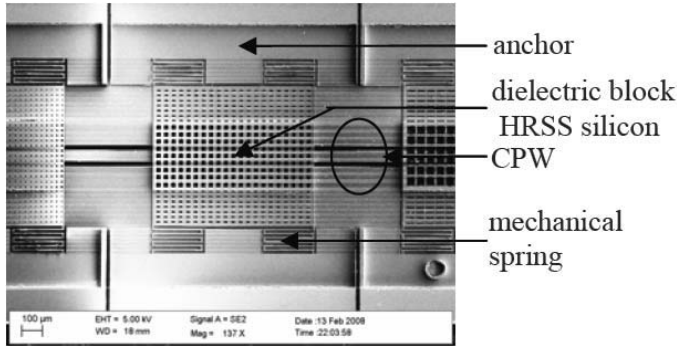


Fig. 3. SEM picture of fabricated 30° stage phase shifter between 45° (left) and 15° (right) stages.

4. MEASUREMENT RESULTS

Fig. 4 represents the return and insertion loss of the dielectric-loaded phase shifter in up and down state, respectively. The measurements show that the return loss is better than -10 dB from 10-100 GHz in both up and down state. The maximum insertion loss is -1.7 dB occurred in the down state position due to the material loss of the silicon substrate which can be improved by selecting low loss material. Fig. 5 shows relative phase shift versus frequency. It is shown that this dielectric phase shifter performs a decent linear phase shift. For loaded t-line length of 760 μm, this phase shifter produces 592° phase shift per cm. Calculating based on the measured insertion loss phase shift of 30°/dB at 77 GHz is obtained. The actuation voltage characterized by the white-light interferometer is 29 V.

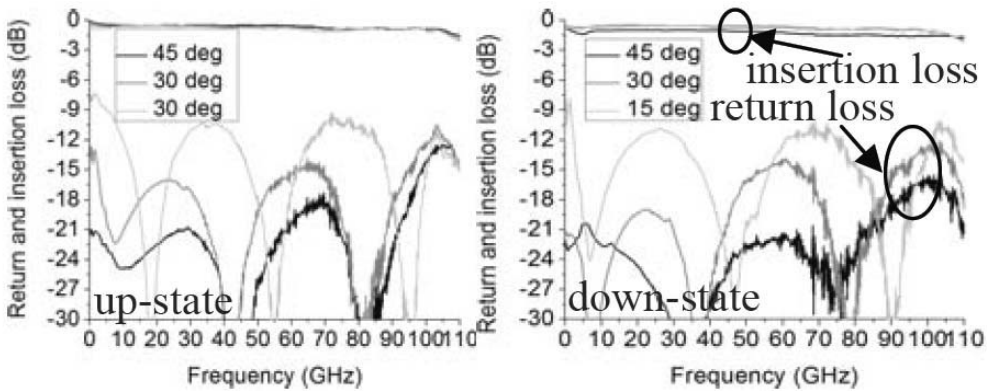


Fig. 4. Return and insertion loss of the 15°, 30° and 45° phase-shifters in up and down state.

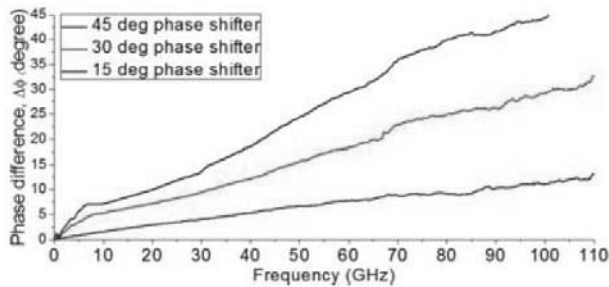


Fig. 5. Phase shifts between the up-state and the down-state for the 15°, 30°, and 45° stages.

2. CONCLUSIONS

The novel phase shifter concept based in dielectric-loaded of the 3d micromachined CPW is introduced. Phase shift can be determined by vertically moving a dielectric block resulting in changing of the propagation constant of the EM wave between up and down state. This kind of phase shifter has RF high-power capability since no thin metallic moving membrane is employed. Therefore, there is no critical current density to be considered when self-actuation occurred. The power limitation can be increased easily by patterning thicker transmission line.

Acknowledgement. This work is part of SARFA project and receives funding through the NORDITE Scandinavian ICT program by Swedish Governmental Agency for Innovation System (VINNOAVA), the Finish Funding Agency for Technology and Innovation (TEKES), and the Research Council of Norway (RCN).

References

- [1] J. HUNG, L. DUSSOPT, G.M. REBEIZ, *Distributed 2- and 3-Bit W-Band MEMS Phase Shifters on Glass Substrate*, IEEE Trans. on Microwave Theory and Techniques, **52**(2), Feb. 2004.
- [2] G.M. REBEIZ, *RF MEMS: Theory, Design, and Technology*, Wiley-Interscience; 1st edition, June 15, 2002.

Compact Reflection-Type RF-MEMS Phase Shifter for Beam-Steerable Reflectarrays

Tatyana PURTOVA¹, Till FEGER¹, Thomas LISEC²,
Bernd WAGNER² and Hermann SCHUMACHER¹

¹University of Ulm, Department of Electron Devices and Circuits,
Albert-Einstein-Allee 45, 89081 Ulm, Germany

²Fraunhofer Institute for Silicon Technology ISiT,
Fraunhoferstraße 1, D-25524 Itzehoe, Germany

Abstract. Design procedure and measurement results of a one-port reflection-type RF-MEMS phase shifter are presented. The circuit was designed for a 26 GHz beam-steerable reflectarray and provides 360 deg phase shift in steps of about 51 deg. The insertion loss at 26 GHz is below 2.5 dB for all 7 states. With the circuit area of about 1×2 mm² the phase shifter is very compact. The phase shifter was fabricated at the Fraunhofer Institute for Silicon technology ISiT (Itzehoe, Germany) using surface micromachining of high-resistivity silicon.

1. INTRODUCTION

Beam-steerable reflectarrays are used in many applications like low orbit communication satellites, automotive radar systems and remote sensing. Among their advantages are low cost, low mass and improved radiation efficiency as compared to phased array antennas or reflectors. Higher radiation efficiency of reflectarrays is mainly due to direct feeding from radiating apertures and not through a separate feeding network, being a significant source of losses in other types of antennas.

Either varactor diodes or MEMS devices can be used to steer the beam in different directions. Here we wish to explore a MEMS-based controlling network, having a potential for very low loss and high linearity. Generally, MEMS reflectarrays can be divided into two groups – 1) with MEMS-tunable load being integrated into the radiating elements itself [1]-[3] 2) with MEMS load being physically separated from the radiating elements [4]-[5].

The purpose of this work is to design a MEMS phase shifter to be used in a reflectarray from [5]. It is a microstrip patch reflectarray, which is slot-coupled to a tunable coplanar load. One segment of the array is shown in Fig. 1. As illustrated, the patches are located on one side of the wafer and the MEMS-tunable loads – on the other and the whole system is fabricated on a single high-resistivity silicon wafer processed from both sides. As it can be seen in Fig. 1, the incoming wave will be reflected by the phase shifter with a particular phase delay depending on the phase shifter state. The desired radiation pattern is formed by providing proper phase distribution at the individual patches across the reflectarray.

Thus a phase shifter with a high resolution and low loss is required. Besides, it should be small enough to fit onto one unit cell, whose dimensions are limited by half a wavelength in free space at the operation frequency (26 GHz).

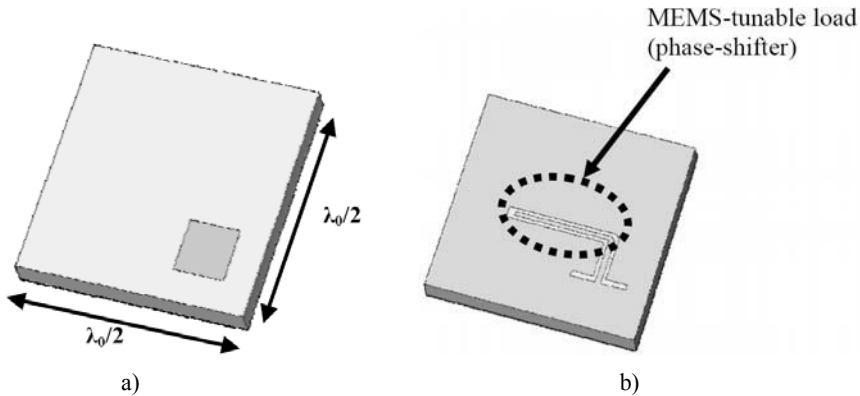


Fig. 1. Unit cell of the MEMS-steerable reflectarray. Microstrip patches are fabricated on one side of the wafer (a) and MEMS-tunable coplanar load on the other (b).

Generally, MEMS phase shifters can be realized as distributed MEMS transmission lines (DMTL), switched delay lines or reflection-type topologies. Owing to the tight space constraints, only the reflection-type phase shifter is feasible and is considered in the following.

2. TECHNOLOGY

The phase shifter was fabricated at the Fraunhofer Institute for Silicon Technology ISiT (Itzehoe, Germany) by means of surface micromachining of high-resistivity Silicon ($\rho > 3\text{k}\Omega\text{cm}$, $508\ \mu\text{m}$) covered with $2\ \mu\text{m}$ of SiO_2 . The fabrication process employs seven masks, including thin metallisation for the under-path layer, two dielectric layers ($300\ \text{nm}$ AlN with $\epsilon_r = 10$ and $300\ \text{nm}$ SiN with $\epsilon_r = 7.5$), sacrificial layer for the air-gap ($2.7\ \mu\text{m}$), MEMS membrane metallisation, electroplated gold for transmission lines and antenna patches ($3\ \mu\text{m}$) and thick Ni for MEMS springs and supports.

3. EQUIVALENT CIRCUIT ADN MODELLING

A. RF MEMS Switch Design

Fig. 2 shows the microphotograph and the cross-sectional view of the shunt capacitive MEMS switch designed for the phase shifter. The coplanar line is covered with a 300 nm layer of AlN ($\epsilon_r=10$); the air-gap in the bridge's up-state is about 2.7 μm .

Depending on the biasing scheme the MEMS bridge can either be grounded, i.e. connected to coplanar line grounds, or floating. Since in this design individual MEMS switches must be controlled independently, using grounded membranes would require either DC-blocking capacitors or separate actuation electrodes. In case of floating membranes, which were used here, these measures are not needed since the actuation signal is applied directly to the MEMS bridge. Moreover, the actuation voltage is lower compared to a grounded-membrane case, since the actuation area is realized using both CPW centre conductor and grounds.

The switched MEMS capacitance is formed by a series connection of C_{signal} and two C_{GND} , which are capacitances between the MEMS bridge and CPW centre conductor and grounds respectively. The series connection reduces the overall MEMS capacitance as compared to a grounded-membrane, there only C_{signal} is present. This is advantageous for the up-state capacitance, since a low C_{up} is desired for better resolution of the phase shifter (see equation (1)). However, in the down-state a high capacitance is required to provide a short-circuit at the operation frequency (26 GHz). By making the ground areas large enough the reduction of the overall capacitance due to two C_{GND} is minimized.

B. Phase Shifter Design

The microphotograph of the phase shifter is shown in Fig. 4. It consists of a coplanar line, loaded with six shunt capacitive MEMS switches. The phase shifter unit cell is formed by a piece of coplanar line of length l and a MEMS switch and is modelled as illustrated in Fig. 4. One end of the coplanar line is used as RF input and output and the other end is short-circuited. Actuating either of the switches creates an RF-short-circuit to ground at different locations along the coplanar line. The input signal travels till the location of the short-circuit, gets reflected there and travels back to the output. When none of the switches is actuated, the signal will be reflected at the short-circuited end of the coplanar line. Thus the necessary physical length of the phase shifter corresponds to one half of the electrical length required for a particular phase delay. Since the phase shifter is intended to be used in a reflectarray, it is a one-port device sharing the same input and output. This eliminates any couplers required in case of two-port circuits, making the phase shifter very compact.

The resolution of the phase shifter, i.e. the minimum phase shift increment, is given by (1): Bias line MEMS Bridge Fig. 2 Microphotograph and a cross-section of the MEMS bridge used in the phase shifter.

$$\varphi = 2\beta s = 2 \frac{\omega}{V_{ph}} s = 2\omega \sqrt{L' \left(C' + \frac{C_{up}}{s} \right)} s \tag{1}$$

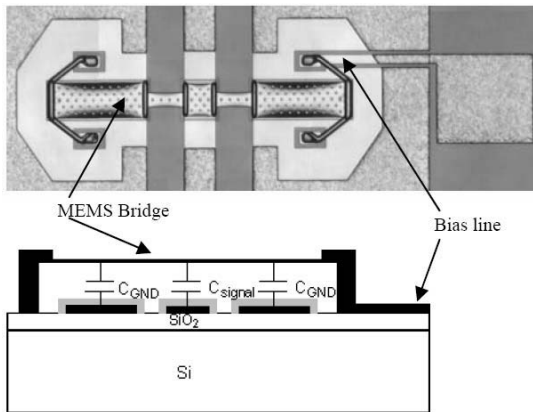


Fig. 2. Microphotograph and a cross-section of the MEMS bridge used in the phase shifter.

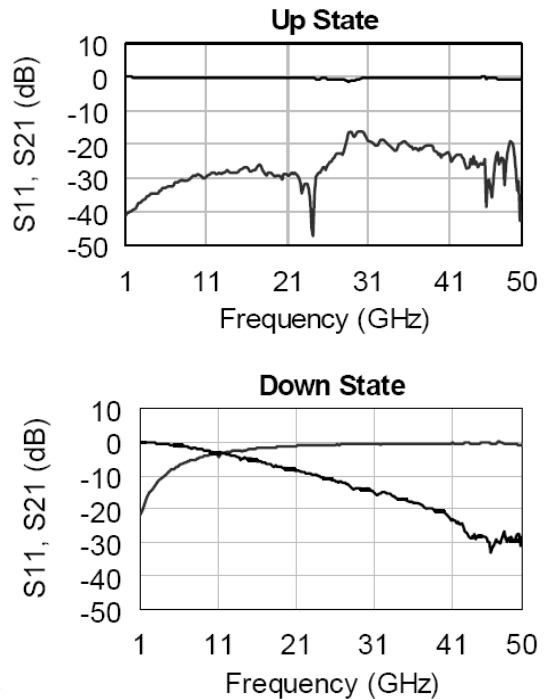


Fig. 3. Measured performance of a single MEMS switch in the up- and down states. The pull-down voltage is about 37 V and the measurements were taken at 45 V.

where β is the phase constant, s is the spacing between neighbouring switches, V_{ph} – phase velocity, L' and C' – distributed inductance and capacitance of the unloaded coplanar line and C_{up} is the MEMS's up-state capacitance. The factor of 2 in (1) takes into account that the signal will travel back and forth, thus twice the distance between the neighbouring switches s .

For maximum resolution the spacing s and the up-state capacitance C_{up} should be minimized. The spacing is set to the minimum value of 262 μm given by the technological constrains. So the choice of the up-state capacitance is the most important for the design. Since the ratio of up- and down-state capacitances is fixed, reducing up-state capacitance simultaneously lowers the down-state capacitance, which may not provide a short-circuit at 26 GHz. For narrow-band applications the reduction in the down-state capacitance can be somewhat compensated by increasing the switch's inductance. This lowers its resonance frequency and increases the isolation at lower frequencies.

With the help of EM-simulations an optimum MEMS membrane geometry was found, which can be seen in microphotographs in Fig. 2 and Fig. 4. The measured performance of the MEMS switch is shown in Fig. 3. The pull-down voltage is about 37 V and all measurements were taken at 45 V. Measured up- and down-state capacitances equal 30 fF and 550 fF respectively. To improve the isolation at 26 GHz, a relatively low down-state capacitance is compensated by an increased MEMS inductance provided by narrow regions of the membrane above CPW gaps ($L_{MEMS}=17$ pH). It is not possible to further decrease the up-state capacitance since then the down-state capacitance is becoming unacceptably low.

With $s=262$ μm and $C_{up}=30$ fF, one phase shift segment results in a phase shift of about 51 degrees at 26 GHz. Thus 360 degrees are covered in seven states provided by six MEMS switches and the short-circuited end of the coplanar line. The resulting reflection-type phase shifter is very compact with an area of about 1×2 mm².

4. PHASE SHIFTER MEASUREMENT RESULTS

Fig. 5 illustrates the phase shift at 26 GHz versus the phase shifter state. 360 deg are covered in seven steps of about 51 deg. A comparison with a linear function indicates a maximum phase error of about 18 deg. There can be two reasons responsible for phase variations. First of all, there can be slight variations in the up-state capacitances of individual MEMS switches owing to stresses developed in membranes during fabrication. This may cause some membrane deformations and lead to a small differences of the up-state capacitances of the neighbouring switches. Besides, phase errors can be introduced if the down-state capacitances of individual switches are not exactly the same and thus reflect the signal with a slightly different phase. Variations in the down-state capacitances are again caused by slight membrane deformation in the fabrication.

As it can be seen from Fig. 6, the phase shifter’s loss at 26 GHz is below 2.5 dB for all states and stays almost constant up to 45 GHz. As frequency increases, the MEMS bridge approaches an ideal short circuit in the down-state and reflects the signal more effectively. On the other hand at frequencies below 20 GHz the down-state capacitance is not high enough to reflect the signal. The signal passes through the switch and travels along the short-circuited coplanar line with a significantly reduced phase velocity due to high loading of the down-state capacitance. Thus the structure is operated closely to the Bragg reflection frequency, leading to high attenuation of the signal at low frequencies.

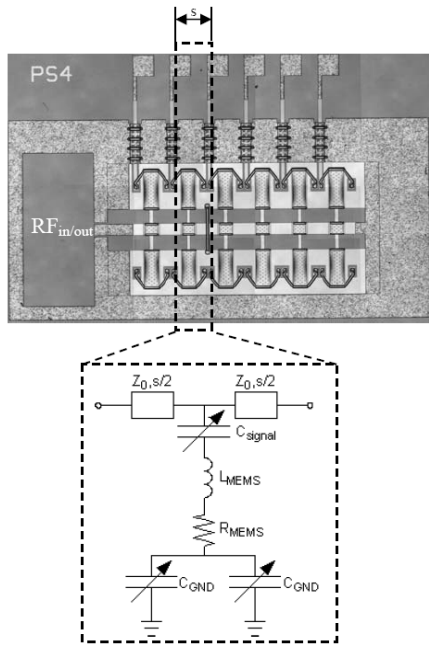


Fig. 4. Microphotograph of the phase shifter and the equivalent circuit of a unit cell.

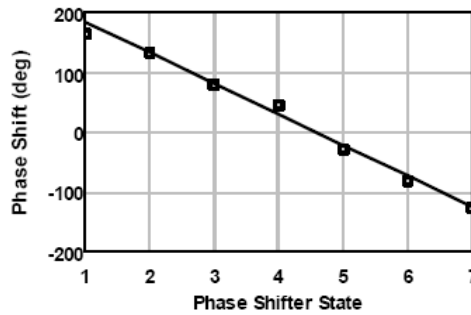


Fig. 5. Measured phase shift versus phase shifter state at 26GHz and comparison to a linear function. 360 deg are covered in seven steps of about 51 deg.

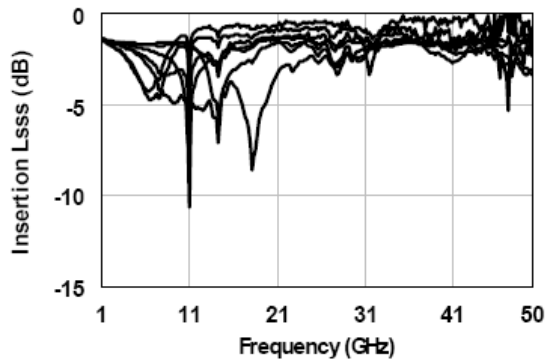


Fig. 6. Measured phase shifter insertion loss versus frequency for all seven states.

5. CONCLUSION

The reflection-type phase shifter was designed which covers 360 deg in steps of about 51 deg at 26 GHz. The phase shifter loss is below 2.5 dB in all seven states. The maximum phase error is 18 deg. The reflection-type topology was chosen due to its compact sizes, which is the main limitation for integration of MEMS-tunable load onto a reflectarray. The shunt capacitive MEMS switch with biased membrane was selected due to a simple biasing circuitry and lowest actuation voltage. The shape of the MEMS membrane was optimized for the 26 GHz operation by locally narrowing the membrane to increase its inductance and reduce the resonance frequency, thus improve the isolation at 26 GHz.

Acknowledgement. This work was supported by the European Network of Excellence AMICOM and was carried out as a part of a North-Star Project RARPA. For more information please see www.amicom.info. The authors wish to acknowledge valuable discussions on the reflectarray requirements with Luca Marcaccioli, Paola Farinelli and Benedetta Mencagli from the University of Perugia, Department of Information and Electronic Engineering, Italy.

References

- [1] J.H. SCHAFFNER, D.F. SIEVENPIPER, R.Y. LOO, J.J. LEE, S.W.L. RAYTHEON, *A Wideband Beam Switching Antenna Using RF MEMS Switches*, Special Session SS-3 MEMS for Antenna Applications, 2001.
- [2] H. LEGAY; B. PINTE; M CHARRIER; A. ZIAEI; E. GIRARD; R. GILLARD, *A Steerable Reflectarray Antenna With MEMS Controls*, Phased Array Systems and Technology, 2003, IEEE International Symposium, pp. 494–499, 14-17 October 2003.

- [3] J. HUANG, R.J. POGORZELSKI, *A Ka-Band Microstrip Reflectarray With Elements Having Variable Rotation Angles*, *Antennas and Propagation*, IEEE Transactions, **46**(5), pp. 650–656, May 1998.
- [4] B. MENCAGLI, R. VINCENTI GATTI, L. MARCACCIOLI, R. SORRENTINO, *Design of Large mm-Wave Beam Scanning Reflectarrays*, 35th EuMC, Paris 3-7 Oct. 2005.
- [5] L. MARCACCIOLI, B. MENCAGLI, R. VINCENTI GATTI, T. FEGER, T. PURTOVA, H. SCHUMACHER AND R. SORRENTINO, *Beam Steering MEMS mm-Wave Reflectarray*, MEMSWAVE2006, Orvieto, 27-30 June 2006.

Low-Loss DMTL Phase Shifter Based on Fast Miniature RF MEMS Switched Capacitors

B. LACROIX, A. POTHIER, A. CRUNTEANU, P. BLONDY

XLIM UMR 6172, Université de Limoges / CNRS, 123 avenue Albert Thomas,
87060 Limoges Cedex, France

Abstract. This paper presents fast miniature RF MEMS switched capacitors used to design and fabricate 90 and 180 degree DMTL phase shifters operating at 20 GHz. The capacitors are only $40 \times 40 \mu\text{m}^2$ and $0.35 \mu\text{m}$ thick and are actuated with a 24 V monopolar bias voltage. Minimum measured switching time is around $1 \mu\text{s}$. Both 90 and 180 degree sections are respectively less than 4.5 and 8.5 mm long. Measured insertion loss is 90°/dB for both sections, and return loss is better than -13 dB and -11 dB. This work presents an improvement in fast reconfigurable network designs based on miniature RF MEMS components.

1. INTRODUCTION

The interest in miniaturizing RF MEMS switches or switched capacitors is justified by the need to improve RF MEMS reliability and switching times in order to design low-loss fast reconfigurable networks based on RF MEMS. Implementing such components to devices as smart antennas or phase shifters reduces loss compared to semiconductor components. Miniature RF MEMS capacitors have recently demonstrated fast switching times [1-2], high pull-up pressure, and are less sensitive than standard RF MEMS to temperature variation and dielectric charging effects.

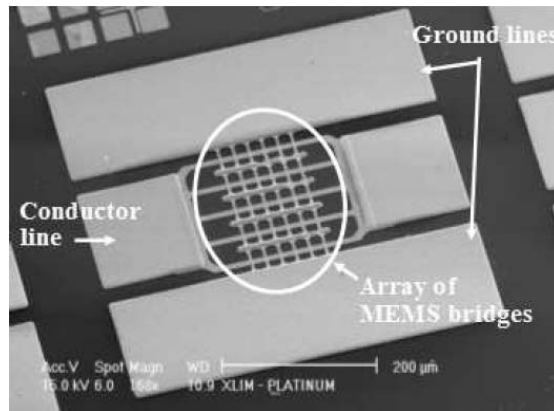
Distributed MEMS Transmission Lines have been widely developed in the past few years for matching networks [3], tunable filters [4] or phase shifters [5-6]. DMTL phase shifters fabricated on a coplanar waveguide often use long bridges suspended above the central conductor line and linking both ground planes. When they actuate, these bridges reduce the line impedance and the wave is slowed down. One way to reduce operation times is to use miniature RF MEMS.

This paper presents a novel DMTL phase shifter design based on fast miniature RF MEMS capacitors with a Con/Coff ratio of 3.1, and designed to provide a 15 degree phase shift per unit cell at 20 GHz. Although capacitors can

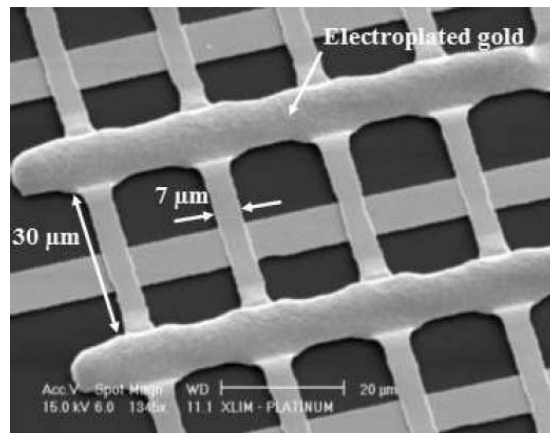
actuate using a 24 V monopolar bias voltage, a 40 V voltage is required to achieve switching times as low as 1 μ s. 90 and 180 degree phase shift sections have been fabricated. Measured insertion loss and return loss are presented here for both sections.

2. SWITCHING TIMES AND MINIATURE RF MEMS CAPACITORS

Miniature RF MEMS switches or capacitors can be fabricated and implemented as arrays to operate with high capacitance values. The SEM picture presented in Fig. 1 shows an array of 30 miniature RF MEMS bridges over a coplanar waveguide. These bridges are only 30 μ m long and 7 μ m wide.



a)



b)

Fig. 1. (a) Miniature RF MEMS array and (b) close-up on miniature bridges.

The miniaturizing effects on switching speed have been previously demonstrated by [1]. Switching times are given by Eq. 1 [7] :

$$t_s \approx 3.67 \frac{V_p}{V_a 2\pi f_0} \tag{1}$$

The applied bias voltage V_s is generally 1,2-2 higher than the pull-in voltage V_p to ensure the bridge actuation. The mechanical resonance frequency is higher for short beams since the spring constant k is more important in this case. The switching time is independent of the beam width w since $\omega_0=(k/m_e)^{1/2}$, and the effective mass m_e and the spring constant k are linearly dependent of w . Fig. 2 presents computed switching times for different lengths of 0.35 μm thick bridges, for a 10 MPa tensile stress, and for $V_s = 1.5 V_p$, where the contact electrode width is twice narrow than the bridge length.

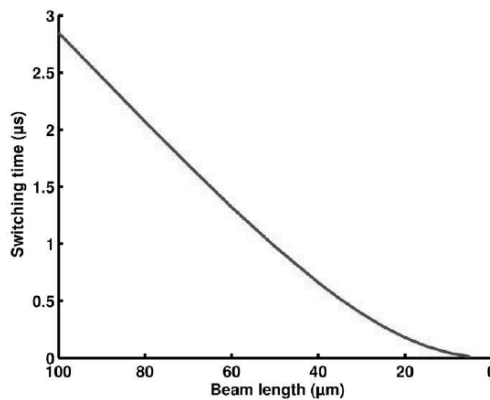


Fig. 2. Switching time as a function of beam length.

Although short beams ensure fast switching times, they require high actuation voltages to be actuated. The pull-in voltage is computed using Eq. 2 [7], where g_0 is the 1 μm gap, ϵ_0 is the dielectric constant of the air, and w and w_{el} are respectively the bridge and the contact electrode widths. As the switching time t_s , the pull-in voltage is also independent of the width electrode since k is linearly dependent of w . Fig. 3 shows the computed pull-in voltages as a function of beam length.

$$V_p = \sqrt{\frac{8k \cdot g_0}{27 \times \epsilon_0 w w_{el}}} \tag{2}$$

40 μm long bridges have been chosen here to design fast DMTL phase shifters since they are a good compromise between actuation voltage and fast switching speed.

3. DESIGN OF THE UNIT CELL

A unit cell has been designed with 40 μm long capacitors. A novel topology has been used since these bridges are not long enough to link both ground lines. The unit cell is obtained with two bridges implemented on each ground line, and contacting the central conductor line when a bias voltage is applied. Indeed, at the middle of the unit cell, two electrodes (one at each side of the central conductor line) are used as bias electrodes in order to actuate the bridges. Fig. 4 presents a photograph of this unit cell and a cross-view section of the designed miniature RF MEMS capacitors.

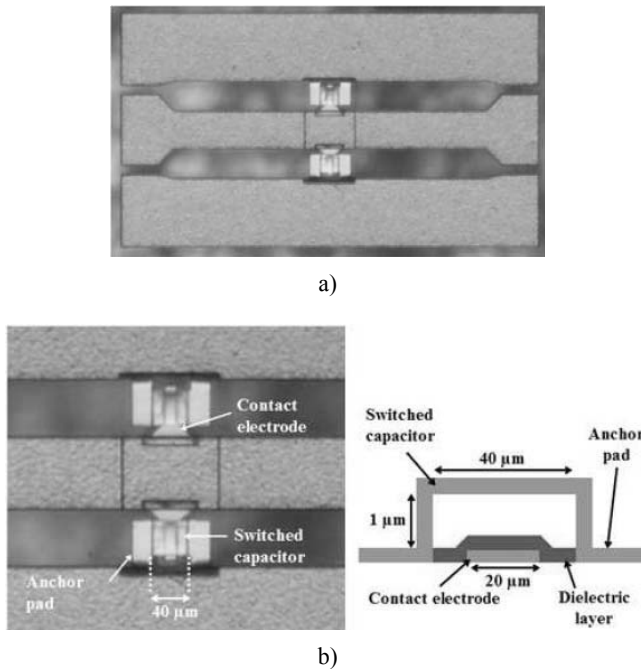


Fig. 4. (a) Photograph of a unit cell. (b) Close-up and crossview section of the miniature switched capacitor.

Both 90 and 180 degree sections have been designed to operate at 20 GHz, following existing design methodology [5]. Return loss is desired to be less than -15 dB and the Bragg frequency is chosen to be only 46 GHz to ensure the capacitance values at both up- and down- states, resulting in a 15 degree phase shift per unit cell. The length s of a unit cell (spacing between couple of bridges) is 660 μm , found using Eq. 3.

$$s = \frac{Z_d c}{\pi f_B Z_0 \sqrt{\epsilon_{eff}}} \quad (3)$$

Z_d is the loaded-line impedance at down-state position, c is the speed of light in vacuum, f_B is the Bragg frequency, and ϵ_{eff} is the effective dielectric constant (2.39 for quartz substrate). The characteristic impedance Z_0 of the unloaded line, also chosen by the designer, is 85Ω .

The capacitance values at the up- and down states are respectively 40.7 fF and 126 fF.

IV. FABRICATION

Fig. 5 shows the fabrication process of a unit cell for the designed phase shifters. The coplanar waveguide line is built on a $525 \mu\text{m}$ thick quartz substrate ($\epsilon_r=3.78$, $\tan \delta=0.0009$). The CPW line width and gap are respectively $W=80 \mu\text{m}$ and $G=60 \mu\text{m}$ to obtain the desired 85Ω characteristic impedance. A first gold deposition is patterned for both signal line fingers, linked together. The second step consists in depositing and patterning a 400 nm dielectric layer (Al_2O_3) to create a capacitive contact with the bridges. The same mask is used to pattern the $1 \mu\text{m}$ sacrificial layer. Then, the CPW lines and the bridges are made by depositing the same 350 nm gold layer by thermal evaporation. Thus, the contact gold electrodes are connected to the CPW line. The transmission line and the ground planes are electroplated with $1 \mu\text{m}$ gold. Finally, the bridges are released and are dried in a carbon dioxide critical point dryer. The fixed-fixed beams are suspended $1 \mu\text{m}$ above the conductor line and are only $40 \times 40 \mu\text{m}^2$ by $0.35 \mu\text{m}$ thick.

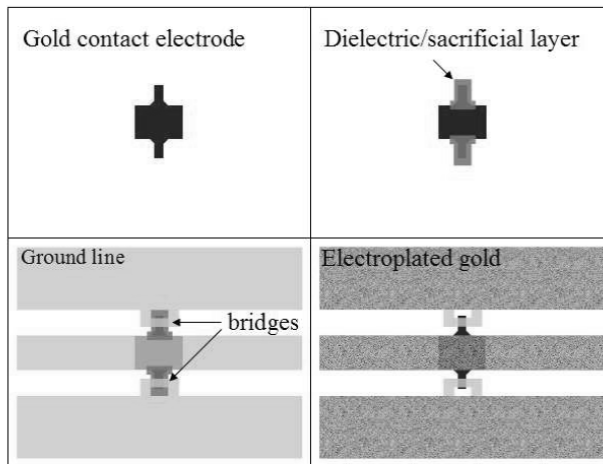


Fig. 5. Fabrication process of a unit cell with miniature RF MEMS bridges.

5. SWITCHING TIME MEASUREMENTS

Switching times have been measured for this unit cell with $40 \mu\text{m}$ long bridges using techniques previously shown in [8]. A continuous wave signal is

applied to the component and is modulated when the bridges actuate. The RF signal modulation is detected since the impedance decreases at the down-state. A 24 V pull-in voltage has been measured, but bridges are here actuated at 40 V to increase the reconfiguration speed. Fig. 6 presents the measured output signal variation that represents the reconfiguration speed of the unit cell. The estimated measured switching time is 1.2 μs .

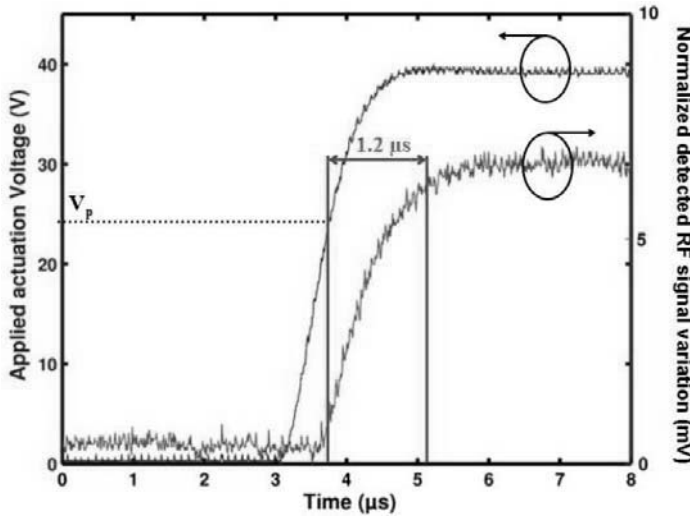


Fig. 6. Measured switching time for a unit cell.

6. PHASE SHIFT SECTIONS AND RF MEASUREMENTS

90 and 180 degree sections are easily achieved by cascading 6 and 12 unit cells. A 90 degree section is presented on Fig. 7. 50 Ω tapers are used at both terminations for probe pad measurements. Bias voltage is applied on the central conductor line. Return loss and insertion loss of both sections have been measured at both states using a Single-Open-Load-Thru calibrated HP 8722ES network analyzer. Results are presented Fig. 8. Return loss is respectively better than -11 dB and -13 dB for 90 and 180 degree phase shift sections. Insertion loss is around 90°/dB for both sections. 95.3 and 173.5 degree phase shifts have also been respectively measured at 20 GHz for the 6-cell and 12-cell phase shifters.

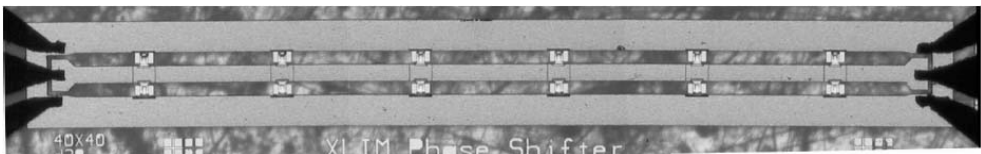


Fig. 7. Photograph of the 90 degree phase shift section.

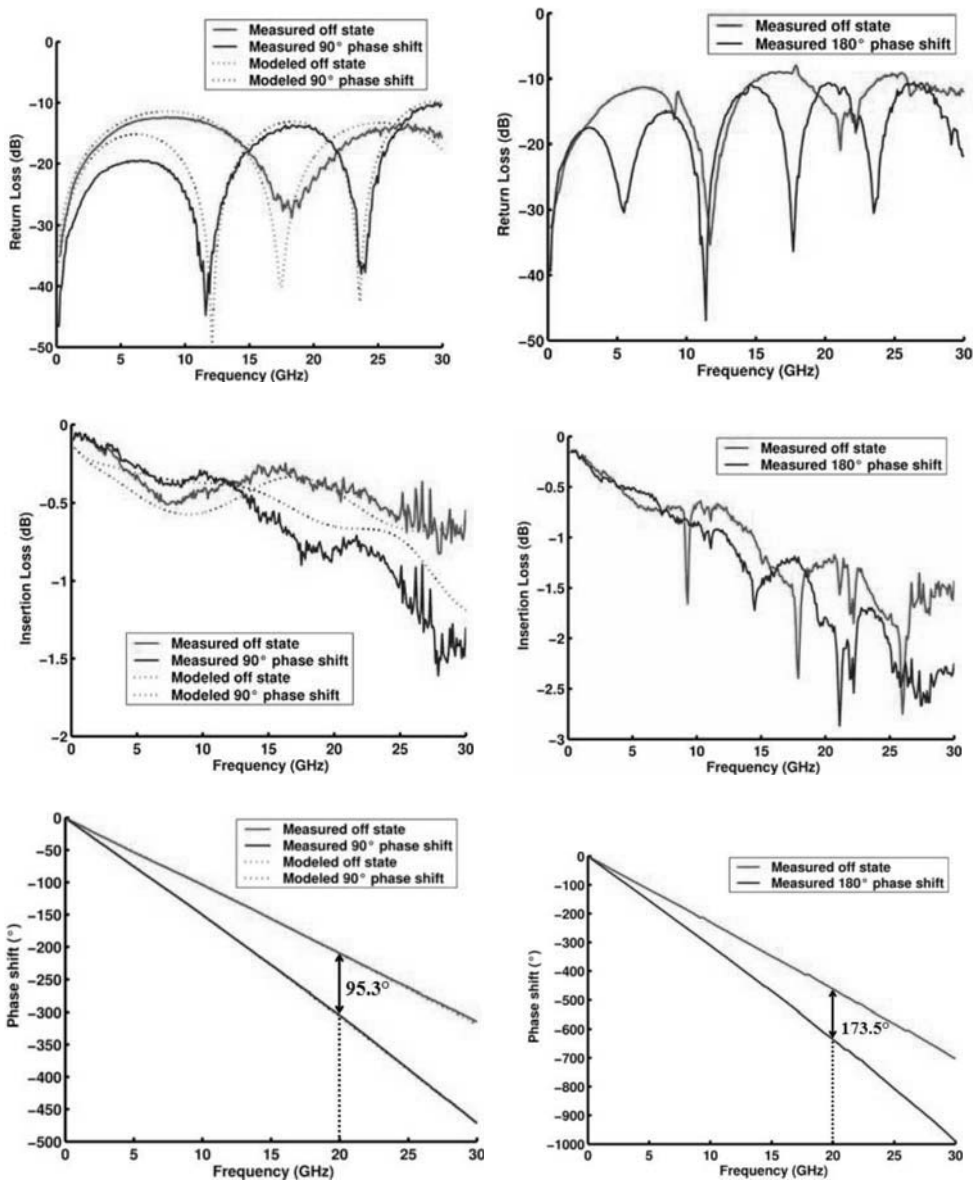


Fig. 8. Measured return loss, insertion loss and phase shift at off- and on- states for 90 and 180 degree phase shifters.

7. CONCLUSION

Low-loss DMTL phase shifters based on miniature RF MEMS capacitors have been designed and fabricated. Return loss better than -13 dB and -11 dB has been measured for two 90 and 180 degree sections respectively. Insertion loss

better than 90 degrees per dB has also been measured. These phase shifters can change the phase velocity in 1.2 μs applying a 40 V bias voltage. This work demonstrates the feasibility in fabricating lowloss and fast reconfigurable devices using miniature RF MEMS switched capacitors.

References

- [1] B. LACROIX, *et al.*, *Sub-microsecond RF MEMS Switched Capacitors*, IEEE Trans. On Microwave Theory and Techniques, **55**, pp. 1314–1321, June 2007.
- [2] B. LAKSHMINARAYANAN and G.M. REBEIZ, *High-Power High-Reliability Sub-Microsecond RF MEMS Switched Capacitors*, IEEE MTT-S International Symposium Digest, pp. 1801–1804, June 2007.
- [3] Y. LIU, A. NAGRA, and R.A. YORK, *Distributed MEMS Transmission Lines for Tunable Filter Applications*, Int. J. RF Microwave CAE, **11**, pp. 254–260, August 2001.
- [4] S. QIN and N. S. BARKER, *Distributed MEMS Tunable Matching Network Using Minimal-Contact RF-MEMS Varactors*, IEEE Trans. On Microwave Theory and Techniques, **54**, pp. 2646–2658, Jun 2006.
- [5] N.S. BARKER and G.M. REBEIZ, *Distributed MEMS True-Time Delay Phase Shifters and Wide-Band Switches*, IEEE Trans. On Microwave Theory and Techniques, **46**, pp. 1881–1890, November 1998.
- [6] G.M. REBEIZ, *et al.*, *RF MEMS Phase Shifters: Design and Applications*, IEEE Microwave Magazine, **3**, pp. 72–81, June 2002.
- [7] G.M. REBEIZ, *RF MEMS Theory, Design, and Applications*, J. Wiley & Sons, 2003.
- [8] D. MERCIER, A. POTHIER, and P. BLONDY, *Monitoring Mechanical Characteristics of MEMS Switches With A Microwave Test Bench*, 4th round table on micro and nano technologies for space, June 2003.

A Single-Pole-Double-Throw Switch Based on Capacitive-Anchored MEMS

David GIRBAU¹, Marco Antonio LLAMAS², Antonio LÁZARO¹,
Lluís PRADELL², Jaume PRADA², Pierre CALMON³,
Patrick PONS³, Robert PLANA³

¹Automatics, Electronics and Electrical Department (DEEEA), Universitat Rovira i Virgili (URV), Av. Països Catalans 26, 43007 Tarragona, Spain

²Signal Theory and Communications Department (TSC), Universitat Politècnica de Catalunya (UPC), C/Jordi Girona 1-3, 08034 Barcelona, Spain

³LAAS-CNRS, University of Toulouse, 7 avenue Roche, 31077 Toulouse cedex 4, France

Abstract. In this paper, a $0^\circ/180^\circ$ phase switch structure for pseudo-correlation radiometers in space missions is proposed. The structure is composed by two networks with same circuit parameters except the transmission phase, shifted by 180° . Switching between networks is performed using Single-Pole-Double-Throw (SPDT) switches based on capacitive-anchored MEMS developed for this purpose in a joint collaboration project between UPC, URV and LAAS-CNRS and fabricated in LAAS-CNRS. The SPDT exhibits isolation better than 30 dB at the design frequency (24 GHz)

1. INTRODUCTION

Pseudo-correlation radiometers for mm-wave space applications require switching between two phase states (0° and 180°) at a given rate (some hundreds of Hz to few KHz). So far this has been done using HEMT or PIN diode switches.

A wideband 180° phase shifter has been proposed in [1]. It consists of switching between two networks that are equivalent for all frequencies except in that the transmission phase difference between the two circuits is exactly 180° . In this topology two SPDT (Single-Pole-Double-Throw), one at the input and the other at the output, are used in order to select between the two networks. The SPDT switching element is implemented with solid-state device technology (FET).

This paper proposes the integration of MEMS switches in a Single-Pole Double-Throw (SPDT) structure to be used in a K-band $0^\circ/180^\circ$ phase switch for the above application. MEMS-based SPDTs feature low power consumption, are

compact and do not require a matching network, as demonstrated in [2-4]. Here, an important issue is the MEMS switching speed, which is addressed in the MEMS switch mechanical design in order to have a mechanical resonance frequency well above the phase switch switching speed. Finally, since the RF signals in radiometer front-ends have small amplitude, no problems concerning RF power handling will be experienced in the MEMS device.

2. SINGLE-POLE-DOUBLE-THROW SWITCH DESIGN

A. Phase Switch Topology and SPDT Requirements

The phase switch topology where the MEMS-based SPDTs are to be integrated is shown in Fig. 1. It consists of two networks (a A network and a coupled-lines network) that are equivalent for all frequencies with the exception of the transmission phase, i.e. the phase shift between the two circuits is exactly 180° [1]. The SPDT structure here proposed performs switching between both networks with bandpass behaviour. Since the RF lines are DC grounded, no DC voltage can be applied to the lines in order to actuate the MEMS switches. Moreover, since all the switches are on the same RF path (CPW line), a mechanism to guarantee independent actuation is required. Finally, the suspended structures should not be large in order to have mechanical resonance frequencies as high as possible. The SPDT presented in next subsection has been designed to fulfil the above requirements.

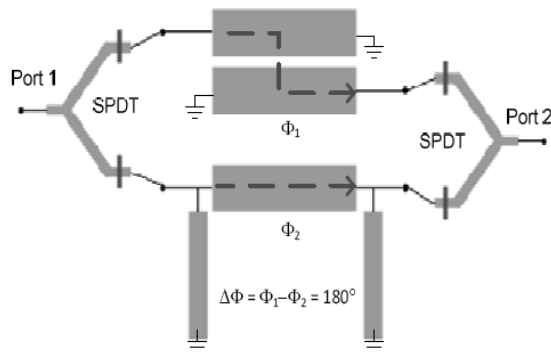


Fig. 1. Structure of the phase switch circuit as proposed in [1], in which the signal is routed either to a A network or a coupled lines network.

B. Capacitive-Anchored MEMS Design

Since switching speed is a critical issue, no external electrodes have been used [5], which would decrease its mechanical bandwidth. Capacitive MEMS switches are used. Since RF lines are DC-grounded, the membranes cannot be directly anchored (resistive contact) to the CPW ground planes but a capacitive

anchor is used for DC isolation. This method will also guarantee independent actuation. For this purpose a new adhesion layer has been introduced to design a MIM structure using the available SiNx layer (same as the one used in the capacitive contacts). This structure is also used in the bias lines. A schematic view of the proposed switch topology and its equivalent model (where losses have been neglected) are presented in Fig. 2.

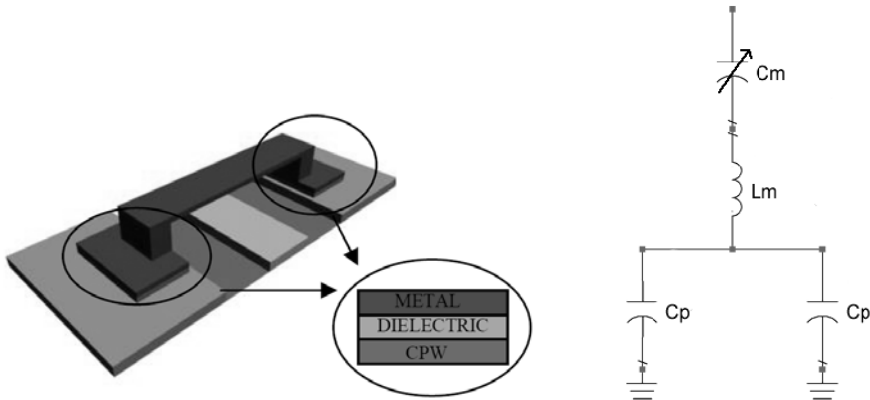


Fig. 2. Capacitive MEMS switch, with capacitive-anchor to the CPW ground planes and its equivalent model.

From the equivalent circuit proposed in Fig. 1 the following resonant frequency can be extracted:

$$f_r = \frac{1}{2\pi \sqrt{L_m \left(\frac{2C_m C_p}{C_m + 2C_p} \right)}} \tag{1}$$

From (1), the initial dimensions are obtained which will be optimised by electromagnetic simulation. Two criteria have been followed to design C_p :

1) to have a small impedance at the working frequency in order to present a good short circuit.

2) to have a small effect on f_r . To this end, the area of the anchors has been designed large enough to guarantee $C_p \gg C_m$. In consequence, at the design frequency, f_r can be controlled with C_m , identically to resistive-anchored capacitive switches.

The bridge dimensions are properly chosen in order to have a mechanical resonance frequency as high as possible. Fig. 3 shows a photograph of the proposed capacitive MEMS switch (capacitive-anchored). It can be observed that the capacitive anchor extends to the DC polarization pads isolated from the CPW

ground plane. Two mask levels are defined in the process for CPW pattern for planarization purposes on the MEMS contact area.

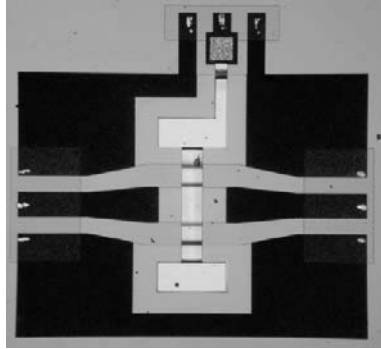


Fig. 3. Photograph of single capacitive MEMS (capacitive-anchored).

Fig. 4 shows a comparison between simulation (EMDS) and measured results of single capacitive MEMS (capacitive-anchored).

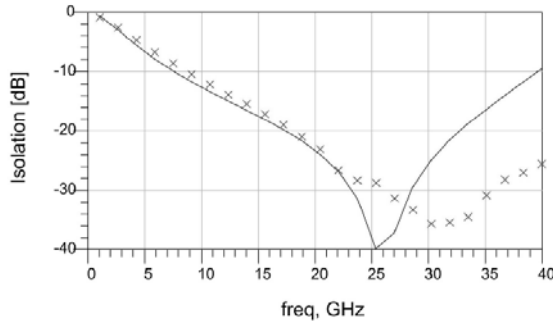


Fig. 4. Simulated and measured isolation of single capacitive MEMS (capacitive-anchored) (simulated and xxx measured).

The measured isolation shows wideband behaviour, better than 30 dB in the frequency range 26-36 GHz. The observed deviation of the resonance frequency between simulation and measurement results is attributed to the fact that the simulated effective capacitive contact area is quite different compared to the real contact area, mainly due to metal and dielectric roughness.

C. SPDT Design

The SPDT is based on two capacitive MEMS switches such as described in Subsection II.B, with capacitive anchor, placed at a $F/4$ distance from the T plane and independently actuated (see Fig. 5).

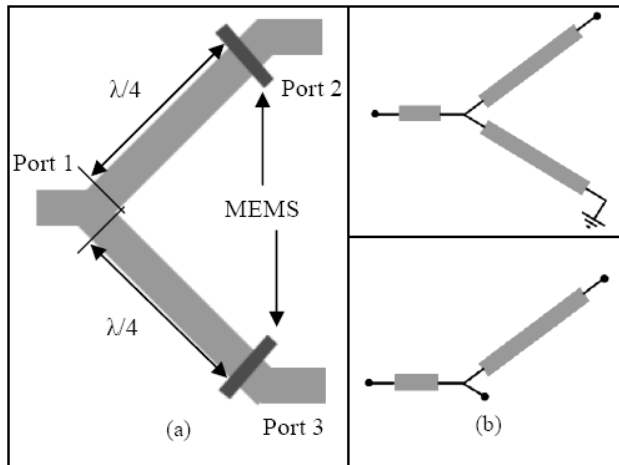


Fig. 5. SPDT principle of operation.

When one of them is actuated (DOWN state) a short circuit to the RF signal is presented at a $\lambda/4$ distance from the T plane at the design frequency, which transforms into an open circuit at the T plane preventing the RF signal to pass through (Fig. 5b). Three air-bridges are used in order to prevent CPW odd mode propagation. Fig. 6 shows the photograph of the fabricated SPDT based on two capacitive MEMS switches with capacitive anchor.

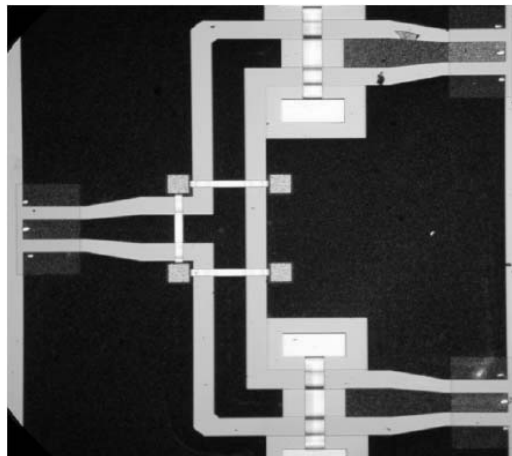


Fig. 6. Photograph of the fabricated SPDT based on capacitive MEMS with capacitive-anchor.

Figure 7 shows simulated (using Agilent ADS Momentum TM) and measured SPDT insertion loss and return loss. The SPDT design frequency is 24 GHz. Insertion loss are better than 3 dB and return loss are better than 20 dB. Fig. 8

shows simulated (using Agilent ADS-MomentumTM) and measured SPDT isolation from port 1 to port 2. The measured isolation is better than 30 dB at the design frequency.

The SPDT simulated and measured results validate the MEMS capacitive-anchor as a successful technique to meet the special 0°/180° phase switch requirements for application to pseudo-correlation radiometers.

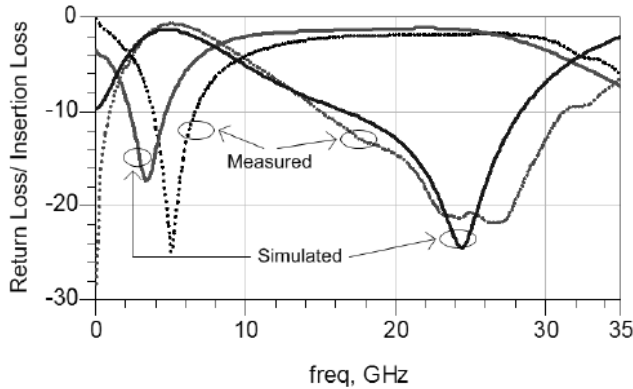


Fig. 7. Simulated and measured SPDT insertion loss and Return loss. ----- Measured results, — simulation.

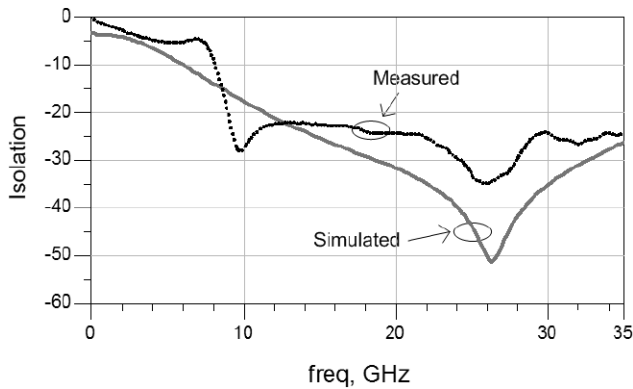


Fig. 8. SPDT isolation. ----- Measured results, — simulation.

4. CONCLUSIONS

This paper has shown the design and characterization of capacitive MEMS switches with capacitive anchor, integrated in a SPDT for 0°/180° phase switches used in mm-wave space pseudo-correlation radiometers. Circuit constraints have been assessed during the MEMS switch mechanical design in order to have a mechanical resonance frequency well above the phase switch switching frequency. A strategy based on switch capacitive-anchor has been described in order to avoid

DC short circuit, due to the particular phase switch circuit configuration, and also to guarantee independent actuation. The SPDT simulated and measured results show a good agreement and behaviour, demonstrating the feasibility and potentialities of capacitive MEMS switches with capacitive anchor.

Acknowledgment. This work has been supported by the Spanish Government Project TEC2007-65705/TCM, the Catalan Government Project 2006ITT-10005 and URV-2007ACCES-17.

References

- [1] D.C. BOIRE, J.E. DEGENFORD, H. COHN, *A 4.5 to 18 GHz Phase Shifter*, Microwave Symposium Digest, MTT-S International, **85**(1), pp. 601–604, June 1985.
- [2] D. DUBUC, L. RABBIA, K. GRENIER, P. PONS, L. BARY, O. VENDIER and R. PLANA, *MEMS-Based Redundant circuits For Millimeter-Wave Space Applications*, 4th Workshop on MEMS for Millimeterwave Communications, pp. A19–A22. July, 2003.
- [3] S.P. PACHECO, D. PEROULIS, L.P.B. KATEHI, *MEMS Single-Pole Double-Throw (SPDT) X and K-Band Switching Circuits*, IEEE MTT-S 2001, Phenix USA.
- [4] P. FARINELLI, F. GIACOMOZZI, G. MANNOCCI, R. MARCELLI, B. MARGESIN, P. MEZZANOTTE, S. DI NARDO, P. RUSSER, R. SORRENTINO, F. VITULLI, L. VIETZORRECK, *RF-MEMS SPDT Switch on Silicon Substrate for Space Applications*, Silicon Monolithic Integrated Circuits in RF Systems, pp. 151–154, 8-10 September 2004.
- [5] B. DUCAROUGE, E. PERRET, F. FLOURENS, H. AUBERT, J.W. TAO, X. CHAUFFLEUR, J.P. FRADIN, D. DUBUC, K. GRENIER, P. PONS, R. PLANA, *Design of MEMS-Based Microwave and Millimeterwave Switches for High Power Measurements*, Intl. Semiconductor Conference, CAS 2003, **1**. September, 2003.

Systems Engineering - a Holistic Approach, Whatever the Requirement ?

Ayman EL-FATATRY¹, Henne van HEEREN²

¹BAE SYSTEMS, Systems Engineering Innovation Centre - SEIC

²enablingMNT

Abstract. Micro and nano technology based (sub)systems are increasing in complexity both as stand alone components and highly interconnected / integrated systems. In essence, micro/nano systems technology is advancing towards the realisation of, multi-functional, intelligent devices such as the lab-on-a-chip for diagnostics or miniaturised inertial measurement units for aerospace / automotive applications. These sub-systems will, in future, become integrated within larger systems to form part of an, intelligent, ambient environment populated with sensors, actuators and wireless transceivers. In such complex environments, intelligence will be distributed and shared via, ad-hoc, wireless networks and data/knowledge will be processed in real-time. The essence of such an ambient intelligent environment forms the basis of a world of systems of systems.

1. Engineering „micro“ Systems

1.1. What is a System?

“A system is a construct or collection of different elements that together produce results not obtainable by the elements alone. The elements, or parts, can include people, hardware, software, facilities, policies, and documents; that is, all things required to produce systems-level results. The results include system level qualities, properties, characteristics, functions, behaviour and performance. The value added by the system as a whole, beyond that contributed independently by the parts, is primarily created by the relationship among the parts; that is, how they are interconnected (Rechtin, 2000)”.

1.2. Systems Engineering

Two aspects characterise microsystems, namely; (i) the multi-disciplinary nature of the underlying technologies and (ii) the level of integration required to

develop multi-functional devices. It is either, or both, of these characteristics which place microsystems in a unique position from the perspective of an overall systems design and/or its evolution as well as the intended application. Systems engineering, as a discipline, addresses all aspects which provide a framework for the integration of people, processes, tools and technologies in order to improve the management of risk, product configuration and technology insertion. This process is equally applicable to the design and commercialisation of microsystems-based components as shown in Fig. 1:

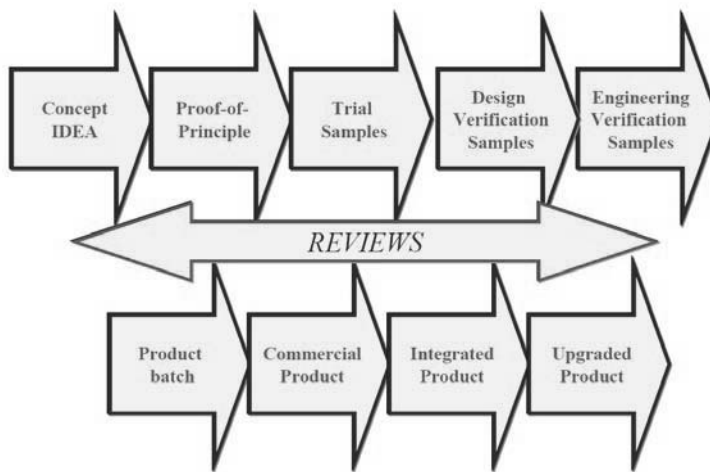


Fig. 1. Systems Engineering – Product Lifecycle.

The diagram illustrates how, given the lifecycle of a product from its conceptual stage to its production (and cradle to grave), a number of specific design and review steps are pursued in order to mitigate the risks associated with novel concepts, technologies and, possibly, new applications. These aspects tend to be associated with microsystems as a general rule).

According to INCOSE (International Council on Systems Engineering), Systems Engineering is defined as; “The set of activities which control the overall design, implementation and integration of a complex set of interacting components or systems in order to meet the needs of users and stakeholders” In essence, systems engineering, as a science in its own right, addresses the salient issues associated with the development and evolution of complex and interactive technologies, namely;

- Evolving system complexity through change in requirements and/or uncertainty;
- Product evolution, lifecycles and obsolescence: basically, from concept through to sustainable maintenance;

- Human factors and human interactions: Manmachine integration within the ambient, intelligent, environment;
- Information and data processing, knowledge management and data dissemination, exploitation and security;
- Intelligent autonomy and decision making;
- Monitoring and diagnostics; leading to self analysis, re-use and reconfiguration and, possibly, self-assembly;
- Modelling, simulation and prototyping.

1.3. Systems of Systems

The relevance of some (if not all) of these issues has become increasingly important to all fields of engineering projects which are characterised by their multi-disciplinary technologies and systems such as microsystems. This is particularly the case for complex multi-national projects incorporating a diverse set of expertise from across the world. The European Union’s frameworks 6 and 7 Integrated Projects are a case in point. Microsystems, although on a different scale, are also tending towards increasing complexity.

In essence, microsystems technology is advancing towards the realisation of, multi-functional, intelligent devices such as the lab-on-a-chip for diagnostics or miniaturised inertial measurement units for aerospace / automotive applications. These sub-systems will, in future, become integrated within larger systems to form part of an, intelligent, ambient environment populated with sensors, actuators and wireless transceivers. Intelligence will be distributed and shared via, ad-hoc, wireless networks and data/knowledge will be processed in real-time. The following diagram in Fig. 2, illustrates, schematically, how the ambient intelligent environment forms the basis of a systems of systems.

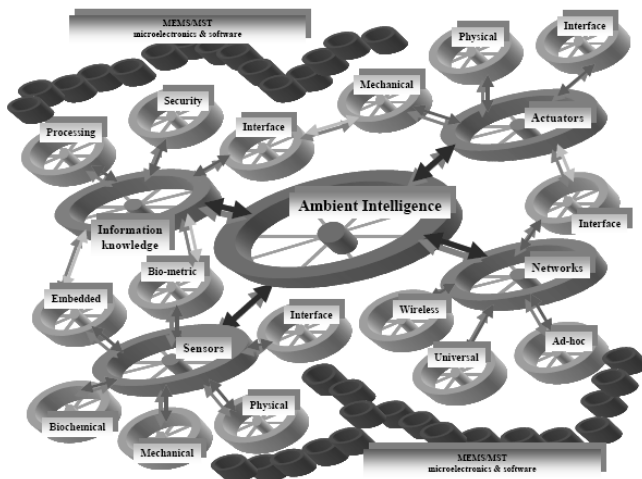


Fig. 2. The ambient intelligent system of systems.

In essence, future components will need to be designed and configured as part of a complete system scenario. The integration will be inherent and the interface ambient and seamless.

2. ARRRO¹ CONSORTIUM CONCLUSIONS

- ◆ RF MEMS have started to enter the market for simple replacement scenarios
 - ◆ BAW duplexers and filter
 - ◆ Next: MEMS oscillators for CE and RF MEMS switches for Test equipment
- ◆ Higher impact when one leverages MEMS for new reconfigurable architectures (performance and integration)
 - ◆ Soon in base stations (by 2010?)
 - ◆ Also in cell phones (2010?)
- ◆ Mid term/ long term roadmap: RF MEMS benefit of nanotechnologies (CNT) and metamaterials
- ◆ It is important not to underestimate alternative technologies
 - ◆ Traditional and emerging component technologies
 - ◆ Alternative systems or concepts

3. ARRRO RECOMMENDATIONS TO EC FOR FP7

- ◆ It is vital to secure the commercialisation supply chain for RF MEMS
 - ◆ Create a pool of MEMS foundries and centres of manufacturing excellence with experience and expertise in RF MEMS
 - ◆ Prescribe the inclusion of a foundry or manufacturing partner within all of their funded R&D projects
- ◆ Enhanced focus of R&D for RF MEMS in Europe
 - ◆ Dedicated R&D projects for key challenges: modelling, simulation, reliability and packaging
 - ◆ Narrowing down the number of applications and components (selection could be driven by results of RF MEMS Roadmap)
 - ◆ R&D resource and funding effort should also be focused on a limited number of industrial and academic partners

4. IN CONCLUSION; SYSTEMS ENGINEERING DELIVERS

- ◆ Improved techniques and technologies for developing integrated systems & systems of systems
- ◆ Mitigation against emergent properties
- ◆ Reducing cost of implementation and operation of complex systems

¹Applied Research Roadmaps for RF micro/nano systems Opportunities.

- ◆ Designs for evolving systems at acceptable cost
- ◆ Reduced cost of system upgrades
- ◆ Enables enhanced supply chain integration
- ◆ Instils best practices

Acknowledgements & CONTACTS ARRRO

NATO: AVT138 Group

EnablingMNT: <http://www.enablingMNT.com>

The SEIC: <http://www.seic-loughborough.com>

Fabrication of an on-Wafer Package for RF MEMS Switches

F. BARRIERE, A. CRUNTEANU, A. BESSAUDOU,
A. POTHIER, F. COSSET and P. BLONDY

XLIM UMR 6172, Université de Limoges/CNRS, 123 rue Albert Thomas, 87060 Limoges
Cedex, France

Abstract. Because they have moving parts, or because they need to work in a specific atmosphere (vacuum, inert gas...), micro-electromechanical system (MEMS) are not compatible with integrated circuit packaging technologies. So, in order to accelerate commercialization of RF MEMS devices, the development of packaging technologies is one of the most critical issues that should be solved. A process has been developed to effectively package RF MEMS switches using a technique called wafer level micro encapsulation. This technology is designed to be compatible with high performance RF MEMS capacitive switch fabrication. This approach has the potential for obtaining lower loss and better performance at high frequencies. The measured performances of an encapsulated MEMS device are characterized by a transmission loss of 0.4 dB and a return loss below -17 dB.

1. INTRODUCTION

The RF MEMS is a fast developing technology due to the strong demands in fields like wireless communication which requires devices and systems characterized by lower power consumption, lower losses, higher linearity and a higher Q factors than conventional communications components. However, packaging represents a large part of the manufacturing cost for these devices.

As RF MEMS contain fragile movable parts or need to operate in a vacuum atmosphere, standard packaging technologies developed for integrated circuits cannot be directly used for MEMS devices. The ideal package technology for RF MEMS devices should provide environmental protection, should preserve the mechanical and electrical performances of the encapsulated device, and should be fabricated at low cost. It should also preserve the RF designed functions should have reduced parasitic effects and minimizes the package resonance. For

reliability- demanding applications the MEMS package should be fabricated at low process temperatures (below $\sim 250^{\circ}\text{C}$) and may need to be hermetically sealed for avoiding stiction of the mobile parts of the packaged devices due to environmental factors.

Two main approaches have been developed for the package of RF MEMS. The first one is based on surfacemicromachining processes for creating thin film as capping layer [1]. These thin film technologies are based on a sacrificial layer which is covering the microstructures during the encapsulating thin film. The second technology is based on wafer bonding includes bonding of a cap wafer (glass, silicon, or ceramic) with cavity to the host wafer using anodic [2], fusion, eutectic [3], and glass frit [4] bonding techniques. Each of these technologies has its own characteristics and can be selected according to the desired application for optimizing the overall system performance.

This work reports on a wafer bonding packaging process (silicon direct bonding) that is applicable to a wide variety of micro machined structures. Some of the advantages of this technology are:

- Extremely small volume cavity
- Requires only RF MEMS processing
- Extremely low insertion loss
- No added parasitics
- Low temperature process
- Hermetic seal
- Strong bond
- Ease of processing
- Low cost

2. PACKAGING FABRICATION

2.1. Fabrication Processes

Figure 1 gives a brief description of fabrication process flow for cap wafer. In the proposed architecture, a micro machined high resistivity silicon wafer which is aligned and bonded on fabricated RF MEMS wafer is used for the package in order to reduce the attenuation of the signals. This phase forms a cavity on the cap substrate with desired height to cover the active part of MEMS. First of all, 250 Å thick chrome is formed on bare wafer as later photolithography mask for the cavity and access. Then, access are made by TMAH (Tetramethylammonium hydroxide) wet etching process all around the future cavities. Cavities, with a depth of 60 μm are also made by TMAH wet etching process to ensure internal space for motion of membrane on device wafer.

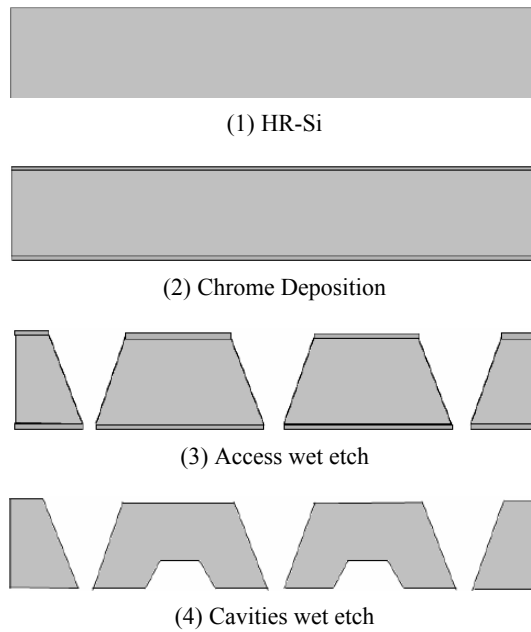


Fig. 1. Cap wafer fabrication process flow.

2.2. Bonding Process

Bonding quality strongly depends on surface conditions. So, oxide layer on top surface and contaminations which are introduced in the former procedure processes should be removed before bonding process. Oxygen plasma is used as surface cleaning method.

Bonding process is performed in wafer scale and bonding parameters include peak temperature, dwell time at peak temperature, applied force etc.

After cleaning process, a very viscous polymer is spin coated on the cap wafer. Cap wafer and device wafer are connected and aligned using this polymer at temperatures below 150°C. The bonding process is shown on Fig. 2.

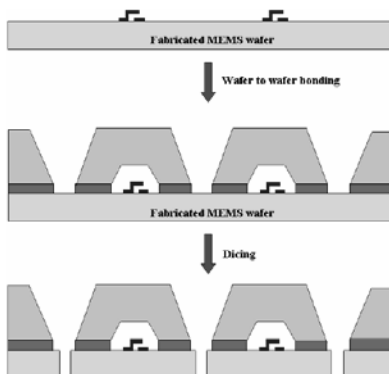


Fig. 2. Bonding process flow.

Figure 3 presents the image of a packaged MEMS switch integrated on a microwave coplanar transmission line after dicing. The cap substrate has an internal silicon micro machined cavity 60 μm deep which is incorporating the MEMS switch built on quartz substrate.

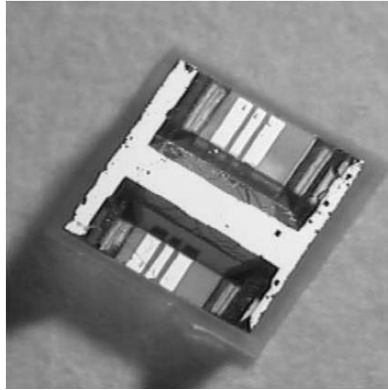


Fig. 3. Optical image of the packaged structure
Containing the MEMS device.

3. DEVICE PERFORMANCES

Low insertion loss is one of the major features for RF MEMS. The package has been simulated using HFSS EM simulator, with simple coplanar line. This structure is shown on Fig. 4. Comparisons between simulations and measurements are shown on Fig. 5 for the return loss and Fig. 6 for the insertion loss. It can be seen that this package presents about -10 dB return loss from 5 to 30 GHz, with straight on the coplanar line. We show that simulations correspond to measurements with a good accuracy.

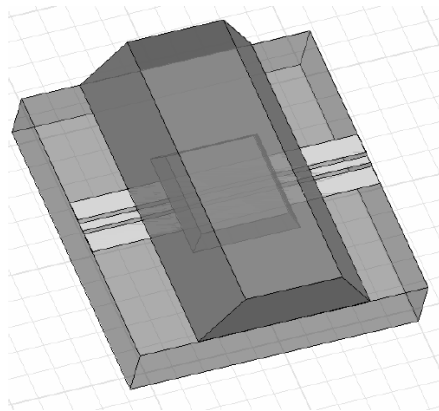


Fig. 4. HFSS simulated structure of an on-wafer
packaged coplanar line.

Fig. 5. Return loss simulation (green) and measurement (red) of an on-wafer packaged coplanar line.

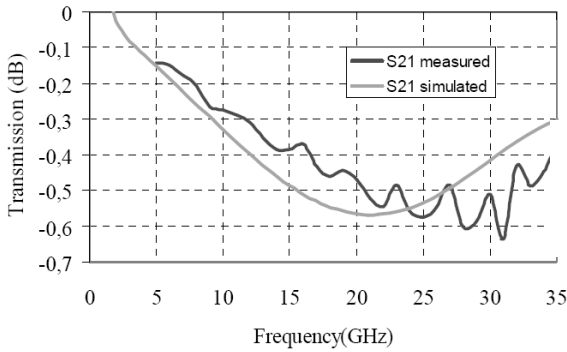
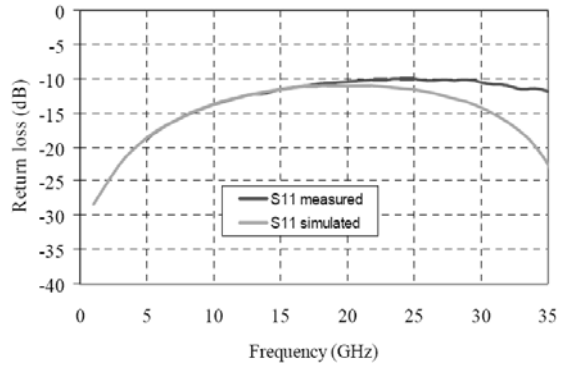


Fig. 6. Transmission loss simulation (green) and measurement (red) of an on-wafer packaged coplanar line.

As bonded wafer is then diced into pieces of device with dimension of 1 mm * 1 mm and around 800 μm in height. These diced devices are subjected to a series of test of insertion loss measurement for RF characteristics. On Fig. 7 are presented the typical performances of an encapsulated capacitive switch fabricated on a quartz substrate. In the activated, ON state, the transmission loss is better than 0.4 dB and the return loss is better than -17 dB from 5 to 30 GHz. Results show that RF-signal could be well transmitted under acceptable loss.

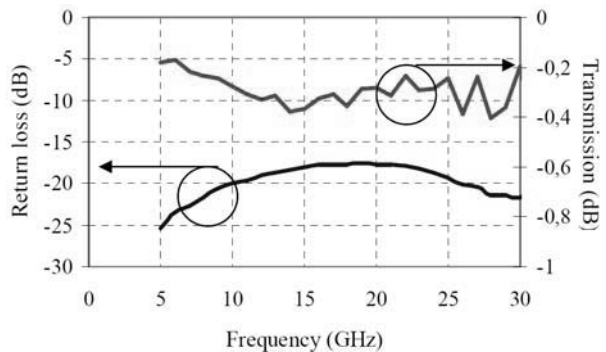


Fig. 7. Measured response of RF MEMS switch.

4. CONCLUSION

A low temperature wafer level packaging scheme for RF MEMS switch is presented. The measured results showed excellent performances (insertion loss of 0.4 dB and return loss below -17dB from 5 to 30 GHz) and no parasitic resonances up to 30 GHz.

References

- [1] C. GILLOT, E. LAGOUTTE, P.L. CHARVET, F. SOUCHON, N. SILLON, *Wafer Level Thin Film Encapsulation for MEMS, High Density Microsystem Design and Packaging and Component Failure Analysis*, Conference, pp. 1–4, June 2005.
- [2] X. ROTTENBERG, G. CARCHON, H. TILMANS, *Optimization of 0-level packaging for RF MEMS devices” Solid-State Sensors, Actuators and Microsystems*, 12th International Conference, **2**, pp. 1915–1918, 2003.
- [3] W. KIM, Q. WANG, K. JUNG, J. HWANG, C. MOON, *Application of Au-Sn Eutectic Bonding in Hermetic RF MEMS Wafer Level Packaging*, 9th Int’l Symposium on Advanced Packaging Materials, 2004 IEEE.
- [4] M. ESASHI, *Wafer Level Packaging of MEMS*, *J. Micromech Microeng*, **18**, pp. 073001–0730013, 2008.
- [5] A. MARGOMENOS, L. KATECHI, *Fabrication and Accelerated Hermeticity “Testing of an On-Wafer Package for RF MEMS*, *IEEE Transactions on microwave theory and techniques*, **52**(6), June 2004.

Glass Cap Packaged High Isolating Ka-Band RF-MEMS Switch

A. STEHLE¹, G. GEORGIEV^{1,3}, V. ZIEGLER¹, B. SCHOENLINNER¹,
U. PRECHTEL¹, H. SEIDEL², U. SCHMID²

¹EADS Innovation Works, Dept: Sensors, Electronics and System Integration, Munich,
Germany

Phone: +49 89 607 29054

²Saarland University, Chair of Micromechanics, Microfluidics/Microactuators,
Saarbrücken, Germany

Phone: +49 681 302 3979

³Brunel GmbH, 85622 Feldkirchen, Germany

Abstract. This paper presents a packaged high-isolation RF-MEMS switch at Ka-band. The package consists of a glass cap with a milled cavity to protect the RF-MEMS. The glass cap, with a low dielectric constant, is bonded to the silicon substrate using ultraviolet light curable glue in a room temperature process. The packaging is non-hermetic but able to withstand water and dust for a limited time period. The switch shows an isolation of -50 dB and an insertion loss of -0.8 dB at 30 GHz. The additional loss due to the package was found to be only 0.1 dB.

Index Terms. Microelectromechanical devices, microwave switch, RF-MEMS, packaging.

1. INTRODUCTION

In the last years, numerous advances in the field of RF-MEMS switches have been made [1]-[2]. Beside a high isolation and a low insertion loss they can also handle moderate temperatures [3]. However, most of the published switches are still unpackaged and therefore restricted to operation under lab environment due to particles and humidity being present under real conditions. To protect RF-MEMS devices efficiently, the corresponding packaging solutions need to be compact in the design and add only low RF losses [4]-[5]. Therefore, the use of a packaging material with low dielectric constant and low $\tan \delta$ is preferred. Another imported issue concerning any packaging approach is that during encapsulation any change

compared to the original performance of the MEMS-device is avoided. In particular, it is not tolerable that the process harms the MEMS-device using too high or too long temperature loads. The optimum packaging process would consequently be applied at room temperature. Also, in terms of integration, it is advantageous to have the package on wafer-level. This paper describes a simple glass cap packaging process for on wafer level packaging that can be applied to a MEMS-device without any temperature load. Furthermore, a very high isolation Ka-Band RF-MEMS switch is presented, packaged by the glass cap and characterized before and after packaging.

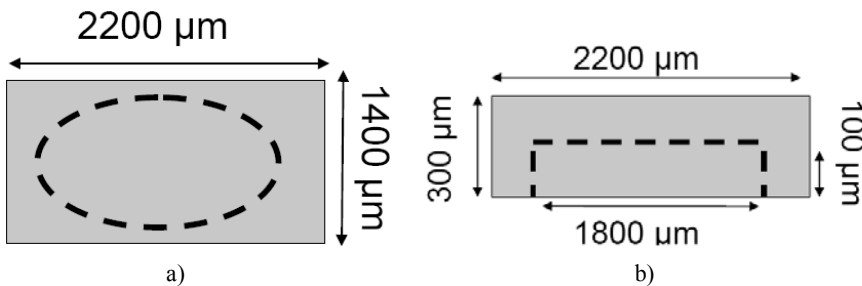
2. GLASS CAP PACKAGING

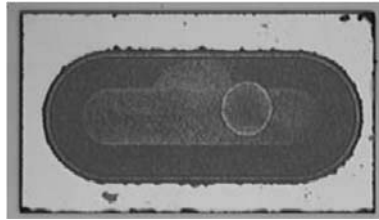
Basically, the glass cap based packaging is applied to protect MEMS-devices e.g. RF-MEMS switches against water, dust etc. during dicing. The package also enables an operation of MEMS-devices under real environment conditions for a limited time period and simplifies the mounting of them as they can be handled by tweezers easily. To demonstrate the feasibility of this packaging approach the glass caps are placed only on a selected number of devices. Although this is not a batch process on that level, it might be advantageous, as the process is extremely flexible and allows MEMS-devices with different designs to be packaged on one chip or wafer.

In contrast to silicon ($\epsilon_r=11.9$) as packaging material, a glass cap ($\epsilon_r=4.6$) exhibits a low dielectric constant and therefore only a negligible influence to the RF-behavior [6]. Furthermore, glass is a transparent material that allows an optical control of the packaged device.

A. Description of the Glass Cap

The glass cap consists of a 300 μm thick glass plate diced from a wafer. A cavity 100 μm in depth is precisely milled into its center to accommodate the RF-MEMS switch. Fig. 1 shows a glass cap without a MEMS-device and the corresponding sketches. This glass cap was used to package the RF-MEMS switch presented in chapter 3.





c)

Fig. 1. Sketch (a), (b) and optical micrograph (c) of the glass cap.
The darker part in the photograph shows the milled cavity.

The design of the glass caps is extremely flexible, since almost any shape and size can be fabricated. It is possible to cover a single chip or even a whole wafer with one single glass cap.

B. Packaging Process at Room Temperature

The whole packaging process is illustrated in Fig. 2. Ultraviolet light curable glue is put in a 20 μm deep cavity. Next, the glass cap, guided by a micromanipulator, is carefully brought into contact with the glue (1+2). Doing so, it is of most importance that no glue flows into the cavity of the glass cap. After the cap is placed on the top of a substrate to cover a MEMS-device, the glue is cured by the exposure of ultraviolet light at room temperature for two minutes (3).

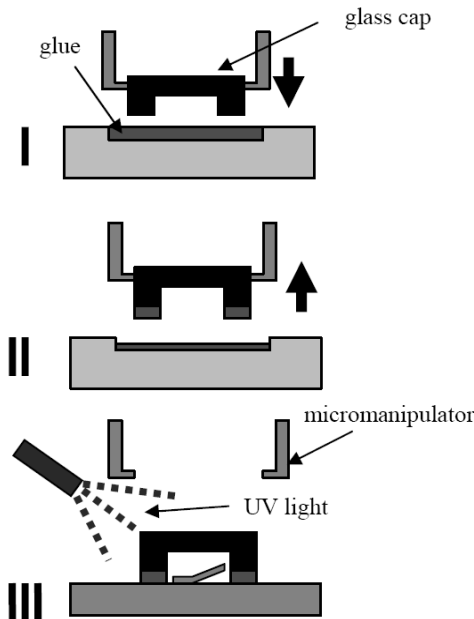


Fig. 2. Visualisation of the packaging process in three steps.

The packaging is non-hermetic due to the used glue, which consists of non-hermetic material. It was tested to be waterproof for a limited time period and to protect the MEMS-device against dust. The adhesion force of the glue was tested to be very strong, as it was not possible to remove the glass cap from the substrate once the glue is cured. Due to these properties of the glass cap packaging, it is possible to protect MEMS-devices effectively against any impacts arising from the dicing or the mounting processes. The properties in terms of RF-performance are shown in the next chapter.

3. Ka-BAND RF-MEMS SWITCH

A. Design of the Switch

The Ka-Band RF-MEMS switch, presented in this paper was realized using the standard low-complexity technology described in [2]. The goal was to obtain an even higher isolation behavior than in [7] and to maintain the low insertion loss. In order to reach these aims the switch was fabricated on an only 100 μm thick silicon substrate, using two cascaded single switches both with 600 μm long cantilevers. (Fig. 3a)

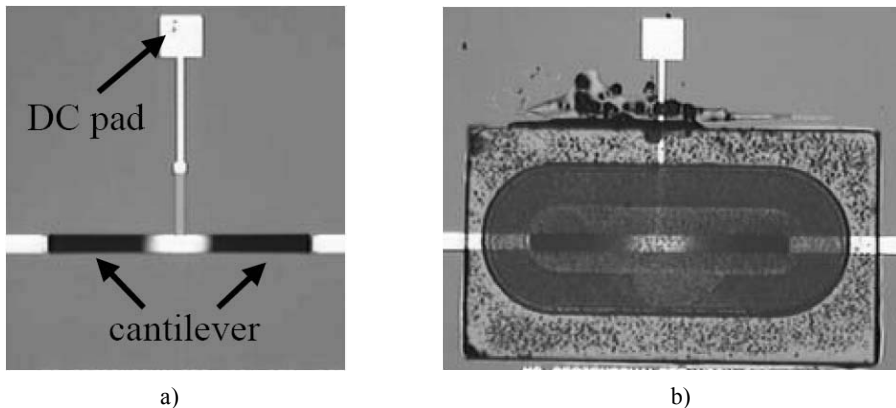


Fig. 3. Optical micrographs of the high isolation RF-MEMS switch without (a) and with (b) packaging. The black-coloured parts of the switch element are bent upwards.

The 100 μm thin substrate minimizes the substrate coupling and hence, leads to a high isolation without a significant increase of the insertion loss [7]. The switch can be actuated by a separate bias pad connected by a carbon line. With a resistivity of about 8 $\text{k}\Omega$, the carbon line decouples the RF from the DC-actuation path effectively, so that the RF is not disturbed by these additional lines.

B. RF-Measurement of the Switch

The unpackaged switch was characterized on-wafer and Fig. 4 shows the simulated and measured S-parameters in the up and down-state.

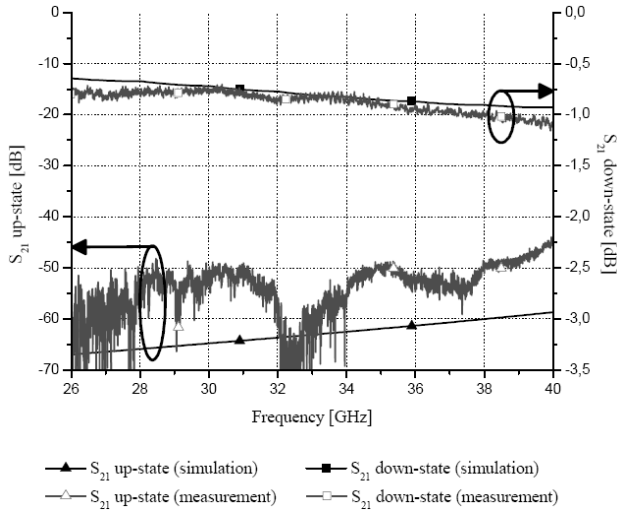


Fig. 4. S-parameter measurement and simulation of the unpackaged switch from Fig. 3a in down-state (right axis) and up-state (left axis).

The measured data show an insertion loss of -0.8 dB and an isolation of -50 dB at 30 GHz. Fig. 5 shows a comparison between the RF-measurement with and without packaging. The switch was packaged according to the description given in chapter 2 and is illustrated in Fig. 3b.

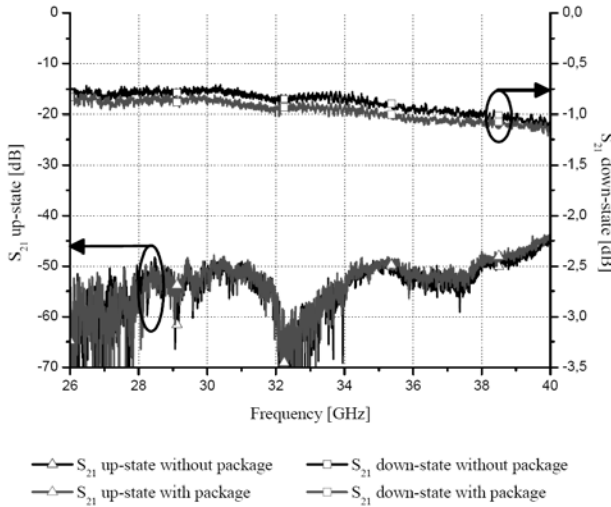


Fig. 5. S-parameter measurement of switch from Fig. 3 with and without packaging in down-state (right axis) and up-state (left axis).

When comparing both modifications in Fig. 5, a significant impact arising from the packaging can not be determined. The insertion loss is increased only slightly by 0.1 dB from 26 to 38 GHz. This fits with the expected results, as the glass-covered bond frame with a width of about 200 μm is very short compared to the wavelength at 40 GHz (2700 μm) and therefore, has a negligible influence on the RF-behavior of the switch. As the cavity has an inner height of 100 μm it can be assumed that only very few lines of the electrical field are disturbed by the glass cap.

4. CONCLUSION

A simple and very flexible packaging for MEMS-devices has been presented. It makes use of glass as a low dielectric material and can be applied at room temperatures. Although the packaging is non-hermetic, it exhibited a strong adhesion to the substrate and was tested to be waterproof for a limited exposure period. Due to these properties it is possible to protect MEMS-devices, such as RF-MEMS switches, effectively against any impacts arising from the dicing or the mounting processes. The influence of the package in terms of RF-losses was tested with a very high isolation Ka-Band RF-MEMS switch. This switch was fabricated on 100 μm thick substrates to minimize substrate coupling and maximize the isolation behavior. The switch showed an isolation of -50 dB and an insertion loss of -0.8 dB 30 GHz. The additional loss due to the glass cap was found to be 0.1 dB. Due to the high isolation and the moderate insertion loss, the switch is suitable for the use in radiometer applications [7].

References

- [1] M. REBEIZ, J.B. MULDAVIN, *RF MEMS Switches and Switch Circuits and Phase Shifters*, HFREVIEW, June 2001.
- [2] A. STEHLE, G. GEORGIEV, V. ZIEGLER, B. SCHOENLINNER, U. PRECHTEL, H. SEIDEL, U. SCHMID, *RF-MEMS Switch and Phase Shifter Optimized for W-Band*; Proc. European Microwave Conf., Amsterdam, 27-31.10, 2008.
- [3] A. STEHLE, C. SIEGEL, V. ZIEGLER, B. SCHOENLINNER, U. PRECHTEL, S. THILMONT, H. SEIDEL, U. SCHMID, *Low Complexity RF-MEMS Switch Optimized for Operation up to 120°C*, Proc. European Microwave Conf., pp. 1229–1232, Munich, 8-12.10, 2007.
- [4] J. MULDAVIN, C.O. BOZLER, S. RABE, P.W. WYATT, C.L. KEAST, *Wafer-Scale Packaged RF Microelectromechanical Switches*, IEEE Transactions on Microwave Theory and Techniques, **56**(2), pp. 522–529, February 2008.
- [5] Y. OYA, A. OKUBORA, M. van SPENGEN, P. SOUSSAN, S. STOUKATCH, X. ROTTENBERG, P. RATCHEV, H. TILMANS, W. De RAEDT, E. BEYNE, P. De MOOR, I. De WOLF, K. BAERT, *A Reliable and Compact Polymer-Based Package for Capacitive RF-MEMS Switches*, Electron Devices Meeting, Issue, pp. 31–34, 13-15 December 2004.
- [6] Pyrex® 7740 Borosilicate Glass, <http://www.corning.com>

- [7] A. STEHLE, D. NÖTEL, C. SIEGEL, V. ZIEGLER, B. SCHOENLINNER, U. PRECHTEL, H. SEIDEL, U. SCHMID, *SPST RF-MEMS Switch Optimized for Ka-Band Radiometer*, submitted to Frequenz - Journal of RF Engineering and Telecommunications.

Millimeter-wave Quarter-Wave Patch Antenna on Benzocyclobutene Polymer

Seonho SEOK, Nathalie ROLLAND, Paul-Alain ROLLAND

IEMN/IRCICA CNRS 8520

Cité Scientifique-Avenue Poincare BP 60069 59652 Villeneuve d'Ascq Cedex; France

E-mail: seonho.seok@iemn.univ-lille1.fr

Abstract. This paper presents design, fabrication and characterization of a millimetre-wave $\lambda/4$ -patch antenna on a benzocyclobutene (BCB) polymer. This antenna is compatible with a wafer level packaging for a miniaturized wireless communication system. All components of this antenna are manufactured by using a gold electroplated and a BCB polymer patterned by a photolithography. The implemented antenna size was $3.5 \times 3.5 \times 0.05 \text{ mm}^3$. The manufactured patch antenna mounted on V-connector was characterized using Agilent network analyzer E8361A for a return loss and a range-calibration setup for a radiation pattern. The fabricated antenna showed a minimum return loss of 30 dB at 51.75 GHz and - 10 dB impedance bandwidth of 5 GHz from 49.5 to 54.5 GHz. The measured gain is - 1.7 dBi and the - 3 dB beam-width is nearly 50 degree. In addition, the effect of various critical parameters of the proposed antenna such as a separation between an RF-feed and a shorting-pin, a ground plane size and the height of BCB polymer was investigated.

1. INTRODUCTION

Recently, smaller-size wireless communication systems with their performance maintained or enhanced are strongly demanded. For example, millimeter-wave band has been interested for wireless personal area network (WPAN) applications because it provides a large bandwidth [1]. System-in-packaging (SIP) with an antenna integrated makes it possible to realize a highly integrated transceiver system. Moreover, millimeter-wave frequency has an inherent merit on a small antenna because its size is determined by operational frequency. There have been a number of reports on antenna at millimeter-wave frequencies related to system-on-package (SOP) [2] and antenna-in-package [3].

Microstrip antennas [4], planar inverted-F antennas (PIFA) [5] and Yagi-Uda antennas [3] were reported as integrated on the package. PIFAs were under much attention due to their potential to a compact size and integration with a package. It is achieved by short-circuiting its radiating patch to the antenna's ground plane under the patch with a shorting-pin and can resonate at a much smaller antenna size for a fixed operating frequency [6]. A variety of dual-band or multiband PIFAs suitable for applications in mobile phones have been demonstrated [6]. Antenna-integrated miniaturized systems have been realized by low temperature co-fired ceramic (LTCC) [3] and polymer substrate on a circuit in a monolithically integrated fashion [7]. The LTCC process provides mechanically strong, hermetically sealed, thermally conductive, chemically inert and dimensionally stable structures with high yield [3]. However, it might suffer from the triggering of unwanted surface waves due to high dielectric-constant substrate even if it can be suppressed by placement of metal strip around the antenna structure [3]. It has been also reported that a thick polyimide layer can increase the bandwidth of the antenna and improve the radiation efficiency [7].

In this paper, a quarter-wave patch antenna based on BCB polymer is presented at millimeter-wave frequency. In chapter II, antenna design will be described using an electromagnetic simulation and the developed fabrication process for the designed antenna will be explained in chapter III. In chapter IV and V, measurement results and parametric studies will be presented.

2. ANTENNA DESIGN

The proposed quarter-wave antenna is shown in Fig. 1. It consists of a rectangular patch on a BCB polymer, a ground plane, a shorting-pin and a vertical interconnection to a RF-feed line. The shorting-pin is placed at the bottom-center of the patch to connect it to the ground plane under the patch. The ground plane is introduced to reduce a patch dimension and protect signal processing circuits such as MMIC from a backward radiation of the antenna. BCB layer exists under the ground plane to isolate the RF-feed from the ground plane. A microstrip line on BCB polymer is used as an RF-feed.

The patch is connected to the ground plane by the shorting-pin and to microstrip RF-feed via a hole in the ground plane by a vertical interconnection to implement a PIFA configuration. Concerning the BCB polymer as a substrate for an antenna, it is chosen due to its low dielectric constant and a compatibility with a wafer level packaging technology. A pyrex glass is adopted as a supporting substrate for a prototype antenna. High resistive silicon (HRS) [8] and a BCB polymer [9] can replace the glass as a wafer level packaging material. The proposed antenna on BCB polymer is independent of the packaging materials properties because it is completely separated from them. Therefore, the proposed antenna can be easily integrated on any package materials reported today.

Chapter V. The microstrip width (W_m) was designed to 80 μm in relation to the height of BCB polymer. It was reduced to 30 μm from the place where it meets a ground plane under the patch to keep a 50 Ω input impedance. The thickness of all metallization (t_{metal}) was designed to 3 μm .

The calculated radiation patterns at the resonant frequency of 52.75 GHz are given in Fig. 2 (a) and (b), which describe the E-plane and H-plane respectively. The calculated gain of the designed antenna is 2.87 dBi.

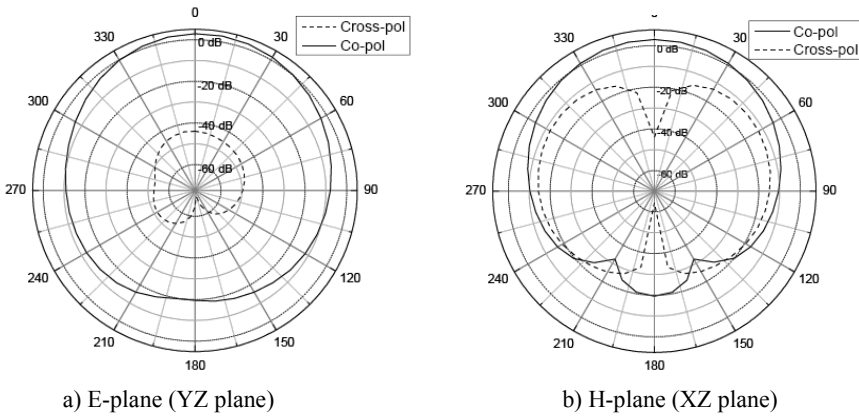
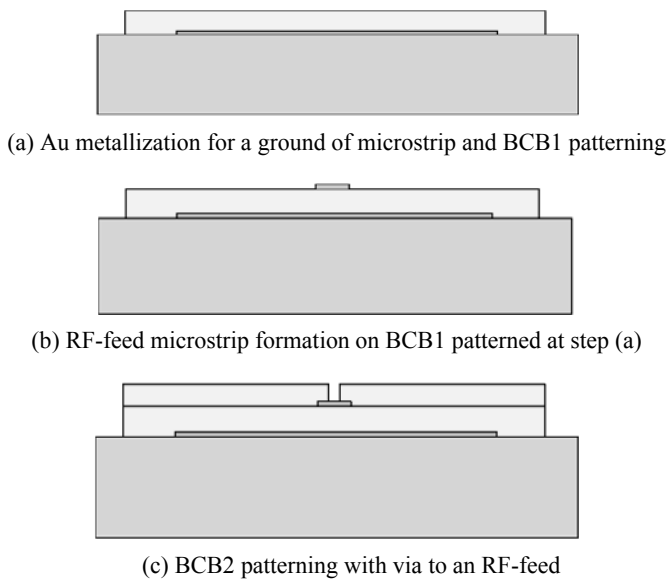


Fig. 2. Calculated radiation patterns.

The fabrication process is presented in Fig. 3. Basically, the process is based on Au electroplating for a patch, a ground plane and a vertical interconnection and the BCB polymer multilayer coating as a supporting layer of an antenna.



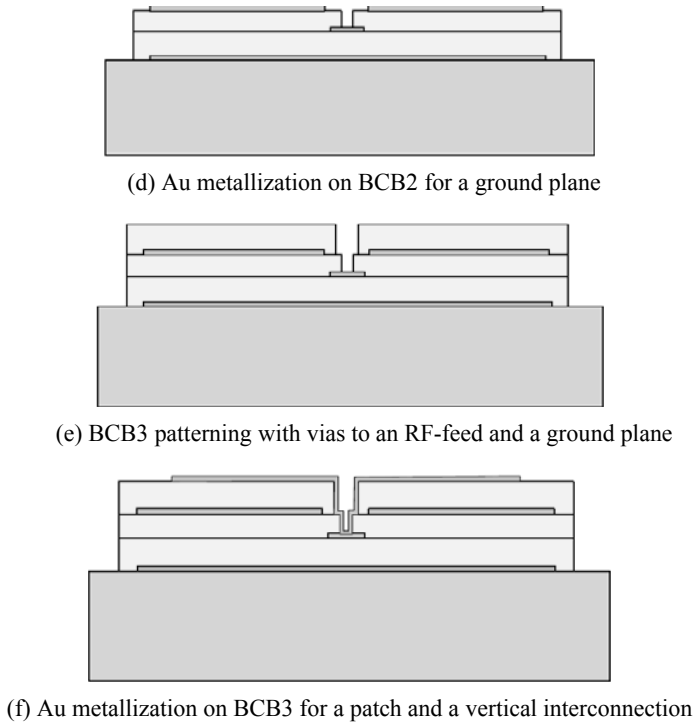


Fig. 3. Process flow.

The pyrex glass #7740 was chosen as a supporting substrate of the prototype antenna for a fabrication. The process flow is described in the following; (a) Ti (100 nm)/ Au (100 nm) seed layers were deposited on the glass substrate. AZ9260 photoresist was patterned for an electroplating mold. Electroplating process was performed for a ground of a microstrip. After removal of a seed layer, BCB was formed photolithographically on the ground. (b) Microstrip signal line was formed on the BCB. (c) The second BCB layer with via to RF-feed was patterned on the microstrip processed at step (b). (d) Ground plane with a circular hole was formed by a gold electroplating. This hole is for a vertical interconnection to RF-feed. (e) The third BCB layer was processed. It has vias to RF-feed as well as a ground plane. (f) Ti/Au seed layers were sputtered on the BCB layer. AZ9260 photoresist was also used as an electroplating mold. Metallization was done to form a square patch as well as a vertical interconnection to RF-feed and a ground plane to complete PIFA configuration.

Fig. 4 shows the fabricated prototype antenna on dice glass wafer.

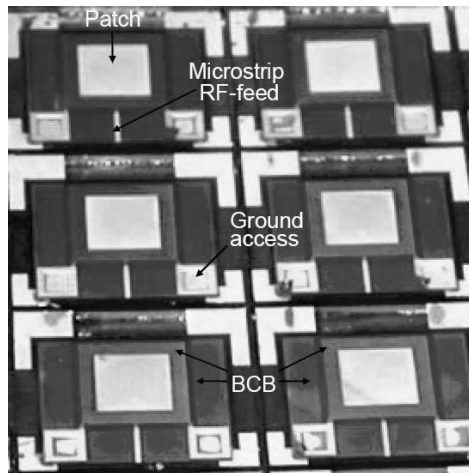


Fig. 4. The fabricated prototype quarter-wave antenna on diced glass wafer.



Fig. 5. Prototype antenna mounted on V-connector.

4. MEASUREMENT RESULTS

The manufactured antenna was mounted on V-connector as shown in Fig. 5 to measure a return loss and a radiation pattern. Return loss was measured from 47 GHz to 57 GHz by Agilent network analyzer E8361A as shown in Fig. 6. It showed a resonant frequency of 51.75 GHz with a return loss of 30 dB. The resonant frequency shift from a designed value is due to the discrepancy of the

relative permittivity of BCB between a simulation and a fabrication. It has also shown a -10 dB impedance bandwidth of 5 GHz from 49.5 GHz to 54.5 GHz.

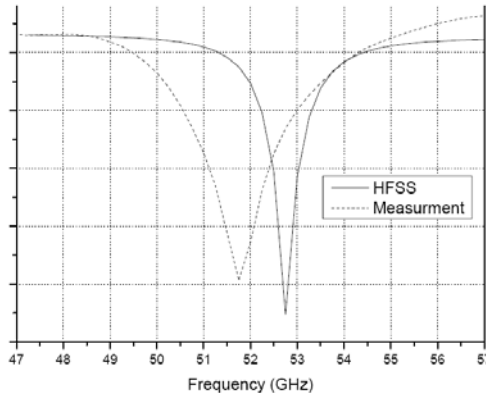


Fig. 6. Measured return loss of the prototype quarter-wave antenna.

After a reference calibration, the fabricated antenna replaced the reference and then the received power was measured at a receiver. Fig. 7 shows the measured radiation pattern at 51.75 GHz in the E-plane. The 3 dB beam width is nearly 50 degrees. The measured gain of the fabricated antenna is -1.7 dBi. This reduced antenna gain resulted from the small ground plane, compact antenna dimension.

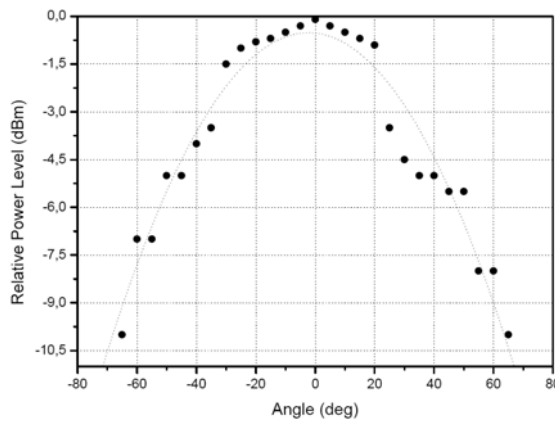


Fig. 7. Measured radiation pattern of the fabricated prototype antenna at 51.75 GHz

5. CONCLUSIONS

It is required to develop a small size wireless communication system for a near future application, for example, wireless sensor network. For this purpose, the

antenna is a critical element to achieve a miniaturized system. PIFA is chosen to minimize the antenna size and is achieved by short-circuiting its radiating patch to the antenna's ground plane under the patch with a shorting-pin. The dimension and geometry of the antenna were optimized to achieve a better impedance matching, a high gain and high radiation efficiency at millimeter-wave frequency. The fabrication process was developed by using an electroplating for electrical signal lines including a patch, a vertical interconnection, a ground plane and a BCB process for a dielectric layer formation. The fabricated antenna was verified to have desired performance for the application. In addition, as the antenna uses a BCB polymer as a supporting layer, it can be easily fabricated and transferred for integration to any packaging material for sensor systems and system-In-packaging (SIP). Therefore, the developed antenna will be one of solutions for a miniaturized sensor system for wireless sensor network.

Acknowledgment. The authors wish to acknowledge the technical staffs of IEMN. This work was supported by European funding FEDER (Fonds Europeen de DEveloppement Regional).

References

- [1] Y.P. ZHANG, M.SUN, and L.H. GUO, *On-Chip Antennas For 60-GHz Radios in Silicon Technology*, IEEE Transactions on Electron Devoces, **52**(7), pp. 1664–1668, July 2005.
- [2] T. SEKI, N. HONMA, K. NISHIKAWA, and K. TSUNEKAWA, *A 60-GHz Multilayer Parasitic Microstrip Array Antenna on LTCC Substrate for System-on-Package*, IEEE Microwave and Wireless Components Letters, **15**(5), pp. 339–341, May 2005.
- [3] Y.P. ZHANG, M. SUN, K.M. CHUA, L.L. WAI, D. LIU, B.P.GAUCHER, *Antenna-in-Package in LTCC for 60-GHz Radio*, IEEE International Workshop on Antenna Technology, pp. 279–282, March 21–23, 2007.
- [4] S. WI, Y. SUN, I. SONG,S. CHOA, I. KOH, Y. LEE, and J. YOON, *Package-Level Integrated Antennas Based on LTCC Technology*, IEEE Transactions on Antennas and Propagation, **54**(8), pp. 2190–2197, August 2006.
- [5] P. BASSET, F. ALFARO, D. NOVOSEL, A. de la PLAZA, D. STANCIL and G. K. FEDDER, *Chip-Size Antennas for Implantable Sensors and Smart Dust*, 13th International Conference on Solid-State Sensors, Actuators and Microsystems, Transducers, pp. 457–460, 05, 2005.
- [6] Kin-lu WONG, *Planar Antennas for Wireless Communications*, Wiley Series in Microwave and Optical Engineering, John Wiley and Sons, 2003.
- [7] A. HIRATA, T. MITOTANI and T. NAGATSUMA, *A 120 GHz Microstrip Antenna Monolithically Integrated With a Photodiode On Si*, Jpn. J. Appl. Phys., **41**, pp. 1390–1394, 2002.
- [8] R.M. HENDERSON, K.J. HERRICK, T.M. WELLER, S.V. ROBERTSON, R.T. KIHM, and L.P.B. KATEHI, *Three-Dimensional High-Frequency Distribution Network-Part II: Packaging and Integration*, IEEE Transaction on Microwave Theory and Techniques, **48**(10), pp. 1643–1651, October 2000.
- [9] S. SEOK, N. ROLLAND AND P.-A. ROLLAND, *Design, Fabrication and Measurement of BCB Polymer Zero-Level Packaging for Millimeter-Wave Applications*, IEEE Transaction on Microwave Theory and Techniq ues, **55**(5), pp. 1040–1045, May 2007.

Acoustical Structures Based on the Thickened Edge Load Solution

Jordi VERDU, Pedro de PACO, Oscar MENENDEZ, Eden CORRALES

Universitat Autònoma de Barcelona (UAB)
Telecommunications and System Engineering Department (TES)

E-mail: Jordi.Verdu@uab.cat

Abstract. The high performance and small size demands in the actual communication systems terminals, requires that the devices which conform them accomplish these features. Acoustical structures based on Bulk Acoustic Wave (BAW) resonators meets the demanded requirements. However, the electrical behavior of the BAW resonators presents some no desired effects due to lateral spurious resonances. In order to improve the electrical behavior, the thickened edge load solution is applied to the resonator, making the lateral spurious resonances being not generated. The improvement in the acoustical resonator can be translate to the acoustical structures based on them. A Stacked Crystal Filter based in the improved resonators has been simulated showing a very good transmission response compared with a SCF based on conventional BAW resonators.

1. INTRODUCTION

The development of mobile communication systems continues towards very small size and high performance handheld units. This development leads us to increase the requirements in these units and ask for a miniaturization of the components. With this purpose, the RF filters based on Surface Acoustic Wave (SAW) devices are being replaced for filters based on Bulk Acoustic Wave (BAW) resonators. This kind of resonators presents some advantages in front of SAW resonators: the working frequency range is up to 20 GHz, large signal handling capability (up to 4W), the size reduction and the compatibility with the standard Integrated Circuit (IC) technology [1].

The BAW resonator consists in a piezoelectric slab sandwiched between two metal electrodes. When a certain voltage is applied to the top electrode, a longitudinal electrical field is excited between both electrodes. At this point, due to

the properties of the piezoelectric materials, an acoustic wave is generated in the thickness direction. In Fig. 1 the schematic geometry of the BAW resonator is shown. The electrical behavior of the BAW resonator can be characterized with the electrical input impedance. The electrical impedance of the resonator is shown in Fig. 1 where two important frequencies are found: the resonance frequency, f_r , when the magnitude of the electrical impedance trends to zero, and the mechanical or anti-resonance frequency, f_a , when the magnitude of the electrical impedance trends to infinite.

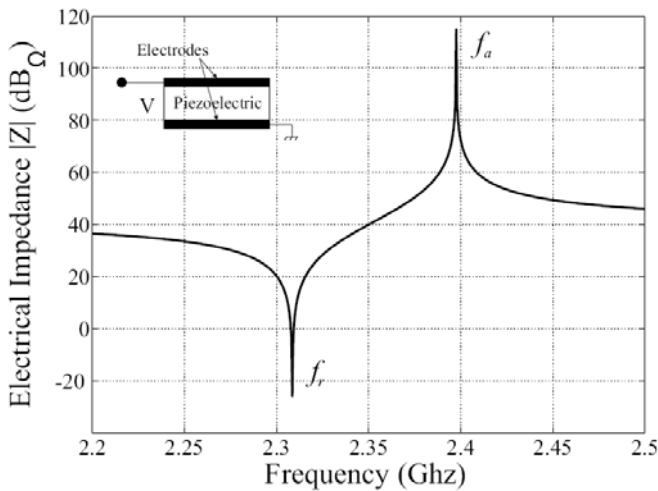


Fig. 1. BAW resonator scheme and its electrical input impedance response.

The electrical response of the resonator can be modelled by means of Mason model [2], which comes from the analysis of the propagation of the acoustic wave in the thickness direction of the resonator. However, there are also lateral modes which generates spurious resonances and no desired effects in the electrical behavior of the BAW resonator. This modes only can be taken into account by means of a 3D simulation of the structure. The main spurious resonances are generated at the interface between the electrode and the piezoelectric and some techniques have been developed in order to eliminate them, or even to do not generate them. One of this techniques consists in apodize the top electrode in order to attenuate the spurious resonance [3]-[4]. However, using this technique, the complete suppression of the spurious modes is not achieved. Another technique is proposed in [5]- [6] where a thickened edge load is added to the top electrode. In this case, the spurious mode is not generated due to the propagation condition in the structure.

First, a brief review of the thickened edge load solution applied to BAW resonators will be exposed. After this, it is well known that the metal electrodes generates a mass loading effect in BAW resonators. However, when the thickened

edge load solution is applied, the effect of the electrodes is not the same since the thickness of the electrode is not the same in the whole surface. By means of Mason model this effect will be discussed. Finally, a 3D simulation of an acoustical structure based on BAW resonators is done. In this work, a Stacked Crystal Filter (SCF) using the improved BAW resonators has been simulated and compared against a SCF based on conventional BAW resonators. It will be shown how the transmission response can be improved significantly.

2. THICKENED EDGE LOAD SOLUTION

The most common way to simulate the electrical response of a BAW resonator is by means of the Mason model. It has been discussed that this model only takes into account the longitudinal propagation of the acoustical wave because the lateral dimensions of the structure are considered infinite. If the geometry of the structure is finite in its lateral dimensions, the called Lamb waves are generated along the structure. Lamb waves are acoustic waves propagating along a finite plate, with the particularity of being dispersive for a certain ratio between the thickness and the lateral dimensions of the structure [7]. The basic scheme of the thickened edge load solution is shown in Fig. 2, where a certain perimetric ring, that is the thickened edge load, has been added to the top electrode. In the region where the thickened edge is applied, the total thickness of the structure is greater, forcing an antiresonance frequency lower than the one in the active area. As it will be discussed in this section, in this region, due to the propagation conditions, the lateral acoustic wave will be exponentially attenuated, avoiding the generation of lateral resonances in the top electrode.

In order to analyze the origin of the spurious lateral modes, the propagation of the lateral Lamb waves must be studied, taking into account the boundary conditions: zero stress at the top and bottom surface of the resonator [5],

$$j\omega \frac{\partial \vec{u}_z}{\partial z} = 0 \quad (1)$$

For simplicity, only the x- and z-direction propagation solution are considered. The boundary conditions take us to have the condition for the wave number: $k = \sqrt{k_x^2 + k_z^2}$. The wave number may be real, leading the propagation of the acoustic wave; it may be imaginary, generating an exponentially attenuating acoustic wave; or it may have a real and imaginary part, condition for a attenuating sinusoidal acoustic wave. The x-z plane of a BAW resonator with the thickened edge load solution is shown in Fig. 3. There are five different regions, however, due to the symmetry of the structure, we can state that region 1 and 5, and region 2 and 4 are equal. The distribution of the mechanical displacement at each region can be expressed as,

$$\Psi(x) = Ae^{-jkx} + Be^{jkx} \tag{2}$$

At the interfaces between regions, the mechanical displacement must be continuous and the stress must be equal on both sides of the interface. This boundary conditions can be written as,

$$\begin{aligned} \Psi_r(x_r = W_r) &= \Psi_{r+1}(x_{r+1} = 0) \\ \frac{d\Psi_r}{dx} \Big|_{x_r = W_r} &= \frac{d\Psi_{r+1}}{dx} \Big|_{x_{r+1} = 0} \end{aligned} \tag{3}$$

where Ψ_r is the mechanical displacement and W_r is the width of the region r . In the active area, which is region 3, a flat mechanical displacement distribution is desired because just this mode will couple with the electrical field, achieving a spurious free resonator.

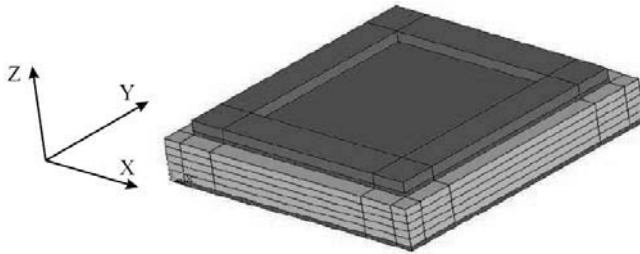


Fig. 2. BAW resonator geometry using the thickened edge load solution.

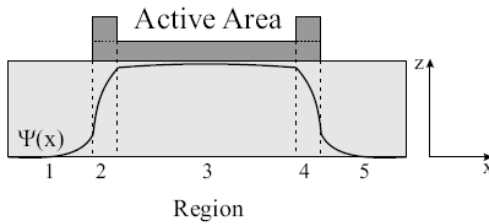


Fig. 3. BAW resonator scheme and its electrical input impedance response.

This mode is achieved when the derivative of Ψ at the region is zero, that is, $\nabla\Psi = 0$. If we apply this condition to the previous development, the relation between the width of the thickened edge load and the wave number at region 1 and 2 is obtained [5],

$$W_2 = \frac{\arctan \frac{K_1}{k_2} + n\pi}{k_2}, \quad n=0,1,\dots,N \quad (4)$$

where $k_1 = jK_1$ is the wave number at region 1, being K_1 a real number, and k_2 is the wave number at region 2.

Since the thickness of the structure determines the antiresonance frequency, we can state that the cut-off frequency at each region of the structure will be different. If the Poisson's ration of the metal electrode is above 1/3, the dispersion is type I, while if the ratio is below 1/3, the type is II [5]. In this work, we will work with Aluminum electrode with a Poisson's ratio equal to 0.362, dispersion type I. The active area of the resonator will fix the operating frequency equal to the cut-off frequency at region 3. Due to the dispersion type, the cut-off frequency at region 2 must be lower in order to have a real wave number at this region, that is, an exponentially decaying acoustic wave. In order to achieve a lower frequency, a higher thickness is needed. The wave number can be related with the dispersion type by means of the dispersion relation,

$$k_r = \sqrt{\alpha(\omega_r^2 - \omega_c^2)} \quad (5)$$

where α determines the dispersion type and has a value of 10^{-8} , and ω_r and ω_c are the cut-off frequency of each region and the operating frequency in the active area. Taking into account the relation in (5) we can state that k_3 will be equal to 0, characteristic of the piston mode. In Fig. 2, the basic scheme of the geometry for a BAW resonator with the thickened edge load solution is shown.

The electrical impedance for a conventional BAW resonator is shown in Fig. 4 compared against a thickened edge loaded BAW resonator using 1D and 3D simulations. It can be seen that the three curves agree perfectly in terms of resonance and anti-resonance frequency. For the 3D simulations, mechanical losses related with a damping ratio of 0.1% have been included in the piezoelectric material, that is why the quality factor in the electrical response has decreased with respect the 1D lossless simulation. The 3D simulation of the resonator shows a spurious response with origin at the interface between the electrode and the piezoelectric slab. This effect can be observed in Fig. 5, where the X- and Z-mechanical displacement distribution is shown, and both have the maximum amplitude at the interface between the electrode and the piezoelectric medium. The thickened edge load solution makes this spurious being not generated as it can be seen in Fig. 4.

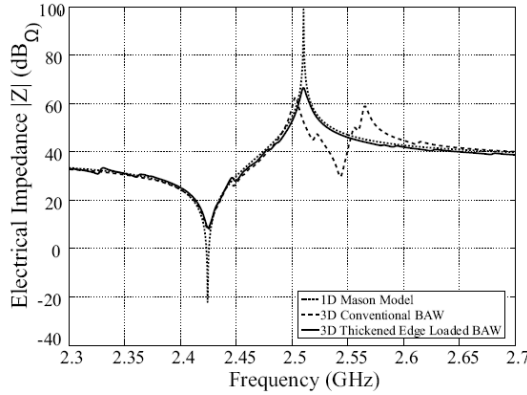


Fig. 4. Electrical response comparison for a 1D BAW resonator simulation, 3D simulation and 3D simulation applying the thickened edge load solution.

3. MASS LOADING EFFECT USING THE THICKENED EDGE LOAD SOLUTION

The mass loading effect are all that effects associated to the deposition of metal electrodes on a piezoelectric slab. The effects can be observed related to some parameters that characterize the electrical and mechanical behavior of the structure. The mass loading affects to the stress in the structure due to the difference between the elastic parameters of electrodes and piezoelectric materials; affects to the energy trapping since regions with different cut-off are created; affects to the resonance and anti-resonance frequency since the total thickness of the structure becomes greater and the main effect can be observed in the electromechanical coupling coefficient k_t^2 [8]. This parameter quantifies the property of the piezoelectric material in convert mechanical energy into electrical and viceversa and it is inherent to the piezoelectric material. At the same time, the frequency difference between the resonance and anti-resonance frequency is given by this parameter, when the electrodes are taken into account, k_t^2 becomes k_{eff}^2 , since not only depends on the piezoelectric material.

$$k_t^2 = \left(\frac{\pi^2}{4} \right) \left(\frac{f_r}{f_a} \right) \left(\frac{f_a - f_r}{f_a} \right) \quad (6)$$

Since the electrodes have a different acoustic impedance, depending on the ratio between the thickness of the electrodes and piezoelectric, the value of k_{eff}^2 will modify its value. Many works have studied the effect of the electrodes in the electrical response of the resonator. In [9], taking advantage of the symmetry of a BAW resonator in the thickness direction, the transcendental equations for the

resonance and anti-resonance conditions can be obtained. Using the expression in (6), the dependence between k_{eff}^2 and the thickness ratio is shown in Fig. 6.

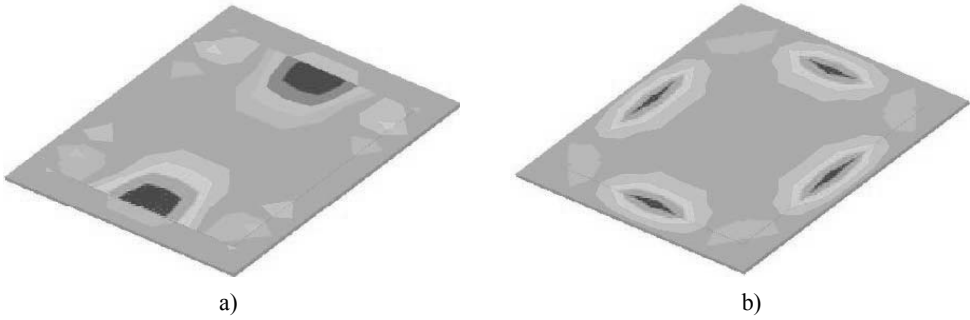


Fig. 5. (a) X-Mechanical displacement distribution. (b) Z-Mechanical displacement distribution.

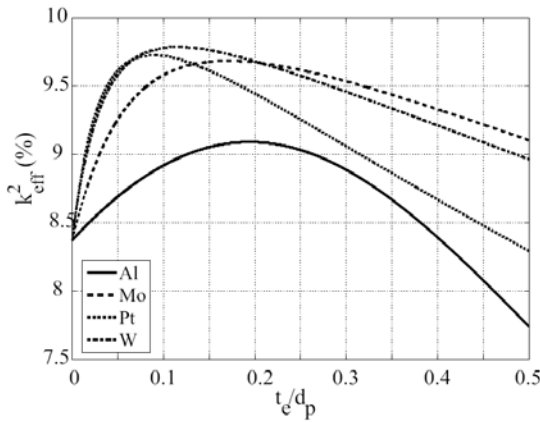


Fig. 6. Effective electromechanical coupling constant as a function of the thickness ratio for Zinc Oxide Piezoelectric material.

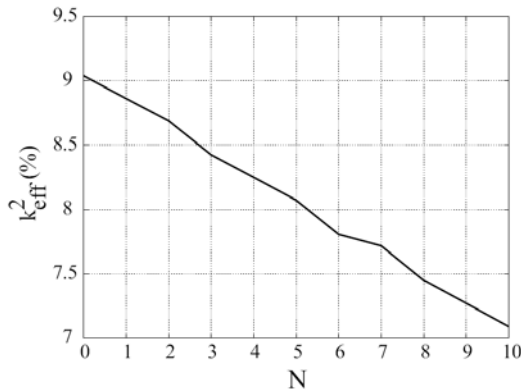


Fig. 7. Effective electromechanical coupling constant as a function of N.

The curve shown in Fig. 6 has been obtained considering the same thickness in all the surface of the electrode. However, applying the thickened edge load solution, the thickness is not the same in the whole surface of the top electrode. From the expression for the width of the region 2 (4), periodical solutions for W_2 exists for different values of N. As we take greater values of N, the width of the region 2 will be wider.

This situation take us to think that an effective thickness of the electrode must be considered instead of the thickness of the active area. At this point, if the ratio of the structure is the one for the optimum value of k_{eff}^2 , and we include the thickness edge load solution, as we increase the value of W_2 , k_{eff}^2 will be degrade. This situation is seen in Fig.7 where the dependence of the k_{eff}^2 with the N-solution of (4) is shown. It is very important then, tho choose the N-solution to have the narrower thickened edge load implementable with the actual fabrication processes.

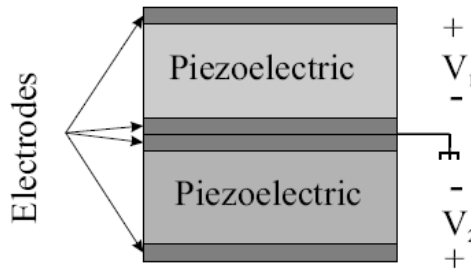


Fig. 8. Basic scheme of a SCF structure and its electrical equivalent circuit.

4. STACKED CRYSTAL FILTER SIMULATION

In the previous sections, the thickened edge load solution has been applied to a BAW resonator, improving its electrical behavior. In this section, we are going to take advantage of these resonators using them in a Stacked Crystal Filter (SCF). In this way, a 3D simulation of the SCF based on improved resonators has been done and compared against a SCF based on conventional resonators achieving some improvements in the transmission response.

A single SCF section structure consists in two BAW resonators coupled acoustically as it is shown in Fig. 8, where the central electrodes on both resonators are grounded. When a certain voltage is applied to the top electrode of one of the BAW resonators, an electric field is generated between the electrodes. This electric field, will generate a mechanical field in the structure which, due to the continuity condition of the structure, is propagated to the next resonator. The mechanical field will be transformed into electrical energy again in the second resonator. The relation between the voltage in the first and second resonator will determine the transmission response of the structure.

The SCF structure that has been simulated consists on two improved resonators. Zinc Oxide (ZnO) has been used as the piezoelectric material and

Aluminum (Al) for the electrodes. A damping ratio of 0.1% has been applied to the piezoelectric material to simulate losses in the structure. The thickness of the piezoelectric slab is $1.06 \mu\text{m}$ and the electrodes thickness is 200 nm . The area of the bottom electrode and piezoelectric slab is $120 \mu\text{m} \times 120 \mu\text{m}$, while the active area, defined with the top electrode, is $100 \mu\text{m} \times 100 \mu\text{m}$. In this case, only the thickened edge load has included on the top electrode. Since the bottom electrode has the same area of the piezoelectric slab, there is no spurious resonances due to the medium change at the interface electrode - piezoelectric. The thickness of the thickened edge load has been set to 400 nm (giving a electrode thickness in this region of 600 nm) and using (4) the width has been set to $1.03 \mu\text{m}$ for $N = 1$. In the case of $N = 0$, the result of the width is 690 nm , which can origin some problem in the fabrication process.

Fig. 9 shows the transmission response for a SCF based on conventional BAW resonators (dashed line) and based in a thickened edge loaded BAW resonators (solid line). These solutions have been obtained by means of a 3D simulation using the commercial software ANSYS. It can be seen how the spurious resonances of the conventional BAW resonators affect to the transmission response causing a big ripple and even, some strong resonances close to the pass band. The mechanical displacement is shown in Fig. 9, and it can be seen how the origin of this spurious resonances is in the interface piezoelectric - electrode. In the case of using improved BAW resonators, this spurious resonances disappears leading a better transmission response.

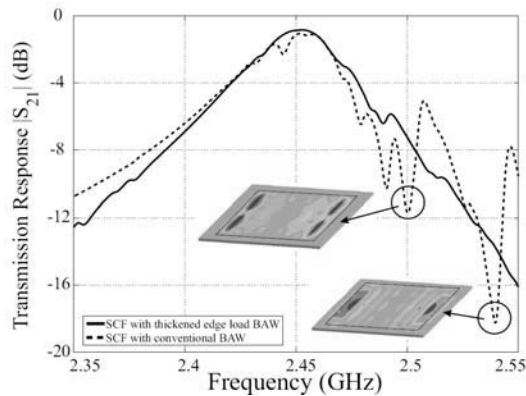


Fig. 9. Transmission response for a SCF based on improved BAW resonators (solid) and SCF based on conventional BAW resonators (dashed).

5. CONCLUSION

BAW resonators presents spurious resonances in the electrical behavior due to lateral waves at the interface piezoelectric - electrode. By means of the thickened edge load solution, the lateral spurious resonances can be not generated. Although

the electrical behavior is improved with this solution, the effective electromechanical coupling can be degraded due to the mass loading effects. Choosing the optimum dimensions for the thickened edge load, a SCF filter based on these resonators has been simulated and compared against a SCF based on conventional BAW resonators, giving an free spurious transmission response.

Acknowledgement. This work is supported by the Spanish Comisi' on Interministerialde Ciencia y Tecnologia (CICYT) del Ministeriode Educacion y Ciencia and FEDER funds through grantTEC2006-13248-C04-01/TCM.

References

- [1] *Bulk Acoustic Wave Coupled Resonator Filters Synthesis Methodology*, 2005.
- [2] W.P. MASON, *Physical acoustics principles and methods*, **1A**, Academic Press, 1964.
- [3] P. BRADLEY J.D. LARSON III, R.C. RUBY, *Bulk Acoustic Wave Resonator Withy Improved Lateral Mode Supression*, (6215375), April 2001.
- [4] R. RUBY, J. LARSON, C. FENG, and S. FAZZIO, *The Effect of Perimeter Geometry on FBAR Resonator Electrical Performance*,. Microwave Symposium Digest, IEEE MTT-S International, 2005.
- [5] FI) Ylilammi Markku (Espoo FI) Ell`a Juha (Halikko FI) Kaitila, Jyrki (Helsinki, *Resonator Structure and a Filter Comprising Such a Resonator Structure*,. (6812619), November 2004.
- [6] S. GIRAUD, S. BILA, and D. CROS, *Bulk Acoustic Wave Resonators 3D Simulation*, IEEE Frequency Control Symposium, pp. 1147–1151, May 2007.
- [7] N. CHEEKE J. DAVID, *Ultrasonic Waves*, CRC Press LLC, 2002.
- [8] A. BALLATO J. KOSINSKI, S. MALLIKARJUN, *Mass Loading Measurements of Quartz Crystal Plates*,. 1989.
- [9] *Accurate Explicit Formulae of the Fundamental Mode Resonant Frequencies for FBAR with Thick Electrodes*, 2003.

A Novel Bulk Acoustic Wave Duplexer Based on Stacked Crystal Filters for WCDMA Handset Applications

Oscar MENENDEZ, Pedro de PACO, Eden CORRALES, Jordi VERDU

Antenna and Microwave Systems (AMS) Group Universitat Autònoma de Barcelona
(UAB), Barcelona, Spain

Email: oscar.menendez@uab.es

Abstract. This work presents a novel duplexer for WCDMA handset applications based on stacked crystal filters. The use of this type of filters, instead of conventional ladder-type filters, allows to fulfil WCDMA requirements using lower order filters. The matching network of the proposed duplexer is composed of two single bulk acoustic wave resonators, instead of the quarterwave transmission line usually used in conventional duplexers based on ladder-type filters which enlarges the device.

1. INTRODUCTION

During the last years, the demand for duplexers with small size, light weight and high performance for modern cellular handsets that require simultaneous transmission and reception has increased significantly [1]–[3]. Duplexers that are available in the market today are mainly based on ceramic and surface acoustic wave filters. However, duplexers based on bulk acoustic wave (BAW) technology are determined to replace these duplexers since they have now evolved to offer better performance [4]–[7].

The guardband specification for a PCS duplexer demands that the transmitter (Tx) and receiver (Rx) filters have an extremely sharp roll-off [1], [2]. For that reason, ladder-type filters are the most used among the different BAW filter configurations [6]. These filters have sharp roll-off but poor stopband rejection [8]. This rejection can be improved by adding more resonators, and thus increasing the filter size.

However, the guardband specification for a WCDMA duplexer is not so stringent since this is about 6 times higher, while the bandwidth assigned to the transmitting and receiving signals is the same (about 3% of the carrier frequency)

[9]. Therefore, for WCDMA duplexers, filters with high stopband rejection, such as stacked crystal filters (SCFs) [10], are more suitable than filters with extremely sharp roll-off, such as ladder-type filters, because these allow to fulfil specifications with lower number of resonators, and thus with smaller size.

This paper presents a novel duplexer for WCDMA handset applications based on stacked crystal filters. The matching network of the proposed duplexer is composed of two single BAW resonators, instead of the quarter-wave transmission line usually used in conventional duplexers based on ladder-type filters which enlarges the device [1]–[3]. The designed duplexer has been simulated and optimized by using a physical simulator, based on the well-known Mason model [11], implemented in a commercial microwave design simulator (Advanced Design System).

2. ESSENTIAL THEORY ABOUT ACOUSTIC RESONATORS

A. BAW Resonator

A BAW resonator resembles a parallel plate capacitor having piezoelectric material for the dielectric sandwiched between two metal electrodes (Fig. 1a) [5]–[7]. Assuming that spurious modes and other lateral acoustic effects can be spurned, the resonator response can be obtained from physical dimensions and material properties by using the well-known Mason model [5], [11], [12].

Fig. 1b shows the typical lossless electrical impedance $Z(\omega)$ of a BAW resonator as a function of frequency. This exhibits two close resonant frequencies: f_a where the electrical impedance approaches infinity, and f_r where the electrical impedance approaches zero. Between these resonant frequencies, $Z(\omega)$ has an inductive behaviour, while a static capacitive behaviour is found outside of this band.

The resonant frequency f_a corresponds to the mechanical resonant frequency of the longitudinal acoustic standing wave generated when an electric field is applied between the electrodes. This is mainly determined by the piezoelectric thickness t_p , but also by the electrode thickness t_e [7]. In a first approach, without taking electrode thickness into account, the resonant condition is established when the piezoelectric thickness corresponds to a half acoustic wavelength. When electrodes are taken into account, the piezoelectric thickness is lower. In such a case, t_p and t_e can be determined using, for example, the Mason model to obtain the desired f_a value.

B. Stacked Crystal Resonator

A Stacked crystal resonator (SCR) consists of two BAW resonators tightly coupled acoustically, separated only by a common ground electrode, as shown in Fig. 2a [10], [12]. In principle, the two BAW resonators that form the stacked-crystal resonator could be different. However, we will assume that both

have the same area A , the same piezoelectric thickness t_p , and that both the input/output electrodes and the common ground electrode have the same thickness t_e .

Fig. 2b shows the typical lossless one-pole transmission response of a stacked crystal resonator. Similar to the previous case, the response of this type of resonators can be obtained from physical dimensions and material properties by using the Mason model, assuming that spurious modes and other lateral acoustic effects can be spurned.

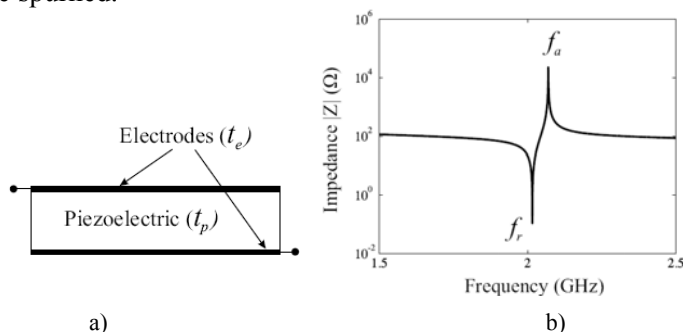


Fig. 1. BAW resonator: (a) Cross section. (b) Lossless electrical impedance as a function of frequency. Y-axis in logarithmic scale.

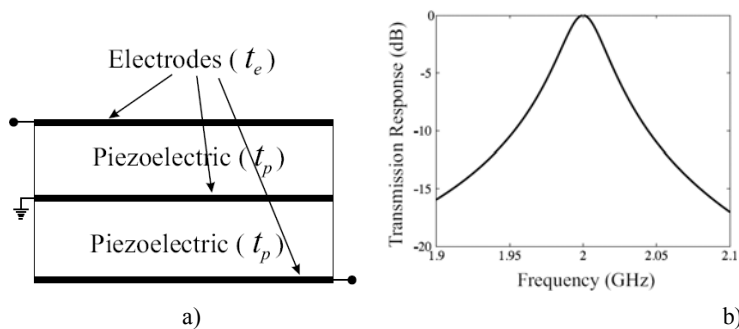


Fig. 2. Stacked crystal resonator: (a) Cross section. (b) Lossless transmission response as a function of frequency.

3. DUPLEXER DESIGN

The design of a duplexer entails in designing both the Tx and Rx filters, and the matching network that connects the filters to the antenna. The next sections deal with the design of each part.

A. Tx and Rx Filters

As explained in the introduction, Tx and Rx filters are based on stacked crystal filters. It is important to point out that each designed filter is only an 2nd-order filter, and they have been designed with Chebyshev response (passband

ripple 3 dB) using the work reported in [12]. Each filter is composed of two identical stacked crystal resonators and three inductors, as shown in Fig. 3. While the two series inductors L_e control the electrical coupling between the resonators and the input/output ports, the shunt inductor L_c controls the electrical coupling between the resonators.

Table 1 shows the design parameters for each stacked crystal filter (Tx filter: 1920-1980 MHz, Rx filter: 2110-2170 MHz) assuming that aluminium nitride (AlN) is used as piezoelectric material: $Z_0 = 3.7 \times 10^7$ Ns/m³, $\epsilon_r = 10.5$, $e = 1.5$ C/m² and $\nu = 11500$ m/s, and thin film molybdenum (Mo) electrodes are used: $Z_0 = 6.56 \times 10^7$ Ns/m³ and $\nu = 6408$ m/s, where e is the piezoelectricity constant, ϵ_r the relative permittivity, Z_0 the characteristic acoustic impedance, and ν the acoustic wave velocity.

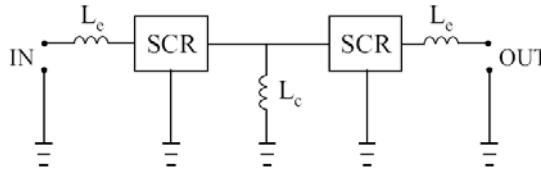


Fig. 3. Schematic illustration of a stacked crystal filter with 2nd-order chebyshev response. The filter is composed of two identical stacked crystal resonators and three inductors that control the different electrical couplings.

Table 1. Design parameters of Tx and Rx stacked crystal filters

	Tx Filter	Rx Filter
t_e (μm)	0.1	0.1
t_p (μm)	2.48	2.22
A (μm)	335×335	322.8×322.8
L_e (nH)	1.76	1.46
L_c (nH)	1.70	1.55

Figure 4 shows the lossless transmission response of the designed filters, along with the theoretical Chebyshev responses. For frequencies close to the passband of each filter, the agreement between both responses is excellent.

B. Matching Network

The aim of the matching network is to connect the Tx and Rx filters to the same antenna ensuring good Tx/Rx isolation. In duplexers based on ladder-type filters, the matching network is usually composed of one quarter-wave transmission line which enlarges the duplexer. In our approach, we connect the filters to the antenna as shown in Fig. 5. The matching network is only composed of two single BAW resonators. For the BAW resonator placed in the Tx branch, t_p and t_e have been designed so that $f_a = 2140$ MHz (high impedance at the center

frequency of the Rx band), while the area A has been chosen to ensure enough high impedance over the Rx band. In a similar way, for the resonator placed in the Rx branch, t_p and t_e have been designed so that $f_a = 1950$ MHz (high impedance at the center frequency of the Tx band), while the area A has been chosen to ensure enough high impedance over the Tx band. Table 2 shows the design parameters (A , t_p and t_e) for each BAW resonator, assuming that AlN is used as piezoelectric material, and thin film Mo electrodes are used.

It is important to take into account that the introduction of a BAW resonator in each branch modifies the transmission response of the corresponding filter, especially the passband. In order to compensate the effect produced by each BAW resonator at the passband of the corresponding filter, the first series inductor of each filter must be modified (L_e^m), as shown in Fig. 5. Table II also shows the new value for the first series inductor L_e^m of each filter.

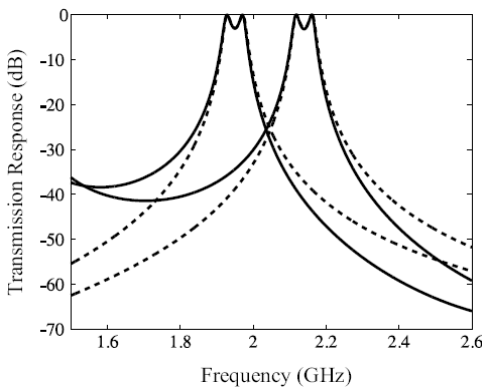


Fig. 4. Lossless transmission response of the designed Tx and Rx stacked crystal filters (continuous line), along with the theoretical response of the 2nd-order Chebyshev type filters (dashed line).

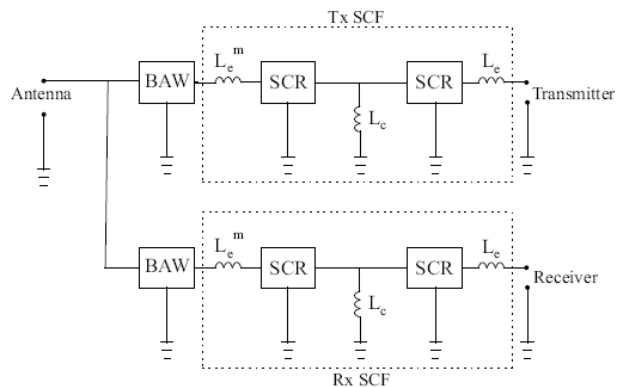


Fig. 5. Topology of the proposed duplexer.

4. PREDICTED PERFORMANCE AND DISCUSSION

Fig. 6 shows the simulated Tx/antenna and Rx/antenna response together with the Tx and Rx return loss of the designed duplexer, while Fig. 7 shows the Tx/Rx isolation. These figures show that the insertion loss is lower than 2 dB and the

isolation is higher than 60 dB in both bands. As expected the return loss in both bands is about 3 dB. These figures have been obtained by using the Mason model, assuming that the quality factor of both the BAW resonators and the stacked crystal resonators is 1000 [13], while the quality factor of each of the three inductors is 32 [14]. The losses introduced by the inductors can be reduced by using extremely thick metal layers in combination with very thick insulation layers underneath the inductor. High quality factors ranging from 30 to 80 at 2 GHz for inductor values ranging from 1.5 nH to 20 nH can be obtained [14], [15]. For example, by using inductors with a quality factor of 60, the insertion loss is reduced in 0.5 dB.

Table 2. Matching network design parameters

	Tx Branch	Rx Branch
t_e (μm)	0.1	0.1
t_p (μm)	2.07	2.33
A (μm)	95×95	100×100
L_e^m (nH)	13	18.8

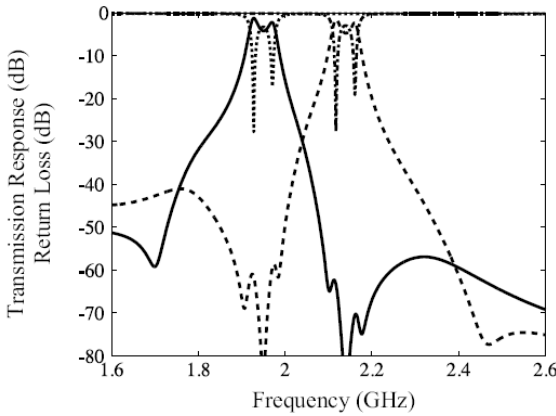
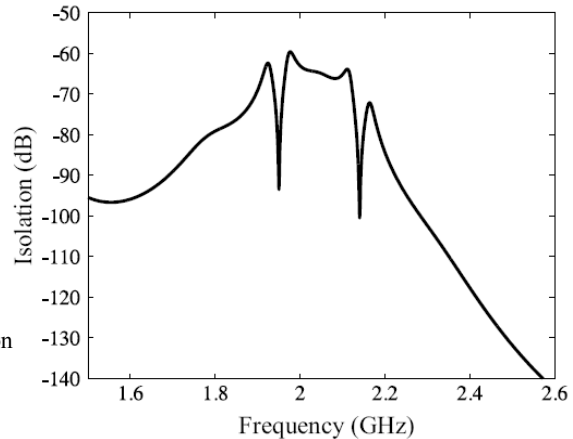


Fig. 6. Simulated Tx/antenna (continuous line) and Rx/antenna (dashed line) response together with Tx return loss (dotted line) and Rx return loss (dash-dot line) of the designed duplexer.

Fig. 7. Simulated Tx/Rx isolation of the designed duplexer.



5. CONCLUSION

In this paper a novel WCDMA duplexer based on stacked crystal filters has been presented. The use of stacked crystal filters allows to fulfil WCDMA requirements with a simpler configuration than using conventional ladder-type filters since lower order filters are required. The matching network of the proposed duplexer is composed of two single BAW resonators, instead of the quarter-wave transmission line usually used in conventional duplexers based on ladder-type filters which enlarges the device.

Acknowledgment. This work is supported by the Spanish Comisi' on Interministerial de Ciencia y Tecnolog' ia (CICYT) del Ministerio de Educaci' on y Ciencia and FEDER funds through grant TEC2006-13248-C04-01/TCM.

References

- [1] R. RUBY, J.D. BRADLEY, J.D. LARSON III, and Y. OSHMYANSKY, *PCS 1900 Mhz Duplexer Using Thin Film Bulk Acoustic Resonators*, Electron. Lett., **35**(10), pp. 794–795, May 1999.
- [2] P. BRADLEY, R. RUBY, J. D. LARSON III, and Y. OSHMYANSKY, *A Film Bulk Acoustic Resonator (FBAR) Duplexer for USPCS Handset Applications*, Proc. IEEE MTT-S Int. Microw. Symp., **1**, pp. 367–370, 2001.
- [3] P. BRADLEY, R. RUBY, B. YU, and K. GRANNEN, *A 3.8 mm × 3.8 mm × 1.37 mm Hermetic FBAR Duplexer for 800 MHz Handsets With Wafer-Scale Packaging*, Proc. IEEE Ultrason. Symp., **3**, pp. 1694–1697, 2004.
- [4] R.R. MANSOUR, *RF Filters and Diplexers for Wireless System Applications: State-of-the-Art and Trends*, Proc. IEEE Radio and Wireless Conference, pp. 373–376, 2003.
- [5] R. AIGNER, *MEMS in RF Filter Applications: Thin-Film Bulk Acoustic Wave Technology*, Wiley InterScience: Sensors Update, **12**, pp. 175–210, 2003.
- [6] K.M. LAKIN, *Thin Film Resonator Technology*, IEEE trans. Ultrason. Ferroelectr. Freq. Control, **52**(5), pp. 707–716, May 2005.
- [7] H.P. LOEBL, C. METZMACHER, R.F. MILSOM, P. LOK, F. van STRATEN, and A. TUINHOUT, *RF Bulk Acoustic Wave Resonators and Filters*, Journal of Electroceramics, **12**, pp. 109–118, 2004.
- [8] O. MENENDEZ, P. De PACO, R. VILLARINO, and J. PARRON, *Closed-form Expressions for the Design of Ladder-Type FBAR Filters*, IEEE Microw. Wireless Compon. Lett., **16**(12), pp. 657–659, December 2006.
- [9] R. RUBY, P. BRADLEY, D. CLARK, D. FELD, T. JAMNEALA, and K. WANG, *Acoustic FBAR for Filters, Duplexers and Front and Modules*, Proc. IEEE MTT-S Int. Microw. Symp., **2**, pp. 931–934, 2004.
- [10] K.M. LAKIN, *Coupled Resonator Filters*, Proc. IEEE Ultrason. Symp., **1**, pp. 901–908, 2002.
- [11] W.P. MASON, *Physical acoustics principles and methods*, Academic Press 1A, 1964.
- [12] R.B. STOKES, and J.D. CRAWFORD, *X-Band thin Film Acoustic Filters on GaAs*, IEEE trans. Microw. Theory Tech., **41**(6/7), pp. 1075–1080, June/July 1993.
- [13] A.A. SHIRAKAWA, J.M. PHAM, P. JARRY, and E. KERHERV, *Design Of FBAR Filters At High Frequency Bands*, International Journal of RF and Microw. Computer-Aided Engineering, pp. 115–122, December 2006.

- [14] M. RAIS-ZADEH, and F. AYAZI, *Characterization of High-Q Spiral Inductors on Thick Insulator-on-Silicon*, Journal of Micromechanics and Microengineering, **15**, pp. 2105–2112, 2005.
- [15] H.A.C. TILMANS, W. de RAEDT, and E. BEYNE, *MEMS for wireless communications: From RF-MEMS components to RF-MEMS-SiP*, Journal of Micromechanics and Microengineering, **13**, pp. S139–S163, 2003.

Bulk Acoustic Wave CRF Design

Eden CORRALES, Pedro de PACO, Oscar MENENDEZ, Jordi VERDU

Antenna and Microwave Systems Group (AMS), Universitat Autònoma de Barcelona
(UAB) Escola Tècnica Superior d'Enginyeria, UAB Campus, Barcelona, Spain

E-mail: eden.corrales, pedro.depaco, oscar.menendez,
jordi.verdu@uab.es

Abstract. In a Coupled Resonator Filter (CRF) a set of passive layers allow partial coupling between its two resonators. This allows for much wider bandwidth filter responses than its predecessor, the Stacked Crystal Filter (SCF). This work presents an all-electrical model for the Coupled Resonator Filter and associates the acoustical coupling with an electrical impedance inverter between resonators. The resulting equivalent circuit makes it possible to directly apply classical filter synthesis techniques based on the coupling control between resonators.

1. INTRODUCTION

In recent years, Bulk Acoustic Wave (BAW) filters have been consolidating in the high frequency RF filter scenario. They present several advantages over other technologies as Surface Acoustic Wave (SAW) or ceramic filters: ability to handle input power in excess of 4 Watts, the high Quality factor inherent in these structures (over 1000), high frequency operation (up to 20 GHz), resistance to Electrical Static Discharge (ESD), compatible with semiconductor technology, high miniaturization and temperature stability [1].

Stacked Crystal Filters (SCF) and Coupled Resonator Filters (CRF) are BAW filters which have their piezoelectric resonators coupled acoustically as shown in Fig. 1. Structurally a Stacked Crystal Filter is made up of two thin plates of piezoelectric material separated by one grounded metallic electrode [2]. This electrode shields the electric field between the two piezoelectric plates and, in turn, enables acoustic wave propagation. The structure is usually suspended on either an acoustic reflector or a thin supporting membrane layer over air, to confine the acoustic wave in the structure, avoiding leakage to the substrate. Depending on the materials of the structure and its dimensions, only at the mechanical resonance

frequency, acoustic energy will be transferred from input to output which will constitute the pass band. In the SCF case, the two stacked resonators behave as only one resonator introducing a single pole in the transmission response. To achieve two poles on the transmission, a set of passive layers can be introduced between the two resonators enabling the control of the coupling between resonators and composing the CRF [3]. Then, wider bandwidths can be achieved.

In [4], Lakin proposes a model for the SCF starting from the Mason lumped element transmission line model and extends it into an all-electrical equivalent circuit PI network representation. This model is highly useful for application using standard filter synthesis techniques. This work extends the contribution of the SCF proposing a novel electrical model for the Coupled Resonator Filter and uses it to design a GPS RF filter with Chebyshev response.

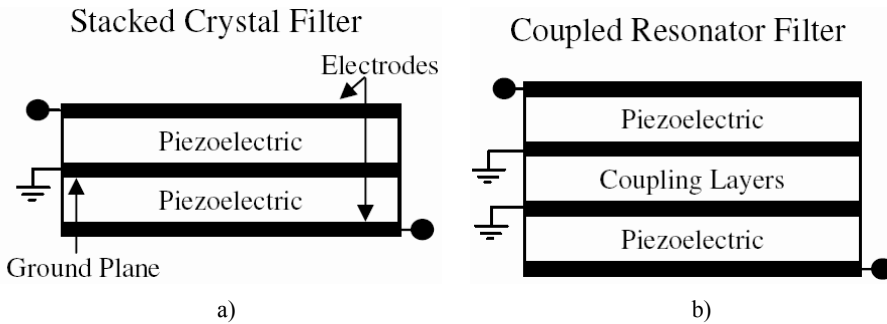


Fig. 1. Basic acoustically coupled BAW filter structures: (a) Stacked Crystal Filter, and (b) Coupled Resonator Filter.

2. EQUIVALENT CIRCUIT MODELING OF COUPLED RESONATOR FILTER

A. Definitions and Network Transformations

Considering a one-dimensional pure mode piezoelectric plate, the Mason model combines, in a simultaneous way, the device's performance in the electrical and the acoustical field [5], [6]. On the one hand, the acoustic wave propagation through the material slab is modeled by an acoustic transmission line between the acoustic ports; the distributed model will be represented by an equivalent lumped element representation in the form of T of impedances as shown in Fig. 2. The values of the impedances are:

$$Z_1 = j Z_p \tan\left(\frac{\theta}{2}\right) \quad (1)$$

$$Z_2 = -j Z_p \operatorname{cosec}(\theta) \quad (2)$$

Where $\theta = kd$ is the electrical length, k is the acoustic wave propagation constant and d is the thickness of the piezoelectric plate given by (3), here neglecting the mass loading effect due to the electrode thickness only for the sake of simplicity:

$$d = \frac{v_p}{2 f_a} \tag{3}$$

Where v_p is the acoustic wave propagation velocity of the piezoelectric and f_a is the anti-resonance frequency in which the input electrical impedance of the resonator reaches its maximum value. The characteristic impedance of the equivalent acoustic transmission line, Z_p , is the acoustic impedance, and depends on both the area A and the acoustic impedance per unit area of the piezoelectric material (Z_{0p}). The piezoelectric effect is included in the model displayed in Fig. 2 by the impedance transformer, representing the conversion of electric energy to acoustic energy, and the negative capacitance [4].

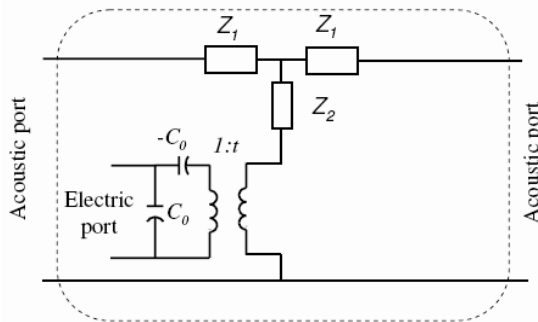


Fig. 2. Mason model for a single one-dimensional piezoelectric slab.

In turn, the dielectric effect is modeled by the shunt capacitor on input of the electric port. The transformer ratio is given by:

$$t = \frac{e}{\epsilon} C_0 \tag{4}$$

Where e (C/m^2) is the piezoelectric constant, ϵ is the material dielectric permittivity and the value of the static capacitor is given by:

$$C_0 = \frac{\epsilon A}{d} \tag{5}$$

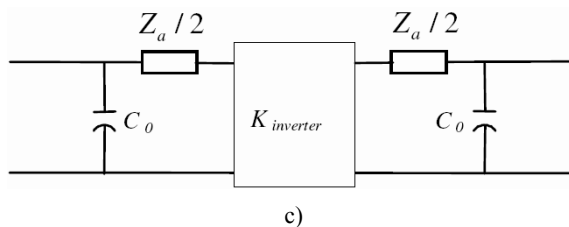
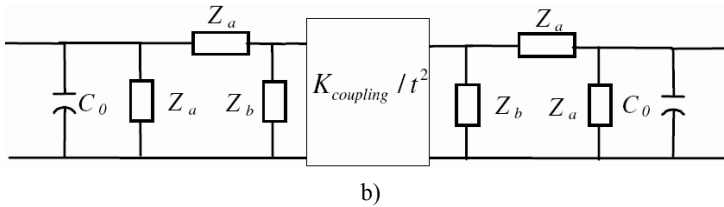
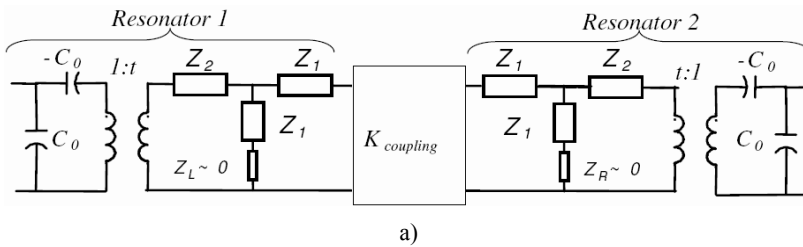
In order to model the Coupled Resonator Filter of Fig. 1b), in a similar way to that used in [4], we start applying the Mason model to each piezoelectric resonator and organizing the circuit as shown in Fig. 3a). The input and output

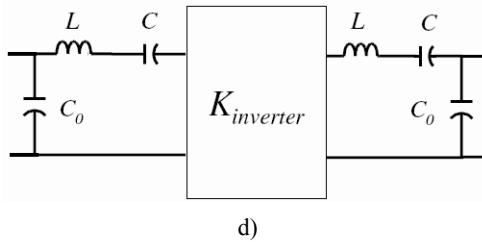
ports of the equivalent circuit are the electric ports of each resonator. The two resonators are connected to each other by means of one of their respective acoustic ports. Unlike an SCF, in a CRF the link takes place by means of the coupling layers modeled with an impedance inverter ($K_{coupling}$). The remaining acoustic ports are loaded by the acoustic impedances Z_L and Z_R respectively. Since we assume two identical resonators, the technological parameters are the same for both, as well as the lumped elements of the model, resulting in a symmetrical topology. In order to simplify the network the impedance transformers are shifted to the same node circuit, so that the effect of the transformers is mutually cancelled due to symmetry. The lumped elements must be modified according to the transformation rules caused by the displacement of the transformers.

Using network analysis techniques with an ABCD matrix cascading scheme it can be shown that the network in Fig. 3a) is equivalent to the circuit shown in Fig. 3b), where:

$$Z_a = \frac{Z_1}{t^2} + 2 \frac{Z_2}{t^2} - \frac{2}{j \omega C_0} \tag{6}$$

$$Z_b = \frac{Z_a Z_1 / t^2}{Z_2 / t^2 - 1 / j \omega C_0} \tag{7}$$





d)
Fig. 3. Networks transformation. (a) CRF implemented with the Mason model. (b) equivalent circuit using network transformations. (c) equivalent circuit after using the approximation of Z_b . (d) all electrical equivalent model for the CRF.

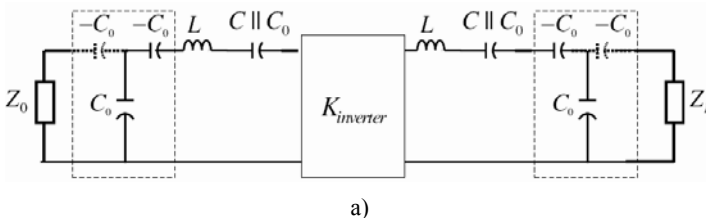
Now, if we suppose that the device operates in a frequency range around the anti-resonance frequency, f_a , we can apply an interesting approximation for Z_b :

$$Z_b \cong -2Z_a \tag{8}$$

Using this approximation the network in Fig. 3b) is equivalent to the more compact circuit shown in Fig. 3c). The value of the central inverter, $K_{inverter}$, models the degree of electrical coupling between resonators, and is directly related to the design parameters of the Coupled Resonator Filter structure: the degree of acoustic coupling that implements the set of coupling layers and the transformer ratio.

$$K_{inverter} = \frac{K_{coupling}}{4t^2} \tag{9}$$

Finally, the impedance $Z_a / 2$ presents an equivalent behavior to a series inductance-capacitance (LC) resonator near the antiresonance frequency. The elements of the LC resonator are determined by the technologic parameters of the material and the geometry of the piezoelectric resonator resulting in the all electrical equivalent CRF model shown in Fig. 3d). The model has been validated operatively at several frequencies, material and structure dimensions. It achieves accurate performances in frequency spans up to 50% with regard to the anti-resonance frequency. The lumped elements of the model correspond to the BVD elements of a single resonator.



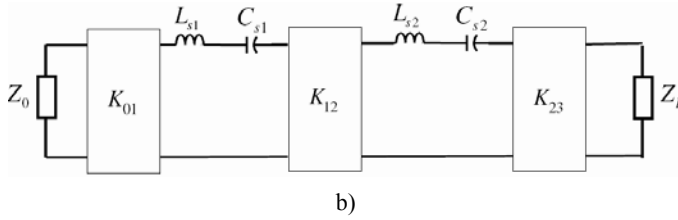


Fig. 4. CRF rearranged model (a) and classical passband filter (b).

$$L = \frac{1}{8} \left(\frac{\pi}{kt} \right)^2 \frac{1}{C_0 \omega_{a1}^2} \quad (10)$$

$$C = \frac{8}{\left(\frac{\pi}{kt} \right)^2 - 8} C_0 \quad (11)$$

where:

$$k_t^2 = \frac{e^2}{Z_a \varepsilon_0 \varepsilon_r v_p} \quad (12)$$

3. DESIGN OF A BASIC CRF FROM THE MODEL

Once we have the all electrical model of the CRF it is direct to apply classical filter theory. Although it is an acoustical device, notice that the model is completely comprised of electrical elements. Hence, the problem to solve is how the input and output impedance inverters can be incorporated. It is well known that an impedance inverter can be constructed by means of a T-configuration of capacitors [7]. This lumpedelement configuration is useful when considering that the negative elements of the inverter could conveniently be absorbed into adjacent elements in practical filters as shown in Fig. 4a). In practice, only the inner negative series capacitor is absorbed while the outer negative series capacitor is neglected. This quasi-inverter approximation is valid in small bandwidths. Using an external series inductor instead of neglecting the outer series negative capacitor, the relative filter bandwidth can be increased.

To obtain the network equivalence we add and remove a series capacitor. The capacitor value is the same as the parallel plate shunt capacitor. The negative series capacitor joined to the shunt capacitor operates as the impedance inverter. The added positive series capacitor is absorbed by the resonator. In Fig. 4a) we have rearranged the CRF model to match it with the classical prototype of a passband filter shown in Fig. 4b) which fulfills the filter requirements by means of a well-known set of relations between inverters and resonator elements [7].

Table 1. GPS RF filter specifications

f_0	1575.42 MHz
Bandwidth	10 MHz
Minimum return losses	10 dB
Z_0	50 Ω
Z_L	50 Ω
Order	2

$$K_{01} = \sqrt{\frac{Z_0 W \omega_0 L_{s1}}{\Omega_c g_0 g_1}} \tag{13}$$

$$K_{12} = \frac{W \omega_0}{\Omega_c} \sqrt{\frac{L_{s1} L_{s2}}{g_1 g_2}} \tag{14}$$

$$K_{23} = \sqrt{\frac{Z_L W \omega_0 L_{s1}}{\Omega_c g_2 g_3}} \tag{15}$$

Where g_i is the low-pass prototype immitances, Z_0 is the source impedance and Z_L the load impedance, W is the relative bandwidth and L_{si} and C_{si} are the lumped equivalent series resonator elements and Ω_c is the normalized cutoff frequency.

Therefore, it is possible to define a two step procedure for the two-pole symmetrical structure.

1) For the resulting series resonators the antiresonant frequency is the same as the filter central frequency.

$$f_0 = f_a = \frac{1}{2\pi} \sqrt{L \frac{C_0 C}{C_0 + C}} \tag{16}$$

2) The input and output inverters are defined by the parallel plate capacitance, and hence, the piezoresonator area.

$$\frac{1}{\omega_0 C_0} = \sqrt{\frac{Z_0 W \omega_0 L_{s1}}{\Omega_c g_0 g_1}} \Rightarrow C_0 = \frac{8 k_t^2 g_0 g_1}{\omega_0 Z_0 W \pi^2} \tag{17}$$

It is important to highlight the close relationship between the impedance inverters obtained from (13)-(15).

$$K_{01} K_{23} = Z_0 \frac{K_{12}}{\sqrt{g_0 g_3}} \tag{18}$$

This means that once the input and output inverters are defined according to the area definition of the parallel plate capacitor, the inner inverter, K_{12} , will also be determined, or equivalently $K_{inverter}$ will be known. Finally, this inner electrical inverter is translated to the acoustical plane by means of (9), and the set of coupling layers can be defined.

4. MODEL AND FILTER DESIGN VALIDATION

In order to validate the reported design procedure we are going to show a design of a GPS RF filter with Chebyshev response. The filter specifications are summarized in Table 1. All the material parameters and electrical elements necessary for reproducing the results are summarized in Table 2. Both resonators are half-wavelength sections of aluminum nitride (AlN).

Table 2. Equivalent circuit model and mason model elements

Mason Model			Equivalent Model		
Symbol	Value	Units	Symbol	Value	Units
Z_{0p} (AlN)	3.7×10^7	Rayls	t	0.322	-
v_p (AlN)	11,500	m/s	k_t^2	5.6%	-
ϵ_r (AlN)	10.5	-	C_0	19.95	pF
e (AlN)	1.5	C/m ²	C	0.96	pF
d	3.65	µm	L	11.09	nH
A	885×885	µm×µm			
$K_{coupling}$	0.295	-	$K_{inverting}$	0.711	-

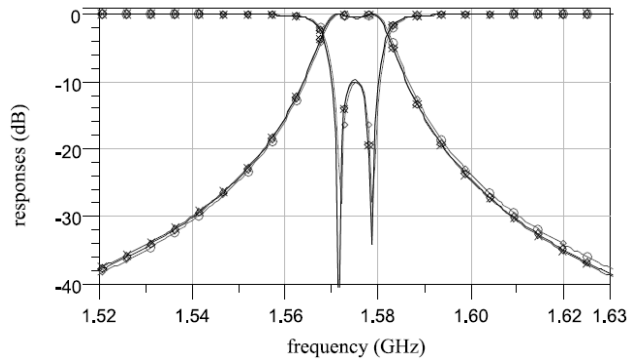


Fig. 5. Ideal GPS RF filter with Chebyshev response (circle line), all electrical equivalent CRF model response (cross line) and device response using the Mason model (diamond line).

Considering a one-dimensional pure-mode piezoelectric plate, the Mason model simultaneously combines the device performance in the electrical and acoustical field [5], and is widely considered to be a validation procedure. Fig. 5 shows the filter transmission response. The ideal filter pass-band prototype transmission response (circle line) agrees with the response obtained through the Mason model (diamond line) and the proposed equivalent Coupled Resonator Filter model (cross line).

5. CONCLUSIONS

This work has proposed a novel equivalent electrical circuit model to a Coupled Resonator Filter. The model has been obtained by means of the Mason model for piezoelectric layers and techniques of network analysis with validated simplifications. The model has been validated operatively at several frequencies, material and structure dimensions. It achieves accurate performances in frequency spans up to 50% with regard to the anti-resonance frequency. From the proposed model, it is possible to systematize the filter design procedure. Moreover a set of closed-form expressions has been provided in a general and systematic procedure to design two-pole coupled resonator filters. The methodology enables us to determine the filter structure dimensions that can synthesize classical response types.

Acknowledgment. This work is supported by the Spanish Comision Interministerial de Ciencia y Tecnologia (CICYT) del Ministerio de Ciencia y Tecnologia and FEDER funds through grant TEC2006-13248-C04-01/TCM.

References

- [1] R.C. RUBY, P. BRADLEY, Y. OSHMYANSKY, A. CHIEN, and J.D. LARSON, *Thin Film Bulk Wave Acoustic Resonators (FBAR) for Wireless Applications*, IEEE Ultrasonics Symposium, **1**, pp. 813–821, 2001.
- [2] K.M. LAKIN, *Thin Film Resonator Technology*, IEEE Trans. Ultrason., Ferroelect., Freq. Contr., **52**, pp. 707–716, May 2005.
- [3] —, *Coupled Resonator Filters*, IEEE Ultrasonics Symposium, **1**, pp. 901–908, Oct. 2002.
- [4] —, *Equivalent Circuit Modeling of Stacked Crystal Filters*, Thirty Fifth Annual Frequency Control Symposium, pp. 257–262, 1981.
- [5] J. ROSENBAUM, *Bulk Acoustic Wave Theory and Devices*. Artech House, 1988.
- [6] K.M. LAKIN, G.R. KLINE and K.T. McCARRON, *High Q Microwave Acoustic Resonators and Filters*, Microwave Symposium Digest, 1993., IEEE MTT-S International, **3**, pp. 1517–1520, 1993.
- [7] J.S.G. HONG and M.J. LANCASTER, *Microstrip Filters for RF/Microwave Applications*. John Wiley & Sons, 2001.

Modelling and Fabrication of FBARs based on Nitrides Micromachined Membranes

D. NECULOIU¹, A. MULLER¹, G. KONSTANTINIDIS²,
C. MOROSANU³, D. VASILACHE¹,
A. KOSTOPOULOS², A. STAVRINIDIS²

¹IMT-Bucharest, Romania

²FORTH Heraklion, Greece

³NIMP Bucharest, Romania

1. INTRODUCTION

Film acoustic bulk resonators (FBARs) have attracted great interest in fabrication of RF devices for cellular phones, navigation, satellite communication, various forms of data communication like WLAN. These applications require small size, high performance and monolithic integration with active electronic devices. FBAR technology is compatible with both silicon and GaAs technologies, allowing integrating of active and passive microwave components in a single chip.

Because acoustic waves propagate approximately four to five orders of magnitude slower than electromagnetic waves, bulk and surface acoustic wave resonators are much smaller than even high permittivity based transmission line structures. FBAR technology is able to produce resonators and filters operating up to 10 GHz by requiring much reduced areas. For these reasons considerable attention has been directed towards microwave acoustic filter development [1].

Microwave acoustic filter efforts of the last years have been, for both solidly mounted and membrane-based bulk acoustic wave (BAW) devices, concentrated on the use of piezoelectric thin films of ZnO [2-3] deposited by sputtering techniques. These devices exhibit good microwave performances but it is difficult to integrate them with other active devices in a compact form. Furthermore, their use in diverse applications require more optimization steps in connection with the quality and the thickness control of the used piezolayers [4] and the thermal budget and contamination aspects should be taken into account when using conventional semiconductor device fabrication lines.

While most BAW and FBAR development effort has been using silicon substrates or silicon-based technology some devices have been fabricated on GaAs substrates [5]. Recent developments of wide band gap (WBG) semiconductor technologies have opened the perspective of manufacturing FBAR devices for applications in the GHz frequency range. The most common WBG materials with pronounced piezoelectric properties are GaN and AlN. The WBG technologies are typical semiconductor technologies offering the compatibility with MEMS technologies and the possibility of monolithic or hybrid integration with other circuit elements. The sub-micron thickness of the GaN or AlN membrane in FBAR devices can increase the operating frequency close to 10 GHz. Such performances are important for 4-th generation of mobile phones, which will probably work in the 3-6 GHz frequency range. Other important applications are the FBAR based sensors with increased sensitivity.

This paper presents the modeling, manufacturing and experimental characterization of nitrides based resonators on high-resistivity (HR) silicon substrate for operation frequencies of few GHz. The modeling integrates electromagnetic (EM) simulations with acoustic circuitual modeling based on 1D Mason approach.

2. FABRICATION

Membrane supported FBAR structures were manufactured using GaN and AlN layers deposited on high resistivity silicon. Conventional contact lithography, e-gun Ti/Au evaporation and lift-off techniques were used to define top-side metallization of the the FBAR structures. Bulk micromachinig techniques were used for the release of the AlN and GaN membranes. The bottom side metallization of the micromachined structure was obtained by means of sputtered gold. Other metallisation systems based on molybdenum deposition were also tested. The photo of the chip with FBAR in series and parallel connection is shown in Fig. 1.

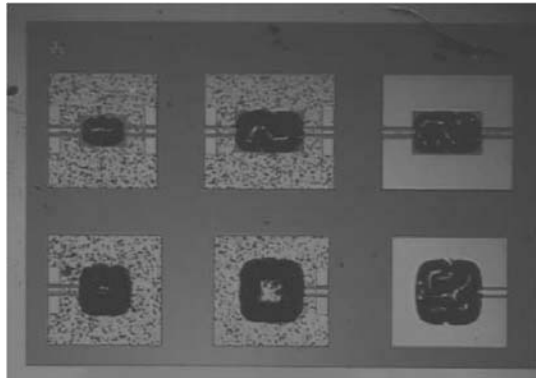


Fig. 1. Photo of the chip with series and parallel FBARs.

3. MODELLING AND SEASUREMENTS

Parallel, series and series/parallel connection of FBAR structures were fabricated. S-parameter were measured with an “on wafer” Automatic Network Analyser and the measurements have shown a pronounced resonance between 1.5 ... 3 GHz, depending on the membrane thickness. In Fig. 2 are shown two FBARs in series configuration connected to the ANA probe tips.

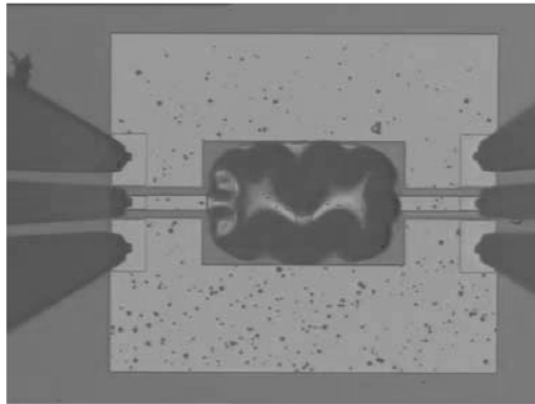


Fig. 2. Photo of two FBARs in series configuration.

Because the structures operate at relative high frequency and the metallization thickness is comparable with the piezoelectric membrane thickness, an advanced modelling technique was developed. The new approach integrates the electromagnetic (EM) simulations (based on Zeland IE3D software package) with the 1D circuitual acoustic Mason model. The EM model uses the IE3D vertical ports feature (ports 3 and 4 in Fig. 3).

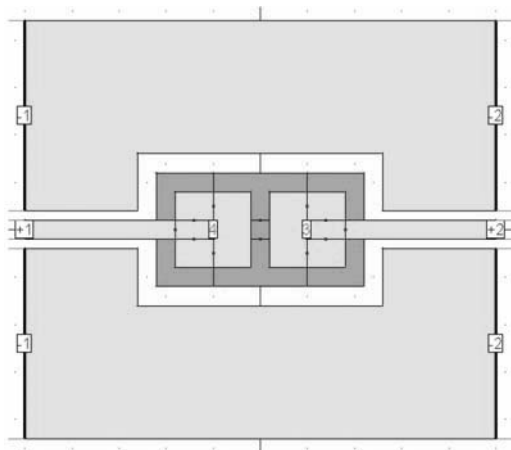


Fig. 3. The layout use for the series FBARs EM model.

The Mason equivalent circuit is shown in Fig. 4 and includes the metallization layers, the active nitride piezoelectric layer as well as the buffer layer (needed for the growth of the GaN on high-resistivity silicon).

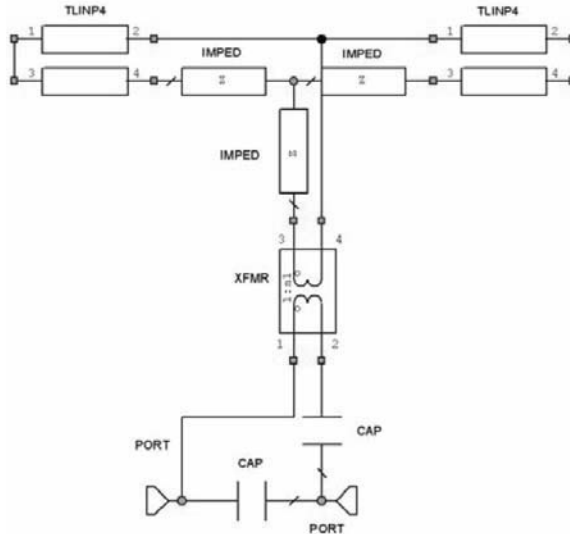


Fig. 4. The 1D Mason model was integrated into advanced electromagnetic simulations (Zeland IE3D).

Two characteristic frequencies can be defined for FBAR: series resonant frequency f_s at maximum conductance and parallel resonant frequency f_p at maximum resistance [6]. For an AlN based FBAR with the membrane thickness of 1 μm , the resistance and the conductance of the two FBARs connected in series are shown in Fig. 5.

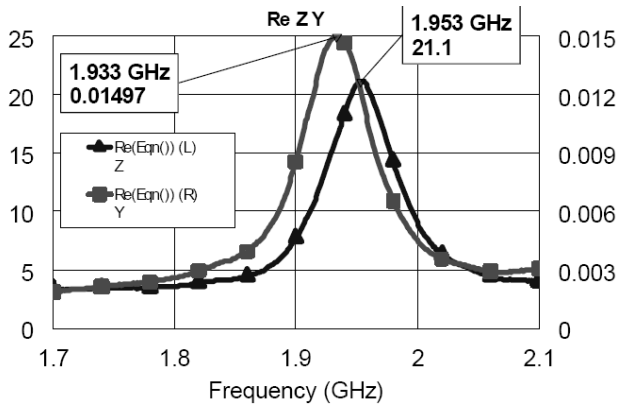


Fig. 5. The conductance (squares) and resistance (triangles) extracted from measurements for the series FBARs.

For these data the following values for the characteristic frequencies were extracted: $f_s = 1.933$ GHz and $f_p = 1.953$ GHz. The calculated effective coupling coefficient is 2.5% and the series quality factor is about 50. These values are for two resonators in series connection and include the acoustic and microwave losses in substrate and feed lines. The extracted bulk acoustic velocity is 11.500 m/s and is in good agreement with other data from literature [7]. Similar results were obtained for FBARs based on AlN and GaN membranes with thickness of 0.36 μm and 0.7 μm , respectively. The resonant frequency for the AlN 0.36 μm FBAR was about 3 GHz.

The measured and the simulated S parameters for the AlN 1 μm thick membrane series FBARs structure is presented in Fig. 6. The agreement is very good.

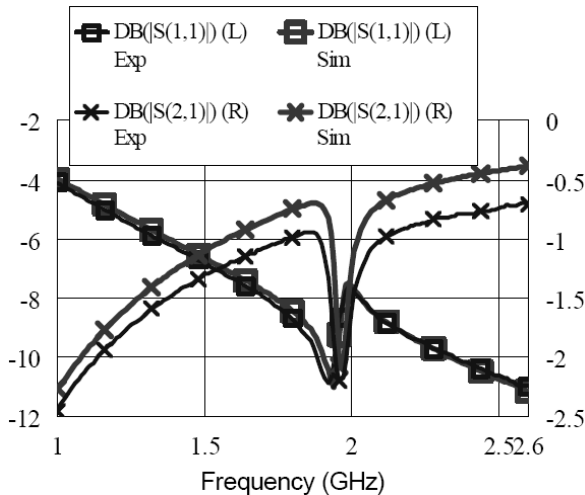


Fig. 6. Comparison between simulated and measured S parameters for the series FBARs.

4. CONCLUSION

Several FBARs based on nitrides micromachined membranes were fabricated and measured. The modelling approach integrated the EM simulations with 1D Mason equivalent circuit. The agreement between the simulated and measured data is good. Resonator structures of this type can be used as building blocks for the fabrication of high Q and wide bandwidth filters, for use in reconfigurable front-ends of various mobile and wireless applications.

References

- [1] IEEE Trans. Microwave Theory and Tech., *Special Issue on Microwave Acoustic Wave Devices for Wireless Communications and Sensing*, **49**(4), April 2001.

- [2] K.K. LAKIN, *Thin Film Resonator Technology*, IEEE Trans. Ultrason., Ferroelectrics and Freq. Control, **52**(5), pp. 707–716, May 2005.
- [3] Q.-X. SU, P. KIRBY, E. KOMURO, M. IMURA, Q. ZHANG, and R. WHATMORE, *Thin Film Bulk Acoustic Resonator Using Zno and Lead-Zirconium-Titanate Thin Films*, IEEE Trans. Microwave Theory and Tech., **49**(4), April 2001.
- [4] E. KWON KIM, T. YONG LEE, H. SUK HWANG, Y. SUNG KIM, Y. PARK, J. TAE SONG, *Improvement of the Crystallinity Of Zno Thin Films And Frequency Characteristics of a Film Bulk Acoustic Wave Resonator by Using an Ru Buffer Layer and Annealing Treatment*, Superlattices and Microstructures, **39**, pp. 138–144, 2006.
- [5] G.R. KLINE and K.M. LAKIN, *1.0-GHz Thin Film Bulk Acoustic Wave Resonators on GaAs*, Appl. Phys. Lett., **43**(8), pp. 750–751, 1983.
- [6] IEEE Standard on Piezoelectricity, ANSI/IEEE Std.176-1987, IEEE, NY, 1988
- [7] xxx <http://www.ioffe.ru>

Development of a Lamb-Wave Sensor for Biological Applications

A.K. PANTAZIS^{1,2,3,*}, E. GIZELI^{2,3}, A. ADIKIMENAKIS^{1,4},
A. GEORGAKILAS^{1,4}, A. STAVRINIDIS¹, G. KONSTANTINIDIS¹

¹Microelectronics Research Group, IESL, FORTH, P.O. Box 1527, Vassilika Vouton, Heraklion, Greece

*E-mail: alepa@physics.uoc.gr; Phone: +302810394105

²Biosensors lab., IMBB, FORTH, P.O. Box 1538 Vassilika Vouton, Heraklion, Greece

³Biology Department, University of Crete, Vassilika Vouton, Heraklion, Greece

⁴Physics Department, University of Crete, P.O. Box 2208, Vassilika Vouton, Heraklion, Greece

Abstract. A variety of acoustic devices are used for detecting different biotargets in real-time. Sensitivity is one of the specifications that a sensor should have and it plays a crucial role in the efficiency of detection. Lamb-wave sensors are devices with great sensitivity due to the fact that they are fabricated on a membrane. Most of today's Lambtype sensors use materials that are being deposited by sputtering like AlN and ZnO. In this paper, we describe the development of a Lamb-Wave sensor, based on epitaxial GaN material, which will be used for biological applications.

1. INTRODUCTION

A great effort is devoted to sensors for applications in biology and medicine. These sensors are divided into electrical, optical and acoustical, depending on the quantity to be measured. Acoustic sensors, like Quartz Crystal Microbalance (QCM), Surface Acoustic Wave (SAW) and Flexural Plate Wave (FPW) or Lamb Wave are used widely for interaction studies and analysis, either between biomolecules or biomolecule - surface. Another interesting application is the detection of specific biotargets, especially when used in human health or environmental monitoring. The most important parameters for a successful biosensor are high sensitivity and low detection limit. The latter is important in cases where the detection of a few biomolecules is required, i.e. pathogenic bacteria.

For bacteria based biosensors the main problem is the detection limit, which is not lower than 10^5 - 10^6 Colony Former Units (CFUs) (single bacterial cells or cell clusters) [1]. However, the Lamb-Wave device is based on a membrane-structure, so all the energy of the acoustic wave is concentrated in a thickness of a few micrometers. This makes the device very sensitive to any changes that occur onto the surface.

Most of the existing Lamb-Wave devices are fabricated on a non-piezoelectric substrate by the deposition of a sputtering piezoelectric film, usually Aluminum Nitride (AlN) [2] or Zinc Oxide (ZnO), on top of it. The membrane thickness in these devices may vary from 50 μm to 2 μm , and it may consist of both the substrate and the deposited material, while the operating frequency is usually in the 1 to 50 MHz range, significantly lower than that used with SAW devices. In this work, instead of sputtering, the piezoelectric used material, which is Gallium Nitride (GaN), was deposited by RF Molecular Beam Epitaxy (RF-MBE), while the membrane thickness was 2 μm .

2. LAMB-WAVE SENSOR

As it was mentioned earlier, FPW or Lamb-Wave sensors are acoustic devices, where an acoustic wave is excited in a membrane. The excitation takes place through an Interdigitated Transducer (IDT) (Fig. 1), when an AC voltage is applied.

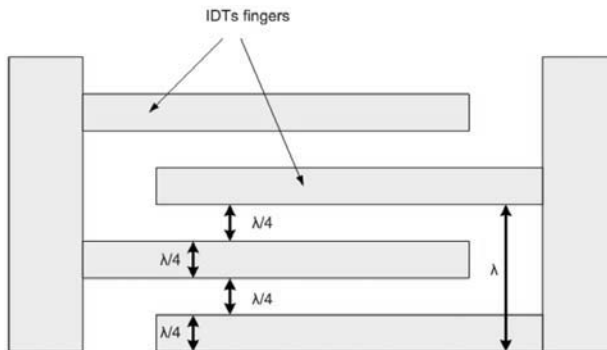


Fig. 1. Schematic representation of an Interdigitated Transducer. The characteristic wavelength is determined by the distance between 2 adjacent fingers connected to the same metal bar.

The characteristic wavelength of an IDT is determined by the distance between 2 adjacent fingers connected to the same metal bar. The width of each IDT finger, as well as the distance between two adjacent fingers connected to two different bars must be equal to $\lambda/4$, so that a period equals to the wavelength λ . Usually, for SAW devices, the operation frequency depends on the piezoelectric material and is:

$$f = v/\lambda \quad (1)$$

where v is the acoustic velocity of the piezoelectric material and λ is the wavelength. However, in Lamb-type devices, the operation frequency does not depend only on these two parameters, but also is affected by the membrane thickness and quality of the piezoelectric material. From literature it was found that there are mathematical formulas that can predict theoretically the operation frequency f . However, as it was mentioned above, quality of material plays a key role. Thus, it is better to characterize these devices experimentally, and check the operation frequency f with a Network Analyzer (NA), rather than relying only on theoretical predictions.

As with the other acoustic sensors, the FPW device can sense quantities that cause changes to the propagating wave, in both amplitude and phase. The propagating waves are divided into two sets: symmetric waves (denoted by S_0 , S_1 , ...), whose particle displacements are symmetric about the neutral plane of the membrane, and anti-symmetric waves (A_0 , A_1 , ...), whose displacements have odd symmetry about the neutral plane [3, 4].

In order for the FPW device to be used for biosensing and chemical sensing in liquids, the membrane configuration must have a thickness d , much less than the supported wavelength λ ($d < \lambda$). In this case, only two waves exist (S_0 and A_0), and there are no losses of the propagated wave towards the liquid that contacts the surface of the device. The device will be “packaged” with a holder and a flow cell. Via a peristaltic pump and tubes the deposition of biomaterials will be implemented. The biorecognition layer will consist of a layer of protein G, followed by an antibody which will be specific for particular bacteria solution [1]. Mass loading on the surface (membrane) of the device, will affect the propagating acoustic wave, in terms of amplitude and phase.

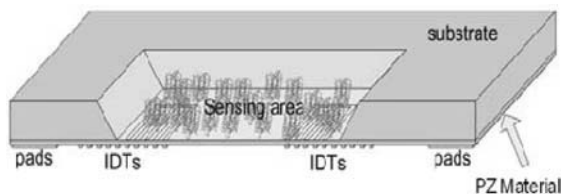


Fig. 2. Lamb-wave biosensor.

The FPW device offers a series of advantages when used for biosensing in liquids. First of all, it consists of 2 interfaces (Fig. 2, 3) allowing the sensing and electrical part to be separated. This means that there is no chance of any short-circuits between liquid and electric circuit during an experiment. Secondly, due to the fact that the acoustic wave is propagating through a membrane of a thickness 2-50 μm , all the energy of the wave is being concentrated into this area, without

any losses towards the bulk. This allows enhanced sensitivity of the device without the need for using a waveguide (like in acoustic Love-wave devices).

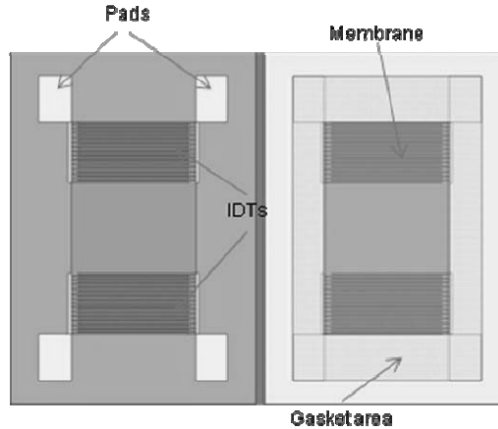


Fig. 3. Front and Back side of a Lamb-wave device.

Last, by choosing proper materials and techniques, the device can be compatible with mass production processing techniques. This means that it can be integrated with other devices or circuits, for the development of novel BioMEMS and Lab-On-a-Chip systems.

3. DESIGN CONSIDERATIONS

In order for a device to achieve maximum functionality, it is very essential to take into account a series of parameters that can or may affect the efficiency of it [5]. These include:

A. Materials

Until now, most of the fabricated Lamb-wave sensors have been based (as mentioned above) on a Si substrate upon which a piezoelectric layer is being deposited by sputtering. AlN and ZnO are the two piezoelectric materials widely used. For the development of our Lamb biosensors materials such as GaN and AlN were chosen. The reasons for choosing these 2 materials are the high acoustic velocity (gives a high operation frequency and, thus, better sensitivity [2]), and the fact that they are semiconductor materials and compatible with processing techniques. Especially, for the III-Nitride group there are a series of advantages comparing with other semiconductors, such as biocompatibility, feasibility of operation in harsh environments and excellent thermal stability.

The main novelty of this concept was that both of these materials were deposited on high resistivity Si wafers by RF Molecular Beam Epitaxy (RF-MBE). So, the final layers (single crystalline material) are of much better quality than those

deposited by sputtering (polycrystalline material), resulting in better signal response. Especially, for the GaN material, there is no report of any Lambwave biosensor based upon it (only SAW type [3]).

B. Geometry of the Device

The wavelength λ of the device depends (Fig. 1) on the width and space of IDTs. The number of IDTs determines the amplification of the signal. The greater the number, the narrower the peak of the signal response. The number of IDTs was chosen based on mathematical formulas and literature. Three different wavelengths were chosen 36 μm , 25 μm and 16 μm , with the number of IDTs pairs being respectively 50, 90 and the 102.

Another parameter is the distance L (also termed delay path) between the two pairs of IDTs (Figure 3). The shorter the distance, the smaller the chip, therefore more chips can be fabricated onto a wafer in every run. However, if the two pairs of IDTs are very close, there is the possibility of cross-talk between them. Additionally, attention should be paid so that the delay path L should be enough, in order to affect the wave, in terms of amplitude and phase, when propagating through the membrane. Based on bibliography, the delay path L was chosen to be 2700 μm .

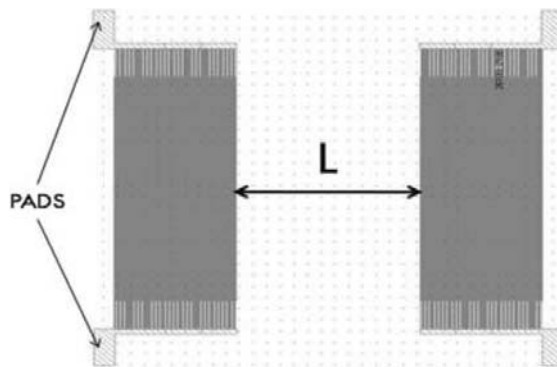


Fig. 4. Top-view of the designed Lamb-wave device.

The size of the membrane defines the sensing area and, subsequently, the volume of tested samples. The membrane size should be enough for fitting the two pairs of IDTs and for providing enough space for effective wave traveling. On the other hand, a large membrane may be fragile, resulting in reliability problems. The size of our membrane was 6570 $\mu\text{m} \times$ 4700 μm .

A final parameter is the size of the chip, which is determined by 2 factors. First, by the size of the contact pads and, secondly, by practical reasons related to easy handling. Also, the size determines the number of fabricated devices after the processing procedure. The size chosen for one chip was 8700 $\mu\text{m} \times$ 6700 μm , so in a 3-inch processed wafer, 60 devices could be fabricated.

4. FABRICATION

A. RF-MBE

High-resistivity ($>10000 \Omega\cdot\text{cm}$) Si (111) wafers, with a thickness of $575 \mu\text{m}$, were used as a substrate. The two chosen piezoelectric materials (GaN and AlN) were deposited inside a Riber 32 RF plasma MBE. For the GaN material structure, the MBE process started with a very thin layer (50 nm) of AlN (Fig. 5). Over this layer, a $0.5 \mu\text{m}$ GaN were deposited, followed by another very thin (10 nm) AlN. Finally, a thick layer of $1.5 \mu\text{m}$ GaN completed the first structure [6]. For the AlN structure, only a $2 \mu\text{m}$ layer of AlN were deposited. During growth, the chamber pressure for both structures were 1.5×10^{-5} Torr.

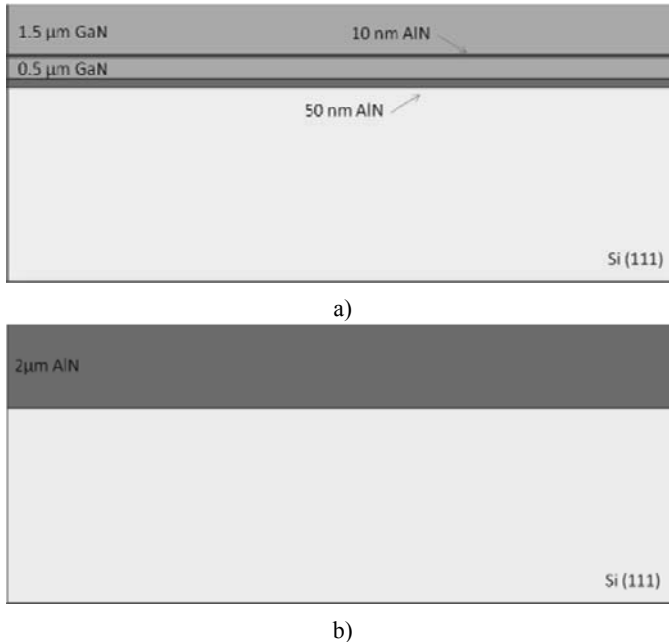


Fig. 5. (a) GaN and (b) AlN MBE structures.

B. Processing

The processing procedure for both structures were the same, due to similar chemistry of GaN and AlN. Five photolithographic masks were designed and fabricated, while conventional contact UV lithography, e-beam metal deposition, metal lift-off and dry etching were used. A Karl-Suss MA6/BA6 mask aligner were used for the alignment of the masks with the wafer. In the first step, alignment marks were fabricated for all steps and subsequently the orientation of the devices was determined, relatively with the major flat of the wafer. This was done, in order

to check if the polarization of the GaN and AlN piezoelectric layer affects the functionality of sensors (despite the fact that polarization is vertical related to the wafer for these two structures).

During the 2nd step, the electric circuit was formed with a metal deposition of 20 nm Cr/200 nm Au, which yielded of the IDTs and the pads (Fig 6a). Additionally, instead of Au, Al was also used in one of the runs. Each of these two materials has an advantage. Au offers better conductivity, while Al reduces the losses from reflections on the IDT structure and leads to better amplification of the signal response.

In the 3rd mask procedure, a front dry-etch took place, where GaN or AlN were etched by using BCl_3 and Cl_2 until the substrate was reached (Fig.6b). By doing this, the chip was well defined and diced after the last step inside the Reactive Ion Etching (RIE) chamber. The RIE chamber is a Vacutec 1360.

After the front side process of the wafer, there are 2 back-side procedures. In the 4th step, the area where the gasket of the flow cell will contact the device, was determined. This was done by Si dry-etch, using SF_6 gas. A depth of 20-50 μm was achieved (Fig. 6c).

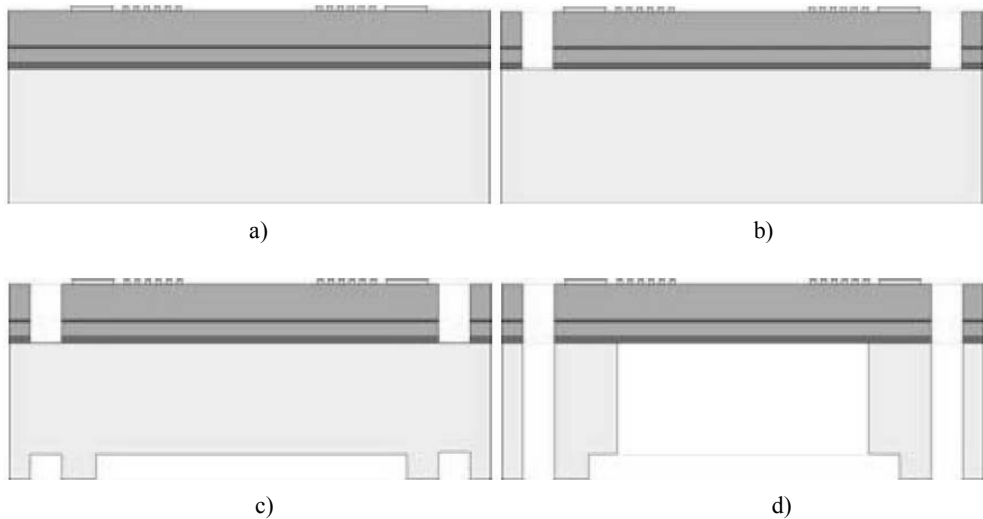


Fig. 6. Process flow for the fabrication of Lamb-Wave sensors.
 (a) Electric circuit formation, (b) Chip's definition, (c)
 Gasket area formation and (d) Membrane formation

The final step, includes the membrane formation. Another Si dry-etch took place (etched $\sim 550 \mu\text{m}$) by using SF_6 gas. During this step, and due to step 2, as it was mentioned above, the chips were diced (Fig. 6d and 7).

Another approach for the two final steps could be by thinning the substrate by lapping techniques [7]. However, it was decided not to follow this approach, despite the fact that it could reduce considerable the etching time, due to the fact

that it would make the device extremely fragile (any mechanical pressure could lead the device to break down).

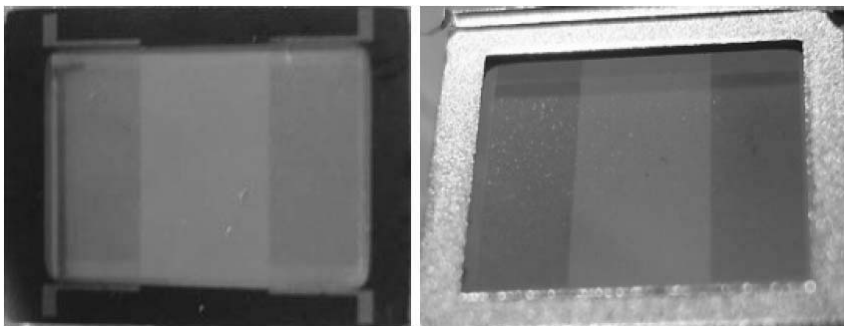


Fig. 7. Front and Back side of a Lamb-Wave biosensor.

5. CONCLUSION – FUTURE WORK

The development of a Lamb-wave sensor based on III-nitride epitaxial material, was presented in this work. A series of design parameters were taken into account before the fabrication of the devices.

The devices will be used for bio-experiments. In these experiments a variety of bio-molecules will be checked in order to test device's sensitivity and efficiency, as well as for optimizing the device. Sensitivity is expected to be 2-3 times greater than that of conventional acoustic devices.

Acknowledgements. The authors wish to acknowledge the support of the European commission through the European Project 507352 “AMICOM” and GGET through PENED No. 03EΔ623.

References

- [1] A. PANTAZIS, G. KONSTANTINIDIS and E. GIZELI, *Towards the Design of a Micromachined Biosystem for Detection of Bacteria*, Proceedings of Protein Biotechnology Summer School, , 23-27 May 2007, Fodele, Crete, Greece.
- [2] H. JEONG, S. KIM, Y. JUNG, H. CHOI, J. LEE and Y. LEE, *Characteristic Analysis of SAW Filters Fabricated Using GaN Thin Films*, Phys. Stat. Sol. A, **188**(1), pp. 247–250, 2001.
- [3] T. LAURENT, F.O. BASTIEN, J. POMMIER, A. CACHARD, D. REMIENS and E. CATTAN, *Lamb Wave and Plate Mode in ZnO/Silicon and AlN/Silicon Membrane. Application to Sensors Able to Operate in Xontact With Liquid*, Sensors and Actuators A, **87**, pp. 26–37, 2000.
- [4] D.S. BALLANTINE, R.M. WHITE, S.J. MARTIN, A. RICCO, E.T. ZELLERS, G.C. FRYE, H. WOHLTJEN, *Acoustic Wave Sensors–Theory, Design and Physico-Chemical Applications*, Academic Press.
- [5] A. PANTAZIS, G. KONSTANTINIDIS and E. GIZELI, “Design considerations for the development of an acoustic Lamtype biosensor”, Proceedings of Protein Biotechnology Summer School, 04-07 June 2008, Fodele, Crete, Greece.

- [6] A. ADIKIMENAKIS, S. SAHONTA, G. DIMITRAKOPULOS, J. DOMAGALA, P. KOMNINO, A. GEORGAKILAS, *Effects of Stress-relieving AlN Interlayers in GaN-on-Si Grown by Plasma-assisted Molecular Beam Epitaxy*, Advances in GaN, GaAs, SiC and Related Alloys on Silicon Substrate, Mater. Res. Soc. Symp. Proc. **1068**, pp. 1068-C06-04 Warrendale, PA, 2008.
- [7] A. PANTAZIS, D. NECULOIU, Z. HATZOPOULOS, D. VASILACHE, M. LAGADAS, M. DRAGOMAN, C. BUICULESCU, I. PETRINI, A.A. MÜLLER, G. KONSTANTINIDIS, and A. MÜLLER, *Millimeter-Wave Passive Circuit Elements Based on GaAs Micromachining*, J. Micromech. Microeng. **15**, pp. 53–59, 2005.

35 GHz Analog Phase Shifter Based on Push–Pull Toggle MEMS Varactor

F. SOLAZZI¹, P. FARINELLI², B. MARGESIN¹, R. SORRENTINO³

¹MemSRaD Group, Fondazione Bruno Kessler (FBK), Via Sommarive 18, 38050 Trento, Italy

²RF Microtech, Via G. Duranti, 93, 06125, Perugia, Italy

³University of Perugia, Dept. of Electronic and Information Engineering, Via G. Duranti, 93, Italy

Abstract. This paper presents the design of two 35 GHz analog MEMS phase shifters to be integrated in reconfigurable reflectarrays. The proposed devices consist of distributed MEMS transmission lines (DMTL) periodically loaded by shunt highly – tunable MEMS varactors. The MEMS varactor exploits a torsion spring anchoring to provide a toggle push – pull mechanism, which allows the device to have a virtually full travel range. A toggle varactor prototype has been electromechanically modeled and manufactured at FBK. The electromagnetic model has also been developed on the basis of the varactor’s measured response and the fitted capacitance values have been used for the design of the phase shifter unit cell. RF full–wave simulations of the phase shifters are presented showing very high RF performance as well as small space occupation allowing their integration in electronically steerable reflectarrays.

Index Terms. Toggle, MEMS Varactor, DMTL, Reflectarray.

1. INTRODUCTION

Radio Frequency Micro-Electro Mechanical Systems (RF-MEMS) have been widely used in the design of low loss circuits for millimeter-waves applications. In particular, several designs of digital phase shifters have been provided by using RF-MEMS switches [1-3]. Smart antenna systems [4] constitute one of the main field of application of RF-MEMS phase shifter, since they allow for extremely low loss and compact reconfigurable systems.

Several examples of MEMS phase shifters can be found based on different architectures. The most common architectures are the distributed MEMS loaded transmission line (DMTL) [1][2] and the TTD MEMS topology [3]. In particular one can distinguish between digital and analog designs. Digital Phase Shifters (DPS) employ capacitive or ohmic switches, able to assume two stable states, *on* state and *off* state, depending on the bridge position with respect to the RF line. In

[2] an example *Ka*-Band 2-bit DMTL is presented, reporting a 128°/dB phase shift at 37.7 GHz.

Digital designs show several advantages such as higher robustness to voltage fluctuations and lower sensitivity to temperature variations. One drawback is the high complexity of the bias network, which increases with the number of bits required. The device space occupation increases with the number of bits as well. As a consequence typically no more than 5 or 6 bits are realized in digital phase shifters, yielding limited angle resolutions.

With respect to DPS, an Analog Phase Shifter (APS) utilizes MEMS varactors to achieve a continuous tuning of the phase shift. The main advantages of this topology for smart antenna applications are the lower complexity of the control network and the higher phase resolution. On the other hand, such a design is more sensitive to temperature variations and the capacitance values can be affected by RF signal power level.

Another drawback in the use of varactors is the low capacitance ratio C_{down}/C_{up} , theoretically equal to 1.5 for a traditional MEMS varactor. Some solutions have been proposed in recent years in order to overcome this limitation [5]-[6]. The APS presented in [6] employs a 6.2 capacitance ratio varactors as unit cell, resulting in a phase shift capability of 170°/dB at 30 GHz. However the device manufacturing is pretty complex and requires the deposition of two sacrificial layers.

This paper focuses on the design of a 35 GHz MEMS analog phase shifter to be used in steerable reflectarrays [7], [8]. It consists of a DMTL [9] periodically loaded by high tuning range toggle MEMS varactors. Two versions are proposed to be integrated in reconfigurable reflectarrays for the electronic beam steering. The first one provides a continuous phase shift in the 0° – 180° range. A 360° phase shift can be achieved by exploiting the reflection of the RF signal, in order to perform a continuous beam steering along one direction. To prevent grating lobes phenomena, array element length has to be less than $\lambda_0/2 < 4.27$ mm at 35GHz. This can concern the width of the circuit, while length can not be subject to any constrains. Hence, no transmission line bending is necessary.

The second version provides a phase shift in the 0° -360° range. Hence, a 720° phase shift can be obtained. By using this version, the reflectarray is able to perform a full scanning along both azimuth and elevation angle, by exploiting the miniaturization capability of MEMS technology. In this case, APS has to be included in a 4.27 mm side square and more than one transmission line bending has to be considered to satisfy this requirement.

The phase shifters employ MEMS varactors based on the push – pull toggle mechanism described in [10]. Such a mechanism virtually allows the varactor tuning capability to cover the whole variation range as well as enriches the device robustness to vibration and selfactuation phenomena. In Section 2, the model of the toggle MEMS varactor is briefly described and some RF measurements are

reported. The optimization of the unit cell of phase shifter is outlined in Section 3. Finally, simulation results of the phase shifter are reported in Section IV. Conclusions and future improvements are drawn in the last Section.

2. TOGGLE MEMS VARACTOR

The design starts from the characterization of a toggle switch designed and fabricated at Bruno Kessler Foundation (FBK) [10]. The Toggle MEMS device consists of a movable $4.8 \mu\text{m}$ thick gold beam anchored to a 50Ω coplanar waveguide (CPW) ground through four torsion springs. The bridge central area ($90 \mu\text{m} \times 90 \mu\text{m}$) represents the varactor top electrode and is suspended $2.07 \mu\text{m}$ above the RF signal line. When internal, or *pull-in*, electrodes are biased with a voltage lower than threshold, the bridge central plate moves down and an increase of MEMS capacitance can be observed. The maximum reachable capacitance before actuation is C_{max} . Similarly, the bridge central plate moves up after biasing external, or *pull-out*, electrodes. Consequently the capacitance decreases down to C_{min} , which is the minimum value before the actuation of external electrode. The actuation voltage V_{act} for both electrode pairs depends not only on the gap between bridge and RF line, but also on torsion spring dimensions and tilt angle α [10].

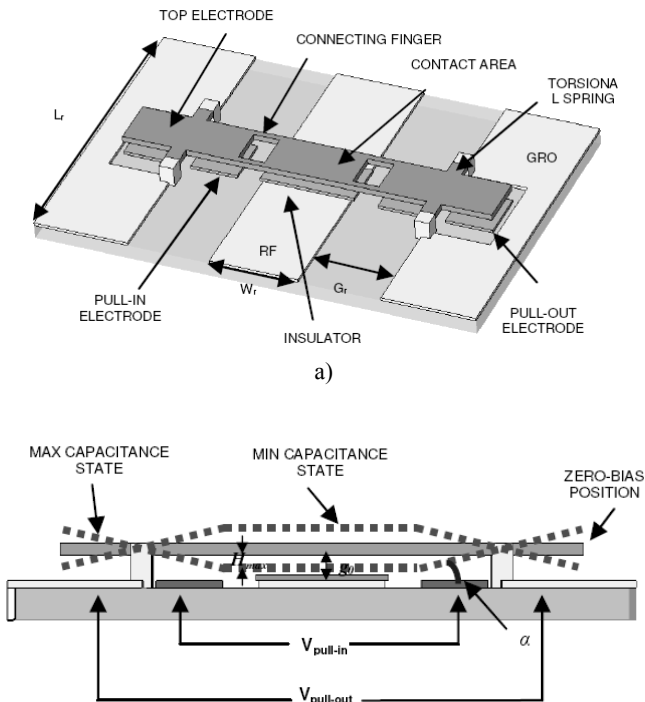


Fig. 1. Toggle MEMS Switch: (a) top view, (b) side view.

The maximum bridge displacement from its zero-bias position before actuation in both up and down directions is indeed:

$$H_{max} = \left(L + \frac{1}{3}l \right) 0.44949 \frac{g_0}{L} \quad (1)$$

when L is the length of mobile electrode, g_0 is the gap between bridge and RF line, and l is the length of connecting finger. As a consequence a proper dimensioning of the bridge actuators and torsion springs may permit the realization of a varactor with theoretically infinite tuning range.

The dimensions of the device under test are $L = 90 \mu\text{m}$, $l = 25 \mu\text{m}$. The torsion spring is $20 \mu\text{m}$ wide, $60 \mu\text{m}$ long and $1.8 \mu\text{m}$ thick. The zero-bias gap g_0 is $2.07 \mu\text{m}$, as mentioned before.

The electromagnetic model of the bridge consists of a variable capacitance C in parallel with a 50Ω CPW. Sparameters measurements have been performed to extract the equivalent values of capacitance, that is, $C_{max} = 77.6 \text{ fF}$ and $C_{min} = 31.4 \text{ fF}$. Hence, the ratio C_{max}/C_{min} is equal to 2.5. This value is higher than the capacitance ratio of conventional MEMS varactors, usually lower than 1.5.

The membrane central part is able to move symmetrically $H_{max} = 1 \mu\text{m}$ upward and downward from its zero-bias position. In any case the device continuous tunability may be increased in order to obtain an H_{max} equal to g_0 from equation (1). RF measurements are reported in Fig. 2, for different values of the pull-in voltage V_{pi} and pull-out voltage V_{po} . The measured pull-in actuation voltage is 35 V whereas the pull-out actuation happens at 37 V.

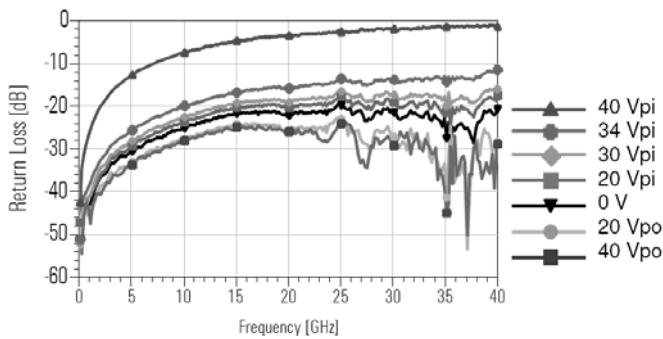


Fig. 2. Return loss measurements of the MEMS varactor for different values of pull-in (V_{pi}) and pullout (V_{po}) voltages.

3. CELL OPTIMIZATION

The APS requirements are reported in Table 1.

Table 1. Phase shifter technical requirements

Constraints Parameters	
Frequency	35 GHz
APS Dimensions (d)	$<\lambda_0/2 = 4.27$ mm
Total CPW Width (S-W+2*G)	352 μ m
Maximum Return Loss (ρ)	15 dB

The design of the phase shifter unit cell follows the optimization procedure described in [9] where the *up* and *down* states of digital MEMS capacitors have been replaced with the *min* and *max* states of the MEMS varactor. The resulting parameters from analytical optimization are listed in table 2.

As a result quartz seems to be the substrate with the best phase shift/attenuation ratio at 35 GHz with respect to silicon substrate. The chosen length for a single cell is $s = 310$ μ m.

Table 2. List of parameters achieved from optimization step

Resulting Parameters	
Substrate: Quartz (ϵ_r)	3.8
Unloaded line Impedance (Z_0)	102 Ω
RF Line width (W)	105 μ m
CPW (G)	123.5 μ m
Cell length (s)	310 μ m
Up State Loaded line Impedance (Z_{up})	60 Ω
Down State Loaded line Impedance (Z_{down})	42 Ω

ADS Momentum® simulations of the phase shifter unit cell are shown Fig. 3. Return loss better than 17 dB and average insertion loss of about 0.3 dB at 35 GHz have been obtained for both limit states of the varactor. The phase shift provided by the single cell is slightly higher than 10°.

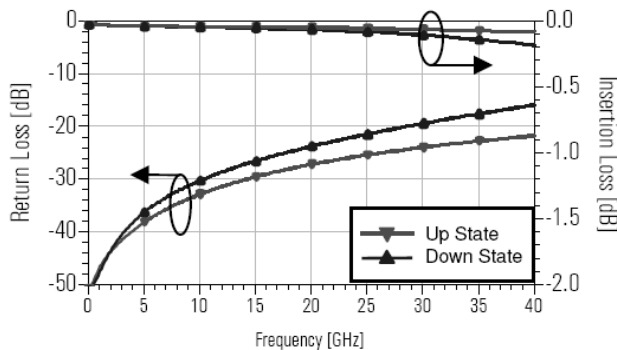


Fig. 3. APS unit cell: comparison between return loss and insertion loss in up state (red) and down state (blue).

4. PHASE SHIFTER DESIGN

The 0° - 180° APS can be achieved by disposing a cascade of $N=17$ unit cells, as shown in Fig. 4. The simulations for the two limit states are shown in Fig. 5.

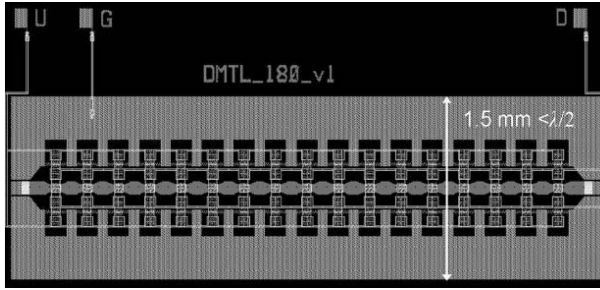


Fig. 4. 0° - 180° APS Layout.

Excellent performances have been obtained in terms of return loss which is better than 15 dB in the 0–40 GHz range. Average insertion loss is 1.1 dB and a phase shift up to 189.1° is achievable at 35 GHz. Hence, the phase shift at 35 GHz is about $163^\circ/\text{dB}$.

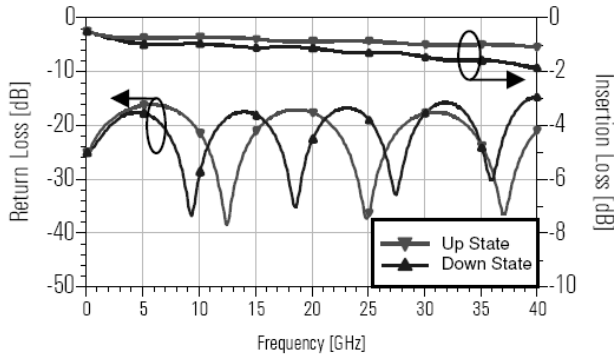


Fig. 5. 0° - 180° APS: comparison between return loss and insertion loss, related to up state (red) and down state (blue)

A short-circuited reflect-type version of this layout can easily be integrated in reflectarray unit cells in order to achieve a 360° phase shift for a full electronic scanning along one direction.

A 0° - 360° APS has also been developed in order to perform beam scanning in both azimuth and elevation directions. It consists of the cascade of 33 cells (Fig. 6) with three 180 degrees bends added in order to keep the device space occupation lower than $\lambda_0/2 \times \lambda_0/2$. The final layout is shown in Fig. 6. A short circuit placed at the end of the transmission line is used to obtain a 720° phase shift by exploiting the reflection of the RF signal.

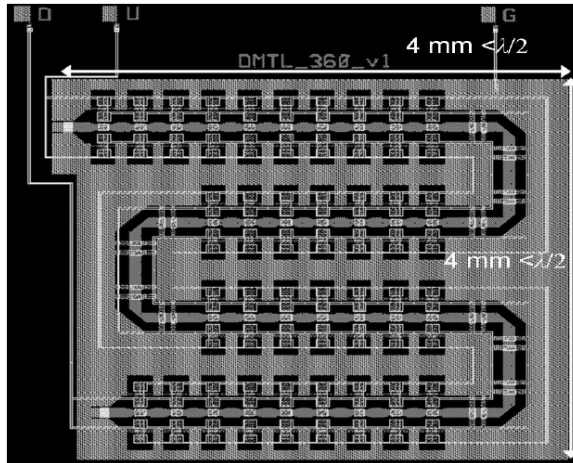


Fig. 6. 0° - 360° APS Layout.

The design of CPW optimized bends has followed the procedure reported in [11] and has been supported by full-wave simulations. The performance of the whole phase shifter is shown in Fig. 7. Note the significant return loss degradation out of the frequency band of interest due to the coplanar bends. Nevertheless, return loss is better than 15 dB at 35 GHz. Because of the CPW bends also the average insertion loss gets worse and a 98°/dB phase shift is obtained, which is a good result despite the complexity of the structure.

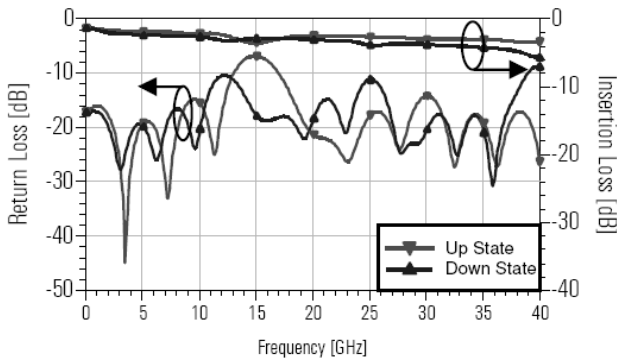


Fig. 7. 0°-360° APS: Comparison between return loss and insertion loss related to up state (red) and down state (blue).

4. CONCLUSION

In this work, the design of two analog phase shifters has been illustrated. The devices employ the wide tuning range MEMS varactors based on push – pull toggle mechanism whose measured performance are presented. Excellent wideband

performances have been achieved with the $0^\circ - 180^\circ$ APS and a $163^\circ/\text{dB}$ phase shift has been obtained. Good performance at 35 GHz have been obtained also for the $0^\circ-360^\circ$ APS, that however can be further optimized in order to reduce the device insertion loss. The APSs fabrication is currently in progress at FBK laboratories in Trento, Italy.

Acknowledgement. This work has been carried out in the framework of the European Network of Excellence AMICOM.

References

- [1] N.S. BARKER, G.M. REBEIZ, *Optimization of Distributed MEMS Transmission-Line Phase Shifters—U-Band and W-Band Designs*, IEEE Transactions on Microwave Theory and Techniques, **48**, November 2000.
- [2] J.S. HAYDEN and G. REBEIZ, *Very Low-Loss Distributed Xband and Ka-Band MEMS Phase Shifters Using Metal–Air–Metal Capacitors*, IEEE Trans. Microw. Theory Tech., **51**(1), pp. 309–314, January 2003.
- [3] B. LAKSHMINARAYANAN and T. WELLER, *Design and Modeling of 4-Bit Slow-Wave MEMS Phase Shifters*, IEEE Trans. Microwave Theory and Techniques., **54**(1), pp. 120–127, January 2006.
- [4] Ahmed El ZOOGHBY, *Smart Antenna Engineering*, Artech House 2005.
- [5] G. McFEETORS, M. OKONIEWSKI, *Distributed MEMS Analog Phase Shifter With Enhanced Tuning*, IEEE Microwave and Wireless Components Letters, **16**, January 2006.
- [6] J. ZOU, C. LIU, J. SCHUTT-AINE, *Development of a Wide Tuning Range Two-Parallel-Plate Tunable Capacitor for Integrated Wireless Communication Systems*, Int. J. RF Microwave CA, **11**, August 2001.
- [7] B. MENCAGLI, R. VINCENTI GATTI, L. MARCACCIOLI, R. SORRENTINO, *Design Of Large mm-Wave Beam-Scanning Reflectarrays*, Proceedings of the 35th European Microwave Conference, 2005.
- [8] [8] H. Legay, B. Pinte, M. Charrier, A. Ziaei, E. Girard, and R. Gillard, *A Steerable Reflectarray Antenna With MEMS Controls*, Proc. IEEE Int. Symp. Phased Array Syst. Technol., October 2003.
- [9] G.M. REBEIZ, *RF MEMS: Theory, Design, Technology*, Wiley & Sons, 2003.
- [10] K. RANGRA B. MARGESIN L. LORENZELLI F. GIACOMOZZI C. COLLINI, MARIO ZEN, G. SONCINI, L. del TIN, R. GADDI, *Symmetric Toggle Switch—a New Type of RF MEMS Switch Fortelecommunication Applications: Design And Fabrication*, Sensors and Actuators, **123-124**, pp. 505–514, September 2005.
- [11] R.N. SIMONS, *Coplanar Waveguide: Circuits, Components and Systems*, John Wiley & Sons, 2001.

A Ka-Band True-Delay-Line Phase Shifter using Capacitive MEMS Switches

Themistoklis PRODROMAKIS¹, Christos PAPAVALASSILIOU¹,
Kostis MICHELAKIS²

¹Circuits and Systems Group, Department of Electrical and Electronic Engineering

²Institute of Biomedical Engineering, Imperial College London, SW7 2AZ, UK

E-mail: t.prodromakis@imperial.ac.uk,
c.papavas@imperial.ac.uk
k.michelakis@imperial.ac.uk

Abstract. We present a monolithic, Si-based, 3-bit phaseshifter for the Ka-band. Our design is based on switched coplanar transmission line segments. Switching is implemented using 12 low insertion loss capacitive MEMS switches. The coplanar junctions (T-junctions) are designed such as phase variations due to switching uncertainties are avoided. Return loss of better than 10dB is reported over a 12.5% bandwidth while the insertion loss is less than 3dB. The proposed phase-shifter topology is capable of a very flat delay over a 35GHz to 45GHz bandwidth with 360° phase control at 45° intervals.

1. INTRODUCTION

Phase-shifters are essential components in electronically steered arrays. The overall performance of such systems is consequently limited by the phase-shifter performance. Conventional designs incorporate FETs as delay path switches. These are easily fabricated and can be switched extremely fast. However, they exhibit high losses, particularly at high frequencies [1]. Alternative designs, utilizing Microelectromechanical systems (MEMS) switches, address this problem and are preferable when high power handling is required. Nevertheless designs found in the literature [2], [3], demonstrate large phase variations due to switching uncertainties. A rather clever approach has been presented by Hacker et. al. in [4], based on a microstrip design on GaAs.

In this paper we present a novel design, based on switched coplanar transmission lines, developed within the AMICOM EU Network of Excellence.

Low insertion loss capacitive MEMS switches are utilized throughout. Two pairs of switches are used for selecting the delay path of each segment and the switches are placed at $\lambda/4$ away from the coplanar junction, ensuring minimal influence of the open sections to the phaseshifter's performance. This design utilizes 12 switches in total resulting in a 3-bit phase-shifter. The device was designed to produce very flat delay time over a 35 GHz to 45 GHz bandwidth with full 360° phase control at 45° intervals. Finally, the system demonstrates a return loss better than 10 dB and less than 3 dB of insertion loss within a 12.5 % bandwidth.

2. RF MEMS CAPACITIVE SWITCH

A. Design Process

The fabrication is based on surface-micromachining using Ni as structural material. The membrane consists mainly of thin evaporated Ni while the anchoring is achieved through thick electroplated Ni. The signal line as well as the ground area below the membrane are formed by a Ta/Pt/Au/Pt stack. The lines outside the switching area and all other interconnections consist of 2-3 μm thick electroplated Au. Two actuation electrodes with an additional plasma-enhanced (PE) nitride isolation of 300 nm are embedded in the ground area for avoiding high actuation voltages. Electroplated air bridges are utilized to ensure ground uniformity on both sides of the actuation electrodes. The substrates are double-side polished 6" silicon with $\rho \geq 3000 \Omega \cdot \text{cm}^{-1}$ and a thickness of 508 μm .

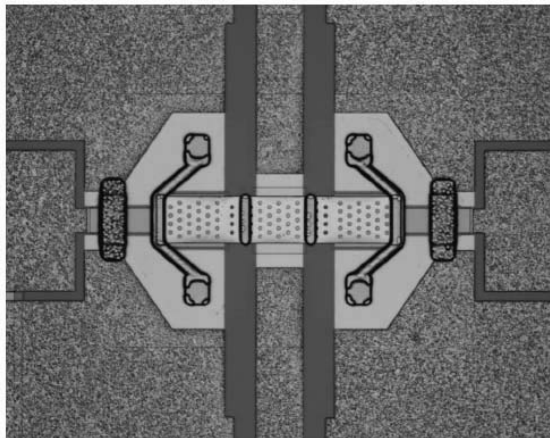


Fig. 1. Photograph of the utilized capacitive MEMS switch.

B. Characterization of the Switch

The overall performance of the phase-shifter will be essentially limited by the performance of the switch. It is therefore necessary to characterize the capacitive switch at the on as well as the off state. The utilized MEMS switch exhibits a rather

low dc/RF contact resistance of 0.3Ω . With an air gap of 2 to 3 μm an on-off capacitance ratio in the range of 20 is expected. In the on state, the switch demonstrates a capacitance of $C_{on}=935 \text{ fF}$ and an inductance of $L_{on}=15.4 \text{ pH}$. In the off-state, the switch can be modeled by a coupling capacitance of $C_{off}=50 \text{ fF}$. These modeled results have been also validated through measurements and they are in excellent agreement [5]. Additionally, the previously discussed process flow provides rather reproducible device characteristics.

When the switch is open, a return loss better than 10 dB 35 GHz and 45 GHz is obtained. Over the same bandwidth, the insertion loss of the switch is less than 0.5 dB, which is one of the lowest so far reported. On the other hand, at the closedstate, the return loss of the switch drops to about 1 dB while the insertion loss is greater than 10 dB at 40 GHz, prohibiting signals to propagate through it.

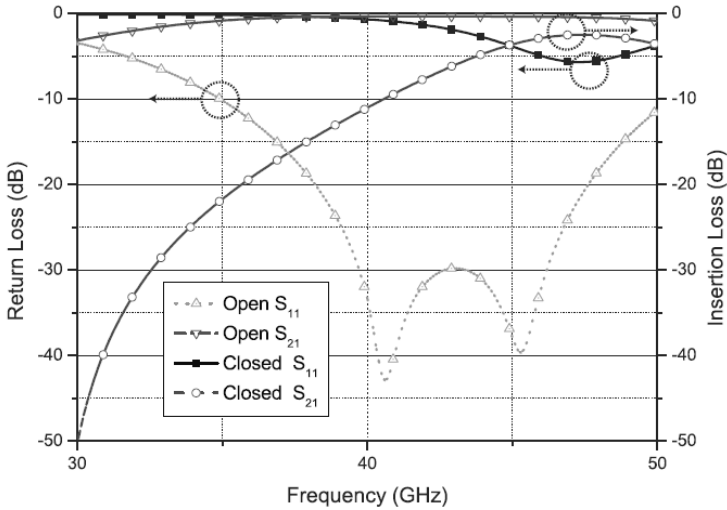


Fig. 2. Simulated return loss and insertion loss for open and close state.

3. PHASE-SHIFTER ARCHITECTURE AND PERFORMANCE

The proposed phase-shifting topology is based on a switchable true-time delay (TTD) network. The TTD network is deployed through 100 μm wide coplanar lines on a 508 μm thick silicon wafer. This architecture comprises three segments each of which two distinct paths can be followed (Fig. 3). The biasing scheme, selects the top or bottom path for each segment. The applied bias actuates two pairs of the previously described MEMS capacitive switches and allows or blocks the propagation of RF signals.

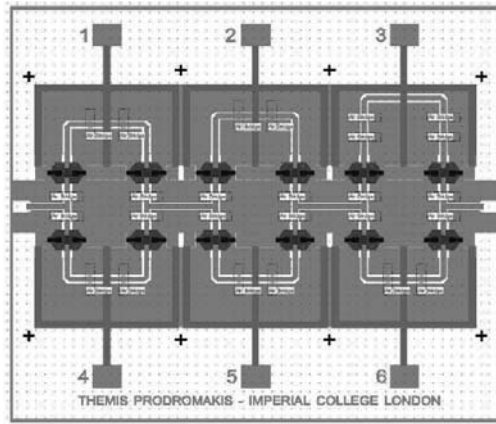


Fig. 3. Layout of proposed phase-shifting topology.

A main drawback of MEMS-based phase-shifters is the phase variation observed due to switching uncertainties. This architecture confronts this problem by utilizing this ultra low insertion loss switch. However, a significant part of this uncertainty is due to the stray admittance of unused delay path as well as part of the switches. Our topology minimizes this problem by efficiently designing the T-junctions, shown in Fig. 3.

The MEMS switches are placed at a quarter of a wavelength ($\lambda/4$) distance from the tee-junction. Therefore, when a switch is closed, the impedance of the stub transforms into an open-circuit at the junction. Consequently, the RF signal is completely reflected at the T-junction, minimizing the contribution of any unintended open stubs. Clearly, this matching scheme holds within the frequency band where the stub is in good proximity of $\lambda/4$. Outside this band, a part of the RF signal will be transmitted through the switch and thus dispersion and consequently phase-variation should be expected.

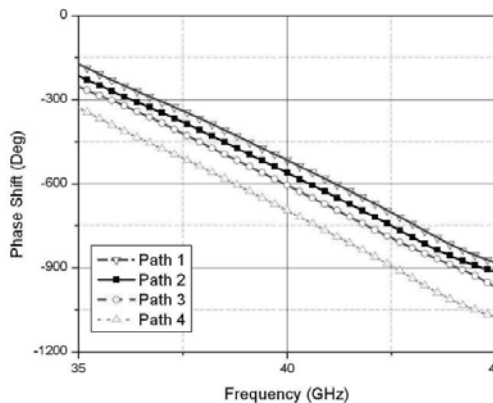


Fig. 4. Simulated phase-shift of all 4 paths.

The proposed system is capable of providing a 360° phase control at 45° intervals. Fig. 4 depicts the simulated phaseshift of four different paths. The first path (000¹), follows the bottom 3 coplanar segments of the device. Path number 2 (100), goes through the top segment of the first section and then the bottom side of the other two segments. With respect to path 1, path 2 exhibits a 45° phase-shift. In analogy, path 3 (010) demonstrates a 90° phase-shift where path 4 (001) is delayed by 360° . Evidently, with appropriate biasing, the above paths can be mixed and different phase-shifts can be obtained.

The recommended architecture validates our expectations for very-low phase variation. Indeed, from 35GHz to 45GHz a rather flat delay time was succeeded. This can be interpreted into a minimal phase variation of $\pm 1.5^\circ$ over the whole 10GHz bandwidth which is valid for all examined delay paths.

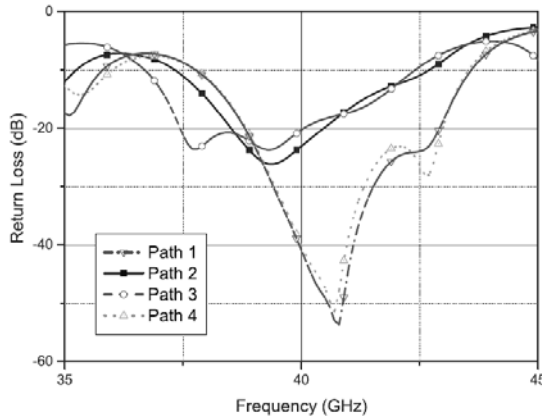


Fig. 5. Simulated return loss of all 4 paths.

Each of the four different delay paths is well matched within a 12.5% bandwidth. As depicted in Fig. 5, the return loss of all possible paths is better than 10dB. Additionally, the simulated insertion loss (Fig. 6) of all possible phase intervals, is less than 3 dB within the same bandwidth. Although the performance of the individual MEMS switch is excellent over a rather wide bandwidth, as represented in Fig. 2, it is quite reasonable the overall performance of the system to be degraded.

Expectedly, this is a 3-bit topology with 12 switches and the overall performance falls well within our expectations. Finally, operating the system at the limits of the device's acceptable performance, the electrical length of the open stubs at the tee junctions deviate from our $\lambda/4$ design goal, justifying the overall slightly narrower bandwidth.

¹This number denotes which of the top or bottom segments are enabled. 0 denotes that the bottom segment is active while 1 denotes that the top coplanar section is selected.

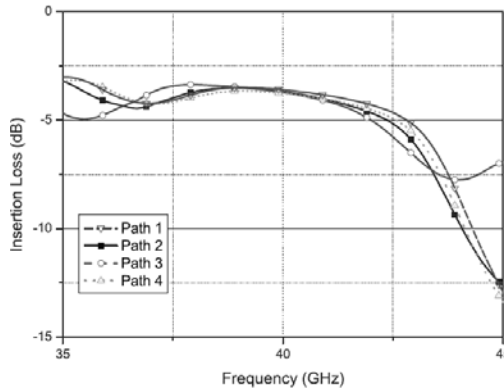


Fig. 6. Simulated insertion loss of all 4 paths.

4. CONCLUSIONS

We have presented a 3-bit Ka-band phase shifter based on a switchable TTD coplanar network. The switching is attained via appropriate biasing of 12 very-low insertion loss MEMS capacitive switches. The proposed phase-shifter has a 360° phase control with a step resolution of 45° . Over the 35 GHz to 45 GHz bandwidth, the attainable phase-variation is $\pm 1.5^\circ$. Additionally, the overall return loss of the system is better than 10 dB while the insertion loss is less than 3 dB within a 12.5% bandwidth. Finally, the system has been fabricated through the AMICOM EU network of excellence MPW platform and the measurements will be presented in a future communication.

Acknowledgments. The authors would like to thank Dr. Thomas Lisec of the Fraunhofer Institute for Silicon Technology for fabricating the device as part of the AMICOM multi-project wafer platform. We also wish to thank Ms. Tatyana Purtova of the Electron Devices and Circuits Department of University of Ulm for providing RF data for modelling the MEMS switch. Finally, we would like to acknowledge the EU AMICOM network of excellence for supporting this work.

References

- [1] E. STENGER, M. SARANTOS, E. NIEHENKE, H. FUDEM, C. SCHWERDT, F.K.D. STRACK, G. HALL, and J. MASTI, *A Miniature, Mmic One Watt w-Band Solid-State Transmitter*, Proc. IEEE International Microwave, Theory and Techniques Symposium, **2**, pp. 431–434, 1997.
- [2] B. PILLANS, S. ESHELMAN, A. MALCZEWSKI, J. EHMKE, and C. GOLDSMITH, *Ka-Band Rf Mems Phase Shifters*, Microwave and Guided Wave Letters IEEE, **9**, pp. 520–522, December 1999.

- [3] S. BARKER and G. REBEIZ, *Distributed MEMS True-Time Delay Phase Shifters and Wide-Bandswitches*, Transactions on Microwave Theory and Techniques IEEE, **46**, pp. 1881–1890, November 1998.
- [4] J.B. HACKER, R.E. MIHAILOVICH, M. KIM, and J.F. DeNATALE, *A Ka-Band 3-Bit RF MEMS True-Time-Delay Network*, Transactions on Microwave Theory and Techniques IEEE, **51**, pp. 305–308, January 2003.
- [5] T. PURTOVA, *Private Communication*, 21 March 2007.

One Single DMTL-based Circuit for RF-MEMS Impedance Tuners and Phase Shifters

Tatyana PURTOVA¹, Tauno VÄHÄ-HEIKKILÄ², Till FEGER¹,
Thomas LISEC³, Joachim JANES³, Bernd WAGNER³
Hermann SCHUMACHER¹

¹University of Ulm, Department of Electron Devices and Circuits, Albert-Einstein-Allee 45,
Ulm, Germany

²MilliLab, VTT Technical Research Centre of Finland, Espoo 02044 VTT, Finland

³Fraunhofer Institute for Silicon Technology ISiT, Fraunhoferstraße 1, Itzehoe, Germany

Abstract. A DMTL-based circuit which can be used both as an impedance tuner and as a phase shifter is presented. It was optimized for the impedance tuner operation and impedance coverage with 256 states is achieved for 25-45 GHz (measured up to 50 GHz). Besides, a 3 bit phase shifter operation is possible, resulting in a phase shift of 180 deg at 35 GHz. This indicates a high potential for designing multi-purpose DMTL circuits. The circuit was fabricated at the Fraunhofer Institute for Silicon Technology ISiT (Itzehoe, Germany) using surfacemicro machining of high-resistivity silicon substrate.

1. INTRODUCTION

Impedance tuners are used as reconfigurable matching networks and in noise parameter- and load-pull measurements of transistors. There exists a variety of tuner topologies, for example stub-based topologies, slug tuners, or loaded-line circuits. Tuning elements can be realized as MMIC varactors or transistors, or as MEMS devices. MEMS technology has a high potential for reducing losses and improving the linearity of the tuners.

Many researchers have been using a stub-based approach to design tuners with good impedance coverage [1]-[3]. These topologies are inherently narrow-band, since they rely on particular electrical lengths of the stubs and connecting lines. Slug-tuners have been successfully realized using MEMS technology [4]. Besides, broadband impedance tuners with good power handling [5], [6] have been designed using DMTL techniques which were originally developed for phase

shifters [7]. Here we present a DMTL circuit which is suitable for both impedance tuner- and phase shifter operation.

2. TECHNOLOGY

The DMTL circuit was fabricated at the Fraunhofer Institute for Silicon Technology ISiT (Itzehoe, Germany) by means of surface micromachining of high-resistivity Silicon ($\rho > 3\text{k}\Omega\cdot\text{cm}$, $508\ \mu\text{m}$) covered with $2\ \mu\text{m}$ of SiO_2 . The fabrication process employs seven masks, including thin metallization for the under-path layer, two dielectric layers (300 nm AlN with $\epsilon_r = 10$ and 300 nm SiN with $\epsilon_r = 7.5$), sacrificial layer for the air-gap ($2.7\ \mu\text{m}$), MEMS membrane metallization, electroplated gold for transmission lines ($3\ \mu\text{m}$) and thick Ni for MEMS springs and supports.

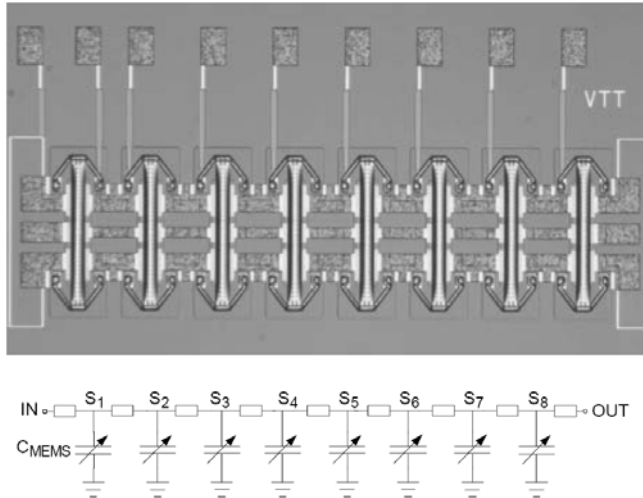


Fig. 1. Microphotograph and the equivalent circuit of the fabricated DMTL impedance tuner and phase shifter.

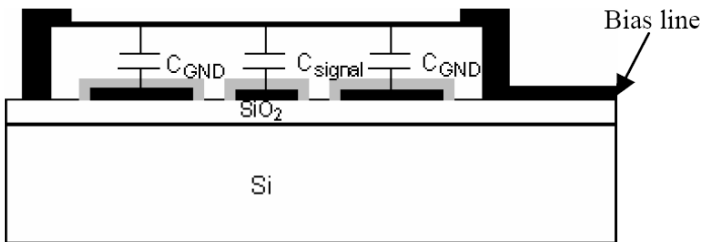


Fig. 2. Cross-sectional view of the MEMS switched capacitor. The total capacitance C_{MEMS} is formed by a series combination of capacitances C_{signal} and C_{GND} , reducing the overall capacitance.

3. DESIGN

A. Equivalent Circuit and Modelling

The microphotograph of the fabricated DMTL impedance tuner and phase shifter is shown in Fig. 1. The circuit consists of a coplanar line loaded with eight shunt capacitive MEMS bridges, operated as switched capacitors (S_1 - S_8) and forming a distributed MEMS transmission line (DMTL). All eight switches are identical and its cross-sectional view is shown in Fig. 2. As illustrated, the bias voltage is applied directly to the MEMS membrane which is isolated from the coplanar line. As a result the total capacitance of the switch, denoted as C_{MEMS} in Fig. 1 is formed by a series combination of C_{signal} and C_{GND} , leading to an overall reduction in the capacitance. Besides, slight downwardsbending of the membrane reduces the air-gap, that increases the up-state capacitance and thus lowers the capacitance ratio. The measured up- and down-state capacitances are about 20 fF and 95 fF respectively. The actuation voltage of the MEMS bridges is about 40 V.

At frequencies well below the Bragg reflection frequency, the characteristic impedance and the phase velocity of the DMTL lines shown in Fig. 1 can be written as:

$$Z_{DMTL} = \sqrt{\frac{L'}{C' + \frac{C_{MEMS}}{s}}} \quad (1)$$

$$V_{ph} = \sqrt{\frac{1}{L' \left(C' + \frac{C_{MEMS}}{s} \right)}} \quad (2)$$

where L' and C' and per-unit-length capacitance and inductance of the unloaded coplanar line, C_{MEMS} is the switched capacitance and s is the spacing between neighbouring MEMS bridges. As it is seen from equations (1) and (2) any change in the MEMS capacitance would modify both the impedance and the phase velocity of the line.

B. Loss Analysis

Impedance tuners are inherently highly mismatched circuits. Thus the commonly used $|S_{21}|$ as a measure of loss is not applicable here. Instead, the loss factor (LF) defined by (3) can be used, which incorporates all losses in CPW line, MEMS bridges and radiation:

$$LF = 1 - |S_{21}|^2 - |S_{11}|^2 \quad (3)$$

Figure 3 illustrates the loss factor versus frequency for the 19 measured states of the impedance tuner. At it can be seen, LF is approximately constant for low frequencies and increases at higher frequencies. Especially above about 45 GHz there is a rapid increase in the loss factor. This can be explained by the fact that the circuit is approaching the Bragg reflection frequency, above which there is no power transfer in the circuit. This frequency region should be avoided in practical circuits.

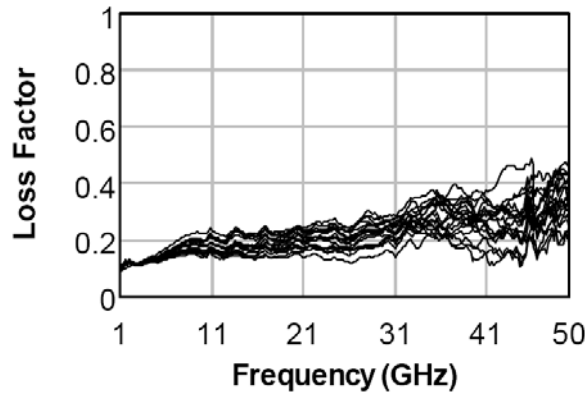


Fig. 3. Loss factor for the 19 measured states of the impedance tuner. The losses start to increase at higher frequencies, which is particularly noticeable above 45 GHz. Above this frequency the effect of Bragg reflections is more and more pronounced leading to no power transfer at the Bragg cut-off frequency.

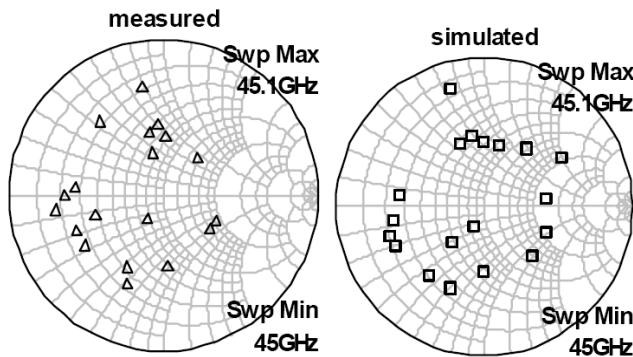


Fig. 4. Impedance coverage for the 19 measured states of the tuner at 50 GHz (left). Good agreement with the simulation is achieved (right).

4. IMPEDANCE TUNER OPERATION

In the impedance tuner operation MEMS switches are actuated in different combinations to create 2^N possible impedances, where N is the number of MEMS

bridges. Owing to the measurement complexity, only 19 states out of $2^8=256$ possible impedance states were measured up to 50 GHz. The measurement results for 45 GHz are shown Fig. 4 (left). An equivalent circuit of the tuner was implemented using AWR Microwave Office and the simulation results for the same 19 states are shown in Fig. 4 (right). Although there are some deviations in the reflection coefficient, the agreement between the measurement and circuit simulation is relatively good.

Simulation results for the remaining impedance states are shown in Fig. 5 (right) for 25–45 GHz. For comparison Fig. 5 (left) shows 19 measured impedances at the respective frequencies. At lower frequencies the produced VSWR is not so high. However, as the frequency increases, a more uniform impedance coverage of the whole Smith Chart is obtained making the circuit particularly suitable for noise-parameter measurements.

5. PHASE SHIFTER OPERATION

The circuit can as well be operated as a DMTL phase shifter by grouping the MEMS bridges into 3 bit segments: one switch provides the least phase shift of bit 1, two switches form the second bit and four switches are used for the bit 3. Thus, in total seven MEMS bridges are required for a phase shifter operation and the 8th one is left unused in the phase shifter mode of the circuit.

Owing to measurement complexity, only the first four states with the lowest phase shift were measured. Fig. 6 shows the measurement results and a comparison to simulation. A good agreement with simulation is obtained. As it can be seen from Fig. 6, the insertion loss of the phase shifter rapidly increases above 45 GHz, indicating that the circuit is approaching its Bragg reflection frequency. The measured phase shift indicates an increment of about 22 degrees at 35 GHz having a potential of being used as a 3-bit 180 degrees phase shifter. Higher phase shifts can be easily obtained by cascading more unit cells. By looking at the return loss, it is below 8 dB up to 37 GHz and degrades sharply above that frequency. The reason is that typical DMTL phase shifters employ high impedance coplanar lines to compensate for increased capacitive load in higher phase shift states and provide good return loss. However, this circuit was optimized for the impedance tuner operation and the dimensions of the unloaded coplanar line were chosen in a way to result in a 50 Ω impedance then loaded with the up-capacitances of the MEMS bridges. This leads to deterioration in the return loss as the capacitive load increases. Still, even without optimisation, at 40 GHz the circuit provides 180 deg phase shift in steps of 22.5 deg and the insertion loss is below 4 dB. This indicates a high potential for designing multi-purpose DMTL circuits.

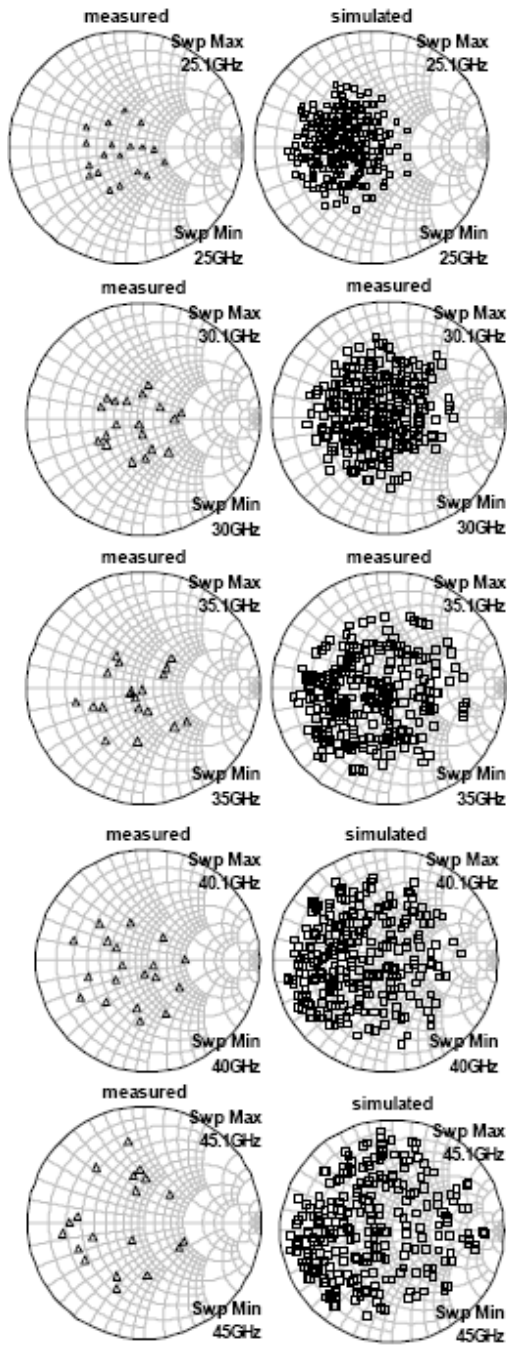


Fig. 5. Simulated impedance coverage for 256 possible states at 25-45 GHz and comparison to the measured 19 tuner states.

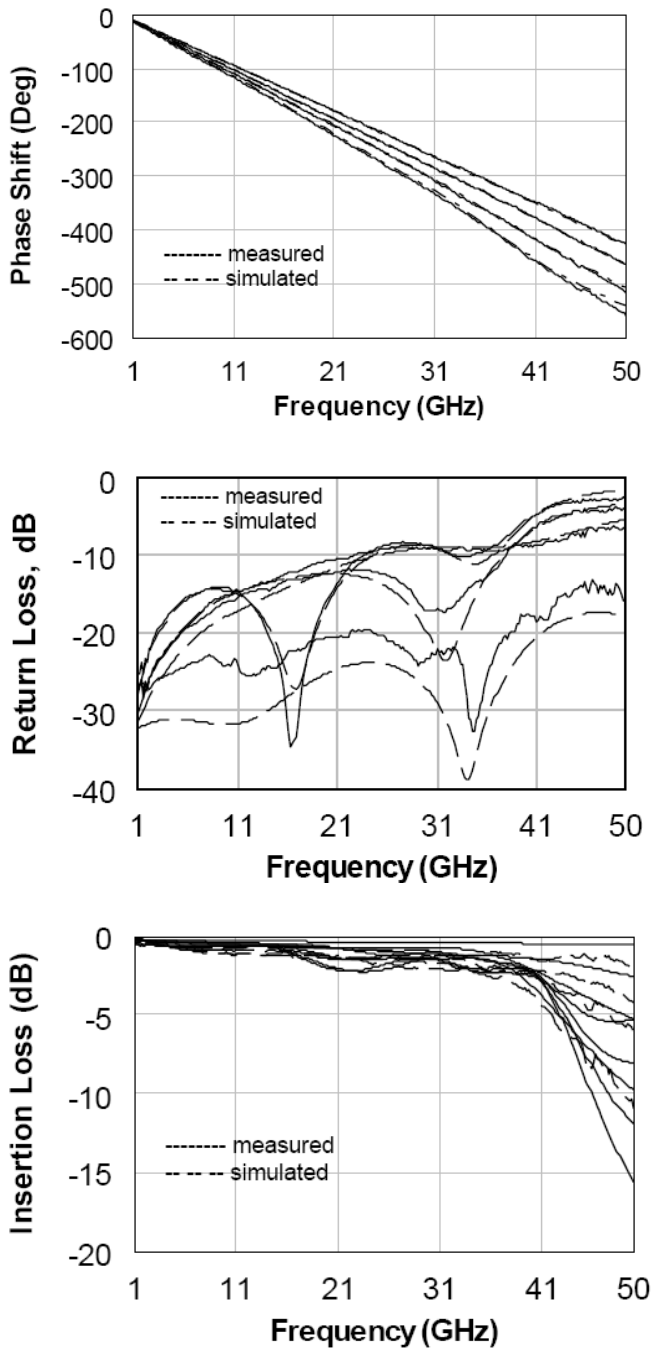


Fig. 6. Measured and simulated performance of the phase shifter in four states corresponding to the lowest phase shift.

6. CONCLUSION

A DMTL-circuit consisting of a coplanar line loaded with eight shunt MEMS switched capacitors was designed. The circuit can be operated as an impedance tuner generating 256 different impedances. Besides, by combining seven MEMS switches into three bit segments, a 3-bit phase shifter operation is possible. Measurement results indicate acceptable performance for both modes of operation indicating a high potential for multi-purpose DMTL circuits.

Acknowledgement. This work was supported by the European Commission through the RF-PLATFORM (Proj. No. 027468). For more information please see www.rfplatform.info.

References

- [1] H.-T. KIM, S. JUNG, K. KANG, J.-H. PARK, Y.-K. KIM, and Y. KWON, *Low-Loss Analog and Digital Micromachined Impedance Tuners at the Ka-Band*, IEEE Transactions on Microwave Theory and Techniques, **49**, pp. 2394–2400, December 2001.
- [2] J. PAPAPOLYMEROU, K.L. LANGE, C.L. GOLDSMITH, A. MALCZEWSKI, and J. KLEBER, *Reconfigurable Double-Stub Tuners Using MEMS Switches for Intelligent RF Front-Ends*, IEEE Transactions on Microwave Theory and Techniques, **51**, pp. 271–278, January 2003.
- [3] T. VÄHÄ-HEIKKILÄ, J. VARIS, J. TUOVINEN, and G.M. REBEIZ, *A 20–50 GHz RF MEMS Single-Stub Impedance Tuner*, IEEE Microwave and Wireless Components Letters, **15**(4), pp. 205–207, April 2005.
- [4] N.S. QIN SHEN BARKER, *A Reconfigurable RF MEMS Based Double Slug Impedance Tuner*, European Microwave Conference, 4-6 October 2005.
- [5] T. VÄHÄ-HEIKKILÄ and G.M. REBEIZ, *A 20–50 GHz Reconfigurable Matching Network for Power Amplifier Applications*, IEEE MTT-S Int. Microw. Symp. Dig., Fort Worth, TX, **2**, pp. 717–720, June 6–11, 2004.
- [6] T. VÄHÄ-HEIKKILÄ and G.M. REBEIZ, *A 4–18 GHz Reconfigurable RF MEMS Matching Network for Power Amplifier Applications*, International Journal of RF and Microwave Computer-Aided Engineering, **14**(4), pp. 356–372, 2004.
- [7] N.S. BARKER, *Distributed MEMS Transmission Lines*, Ph.D. Dissertation, Elect. Comput. Eng. Dept., Univ. Michigan at Ann Arbor, Ann Arbor, MI, 1999.

Reconfigurable RF-MEMS Based Impedance Matching Network for a CMOS Power Amplifier

J. IANNACCI¹, A. GNUDI², B. MARGESIN¹, F. GIACOMOZZI¹,
L. LARCHER³, R. BRAMA³

¹Fondazione Bruno Kessler (FBK), Via Sommarive 18, 38050 Povo-Trento, Italy
Phone: +39 (0) 461 314441

²University of Bologna, ARCES, Via Risorgimento 2, 40136 Bologna, Italy
Phone: +39 (0) 51 2093013

³University of Modena and Reggio Emilia, DISMI, Via Amendola 2, Reggio Emilia, Italy

Abstract. In this work we present a reconfigurable impedance matching network for a CMOS Power Amplifier (PA), implemented in MEMS technology. The matching network is based on cascaded LC stages and is synthesized in order to match the PA optimum output load to 50Ω at 900 MHz and 1.8 GHz. The MEMS network is implemented in two different ways, both employing switch based variable capacitors and inductors. The technology relies on a surface micromachining process available at the Bruno Kessler Foundation (FBK) in Trento, Italy.

1. INTRODUCTION

Employment of MEMS devices and sub-systems within Radio Frequency (RF) functional blocks is emerging as a promising solution in order to obtain high-performance reconfigurable transceivers [1]. High quality-factor, together with wide tuning range and reduced insertion loss, are some of the key-points making MEMS technology an enabling solution for multi-standard RF platforms [2]. In this paper we present an impedance matching network realized in MEMS technology and designed to be integrated with a CMOS PA [3].

2. FBK RF-MEMS TECHNOLOGY

The RF-MEMS technology available at the Bruno Kessler Foundation (FBK) relies on a surface micromachining process based on gold. High resistivity silicon wafers are employed as substrate and are covered by $1 \mu\text{m}$ field oxide. High

resistivity PolySilicon and TiN/Ti/Al/TiN/Ti multilayer are exploited for the DC biasing of suspended membranes and RF signal lines respectively (see Fig. 1).

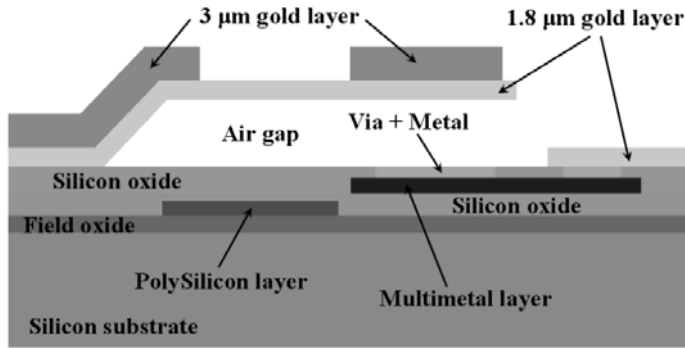


Fig. 1. Schematic cross-section of the FBK RF-MEMS technology. A cantilever based suspended structures realizes a ohmic micro-switch. PolySilicon and multimetal layers are visible together with the two gold metallizations (1.8 μm and 3.0 μm) for the suspended structure.

Both conductive layers are covered by silicon oxide, enabling the realization of metal-insulator-metal (MIM) capacitors as well as ohmic contact where vias are defined. The surface metallization consists of a 1.8 μm electroplated gold layer and the air-gaps are obtained wherever such a layer is deposited over a 3 μm sacrificial photoresist layer. In order to get stiffer gold membranes, for instance in correspondence with anchors and suspended membranes that are meant not to deform, a second gold metallization (about 3 μm thick) is electroplated over the first one mentioned above. Wherever vias to the multimetal are opened, a thin metal layer (150 nm of gold) is sputtered in order to get a gold-to-gold contact when the suspended membranes are actuated. Figure 1 reports a schematic cross-section of the FBK technology taking as example a cantilever switch.

3. RECONFIGURABLE MEMS IMPEDANCE MATCHING NETWORK

The layout of the MEMS-based impedance matching network is shown in Fig. 2 and employs $\frac{3}{4}$ -a-circle gold inductors, ohmic switches and MIM capacitors (Metal-Insulator-Metal) [4]. The network is configured for GSG (Ground-Signal-Ground) probing, enabling the characterization of the network alone, and the subsequent on-board mounting and wire bonding to the Power Amplifier.

The schematic of the MEMS network is shown in Fig. 3. It is based on an LC-series input stage (L_{IN} and C_{IN}) followed by two cascaded LC sections (L_1C_1 and L_2C_2). More in details, an ohmic-series switch (circled in Fig. 2) allows shorting of the C_{IN} capacitor while an ohmic shunt MEMS switch reconfigures the C_2 capacitance. Depending on the MEMS switches state, the network matches the

12 Ω impedance in input to 50 Ω in output at 900 MHz (actuated switches) and at 1.8 GHz (non-actuated switches). The network of Fig. 3 does not account for the parasitic associated to MEMS devices. Details about the topology of the switch circled in Fig. 2 are shown in Fig. 4.

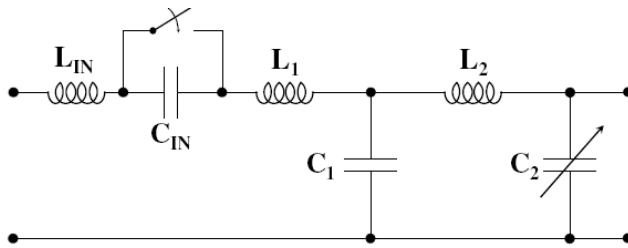


Fig. 3. Lumped element schematic of the network of Fig. 2. The LC-series input stage and the two cascaded LC sections are visible.

It is an ohmic-series switch that behaves as the parallel of two MIM capacitors when the plate is not actuated. Whereas, when the bridge is actuated the two capacitors are shorted due to the ohmic contact between the suspended membrane and the input/output RF lines. In the right part of Fig. 4 the gold metallizations are hidden to get a clear view of the actuation fingers to bias the suspended plate and the RF lines, realized on two different conductive layers.

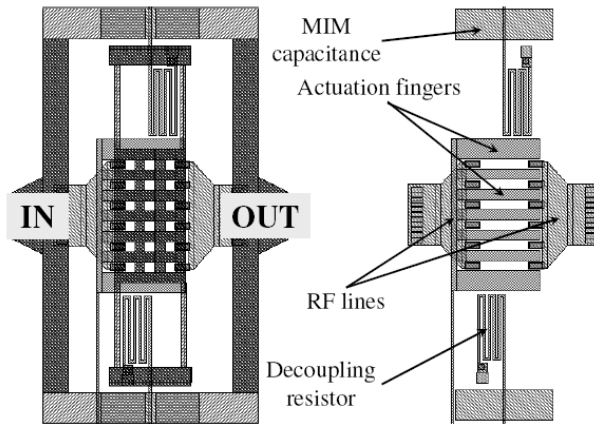


Fig. 4. Close-up of the ohmic-series switch circled in Fig. 2. The left figure shows the layout of the entire switch while the right one reports only the bias and RF lines scheme. In particular, the non-connected input/output RF lines are visible.

The other switch included in the network of Fig. 2 is an ohmic-shunt one (not discussed here), and its behaviour is opposite to the switch of Fig. 4 (i.e. closed when the switch is not actuated and shorted to ground when the plate reaches the pull-in). Measured S-parameters of the network of Fig 2 (without PA) are

compared with the simulation in Agilent ADS™ for the two switches states and are shown in the Smith charts of Fig. 5 at 900 MHz (actuated switches) and of Fig. 6 at 1.8 GHz (non-actuated switches). Since the network is measured with 50 Ω calibrated probes, it has to present a 12 Ω impedance to the left port of Fig. 2 when the right one is loaded with 50 Ω.

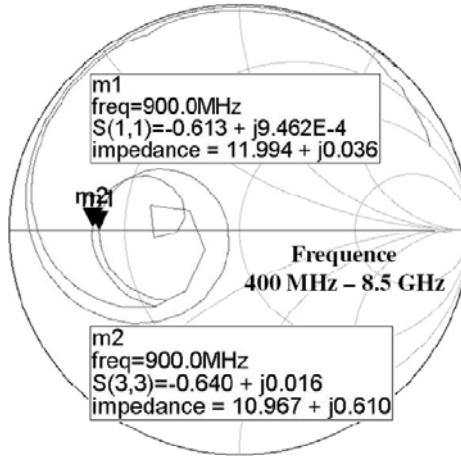


Fig. 5. Smith chart plot for the simulated (S11) and measured (S33) return loss of the impedance matching network at 900 MHz (i.e. actuated switches). The return loss refers to the left port of the network scheme reported in Fig. 2.

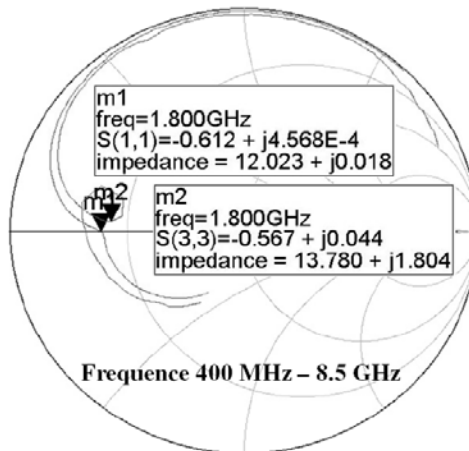


Fig. 6. Smith chart plot for the simulated (S11) and measured (S33) return loss of the impedance matching network at 1.8 GHz (i.e. non-actuated switches). The return loss refers to the left port of the network scheme reported in Fig. 2.

In Figs. 5 and 6 the S_{11} curves represent the return loss of the left port of Fig. 2 while S_{33} the measured return loss. The markers placed at 900 MHz and 1.8 GHz show an offset from 12Ω of measured data compared with simulations due to parasitic effects introduced by a non-perfect opening of vias connecting the gold metallization to the underneath multilayer. This effect has been reduced in the subsequently fabricated samples thanks to a 300°C annealing step.

4. RF-MEMS SERIES OHMIC SWITCH

In this section details about the electromechanical behaviour of the RF-MEMS ohmic switch discussed in previous section are reported. The electromechanical characterization of the switch was performed with an optical profiling system (Veeco™ WYKO NT1100 DMEMS) based on interferometry and stroboscopic illumination for dynamic measurements. Fig. 7 shows the 3D image of the ohmic series switch. In it the ground-signal-ground (GSG) configuration for the RF lines is visible as well as the central rigid plate suspended by means of four straight beams. The switch included in the matching network of Fig. 2 (and reported in Fig. 4) is not available alone with MIM capacitors. However, standalone devices are available on-wafer with the topology of the intrinsic micro-switch (see Fig. 7) which is identical to the one of Fig. 4. The absence of MIM capacitors does not affect at all the electromechanical behaviour of the MEMS switch. Consequently, data collected on the switch of Fig. 7 that are going to be shown are consistent with the device of Fig. 4 included in the impedance matching network.

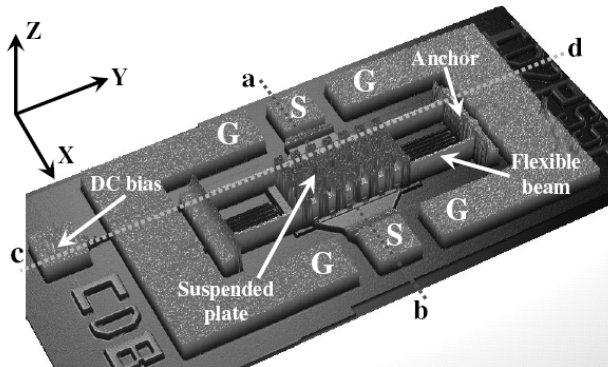


Fig. 7. 3D image of an ohmic series switch obtained with an optical profiling system. The color scale refers to the height along the Z-axis.

Figures 8 and 9 show the vertical profile of the ohmic switch along the **ab** (X-axis) and **cd** (Y-axis) lines respectively. In Fig. 8 the markers are placed on the surrounding ground line and on the suspended bridge, showing an air gap of about $5 \mu\text{m}$. This value, larger than the nominal $3 \mu\text{m}$ gap (see section 2), is due to a

thicker sacrificial layer which was spun on the wafer to intentionally obtain increased air gaps.

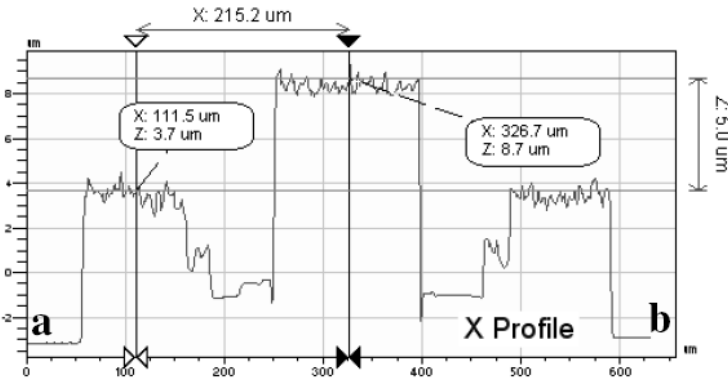


Fig. 8. Vertical profile of the MEMS switch along the **ab** line (X-axis) of Fig. 7. The two markers show the difference of height between the ground lines and the suspended plate (about 5 µm).

In Fig. 9 the markers are placed on one flexible suspension and on the plate to show that the thickness of the second gold metallization over the bridge is around 3 µm as described in section 2. Finally, the experimental pull-in/pull-out characteristic of the switch is shown in Fig. 10.

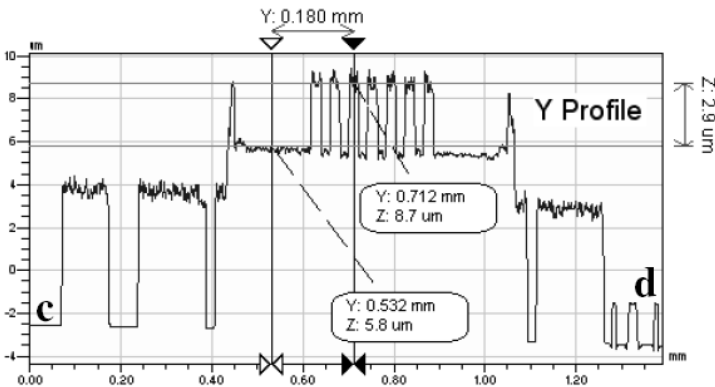


Fig. 9. Vertical profile of the MEMS switch along the **cd** line (Y-axis) of Fig. 7. The height difference (3 µm) between the single gold metallization of the beam and the double gold layer of the central plate is highlighted by the markers.

It is obtained exploiting the stroboscopic illuminator and a triangular bias voltage centred across 0 (i.e. zero mean value) with a very low frequency (20 Hz) is applied in order to get a quasi-static characteristic. The pull-in voltage is around 56 V while the pull-out is observed at 30 V.

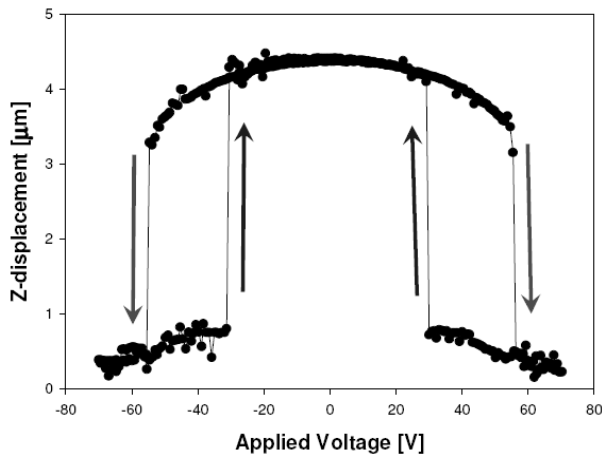


Fig. 10. Static pull-in/pull-out characteristic of the ohmic switch of Fig. 7 measured with the profilometer applying a triangular bias voltage with a frequency of 20 Hz.

5. CONCLUSION

In this work we presented an impedance matching network entirely based on MEMS technology. The network has to be interfaced to a CMOS Power Amplifier (PA) in order to match its optimum 12Ω load to 50Ω impedance at 900 MHz and 1.8 GHz. First collected experimental data of the matching network alone showed a drift from the simulated behaviour because of parasitics introduced by a non-perfect vias opening. However, a 300°C annealing step performed on the subsequently fabricated samples enhanced the agreement of the measured S-parameters compared with simulated data. Moreover, the electromechanical characterization of a series ohmic switch identical to the one employed within the impedance matching network has been shown. In particular, the quasi-static pull-in/pull-out characteristic was observed by means of an optical profiling system based on interferometry. Observation of the sample 3D profile allowed to verify the effective value of important features like the air gap height and the flatness on suspended gold membranes.

References

- [1] M. BEDANI, F. CORAZZA, R. GADDI, A. GNUDI, B. MARGESIN and F. GIACOMOZZI, *A Reconfigurable Impedance Matching Network Employing RF-MEMS Switches*, Proceedings of DTIP, 25-27 April 2007, Stresa, Italy.
- [2] R. GADDI, A. GNUDI, E. FRANCHI, D. GUERMANDI, P. TORTORI, B. MARGESIN, F. GIACOMOZZI, *Reconfigurable MEMS-enabled LC-tank for Multi Band CMOS Oscillator*, IEEE MTT-S 2005 International Microwave Symposium Digest (IMS2005), 12-17 June 2005, Long Beach, CA, USA.

- [3] F.H. RAAB, P. ASBECK, S. CRIPPS, P. B. KENINGTON, Z. B. POPOVIC, N. POTHECARY, J.F. SEVIC, and N.O. SOKAL, *Power Amplifiers and Transmitters for RF and Microwave*, IEEE Transactions on Microwave Theory and Techniques **50**(3), pp. 814–826, March 2002.
- [4] R. GADDI, M. BELLEI, A. GNUDI, B. MARGESIN and F. GIACOMOZZI, *Interdigitated Low-Loss Ohmic RF MEMS Switches*, Proceedings of NSTI, Nanotechnology Conference and Trade Show, Nanotech, **2**, pp. 327–330, 7-11 March 2004. Boston, MA, USA.

Numerical Simulation of a Cathode Micro-Unit With Silicon Field Emitter

V. A. FEDIRKO, S. V. POLYAKOV

Joint Center for Mathematical Modeling – Moscow State University of Technology
"Stankin" and Institute for Mathematical Modeling Russian Academy of Science,
Moscow, Russia

E-mail: vfed@mail.ru

Abstract. Physical and mathematical model for full 2D numerical simulation of a cold emitter unit with semiconductor nano-edge micro-cathode is worked out, which is applied for numerical study of the peculiarities of field emission from semiconductor tip and emission characteristics.

1. INTRODUCTION

Silicon is considered as one of the most suitable material for vacuum micro- and nano-electronics (VM) based on field emitter array (FEA) concept[1]. Silicon, though has orders of magnitude fewer conduction band electrons than metals, has emitting characteristics comparable to metals, and highly developed silicon batch technology can be applied to make various VM devices, including transistor-like structures (see, e.g.,[2]).

Field emission from semiconductors has peculiar features[3, 4] vital for successful development of VM devices. High electric field penetrates deep enough into the semiconductor and results in intense electron heating near the emitting surface[4, 5]. Since the tunneling coefficient exponentially depends on energy, this drastically affects the emission characteristics and heat dissipation. Thus the electron transport in semiconductor field emitter is in fact highly non-equilibrium hot electron process and is an actual physical and practical problem.

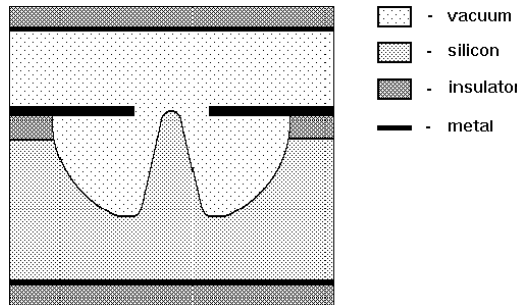


Fig. 1. Scheme of a cathode triode-like cathode micro-unit.

2. RESULTS AND DISCUSSION

We report on a theoretical investigation and numerical simulation of hot electron transport in a wedge n-type silicon field micro-emitter with a nano-edge.

We consider the single diode FEA cell of real geometry and use 2D quasi-hydrodynamic self-consistent approach[6] based on continuity equation, energy balance equation and Poisson's equation added by the material equations as a model. Relaxation time approximation is admitted and impact ionization is taken into account when modeling the hot electron transport in semiconductor cathode. Lattice heating is also taken into account. The quasi-electrostatic problem in a vacuum microcell's space outside the cathode is solved self-consistently to obtain current - voltage characteristics.

We have elaborated the relevant numerical method to cope with strong non-linearity and complex geometry of the problem. Original finite difference scheme with alternating triangle grid has been worked and parallel processing has been used to realize effectively the numerical scheme.

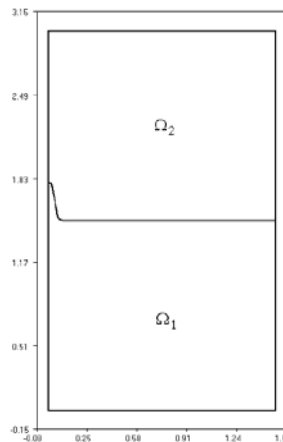


Fig. 2. Computation domain for a diode-like cathode micro-cell;
 Ω_1 – vacuum, Ω_2 – semiconductor.

We have calculated 2D steady-state distributions of the electric field in the cell, and the charge carrier's density and electron temperature distributions in the semiconductor cathod

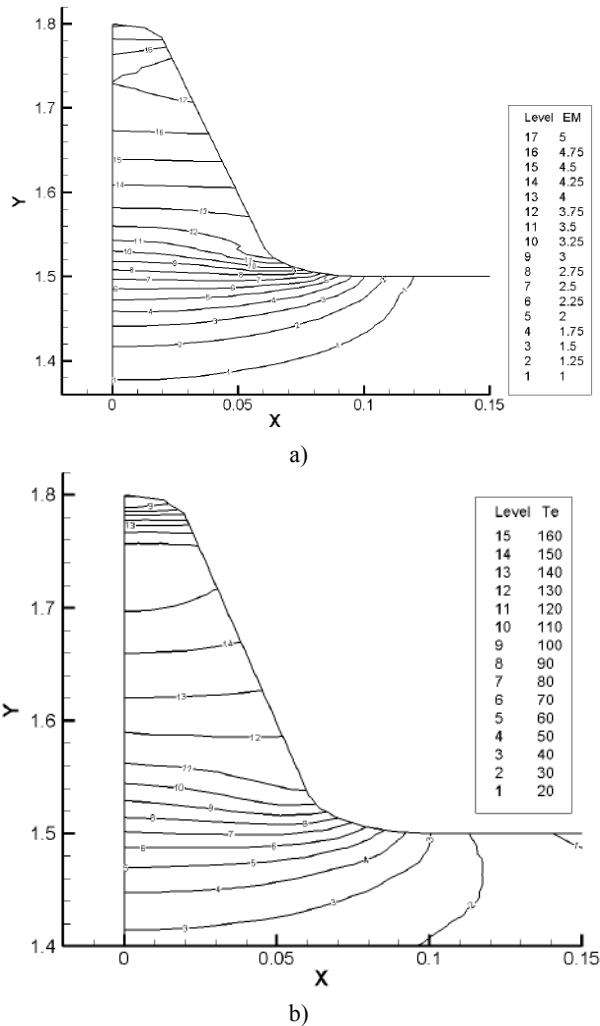


Fig. 3. The electronic field modulus, E_M , (a) and the electron, temperature, T_e (b) distribution in semiconductor cathode neaits apex above the field emission threshold.

We have shown that hot elerons dominate the emission in actual fields and impact ionization may contribute markedly to the electron transport near the edge of the cathode. The electric field is concentrated near the apex of a cathode. That stimulates strong electron heating at the tip a semiconductor cathode and results in the high electron field emission current.

The emission current-voltage characteristics of a cell have been simulated. A kind of a threshold current jump is observed in numerical experiments resulting from the strong non-linearity of coupled quasi-hydrodynamic equations.

4. CONCLUSION

In conclusion, we have elaborated physical and mathematical model for full 2D numerical simulation of entire field emitter microcell with semiconductor nano-edge micro-cathode. The emission characteristics of a cell have been simulated using highly efficient parallel processing. We have shown that electron heating drastically affects field emission from a silicon micro-cathode and impact ionization may contribute markedly to electron transport. Heavy local electron heating may also result in cathode edge instability due to intensive energy exchange between the electron gas and the lattice.

Acknowledgement. The work is supported by the Russian Basic Research Foundation, Project No 06-01-00097. The authors also wish to acknowledge the assistance from the Organizers of the MEMSWAVE2007.

References

- [1] K.R. SHOULDERS and L.N. HEYNICK, *US patent* 3, 453, 478, filed 31 May 1966.
- [2] H.F. GRAY, *Techn. Dig. of the 11th IVMC'98*, 278, 1998.
- [3] V.I. MAKHOV, V.A. FEDIRKO, N.A. DUZHEV, S.A. KAZMINA, *Techn. Digest of IVMC'91*, 136, 1991.
- [4] V.A. FEDIRKO, N.A. DUZHEV, AND V.A. NIKOLAEVA, *Suppl. a la Revue "Le Vide, les Couches Minces"*, **271**, the 7th IVMC, 158, 1994.
- [5] V.A. FEDIRKO and S.V. POLYAKOV, *Proc. SPIE*, **4187**, 94, 2000.
- [6] V.A. FEDIRKO, Yu.N. KARAMZIN and S.V. POLYAKOV, *Simulation of Electron Transport in Semiconductor Microstructures: Field Emission From Nanotip*, in the book: *Mathematical Modeling: Problems, Methods, Applications*, ed. by L.A. Uvarova and A.V. Latyshev, Kluwer Academic/Plenum Publishers, pp. 79-89, New-York, Boston, Dordrecht, London, Moscow, 2001.

Dimensioning of the Stoppers Used to Reduce the Sticking Effect in Electrostatic Capacitor Switches

H. ACHKAR¹, J. RUAN¹, C. VILLENEUVE¹, D. PEYROU¹, F. PENNEC¹,
M. SARTOR², P. PONS¹, R. PLANA¹

¹Université de Toulouse, LAAS-CNRS (MINC), 7 Av du colonel Roche, Toulouse, France
Phone: +33 5 61 33 69 30

²Université de Toulouse, INSA, UPS, LGMT, 135 Av de Rangueil, Toulouse, France
Phone: +33 5 61 55 97 06

Abstract. This paper deals with the problem of sticking in electrostatic RF-Micro switches by proposing a structure which ameliorates the restoring force without changing the pull-in voltage. First we showed the need of different stiffness of the structure between the state before actuation and after it collapses. A methodology for dimensioning the stoppers is then explained and applied to the test structures that we want to fabricate in order to validate our concept.

1. INTRODUCTION

The use of RF micro-switches in mobile applications is conditioned to a low actuation voltage of these components [2]. In the case of electrostatic actuated switches, which are the most common, the reduction of the actuation voltage can be obtained by: the initial gap reduction, the addition of large area actuation pad and the reduction of the bridge's mechanical stiffness. Due to RF issues, the bridge height is often between 2 μ m and 3 μ m and cannot be reduced any more. Even with large electrode area, it is then necessary to design microstructure with low mechanical stiffness. The drawback of a low stiffness is that the switch becomes more sensitive to sticking effect such as dielectric charging [3]. One solution to reduce this problem is to design switches with two states of mechanical stiffness: a low stiffness before actuation and a higher stiffness after actuation.

The objective of this paper is to give a methodology for pre-designing switches with nonlinear stiffness states and to dimension the stoppers height. A first Study was done to verify this concept, the initial stress was studied to analyse

their effect. We ran some simulations to get more precise values of the stiffness for the different proposed topologies and which includes the initial stress effect.

2. PROBLEM DESCRIPTION

Two important characteristic of an electrostatic switch are the Pull-in voltage and the Pull-out voltage which can be summarized by the hysteresis of the C-V curve shown in Fig.1. In the case of a simple bridge as shown in Fig. 2, the analytical expression of the Pull-in (1) and the Pull-out (2) [1] voltages are given by:

$$V_{in} = \sqrt{\frac{8K \left(g_0 + \frac{t_d}{\epsilon_r} \right)^3}{27W W_a \epsilon_0}} \tag{1}$$

$$V_{out} = \frac{t_d}{\epsilon_r} \sqrt{\frac{2K g_0}{W W_a \epsilon_0}} \tag{2}$$

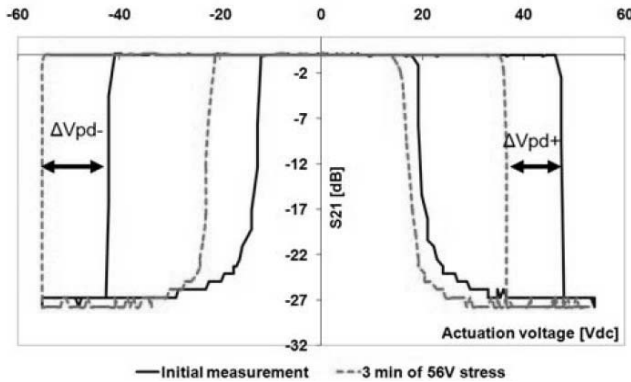


Fig. 1. The hysteresis in electrostatic switch as measured.

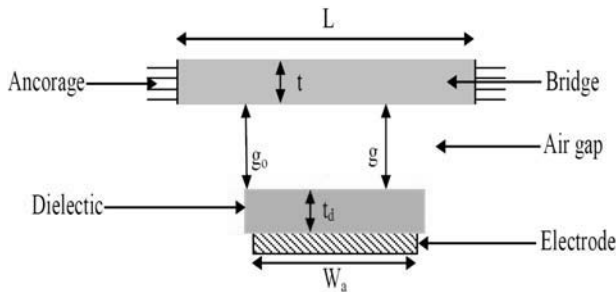


Fig. 2. The structure of a double clamped straight bridge.

We considered that the bridge is actuated through the signal line so the actuation pad has the length of the signal line width and its width is the bridge width. In the expressions the variables signify:

- t: Bridge thickness.
- t_d : Dielectric thickness.
- W: Bridge width.
- W_a : Signal line width.
- L: Bridge length.
- K: Stiffness of the structure f (W, t, L).
- g: Distance between dielectric and bridge.
- g_0 : Initial gap.
- ϵ_0 : Permittivity of air.
- ϵ_r : Dielectric relative Permittivity.

We can see from the expressions (1)&(2), decreasing K to decrease V_{pin} , leads to a decrease in the V_{pout} which will increase the failure of the switch due to dielectric charging. The goal is then to decrease the actuation voltage V_{pin} and increase the release voltage V_{pout} . To do so, we need a structure with two states of stiffness or a nonlinear spring behavior. The stiffness of the structure is given by (3)[1]:

$$K = 32EW \left(\frac{t}{L} \right)^3 \frac{1}{8 \left(\frac{W_a + L}{2L} \right)^3 - 20 \left(\frac{W_a + L}{2L} \right)^2 + 14 \left(\frac{W_a + L}{2L} \right) - 1} \quad (3)$$

The only parameter that we can obtain with two states is the length L, and this is by reducing the anchorage point or an equivalent of this by adding two points of contact at the needed length.

3. STRUCTURE WITH TWO STIFFNESS STATES

As already explained, a structure with two stiffness states is needed. That is a low stiffness in the up states in order to have low actuation voltage and a high stiffness in the down state in order to have high restoring force.

This structure shown in Fig. 3 permits a low initial stiffness which we can control by the length L and a high stiffness once the bridge contacts the stoppers since at this moment it is the length L_s which is working. L_s and t_s being respectively the distance between the stoppers and their height. Fig. 4, shows the restoring force and the electrostatic force as a function of the distance, g, between the bridge and the actuation electrode. We can see that initially the slope of the restoring force is low which indicates a low stiffness, and after contact of the stoppers the value of the stiffness has been increased.

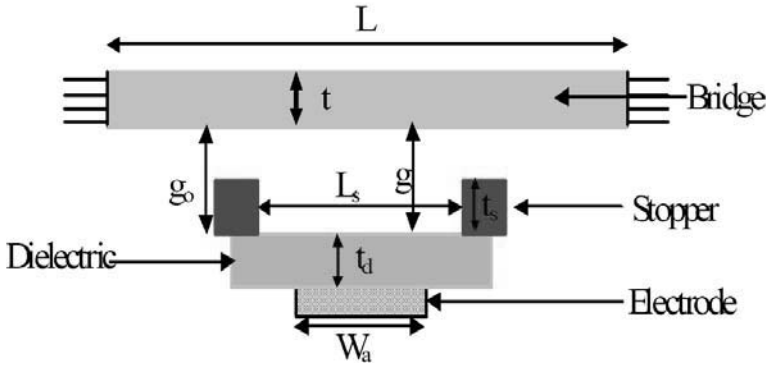


Fig. 3. The structure of a double clamped straight bridge with stoppers.

The graph of Fig. 4, was done using analytical models.

Table 1. Summary of the model parameters

Bridge Parameters		Material Properties	
L	1330 μm	E_{AU}	70 GPa
W	80 μm	ν	0.3
W_a	100 μm	ϵ_r	6.5
t	3 μm	Stoppers Parameters	
t_d	0.25 μm		500 μm
g_0	2.5 μm		1.5 μm

We can read on the graph that for a same pull-in voltage, we succeeded to ameliorate the restoring force five times more. The specifications of the model are in Table 1.

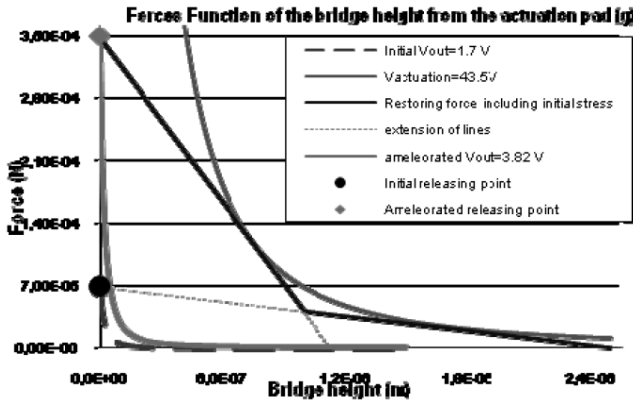


Fig. 4. Graph of the restoring force as a function of the bridge height, showing the two states of stiffness.

A. Dimensioning the Stopper

All over our design, the initial stress was considered to be 50 MPa with about 20% of uncertainty due to process. The length L is imposed by the design specifications to get a low actuation voltage. The distance between the stoppers L_s is depending on the restoring force needed without ignoring the quality of the capacitance in the actuation state. After fixing all these parameters, we need to calculate the height t_s of the stoppers which will define the point of deflection in the stiffness.

To dimension the stoppers, we have two unknowns to be calculated. First we fix the pull-in and the pull out voltages in order to calculate the two states of stiffness using (1) and (2). Once we have K and K_s , with the consideration that the pull in stays the same, we use (4) to calculate g'_0 which is the imaginary initial gap for the stiff state. K_s is the stiffness of the structure after contact.

$$g'_0 = g_0 \sqrt[3]{\frac{K}{K_s}} + \frac{t_d}{\varepsilon_r} \left(\sqrt[3]{\frac{K}{K_s}} - 1 \right) \quad (4)$$

This formulation is obtained by equating the pull-in of two switches having different stiffness and different initial gap. For our model g'_0 was found to be 1.13 μm . We called g_s the point of intersection of the lines describing the restoring forces for the two lengths. The value of g_s was calculated using (5) and was found to be 0.98 μm .

$$g_s = \frac{K g_0 - K_s g'_0}{K - K_s} \quad (5)$$

The value of g_s signifies the height of the bridge at which contact should take place. This value is given at the middle of the bridge, so to have the exact dimension of the stoppers; we need to look to the height of the bridge in the place where the stoppers are placed. The height of the stoppers that have to be placed at a distance of 250 μm from the center is $t_s = 1.47 \mu\text{m}$.

B. Comparing Analytical and Simulated Results

The analytical model of the bridge without stoppers gave an actuation voltage of 43.5 V. We designed the stoppers in a way to keep the same pull-in, but we increased the pull-out voltage from 1.7 V to 3.8 V. If we interpolate linearly the results, we can say that the ratio of the ameliorated pull-out to the original one is of the same order as the ration of the beam length to the distance between the stoppers.

The switch was simulated using Coventor in order to validate the analytical model. The pull-in obtained by simulation was about 42 V weather with or without

stoppers, as it was designed to be. A pull-out voltage less than 5 V was also found for both cases (with and without stoppers). More precise simulations will be done near the pull-out voltage by decreasing the step size. The obtained results are summarized in Table 2.

Table 2. Summary of the results

Analytical Values			
Without stoppers		With stoppers	
V_{in}	43.5 V	V_{in}	43.5 V
V_{out}	1.7 V	V_{out}	3.8 V
Simulated Values			
Without stoppers		With stoppers	
V_{in}	42 V	V_{in}	42 V
V_{out}	< 5 V	V_{out}	< 5 V
Error on V_{in}		3.5 %	
Amelioration of V_{out}		2.2 times	

4. TECHNOLOGY

To realize these stoppers, there are some technological constraints and parameters that should be studied in order to obtain the function that we need. We had different possibilities to fabricate these stoppers, Fig. 4, 5 and 6 shows the different ways we thought about.

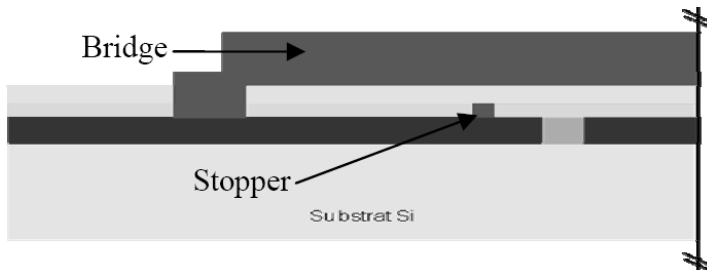


Fig. 5. This photo shows a solution to fabricate the stoppers on the substrate; half of the structure is shown due to symmetry.

The problem in the solution showed in Fig. 5 is that the sacrificial layer will follow the topography of the layers underneath it (which is not shown on the figure) and the bridge will be deformed and will never touch the stopper. Another solution was putting the stoppers in the bridge in order to overcome the flatness problem. For that solution we had two methods, either use two sacrificial layers where the second will define the thickness of the stopper, or the use of only one layer of photoresist and insulate it partially as shown in Fig. 6 and 7.

The first option was a bit complicated due to adhesion reasons between the two layers. Moreover, the thicknesses could not be well controlled and is limited to

the thicknesses that the second photoresist can take. The partial insulation, shown in Fig. 7, method was adopted but it needed some tests to be done on the feasibility of the stopper and the precision of its dimensions. This stopper will affect the flatness of the bridge but since its position is far from the capacitance formation it will have no effects on the RF performance.

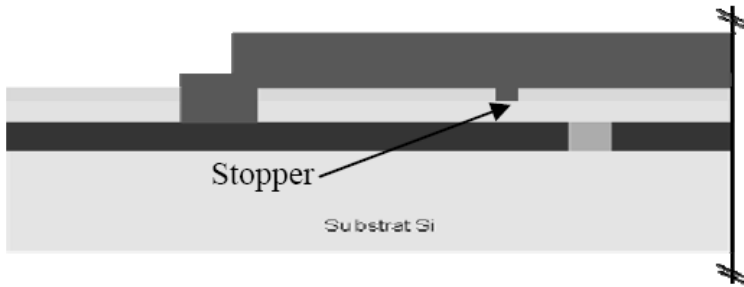


Fig. 6. This photo shows a solution to fabricate the stoppers on the bridge using two photoresist layers; half of the structure is shown due to symmetry.

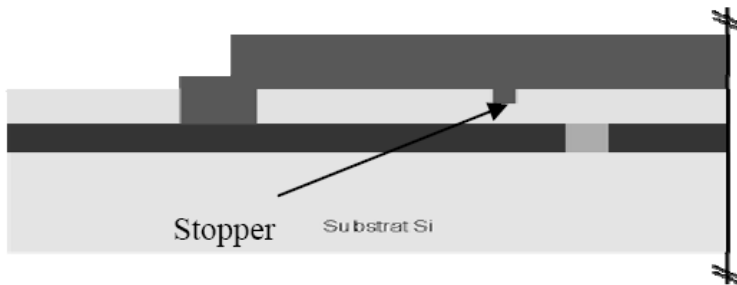


Fig. 7. This photo shows a solution to fabricate the stoppers on the bridge using one photoresist layers and partially insulating it; half of the structure is shown due to symmetry.

Different runs were launched to study the precision of the depth of the stopper and the time needed to have a specific depth. The graph shown below in Fig. 8, shows different holes drilled in the photoresist. The uncertainty obtained on the depth of the drilled hole is about 60 nm. The width of the drilled hole is about 200 μm , but for our application a width of 5 μm has to be studied.

We can realize that near the drilled hole, the photoresist creates a small bump that will perturb the flatness of the bridge. The same problem is expected to be at the anchorage and over the coplanar lines so we need to place the stoppers in a region far from the coplanar lines gap in order to have a good reference for our contact. The profile of the photoresist at the anchorage as well as at the coplanar lines gap is shown in Fig. 9.

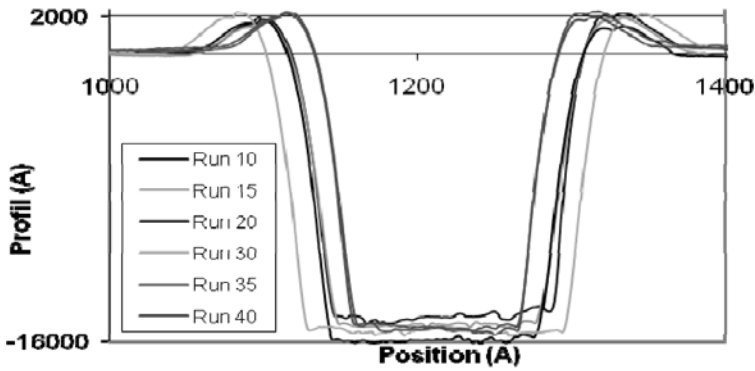


Fig. 8. This graph shows the different profiles of the drilled holes inside a photoresist using the partial insolation, the insolation time was studied for different depths.

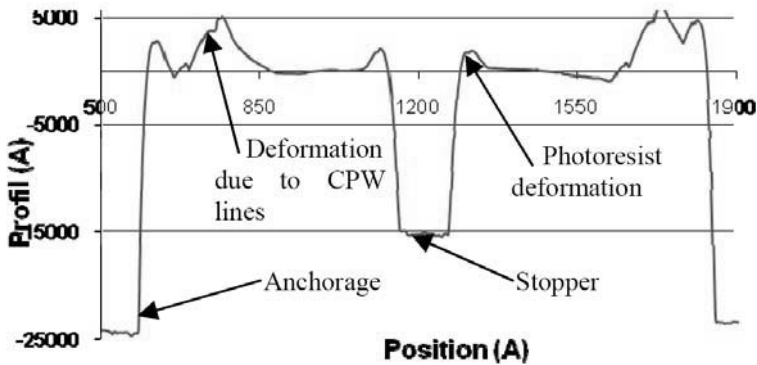


Fig. 9. This profile is for the photoresist deposited on the CPW lines and shows the drilled hole in the middle of the bridge as well as the anchorage at the sides.

5. CAPACITANCE STUDY

When adding the stoppers, a higher restoring force was applied to the structure leading that may lead to a bad contact between the surfaces forming the capacitance. For this reason, a study of the effect of stoppers on the capacitance value was done in order to check if the loss in the capacitance value is reasonable or not.

In Coventor, we calculated the capacitance in the down state of the switch with and without stoppers. The theoretical value of the capacitance, by considering two perfect surfaces is calculated to be 1.84 pF while the one simulated without stoppers is 1.788 pF which is 3% of error. This simulation shows that the stoppers didn't affect the value of the down state capacitance but these values of capacitance

are much less than that, in fact the surface roughness of the dielectric and the bridge creates micro air gaps and the value decreases significantly.

Simulations have been done with perfectly flat bridge and we will perform simulation with real bridge profile as described in Fig. 9.

6. CONCLUSION

After studying the problem of electrostatic micro switches, we found a need to increase the pull-out voltage the maximum possible or in other words to bring the pull-out voltage the nearest possible to the pull-in. Since ameliorating the first affects negatively the second, we proposed a new design that offers a two state stiffness. Just by adding stoppers under the bridge, we obtained a weak initial stiffness which is good to reduce the pull-in voltage and a high stiffness once the bridge touches the stoppers, that is in the down state. A methodology to design and dimension the structure and the stopper in the best way to serve our application was described in this paper. The analytical model was compared to the simulations, always including 50 MPa of initial stress. The simulated results show the amelioration of the pull-out voltage of 2.2 times. If we consider that the lifetime of the switch is proportional to the distance between the zero voltage (where the hysteresis cuts the Y-axis) and the pull-out voltage we can say that we ameliorated the life of the switch 2.2 times more. Effectively, the dielectric charging is faster at the first cycles, and then it becomes more linear so the figure of merit stated above is for the worst case and we can say that the amelioration is more than 2.2 times.

The technological problems were studied and we found that the concept is feasible. The uncertainties on the dimensions due to etching as well as etching parameters were investigated and the process steps were fixed.

The results obtained are promising but still needs to be validated by experimental measurements. Test structures are in the phase of fabrication meanwhile.

Acknowledgement. I would like to acknowledge the reliability team in LAAS and the clean room members in this team for their constructive discussions and for their support in this work.

References

- [1] G.M. REBEIZ, *RF MEMS Theory Design and Technology*, 1st edition, Wiley, Ch. 2.
- [2] P. PACHECO, LINDA P.B. KATEHI, and CLARK T.-C. NGUYEN, *Study of low actuation voltage RF MEMS Switch*, Radiation Laboratory and center for Microsystems, University of Michigan. 2000 IEEE.
- [3] J.R. REID, *Simulation and Measurement of Dielectric Charging in Electrostatically Actuated Capacitive Microwave Switches*, Antenna technology branch, US force Research laboratory, AFRL/SNHA.

- [4] F.M. GUO, Z.Q. ZHU, Y.F. LONG, W.M. WANG, N. LI, G.Q. YANG, W. LU, *Study on Low Actuated MEMS RF Capacitive Switches*”, Elsevier, *Sensors and Actuators A*, **108**, pp. 128–133, 2003.
- [5] S. PAMIDIGHANTAM, R. PUERS, K. BAERT, H.A.C. TILMANS, *Pull-In Voltage Analysis of Electrostatically Actuated Beam Structures With Fixed-Fixed and Fixed-Free end Conditions*, *Journal of micromechanics and microengineering*, **12**, pp. 458–464, 2002.
- [6] S.P. TIMOSHENKO, J.N. GOODIER, *Theory of Elasticity*, 3rd Edition, Ch. 11, pp. 354–361.

Stiction Induced by Dielectric Breakdown on RF-MEMS Switches

A. TAZZOLI, E. AUTIZI, V. PERETTI, G. MENEGHESSO

University of Padova, Department of Information Engineering, Via Gradenigo 6/b,
35100, Padova, Italy

Phone: +39 049 827 7664

E-mail: augusto.tazzoli@dei.unipd.it

Abstract. Dielectric breakdown of the insulator between suspended membrane and actuation layer under anchorages can lead to a new stiction mechanism on electrostatically actuated RF-MEMS switches. Actuator current is investigated as an indicator of stiction issues, and charge trapping phenomena. A simple design guide-line to improve RF-MEMS switches reliability is also furnished.

1. INTRODUCTION

RF-MEMS devices are becoming very attractive for their potential of overcoming the limits of both traditional solid state devices (Si, SiGe, GaAs, GaN, etc...), and space- and weight-consuming mechanical implementations (coaxial switches, phase delayer, etc...) [1]. Despite RF-MEMS devices have been introduced to the research world a couple of decades ago, the reliability of such devices is still an open issue [2].

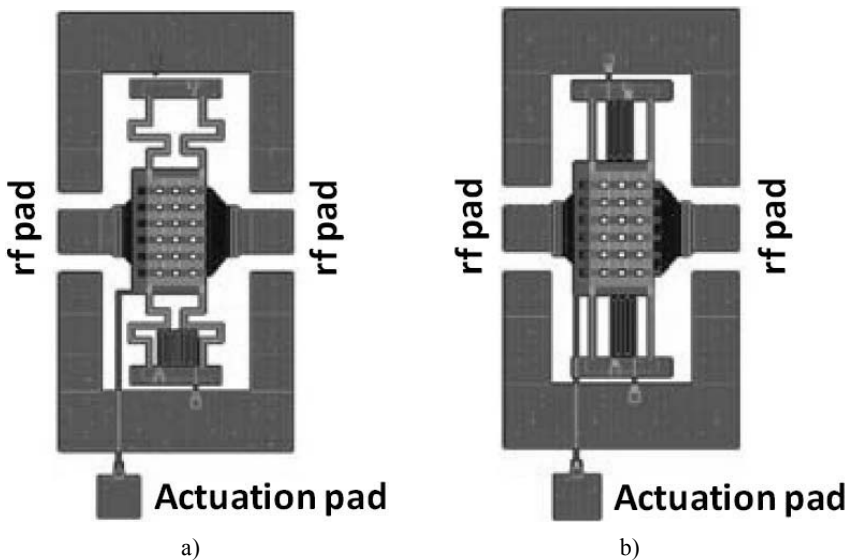
Stiction is nowadays considered one of the most critical problem of electrostatically actuated RF-MEMS switches, typically induced by charge entrapment [3], or suspended membrane fusion with the bottom RF-signal line (metal-to-metal fusion in ohmic switches) [4]-[6]. In both the cases, the suspensions restoring force cannot be sufficient to separate the surfaces in contact, leading to an useless device. Furthermore, the presence of moving parts, in conjunction with the small device dimensions, can make the membrane very sensible to surface-to-surface attraction forces (as the Van der Waals one), and strong adhesion phenomena can be easily reached [6].

Dielectric charging phenomena are typically due to the high electric field applied between the MEMS membrane and the actuation pad underneath it. In fact, the voltage applied can inject charge into the oxide and generate a parasitic electrical field which can, depending on the trapped charge sign, increase the actuation electrostatic field or partially screen it [7]-[8]. Also in this situation, the parasitic field can be strong enough to maintain the MEMS membrane in the actuated position even if the bias voltage has been zeroed.

In this work we have investigated the current drained by the actuation electrode (IACT), finding interesting correlation between IACT and the actuation voltage, and the presence of charge trapping phenomena. Furthermore, we have found that stiction can also be induced by the dielectric breakdown of the insulator between the suspended membrane and the actuation electrode layer. In this case, IACT can predict stiction issues occurrence.

2. DEVICES OVERVIEW AND MEASUREMENT SETUP

Several kinds of ohmic series and shunt switches, built by FBK-IRST (Trento, Italy), have been the focus of this work. The technology utilized for the fabrication of tested ohmic RF-MEMS switches consists of a surface micromachining process based on electrodeposited suspended gold for the membrane layer. The RF signal path is made with the same gold layer to achieve a lowlosses gold-gold ohmic contact upon actuation. A high resistivity poly-silicon layer is used for actuation electrodes, and an Al-Ti-TiN layer is used for the RF signal underpasses. A detailed process description is given in [9]. We have tested several typologies of ohmic RF-switches, in both shunt (normally closed) and series (normally opened) configuration.



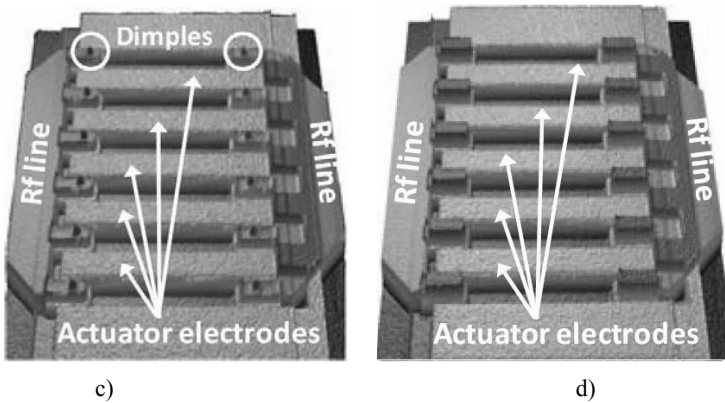


Fig. 1. Tested devices layout: meander based suspensions (a), and straight beam suspensions (b). Optical profilometer image of series switches after suspended membrane removal with (c) dimples, and without (d). Actuator electrodes and dimples are highlighted in the picture.

Two main variables of device geometries were used. The first one is the shape of the suspended gold springs (suspensions): meander based (see Fig. 1a), or with straight beams (Fig. 1b). The second difference is the type of membrane / transmission line contact: flat surfaces, instead of the usage of dimples and winglets (see Fig. 1c, and 1d).

An interdigitated topology has been adopted for signal underpass and actuation electrodes, which is useful for reducing charge trapping phenomena. A detailed description of the test devices can be found in [10]. We have developed different semi-automatic measurement setups based on a HP 6753A Vector Network Analyzer (VNA), a HP 8114A solid state pulser, and a Keithley 2612 Source Meter, in order to test the electrical characteristics of RF-MEMS devices. A complete description of the measurement technique and adopted setups is reported in [11], whereas the bias evolution used during our tests is reported in Fig. 2.

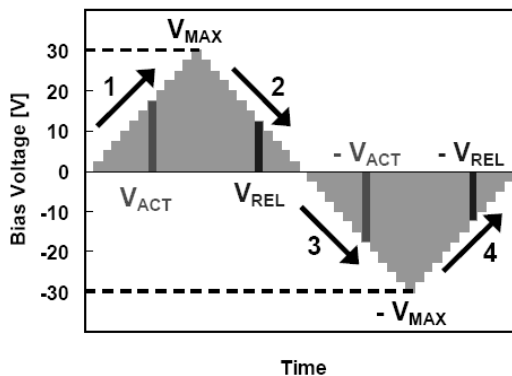


Fig. 2. Bias evolution adopted for the DC characterization of RF-MEMS switches.

Both meanders and straight beams based devices have been fully characterized. Thanks to the low spring constant value, given by the meander shaped anchors, type (a) devices, both shunt and series topologies, have shown very low values of actuation and release voltages ($|V_{ACT}| \approx 12$ V, $|V_{REL}| \approx 6$ V). Straight beams devices (with higher spring constant values), are characterized by a more ideal actuation characteristic graph, and present higher values of both actuation and release voltages ($|V_{ACT}| \approx 36$ V, $|V_{REL}| \approx 18$ V), as shown in Fig. 3.

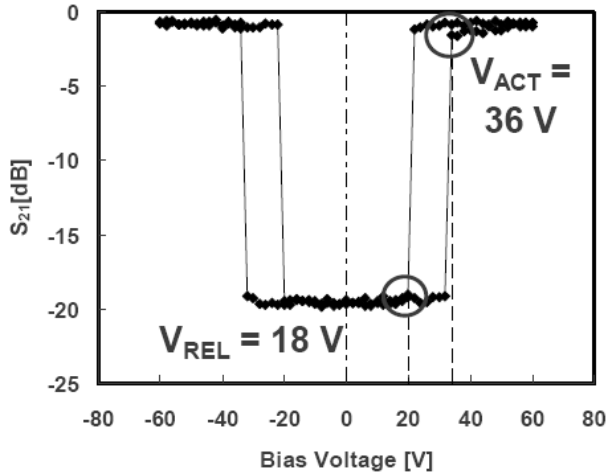


Fig. 3. DC Characterization of straight beam based suspensions switch.

All devices have shown good RF performances (Sparameters measurement conditions: RFreq = 6 GHz, RFpower = 0 dBm), and, as demonstrated by the graph symmetry, these RF-MEMS are not affected by charge trapping phenomena during the first characterization procedure. Optical profilometer analysis, carried out on fresh devices, showed that almost no residual stress existed in the suspended structure of the tested RFswitches (3 μ m air gap).

In conjunction with the traditional measure of both RF and electro-mechanical parameters of MEMS switches, we have studied the measurement of IACT: during the Sparameters characterization (*i*), and in a fastest way considering only the actuator structure (*ii*, sweeping the voltage at the actuation pad vs. ground).

In order to better understand the evolution of the actuator current, we have also fully characterized ad-hoc developed test structures. These are square capacitors (440 μ m \times 440 μ m), without any movable parts, made with a polysilicon top electrode, a 100 nm SiO₂ LTO, and an Al1%Si bottom electrode. These capacitor test structures has allowed us to investigate the influence of the trapped charge on the actuator current and, in general, on the behavior of the full MEMS switch. The measurement setup used for the capacitors is the same used for

switches characterization, but, in this case, only I_{ACT} has been measured (no S-parameters).

3. DIELECTRIC CHARGING AND ACTUATOR CURRENT

The comparison of S_{21} and I_{ACT} measurements of a shunt, meander-based switch is reported in Fig. 4.

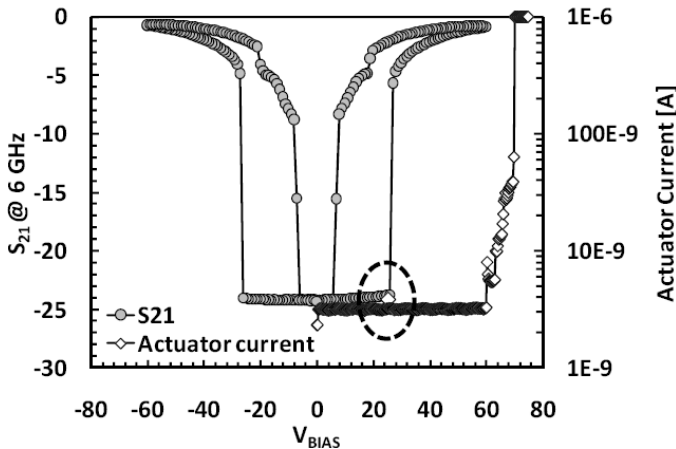


Fig. 4. Comparison of S_{21} and I_{ACT} measurements of a shunt, meander-based switch. I_{ACT} compliance limited to $1 \mu\text{A}$.

As it is possible to notice, I_{ACT} can furnish a precise value of the switch actuation voltage ($V_{ACT} = 25.5 \text{ V}$, as highlighted by the dotted circle in Fig. 4), due to the transient increase of the capacitor displacement current, and the value is in perfect agreement with the S_{21} variation due to the actuation of the switch. Furthermore, it is interesting to notice that I_{ACT} suddenly increases after about 60 V, precursor of the breakdown of the dielectric layer. It must be noted that a compliance level of $1 \mu\text{A}$ was set during the measure shown in Fig. 4. Without setting a compliance value on the maximum current level, the device could remain stuck, as we will discuss in the next section.

In order to better investigate the behavior of I_{ACT} , we have repeated similar measurements on capacitors test structures. An example of a typical I-V curve shown by a fresh capacitor is shown in Fig. 5. Like in the measurement of a full switch, at about 60 V the current starts to increase (phase 1), and, during the phase 2, the current decreases showing an hysteresis-like behavior.

This phenomenon can be attributed to the upward bending of the oxide band diagram (see the inset in Fig. 5: X_C = charge barycentre, t_{ox} = oxide thickness), leading to a reduction of the current flowing through the oxide (tunnel effect, or trap-assisted tunnel mechanisms) [12].

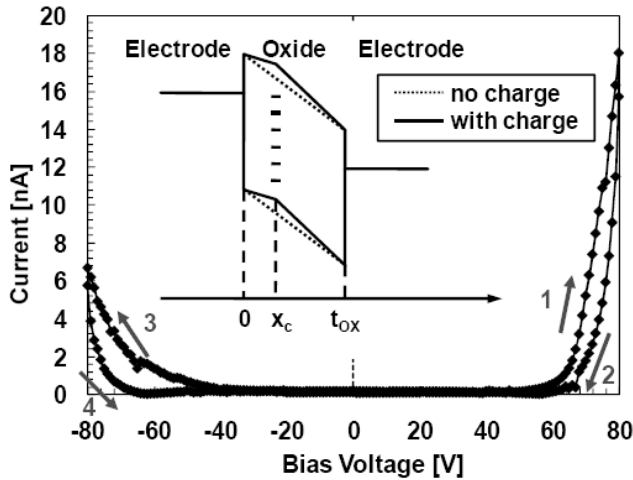


Fig. 5. Evolution of I_{ACT} on a fresh test structure during the test. The arrows indicates the sweep direction. The inset shows a simplified schematic of the capacitor bands diagram before (dotted line) and after (continuous line) negative charge injection in the oxide.

We have consecutively repeated the measurements for 100 times, and in Fig. 6 it is reported the evolution of selected (#1, #10, #100) I-V characteristics during the test.

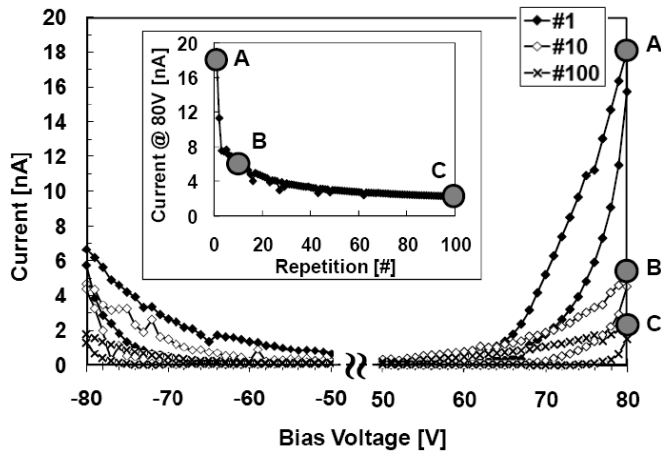


Fig. 6. Evolution of I_{ACT} after 1, 10, and 100 measurement cycles. The x-axis is split for clarity purpose. The inset shows the decrease of I_{ACT} (@ 80 V) caused by charge entrapping.

In order to investigate the evolution of the current during the test, we have graphed (see the inset of Fig. 6) the current value measured at 80 V. It decreases exponentially, and this can be explained by a continuous injection of negative

charge in the dielectric. The negative charge causes an increase in the oxide barrier leading to a decrease in the current, with a saturation on the charge accumulation value after some repetitions of stress.

4. STICTION INDUCED BY DIELECTRIC BREAKDOWN

As already shown in Fig. 4, it is interesting to note that IACT starts to suddenly increase for $V_{BIAS} > 60$ V, due to the breakdown of the oxide layer between the suspended membrane and the actuator line. The region affected by the dielectric breakdown is highlighted in Fig. 7b.

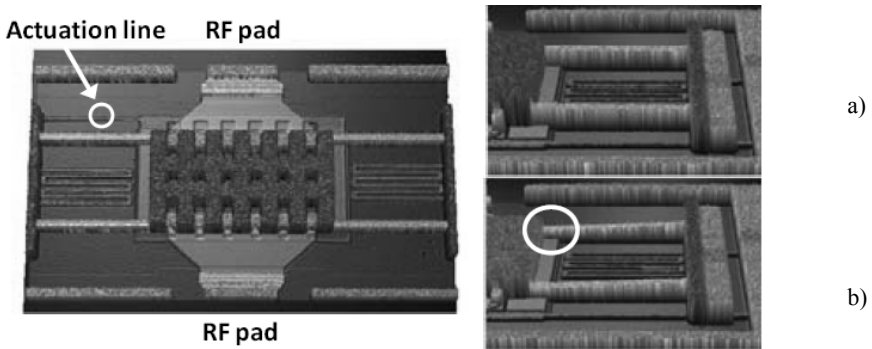


Fig. 7. Optical profilometer images of tested devices: unactuated (a), and actuated ($V_{BIAS} = 60$ V). The circle in (b) highlights the zone where the dielectric breakdown occurs.

We have seen that if the actuator current is not limited (setting the current compliance level to a maximum value of $1 \mu\text{a}$), the dielectric breakdown can lead to a permanent stiction of the suspended membrane. In Fig. 8 we show the evolution of S-parameters and actuator current during the test with no compliance set on I_{ACT} .

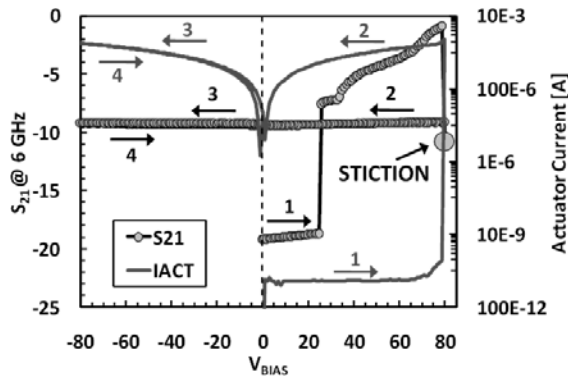


Fig. 8. Comparison of S21 and IACT measurements with no current limit. The device remains stuck, in the point highlighted by the emission microscope image reported in Fig. 9.

At $V_{\text{BIAS}} \approx 80$ V, I_{ACT} increases up to about 2 mA; from that point the actuator assumes an ohmic behavior and the S_{21} parameter does not show any variation during the test. In this case the dielectric breakdown has lead the device to remain stuck and partially bended, since the S_{21} parameter assumes an intermediate value between the not-actuated, and the actuated values. Furthermore, the stiction occurrence has been confirmed by the prickling of the membrane, showing the bridge rotating around the point in which the breakdown occurred. Another confirmation is given by emission microscope (Hamamatsu PHEMOS-200) measurements, that clearly indicates the point where the failure has occurred, as shown in Fig. 9.

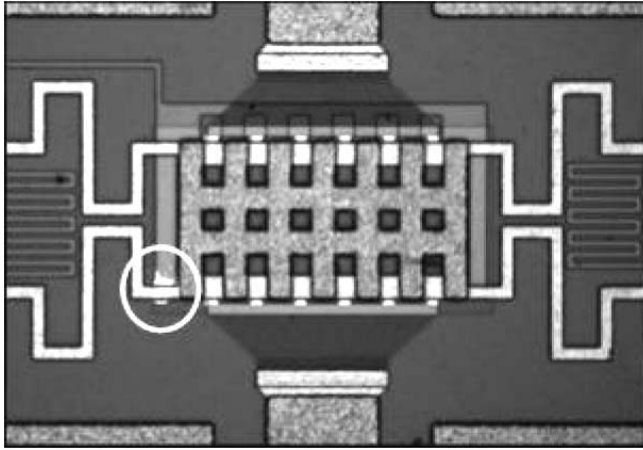


Fig. 9. Emission microscope image of the stuck device after the dielectric breakdown (see Fig. 8). The stiction has occurred in the area highlighted by the circle.

Devices with different anchorage layout (without crossing with the actuation electrodes) have been tested, obtaining an highly increased robustness. The next step will be the study of the Time-to-Breakdown (TTBD) of such failure mode.

From this excerpt of the breakdown characterization between suspension and bottom actuator electrode, a simple design guide-line that should be observed to improve the reliability of such devices, could be avoid the crossing between the actuator area and the suspended structure.

6. CONCLUSION

In this work we have investigated the current drained by the actuation electrode, finding interesting correlation between I_{ACT} and the actuation voltage, and the presence of charge trapping phenomena.

Capacitor test structures have been characterized, investigating the influence of charge trapping in the evolution of the leakage current.

We have shown that stiction phenomena can also be induced by the dielectric breakdown of the insulator between the suspended membrane and the actuation electrode layer, and, like in the previous cases, I_{ACT} can furnish interesting information on the stiction and breakdown occurrence.

Acknowledgement. The authors would like to thank Karl Süss for providing a PM8 probe station in order to build the RF measurement setup. Authors would also like to acknowledge Benno Margesin and Flavio Giacomozzi (FBK-IRST, Trento, Italy) for devices fabrication, Jacopo Iannacci (ARCES-DEIS, now with FBK-IRST), and Roberto Gaddi (ARCES-DEIS, now with Cavendish Kinetics) for devices design and fruitful discussions.

References

- [1] R. PLANA, *What's Hot in RF Components and Systems*, Microwave Journal, pp. 22–28, February 2006.
- [2] J. MACIEL, *Recent Reliability Results in RF MEMS*, Proceedings of the 2005 IEEE MTT-S Int. Microwave Symposium, Workshop Notes, WFE Recent Applications in RF MEMS, Long Beach, CA, June 12-17, 2005.
- [3] X. YUAN, *et al.*, *Initial Observation and Analysis of Dielectric-Charging Effects on RF-MEMS Capacitive Switches*, IEEE MTT-S Digest, pp. 1943–1946, 2004.
- [4] W.M van SPENGEN, *et al.*, *Experimental characterization of stiction due to charging in RF MEMS*, Proceedings, IEDM, pp. 901–904, 8-11 December 2002.
- [5] I.De WOLF, *Reliability of MEMS*, 7th Int. Conf: on Thermal, Mechanical and Multiphysics Simulation and Experiments in Micro-Electronics and Micro-Systems, EuroSimE, 2006.
- [6] B. Stark, “MEMS Reliability Assurance Guidelines for Space Applications”, JPL Publication 99-1.
- [7] S. MELLÉ, *et al.*, *Reliability Modeling of Capacitive RF MEMS*, IEEE Transactions on Microwave Theory and Techniques, **53**(11), pp. 3482–3489, November 2005.
- [8] X. ROTTENBERG, *et al.*, *Distributed Dielectric Charging and its Impact in RF MEMS Devices*, 34th European Microwave Conference, pp. 77–80, Amsterdam, 2004.
- [9] F. GIACOMOZZI, *et al.*, *Electromechanical Aspects in the Optimization of the Transmission Characteristics of Series Ohmic RF-Switches*, Proceedings of the 5th MEMSWAVE Workshop, Uppsala, pp. C25–C28, Sweden, 30 June–2 July, 2004.
- [10] R. GADDI, *et. al.*, *Interdigitated Low-loss Ohmic RFMEMS Switches*, Proceedings of the Conference NSTI Nanotech, **2**, pp. 327–330, 2004.
- [11] A. TAZZOLI, *et al.*, *Electrostatic Discharge and Cycling Effects on Ohmic and Capacitive RF-MEMS Switches*, IEEE Trans. on Device and Materials Reliability, **7**(3), pp. 429–437, Sept. 2007,.
- [12] R. KIES, *et al.*, *Improved Method for the Extraction of Oxide Charge Density and Centroid from the Current-Voltage Characteristic Shifts in a MOS Structure After Uniform Gate Stress*, Proceedings IEEE 1997 Int. Conference on Microelectronic Test Structures, **10**, pp. 111–115, March 1997.

Investigation of Charging Processes in Dielectrics for RF-MEMS Capacitive Switches

E. PAPANDREOU¹, G. PAPAIOANNOU¹, F. GIACOMOZZI²,
M. KOUTSOURELI¹, B. MARGESIN², S. COLPO²

¹University of Athens, Solid State Physics Section, Panepistimiopolis Zografos, Athens, Greece
Phone: +307276817

²Fondazione Bruno Kessler (FBK-irst), Via Sommarive 18, 38050 Povo Trento, Italy
Phone: +390461314432

Abstract. The charging processes have been investigated in dielectrics used in RF MEMS capacitive switches. The investigation included various silicon oxides and nitrides. Finally, the effect of substrate, bottom electrode, has been taken into account.

1. INTRODUCTION

The dielectric charging in RF-MEMS capacitive switches constitutes a key issue parameter for their commercialization. Although the basic charging processes are well known from the elementary theory of dielectrics they still cannot be fully applied to MEMS devices. This is because the dielectric film is amorphous and deposited under various conditions on various substrates at low temperatures. This affects significantly the material stoichiometry and stress. The density of defects in such materials may be in excess of 10^{18}cm^{-3} , for SiN, giving rise to charge trapping and dipole formation. Moreover the presence of hydrogen in PECVD deposited dielectrics may affect significantly the intrinsic charge distribution through transport under high electric fields.

The charging processes in silicon nitride and oxide dielectrics have been investigated intensively in order to find application in MEMS capacitive switches. The investigation has been performed by using both Metal-Insulator-Metal (MIM) capacitors and MEMS switches [1-4]. In so far only these studies have been isolated and no comparison has been performed in order to draw comparative conclusions.

The aim of the present work is to investigate the electrical properties and charging processes in silicon-nitride, silicon-oxide and silicon-oxinitride dielectrics deposited under different conditions and on different substrates. The investigation is performed by applying the Thermally Stimulated Depolarization Current method (TSDC) on MIM capacitors.

2. EXPERIMENTAL DETAILS

On all wafers field oxide (thermal oxide) 300 nm was grown to isolate from the Si substrate. Two bottom electrodes have been used:

- Polysilicon deposited at 620°C with a thickness of about 600 nm and doped with boron and
- Metal multilayer deposited by sputtering with a total thickness of about 550 nm.

The investigated dielectrics were deposited under different conditions and on different substrates. All methods and lower contacts composition are summarized in Table 1.

The MIM capacitors were assessed with the aid of thermally stimulated depolarization current method. The dielectric was polarized by applying an electric field of 10^6 V/cm at 450 K. Then the samples were cooled under electric field down to 200 K. Finally, the depolarization current was measured with the aid of a Keithley 6485 picoampere meter while the samples were heated under constant rate of 2.5 K/min.

3. THEORETICAL BACKGROUND

The dipolar polarization in inorganic crystals may be caused by structural properties of the crystal lattice or it may be due to lattice imperfection or doping. The time and temperature dependence of polarization and depolarization processes are determined by the competition, between the orienting action of the electric field and the randomizing action of thermal motion. Thus, the decay of polarization after removal of electric field is given by an exponential function of time. In the case of a MIM capacitor, the depolarization process induces a short circuit discharge current transient (DCT) that is given by

$$I_{dis}(t) = -\frac{dP(t)}{dt} \quad (1)$$

The current that is produced by the progressive decrease in polarization in the course of a TSDC experiment, where time and temperature are simultaneously varied, is approximated by [5]:

$$J_D(T) \approx \frac{P_s(T_p)}{\tau(T)} \cdot \exp\left[-\frac{1}{\beta\tau(T)} \cdot \frac{kT^2}{E_A}\right] \quad (2)$$

where β is the heating rate (K/sec), E_A the depolarization mechanism activation energy, $P_s(T_p)$ is the equilibrium polarization at the polarizing temperature T_p , $\tau(T)$ the thermally activated relaxation time determined by and τ_0^{-1} the characteristic frequency factor, which is usually directly related to the vibrational frequency of the material

$$\tau(T) = \tau_0 \exp\left(\frac{E_A}{kT}\right) \quad (3)$$

Table 2. Summary of investigated structures

Sample n°	Botom Electrode	Dielectric	Top Electrode	Film Thickness (nm)
1	Polysilicon	LPCVD Nitride	Al 1% Si	98
2	Polysilicon	TEOS	Al 1% Si	200
3	Polysilicon	LOT	Al 1% Si	114
4	Polysilicon	PECVD Nitride HF	Al 1% Si	106
5	Al 1% Si+Ti+TiN	LTO	Cr/Au	114
6	Al 1% Si+Ti+TiN	PECVD Oxide LF	Cr/Au	88
7	Al 1% Si+Ti+TiN	PECVD Nitride HF	Cr/Au	106
8	Al 1% Si+Ti+TiN	PECVD Oxidi Nitride	Cr/Au	98

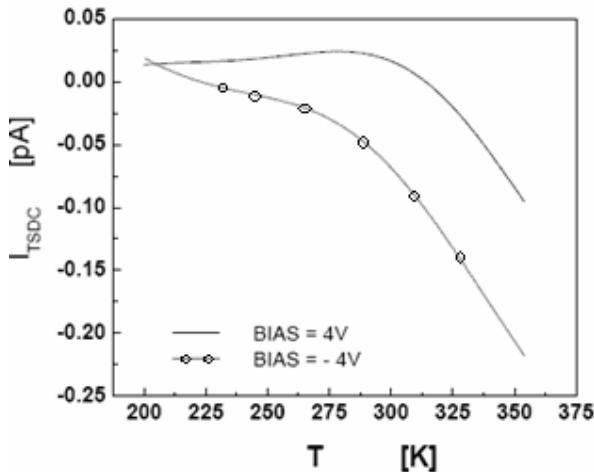


Fig. 1. Asymmetric TSDC spectra obtained in SiNx.

In the case of space charge polarization the processes leading to thermally stimulated depolarization current are far more complex because several

mechanisms such as the counteracting action of diffusion, the loss of migrating carriers due to recombination, the blocking effect of the electrode-dielectric interfaces, the charge trapping and the influence of local electric fields can be involved simultaneously. Under these circumstances the TSDC spectra show the characteristic properties of distributed processes, such as extension over a wide temperature range. In addition, only a part of the space charge decay is monitored in the MIM capacitors current as a consequence of:

- i) the partial dissipation of excess charges by space independent intrinsic conductivity that passes unnoticed in the external circuit,
- ii) the incomplete release of the image charges induced at the electrodes due to their partial neutralization by the excess charges and
- iii) the dependence of the diffusion released current on the blocking character of the electrodes.

The efficiency is greatly improved by using an insulating electrode adjacent to the non-metalized side of the sample, an insulating foil or air gap, which may partially resemble a MEMS switch in the up-state.

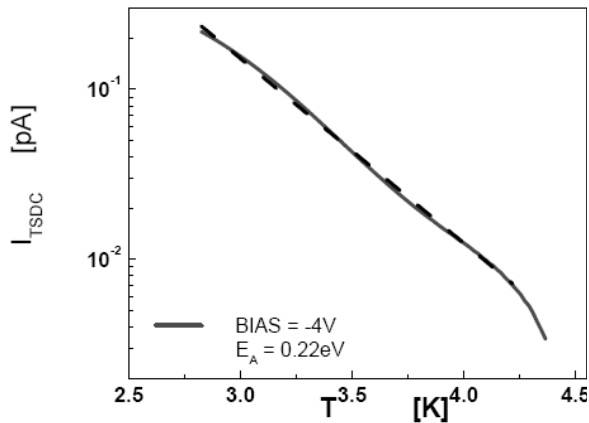


Fig. 2. Arrhenius plot of TSDC spectrum revealing activation energy of 0.22eV.

4. RESULTS AND DISCUSSION

Typical TSDC spectra obtained after polarization of the dielectric film with a positive or negative bias, which was been applied to the top electrode of a PECVD SiN_x MIM capacitor, are presented in Fig. 1. The spectra have a complex structure consisting of a semi-continuum distribution of defects. Moreover, the spectra are asymmetrical. In the case of SiN_x this behavior has been attributed to the asymmetrical electrodes and the dielectric film properties. The latter is because the amorphous silicon-rich alloys behave like α -Si:H with expected differences that arise from nitrogen doping/incorporation and the rapid increase in the strength of

the valence band tail as the degree of disorder increases with nitrogen content [6]. The current transport in silicon rich α -SiN_x:H MSM structures is strongly controlled by the barriers at the metal–semiconductor interfaces. The injected electrons from cathode electrode may recombine with holes, which are “injected” from anode electrode and are either trapped at Si dangling bond midgap defects or are located in valence band tail.

Since the source of asymmetry is still not defined and since a larger charge is collected when the top electrode is negative, during polarization, the data analysis was focused on the spectra obtained after polarization with the top electrode being negative.

The TSDC spectra for SiO dielectric show the same pattern like the one presented in Fig.8 of [7], obtained in MOS capacitors. The TSD current is negligible up to almost 150 K and beyond this temperature increases with temperature. Apart from of this similarity we must emphasize that in the case of an MOS capacitor the TSDC current is also affected by the presence and modulation of the depletion layer.

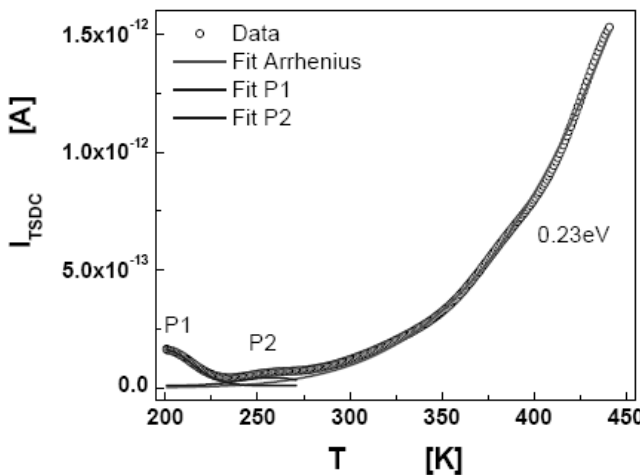


Fig. 3. Analysis of TSDC spectrum of PECVD LF SiN_x film.

The TSD current exhibits the same behavior in the case of SiN_x, as already reported [8, 9]. In principle in all materials the spectra reveal that at higher temperatures dominates an isolated defect with a high concentration. The peak appears at temperatures higher than 450 K (see Fig. 1). This allows us to simplify Eq. 2 from which we can identify a linear region where, applying the Arrhenius law, we can estimate the activation energy of the resulting discharge current process. This is clearly shown in Fig. 2 and the calculated activation energy was found to be about 0.22 eV. Here it must be pointed out that the almost continuous defect distribution is expected since it is well known that in MEMS the deposited

insulating films contain a large density of electrically active defects. These defects can trap negative and positive charges or both depending on their microscopic structure.

In all cases the TSDC spectra were further analyzed in order to extract additional information. Depending on the material deposition method and nature of substrate, the number of monitored defects contributing to dielectric charging may change dramatically. Such examples are presented in Fig. 3 and 4 for LF SiNx and LTO SiO₂ presented in Fig. 3 and 4 respectively. The analysis of all spectra and the identification of various contributing defects is not included in the present work. Instead of this emphasis has been given to the total stored charge and its dependence on substrate/bottom contact. The stored charge in the present work experiments can be calculated from:

$$Q = \frac{1}{\beta} \int_{T_1}^{T_2} I_{TSDC}(T) dT \quad (4)$$

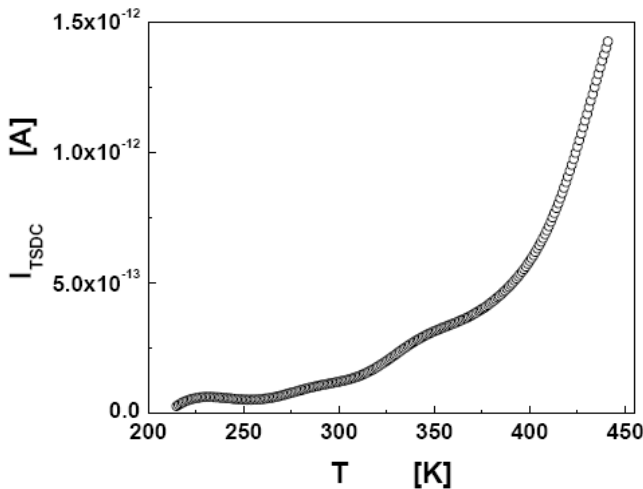


Fig. 4. TSDC spectrum of LTO SiO₂ film.

The stored charge was calculated from TSDC spectra integration in the temperature range of 200K to 450K. The charge dependence on the dielectric material and the bottom electrode composition is presented in Table II. Comparing the results of Table II, on a first approach the spectra integration reveal that the larger charge storage is observed in LTO independently of substrate/bottom electrode nature. The LPCVD SiNx seems to constitute another material with high charge storage, of similar magnitude with the one of LTO. All other dielectrics were found to store much lower charge when the bottom electrode was TiN. This effect is presently not well understood and is under further investigation. Finally, TEOS seems to be the material that exhibits the lowest charge storage.

Table. 2. Effect of bottom electrode

Dielectric	Bottom Electrode	Charge ($\times 10^{-7}C$)
LPCVD Nitride	Polysilicon	5.52
TEOS	Polysilicon	0.01
PECVD Nitride HF	Polysilicon	1.20
LTO	Polysilicon	4.55
LTO	Al 1% Si÷Ti÷TiN	8.70
PECVD Oxide LF	Al 1% Si÷Ti÷TiN	0.16
PECVD Nitride HF	Al 1% Si÷Ti÷TiN	0.16
PECVD Oxynitride	Al 1% Si÷Ti÷TiN	0.12

In the case of oxynitride it has been already shown that the incorporation of O or N atoms into Si nitride or Si oxide films, respectively, improves the qualities of the insulating films [10]. The charge-trapping and carrier transport mechanisms of silicon-rich oxynitride (SRO:N) have been investigated by Z. Yu *et al.* [11]. Their study revealed that there are two conduction regimes-when the applied voltage is smaller than a threshold voltage V_T , the current is dominated by the charge transfer between the SRO:N and substrate; while when the voltage is large than V_T , Poole-Frenkel mechanism dominates the conduction. This conclusion seems to be in present work. The stored charge in PECVD oxynitride, when deposited on Al 1%Si+ Ti+TiN bottom electrode, is lower the one in PECVD oxide or nitride (Table II). Z. Yu *et al.* also reported that nitrogen incorporation increases the density of silicon nanodot in the bulk of the SRO: N layer a fact that needs further investigation.

4. CONCLUSION

The charging processes have been investigated in a wide range of materials deposited on two different substrates/bottom electrodes. The investigation revealed that the amount of stored charge depends strongly on the nature of bottom electrode. Specifically, the deposition of dielectric films on polycrystalline silicon seems to increase the amount of stored charge. On the other hand the deposition of the same materials on TiN seems to greatly decrease the stored charge. Among the deposited dielectrics, LTO suffers from excess charging that seems to be independent of the nature of the bottom electrode. Here the authors would like to emphasize that the presented results arise from an experimental work that is in early phase and further work is in progress.

Acknowledgement. Authors would like to acknowledge that the present work has been supported by the bilateral scientific collaboration between Italy and Greece and the NKUA projects frame Kapodistrias.

References

- [1] C.L. GOLDSMITH, D.I. FOREHAND, Z. PENG, J.C.M. HWANG, and J. L. EBEL, *High-Cycle Life Testing of RF MEMS Switches*, International Microwave Symposium, pp. 1805–1808, June 2007
- [2] G. PAPAIOANNOU, J. PAPAPOLYMEROU, P. PONS and R. PLANA, *Dielectric Charging in Radio Frequency Microelectromechanical System Capacitive Switches: A Study of Material Properties and Device Performance*, Applied Physics Letters, **90**, pp. 233507, June 2007
- [3] G.J. PAPAIOANNOU, F. GIACOMOZZI, E. PAPANDREOU and B. MARGESIN, *Charging Processes in RF-MEMS Capacitive Switches with SiO₂ Dielectric*, MEMSWAVE 2007
- [4] E. PAPANDREOU, M. LAMHAMDI, C.M. SKOULIKIDOU, P. PONS, G.J. PAPAIOANNOU and R. PLANA, *Structure Dependent Charging Process in RF MEMS Capacitive Switches*, Microelectronics Reliability, **47**, pp. 1822–1827, 2007
- [5] J. VANDERSHUEREN and J. CASIOT, *Thermally Stimulated Relaxation in Solids*, P. Braunlich (Ed.) Topics in Applied Physics, **37**(4), p. 135, Springer-Verlag, Berlin, 1979.
- [6] J.M. SHANNON, S.C. DEANE, B. MCGARVEY, and J.N. SANDOE, *Current Induced Drift Mechanism in Amorphous SiN_x:H Thin Film Diodes*, Applied Physics Letters, **65**, pp. 2978–2980, 1994.
- [7] R.A. REBER and D.M. FLEETWOOD, *Thermally Stimulated Current Measurements of SiO₂ Defect Density and Energy in Irradiated Metal-Oxide-Semiconductor Capacitors*, Rev. Sci. Instruments, **63**, pp. 5714–5725, 1992.
- [8] R. DAIGLER, G.J. PAPAIOANNOU, E. PAPANDREOU and J. PAPAPOLYMEROU, *Dielectric Charging in Low Temperature Silicon Nitride for RF-MEMS Capacitive Switches*, MRS Spring Meeting, Los Angeles March 2008.
- [9] G. PAPAIOANNOU, J. PAPAPOLYMEROU, P. PONS and R. PLANA, *Dielectric Charging in Radio Frequency Micro-Electro-Mechanical-System Capacitive Switches: A Study of Material Properties and Device Performance*, Applied Physics Letters, **90**, pp. 2335071–3, 2007.
- [10] S. HASEGAWA, S. SAKAMORI, M. FUTATSUDERA, T. INOKUMA and Y. KURATA, *Structure of Defects in Silicon Oxynitride Films*, Journal of Applied Physics, **89**, pp. 2598–2605, 2001.
- [11] Z. YU, M. ACEVES, J. CARRILLO and R. LÓPEZ-ESTOPIER, *Charge Trapping and Carrier Transport Mechanism in Silicon-Rich Silicon Oxynitride*, Thin Solid Films, 515, pp. 2366–2372, 2006.

Nanoscale Investigations in Dielectrics Charging by Electrostatic Force Microscopy

A. BELARNI¹, M. LAMHAMDI¹, P. PONS¹, L. BOUDOU²,
J. GUASTAVINO², Y. SEGUI², G. PAPAIOANNOU³,
M. DILHAN¹, R. PLANA¹

¹University of Toulouse LAAS CNRS, 7, avenue du Colonel Roche, Toulouse France

²University of Toulouse LAPLACE, 118, route de Narbonne, 31077 Toulouse France

³Solid State Physics Section, Univ. of Athens, Panepistimiopolis Zografos, Athens Greece

Abstract. We shall describe in this article the technique of use the electrostatic force microscope like a tool for charging a dielectric and imaging. The images obtained enable us to represent the evolution of the charges according to time and this way of understanding the mechanisms of transport of the charges in the dielectric one.

1. INTRODUCTION

RF MEMS capacitive switches are enabling component technologies. However, in spite of excellent performance of these components, their deployment has been hindered by reliability problems.

For electrostatic actuation, the major reliability problem is stiction between the metal layer (top electrode) and the dielectric layer covering the bottom electrode [1] [2] [3] [4] [5] [6]. When the bridge is in contact with the dielectric, charges are injected into the dielectric through the actuation voltage. When the bridge is straightened, the charges are spreading more or less slowly toward the counter-electrode depending on the nature of the dielectric. The retention of charges by the dielectric leads to a shift in the actuation voltage and then to a stiction failure.

The optimization of the dielectric behavior, in view of reducing the charging problems, lead to a lot of experiments through fabrication and characterization of many switches with different dielectric. Among various proposed assessment methods the Electrostatic Force Microscopy (EFM) proved to be a powerful and efficient tool to study this charging problem.

Indeed the switch behavior in up and down position is close to the EFM configuration. In down position the biased EFM tip act as a local contact between the bridge and the dielectric and then deposit charges onto the dielectric surface. In up position, the tip scans the electrical properties of the charged area with an open circuit. The charge injection is achieved by positioning the metallic AFM tip above a chosen point of the scanned area, disengaging the feedback control of the probe, then lowering the tip toward the sample surface. The bias voltage can be then applied, for few seconds to several ten of minutes, between the tip and the sample grounded. The bias level can be fixed between -12 V and +12 V. In order to prevent any influences on the EFM data from the topography, a dual-pass scheme is usually adopted. First the topography is recorded in the tapping mode along a line scan. Next, phase information is recorded along the same line while the probe is lifted parallel to the topography at a constant height. This dual-pass technique assumes that the influence from the short-range forces can be ignored at the lift height, and only electrostatic force affects the oscillation amplitude, frequency or phase of the cantilever. However, it turns out that residual electrostatic force can still influence the topography measurement during the first pass, [6] and is critical for quantitative measurements.

Electrostatic force microscopy (EFM) can map out the phase shift ($\Delta\phi$) of the cantilever directly linked to the electrical force gradient $\left(\frac{dF}{dz}\right)$ which the tip feels using the relation of:

$$\Delta\phi \approx -\frac{Q}{k} \frac{dF}{dz} = -\frac{Q}{2k} (V_{tip} - V_{\sigma})^2$$

Where Q and k is the quality factor and the stiffness constant of the tip and V σ the potential created by the charges. The more detailed and practical information about EFM is discussed elsewhere [7]. Different methods were elaborated to quantify the amount of charge injected on dielectric surfaces. Most of these methods are based on the capacitance geometry tipdielectric-substrate, image charge method and analytical Green method [8].

The aim of the present work is to exploit the technology of EFM microscopy and investigate the charging and discharging processes in different material dielectric films. The distribution of resulting EFM signal and its evolution with time will be examined.

2. EXPERIMENTAL

Our experiment used a Veeco 3100 scanning probe microscope with a Nanoscope IV controller. Our measurement sample consisted of thermally silicon dioxide on silicon substrate (thickness: 100nm), PECVD silicon nitride (thickness: 400 nm) on silicon substrate and low thermal silicon oxide (thickness 100 nm). The

EFM probe cantilever (Model: SCM-PIT) exhibiting a spring constant k : 1-5N/m, f_0 : 60-100 kHz.

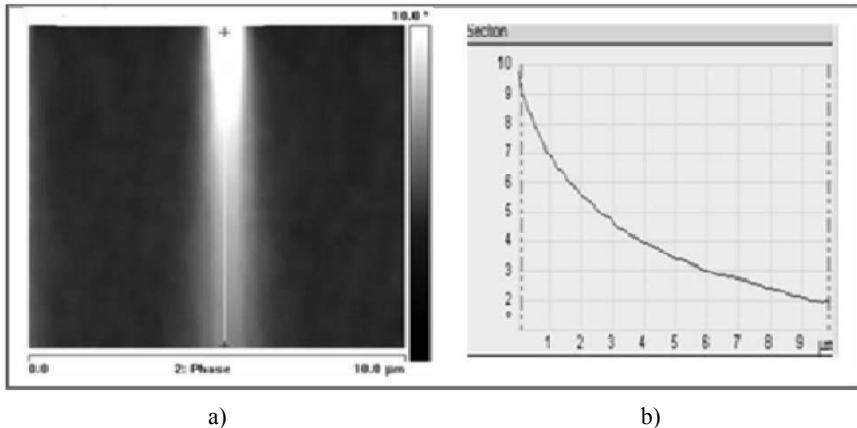


Fig. 1. (a) Real time evolution of tapped charge distribution after voltage stress (b) Evolution of phase drift with time.

3. RESULT AND DISCUSSION

Figure 1 present an example of recorded data by EFM. The charges were deposited during 60s by applying +12V on silicon nitride LF. X axis and y axis indicate the distance and measurement time, respectively. In Fig. 1b it is shown the evolution of peak phase shift, which in act is proportional to the square of surface potential.

Two parameters are important to optimize measurements during the imaging: bias of the tip (V tip) and the lift of the tip (z).

The choice lift height must hold account owing to the fact that the detection of phase is valid only for one operation in linear mode (low amplitudes of oscillation).

The polarization of the tip highlights the contrast inversion between the positive charges and the negative charges.

It turn out that the residual electrostatic force can still influence the topography measurement during the first pass, [9] [11] and is critical for quantitative measurements, especially for phase-shift measurements.

We notice that the polarization of the point increases the sensitivity. The tip point does not affect significantly the apparent kinetics of discharge process. In fact the time constant increases by almost 50% with respect to the non bias tip.

As shown in the figure, the phase-shift evolution in function of time (the phase-shift phase is proportional to the quantity of charges deposited on dielectric surface), indicating dissipation of the injected charge. After a time, the phase-shift is nullified indicating that the trapped charge decays to the background level. The dissipation of the trapped charge is actually due to the de-trapping and the drift,

under the presence of internal fields, and the diffusion current mechanisms towards the bottom electrode [11].

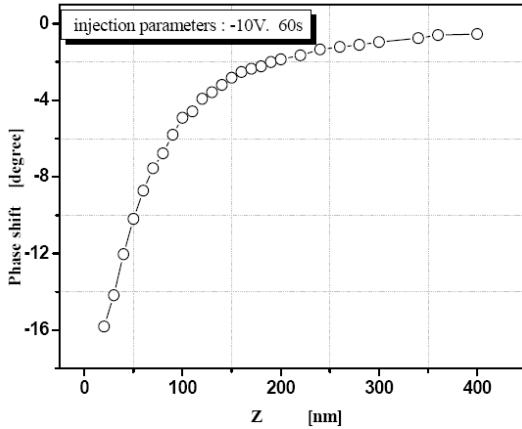


Fig. 2. graph of evolution of phase shift for negative charges deposited (-10V; 60s) in function of the lift z.

Fig. 3. A series of line of the topographic image containing a charge. The arrow indicates the increasing of the amplitude oscillation set point. The charge was deposited in silicon oxide (thickness: 100 nm) with V Tip = -10V during 30s.

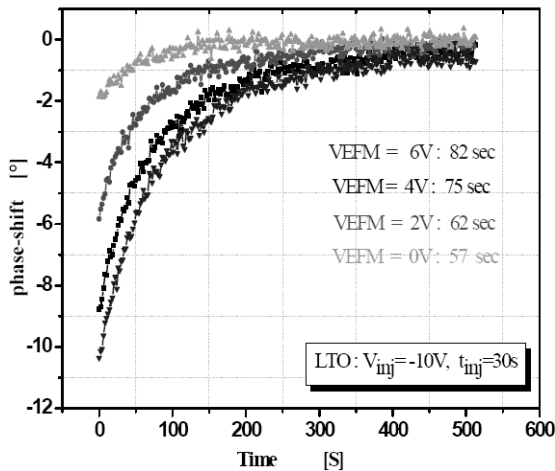
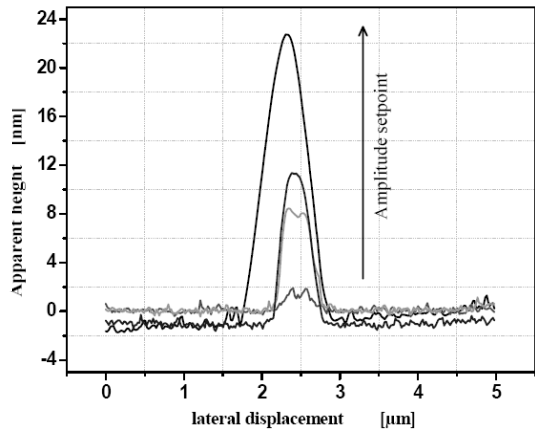


Fig. 4. Evolution of phase-shift in function of time for four tips Bias (6V, 4V, 2V, and 0V).

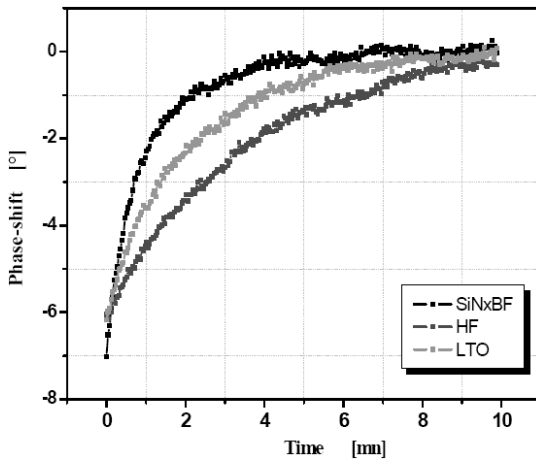


Fig. 5. Phase-shift decay as a function of time with three dielectric materials (LTO, Silicon nitride LF and HF).

A comparison of the decay process, for three different materials, is presented in Fig. 5. The materials were chosen on the basis of relative high leakage current, the low frequency SiN, and low leakage high frequency SiN. Both materials are compared with low temperature silicon oxide. The experimental data show that the decay process is faster in LF silicon nitride and much slower in HF SiN. The case of LTO can be considered as an intermediate one and further investigation is required.

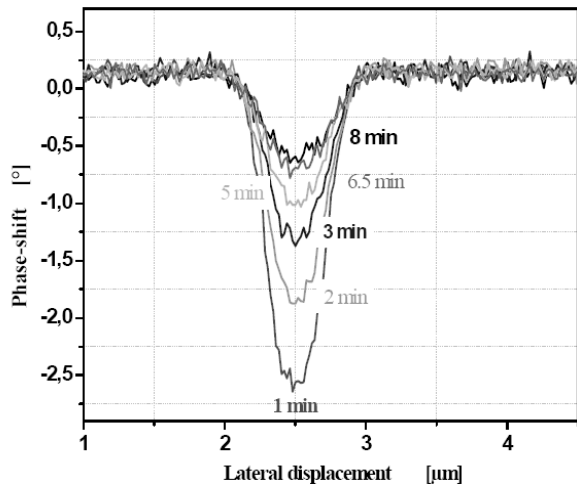


Fig. 6. Evolution of profile of distribution of charges in function of time for SiO₂ dielectric (100 nm thickness).

The profile of deposited charges indicates clearly that the diffusion process is very low. Practically the injected charges do not spread over the dielectric surface and the redistribution has most probably to be attributed to transport under the presence of internal electric fields. Here it must be pointed that the probability of

charge trapped on the surface of dielectric, which tends to propagate towards the substrate, may not be overruled.

6. CONCLUSION

We have shown that the AFM can be a powerful tool to evaluate rapidly the dielectric charging into RF switches, using electrostatic force gradient imaging. These imaging were obtained by monitoring phase shift as a function of time. The parameters of charge deposition are: tip bias injection and time of injection. We have shown principally diffusion in depth of dielectric, and not lateral displacement of the packet of charge is observed. This clearly verifies that the mechanism of charge diffusion must not be taken into account in the charge redistribution in silicon nitride and LTO.

References

- [1] G.M. Rebeiz, *RF MEMS Theory, Design and Technology*, Haboken, New Jersey: J. Willey and Sons, 2003.
- [2] C.L. GOLDSMITH, et al., *Lifetime Characterization of Capacitive RF MEMS Switches*, IEEE MTT-S Int. Microwave Symp. Digest, 227, 2000.
- [3] S. MELLE, D. DE CONTO, L. MAZENQ, D. DUBUC, B. POUSSARD, C. BORDAS, K. GRENIER, L. BARY, O. VENDIER, J.L. MURARO, J.L. CAZAUX, R. PLANA, *Failure Predictive Model of Capacitive RF-MEMS*, Microelectronics Reliability, **45**, pp. 1770–5, 2005.
- [4] G. PAPAIOANNOU and J. PAPAPOLYMEROU, *Dielectric Charging Mechanisms in RF-MEMS Capacitive Switches*, European Microwave Week, EuMIC, pp. 359–362, 2007.
- [5] M. LAMHAMDI, et al, *Charging-Effects in RF Capacitive Switches Influence of Insulating Layers Composition*, Microelectronics Reliability, **46**, pp. 1700–1704, 2006.
- [6] G. PAPAIOANNOU, et al, *Effect of Space Charge Polarization in Radio Frequency Micro-Electro- Mechanical System Capacitive Switch Dielectric Charging*, Appl. Phys. Lett., **89**, pp. 103512, 2006.
- [7] C.H. LEI et al, *Quantitative Electrostatic Force Microscopy-Phase Measurements*, Nanotechnology, **15**, pp. 627–634, 2004.
- [8] J. LAMBERT, G. de LOUBENS, C. GUTHMANN, and M. SAINT-JEAN, *Dispersive Charge Transport Along the Surface of an Insulating Layer Observed by Electrostatic Force Microscopy*, Physical Review B, **71**, pp. 155418 1–6, 2005.
- [9] C. GUILLEMOT, et al, *Imaging of Stored Charges in Si Quantum Dots by Tapping and Electrostatic Force Microscopy*, Europhys. Lett., **59**(4), pp. 566–571, 2002.
- [10] G.H. BUH, H.J. CHUNG, and Y. KUK, *Real-Time Evolution of Trapped Charge in a SiO₂ Layer: An Electrostatic Force Microscopy Study*, Applied Physics Letters, **79**, pp. 2010–2012, 2001.
- [11] M. YAN et al, *A Quantitative Method for Dual-Pass Electrostatic Force Microscopy Phase Measurements*. Surf. Interface Anal., pp. 354–358, 2007.

RF MEMS Dielectric Charging Effect Estimation Due to High Energy Electrons Irradiation

V.G. THEONAS¹, G.J. PAPAIOANNOU¹, G. KONSTANTINIDIS²

¹University of Athens, Physics Department, Panepistimiopolis Zografos, 15784 Athens, Greece

Phone: +302107276722

²FORTH, Institute of Electronic Structure & Laser, Vassilika Vouton, 71110 Heraklion Crete, Greece

Phone: +302810394142

Abstract. MEMS based switches and actuators have emerged as a serious alternative to GaAs or Si based solid state devices, especially in microwave applications. SiO₂, Si₃N₄, Al₂O₃ and other insulating films are used in MEMS technology. However, their tendency for electrostatic charging diminishes the device reliability. The charging effect becomes significant when these devices are subjected to ionizing radiation, especially when utilized in aero-space applications. The irradiation induced charging depends on the nature of irradiation, the vicinal metal layers and the metal-insulator interface properties. RF MEMS capacitive switch dielectric sensitivity to 0.1 MeV – 10 MeV electrons is presented, taking into account the simulation of total energy deposition by primary electrons and secondary photons and electrons generated within the device, in a M.I.M structure with different insulating layer composition and thicknesses.

1. INTRODUCTION

The MEMS based devices have attracted great interest, especially in the field of micromechanics. Up to now packaging and reliability issues are the major limiting factors that restrain the massive production of such devices. In microsystems technology, thin films materials of high insulation resistance, dielectric constant and breakdown field strength, are used in order to protect the devices against short-circuit. RF MEMS reliability is mainly restricted by the charging effect that occurs in the dielectric material of the devices. Parasitic charge buildup can become uncontrollable during handling, operation or storage of the

device, especially in a radiation rich environment which potentially enhances this effect [1].

There are several reports concerning the dielectric material charging effect of electrostatically actuated capacitive RF MEMS switches, operated in a radiation free environment. It is widely accepted that charges trapped or displaced during processing and/or during the actuation of the devices can result in their latching or selfbiasing [2-5]. The aim of our work is to investigate the MEMS dielectric charging effect, while subjected to electromagnetic and/or particle ionizing radiation. The target is to obtain a better understanding of RF MEMS and their sensitivity to ionizing radiation, by combining the information on dielectric polarization process [1-5] with simulations on charging due to ionizing radiation [6-8]. The goal of this work is to derive the origin of each contributing constituent to dielectric charging, which give arise from electron radiation, taking into account the charge kinetics in order to understand the degradation of these devices when they are operating or stored in radiation rich environment [10-14].

2. FAST ELECTRONS EARTH ORBITAL RADIATION

It is well known that electronics on satellites must be hardened against radiation since for example an object satellite, shielded by 3 mm of Al, receive about 2500 rem/year. Earth orbital satellites operation is mainly affected by the Van Allen Radiation Belt, a torus of energetic charged particles (plasma) around Earth, held in place by Earth's magnetic field. Energetic electrons form two distinct radiation belts, while protons form a single belt. These belts are not only hazardous for artificial satellites and moderately dangerous for human beings, but also difficult and expensive to shield against. The outer belt consists mainly of high energy (0.1–10 MeV) electrons and less by ions in the form of energetic protons, alpha particles and O⁺ ions. The inner Van Allen Belt contains high concentrations of protons with energies exceeding 100 MeV and electrons in the range of hundreds of keV, trapped by the strong magnetic fields in this region. Energetic particles within these belts are capable of penetrating about 1 g/cm² of shielding (e.g. 1 mm of Pb).

Van Allen belts electron radiation effect on the dielectric film of RF MEMS devices operated in earth orbital space applications is the target of this work. Therefore, incident electrons beam was assumed to have energies 0.1, 0.5, 1.0, 5.0 and 10.0 MeV in order to estimate the effect of the inner and outer Van Allen belt electrons interaction with the device.

3. DESCRIPTION OF INSULATING FILM CHARGING

The transport of electrons and other charged particles is fundamentally different from that of neutrons and photons. The interaction of neutral particles is

characterized by relatively infrequent isolated collisions, with simple free flight between collisions. By contrast, the transport of electrons is dominated by the long-range Coulomb force, producing a “radiative” stopping power that besides energy loss, leads to angular deflections of the initial electron. Additionally a “collisional” stopping power decelerates the electron’s track in matter. Both collisional and radiative mechanisms result, is a large number of small interactions and a continuous energy loss procedure. In principle there are three basic electron energy loss mechanisms. The collisional electron – impact ionization, that generates secondary “knock-on” electrons in the material, the electron induced production of fluorescent X-rays and the emission of bremsstrahlung photons due to primary electron deceleration. Those secondary generated electrons (SE) and photons (SP) also interact with matter and may produce new particles within the device volume. For example fluorescent X-ray or bremsstrahlung photons may interact with matter and produce electrons due to photoelectric effect or Compton scattering. Consequently fast electrons irradiation and transport in matter is followed by a cascade of secondary particles generation that also deposit energy within the device active volume.

This energy deposition is responsible for charge generation in the dielectric film. Induced charge distribution will depend on the insulator density, band gap, photons absorption coefficient as long as the contribution of each energy loss mechanism to the totally deposited energy and the structure of the device and the vicinal metal layers.

When the secondary “knock – on” or photoelectrons and Auger electrons are extracted – emitted from atoms situated close to the dielectric surface, these electrons may escape into vacuum. Electrons escape length is determined by their kinetic energy and the density of the dielectric. The first effect of this process is the formation of a positively charged surface layer in the dielectric. The thickness of this layer corresponds roughly to the total path the corresponding electrons would have in the bulk and is greater than the Inelastic Mean Free Path (IMFP). On the other hand, those electrons energy deposition along their track before exiting the insulating film, lead to free carriers generation (production of e – h pairs) within the film. Escaping electrons and photons do not contribute further to carrier generation in the dielectric. The later is also valid for SE emitted from atoms located in the bulk of the film and cannot manage to escape. These electrons contribute to free carrier generation within the insulating film, but they do not change the ionization state of the film.

In RF MEMS capacitive switches, the dielectric layer is deposited on a conducting substrate, the coplanar transmission line and above the dielectric lays the suspended bridge. Due to the higher density of metal bridge and transmission line, SE and SP generation by the incident fast electrons will be in principle stronger. Thus secondary electrons and photons generated mainly in the irradiated bridge and the (non irradiated) transmission line will be emitted into dielectric.

Dielectric escaped electrons that will be collected by metal electrodes will not contribute anymore to the dielectric charging effect, except if their energy is still large enough to generate Auger electrons close to the metal surface that have the possibility to be re-emitted in the dielectric. Finally, the dielectric escaped fluorescence photons may contribute to the generation of secondary electrons, part of which may be injected back into dielectric. This process is plausible since the transmission line is in contact with the dielectric film and bridge distance from the dielectric is of the order of few microns that diminishes the probability of scattering events of ejected electrons with the atmosphere atoms in the capacitor's gap. Electrons injection from the adjacent electrodes will contribute to the generation of $e - h$ pairs within the film, and it is possible to change dramatically the ionization state of the film. Since it is a dynamic process, the dielectric surface ionized layer may change polarity and the thickness of this layer will be determined by the balance between the corresponding IMFPs of the ejected and injected electrons. The presence of injected electrons will affect the charge status of ionized, due to Auger emission, dielectric atoms. The recovery from the charged state will be much faster due to the presence of the injected excess electrons. In any case this dynamic process and others such as charge trapping in defects and metal-insulator interfaces as well as the effect of interface roughness are out of the scope of the present work, which focuses on the distribution of the ionizing radiation generated charge and the effect of the materials that are in the vicinity of the dielectric film.

4. SIMULATED DEVICE STRUCTURE

The structure of the device used in the simulation procedure is presented in Table 1. In order to understand the effect of fast electrons irradiation on capacitive RF MEMS switch dielectric film charging we study a Metal-Insulator-Metal (M.I.M.) structure, which allows the monitoring of contribution of adjacent metal electrodes to dielectric ionization and bulk charging. The dielectric materials chosen for investigation are SiO_2 and Al_2O_3 , based on their compatibility to RF MEMS technology [2].

Table 2. Simulated device structure

Composition	M.I.M. Structured Device
Contact Bridge (Au)	100 nm
Insulating Film	100 nm – 420 nm
Transmission line (Au)	200 nm
Cr	20 nm
SiO_2 substrate	5 μm

As already mentioned, we estimated that the small capacitor's gap between the metal bridge and the dielectric will not induce scattering events of ejected

electrons with the atmosphere atoms in the gap. Therefore we assumed that the metallic bridge is in contact to the dielectric film as it happens when the switch is on the “down” state. As long as we are focused in radiation induced dielectric charging effects, this M.I.M structure is representative for both “up” and “down” states of the device. Simulated device was considered to have an active area of $60 \times 60 \mu\text{m}^2$. The dielectric layer thickness was varied from 100 nm to 420 nm and consisted of cubic cells of 20 μm dimension. Finally, electron beam was assumed to be vertically incident on the surface of the metallic electrodes central cell, located to the center of the device’s contact bridge.

Simulation was performed by the MCNP 4C Monte Carlo code [9]. Electrons transport, consist on large numbers of small interactions causing a great increase in computational complexity that makes a single–collision Monte Carlo approach to electron transport unfeasible. The MCNP algorithms are based in a variety of analytic and semi-analytic multiple-scattering theories for the transport of charged particles, using the fundamental cross sections and the statistical nature of the transport process to predict probability distributions for energy loss and angular deflection. These theories are the Goudsmit–Saunderson theory for angular deflections, Landau theory of energy loss fluctuations and the Blunck–Leisegang enhancements of the Landau theory. Finally, appropriate probability distributions are sampled for the production of secondary particles (electron induced fluorescent X–rays, “knock–on” electrons and bremsstrahlung photons). In order to follow an electron through a significant energy loss, the code breaks the electron's path into many steps. The “condensed history” Monte Carlo method used by MCNP constitutes on the subsumption of the effects of many individual collisions into single steps that are sampled probabilistically. Hence the code takes into account all the possible mechanisms of electrons interactions with matter and calculates the SE and SP populations that also interact with matter. The MCNP code tally consists on the magnitude and distribution of ionization and energy deposited in the device layers, which is attributed to all the (primary and secondary) particles that lose energy in the device. The later gives the ability to calculate the e–h pairs concentration within the insulating layer.

In Ref [15], there is a model describing the kinetics of free charge carriers induced in dielectrics by ionizing irradiation. The production rate of free electrons and holes is calculated by:

$$\dot{G} = g_e \cdot \dot{D} \quad (1)$$

\dot{D} is the dose rate and g_e a proportionality coefficient ($g_e \leq \rho/E_g$), where E_g is the band gap and ρ is the insulator density. The calculation of free e-h production population in our work is based on the ratio of the deposited energy (E_{dep}) and the energy to produce an e – h pair (ε) for a specific dielectric material. MCNP code (taking into account the insulator’s density) calculates the magnitude of E_{dep} that is

attributed to all (primary and secondary) particles that lose energy in the insulator. On the other hand ϵ is a value well known for common dielectric materials (evaluated as a function of material's E_g). Therefore the calculated free e-h population is more accurate because it evaluates the effective irradiation dose, taking into account not only the incident (primary) energetic particles but also its descendants that deposit energy to the insulator.

5. RESULTS AND DISCUSSION

The initial ionization state and free carriers concentration induced by fast electrons irradiation is attributed to both primary and secondary particles that escape or accumulate and lose energy within the dielectric film volume. For the examined device structure and for both dielectric materials, the dominant secondary electrons (SE) generation mechanism is impact ionization ($\approx 95\%$ of SE), followed by electron Auger mechanism ($\approx 5\%$ of SE). Electrons irradiation in devices with Al_2O_3 in the insulating film generates more SE within their volume due to its higher density than SiO_2 . Insulating film thickness increase (from 100 to 420 nm), raise the SE generation rate for both materials and especially to the denser Al_2O_3 . As the incident electrons energy raise, the SE generation rate is drastically decreased and PE and SE escape rate is raising, especially for the device containing the less dense insulator (SiO_2) and the thinnest insulating film. Finally the calculated average (PE and SE) track mean free path in the insulating layer of the device is higher for the less dense insulator (SiO_2) and the thinnest insulating film and is drastically increased as the PE energy raise.

The secondary photons (SP) generation rate is very low in all of the examined cases (less than 0.5% of PE) indicating that SP contribution to dielectric ionization and charging is nearly negligible. The dominant SP generation mechanism is bremsstrahlung ($\approx 70\%$ of SP), followed by the electrons X-ray mechanism ($\approx 30\%$ of SE).

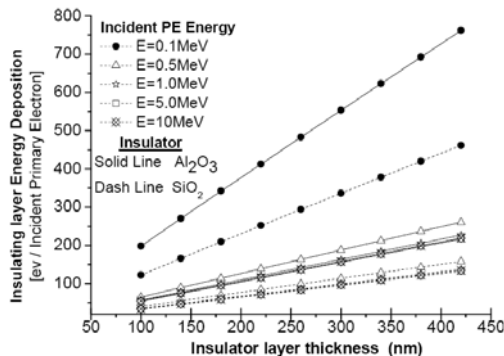


Fig. 1. Energy deposited in Al_2O_3 and SiO_2 films induced by one primary and all generated secondary electrons and photons, for all examined primary electrons energies, as a function of insulating layer thickness.

The above mentioned parameters affect the device and its dielectric layer ionization and charging. Simulation results indicate that radiation induced energy deposition that is responsible for dielectric bulk charging effect is higher for the denser insulator (Al_2O_3), raises almost linearly to the insulating film thickness increase and is more intense for the lower PE energy. On the other hand, insulating layer initial ionization state, that is controlled by the balance between the corresponding IMFPs of the insulator ejected and metal injected SE, was found to be negative in all examined cases, attributed to metal oriented SE accumulation within the insulating layer. The electrons radiation induced energy deposition in the examined insulating layers is presented in Fig. 1. Insulating film thickness increase, raise the energy deposition. The most “productive” PE energy among those examined is 100keV. The results for PE energies grater than 1MeV are almost identical due to the large track mean free path of PE and SE in the insulating layer.

Figure 2 illustrates the irradiation induced ionization distribution to the insulating film constituent by the densest examined insulator (Al_2O_3). Ionization distribution profile is similar for both examined materials, indicating that there is a strong (metal oriented) SE accumulation within the insulating layer.

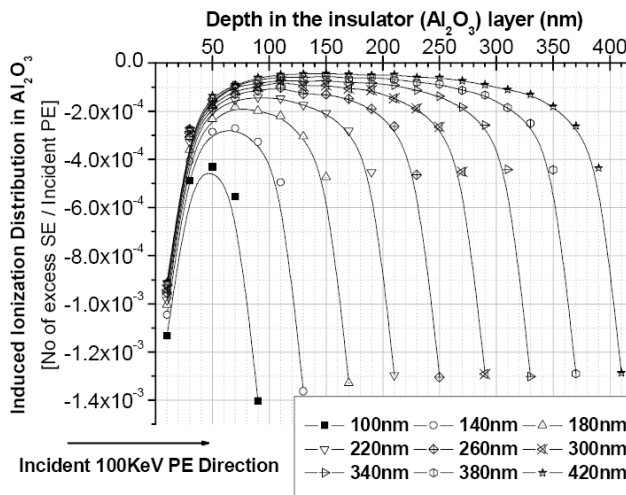


Fig. 2. Normalized ionization distribution in Al_2O_3 film induced by one 100keV primary electron (PE), for all examined insulating film thicknesses (100–420 nm).

Figure 3 illustrates the irradiation induced normalized energy distribution to the insulating film constituent by the densest examined insulator (Al_2O_3) for the most “productive” PE energy. Energy distribution profile indicates that energy deposition is more intense in the region near the metal–insulator interfaces, especially in the vicinity of the irradiated contact bridge.

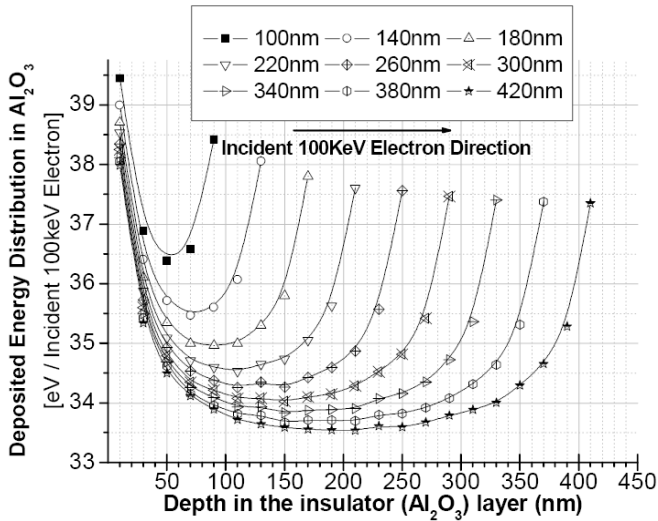


Fig. 3. Normalized distribution of energy deposited in Al_2O_3 film, induced by one primary and all generated secondary electrons and photons, for all examined insulating film thicknesses (100–420 nm).

6. CONCLUSION

The amount of energy deposited within the dielectric layer of an RF MEMS MIM structured (capacitive) switch by incident radiation and consequently the free carriers concentration that will finally determine the dielectric charging effect are strongly affected by the kinetics (population and energy during transport) of secondary electrons (SE) that incident fast electrons (PE) generate within the device layers.

Simulation results indicate that less energetic primary fast electron interactions with matter generate higher amount of SE within the device. Each one of these SE is free to propagate within the device layers. Fast electrons during their transport undergo continuous energy deposition (dE/dx) along their track to the target material, regardless of the outcome of the track (electron escapes to vacuum or it is captured and accumulates in a device layer).

The distribution of the induced ionization within the dielectric layer of the examined device, indicate that the phenomena is dominated by SE electrons injection by both the metallic electrodes of the device, towards the insulating film. The SE injection is more intense by the irradiated contact bridge, than from the non-irradiated CPW or MSL transmission line. The backscattering SE injection from the transmission line towards the dielectric film is reducing as the PE energy rise.

The selected simulation procedure gives the ability to calculate the initial charging – ionization state of an RF MEMS capacitive switch dielectric film, taking into account the magnitude, concentration and distribution of: (a) the free carriers (e – h pairs) that will be the dominant charging population in the dynamic state of the device and (b) the PE and SE that escape or accumulate within the insulating layer, causing the film’s ionization profile.

The sign and magnitude of the local charge region that will be finally formed, under an applied electric field, within the dielectric film of the device, will be strongly affected by the material’s trapping parameters and determined by the ratio of trap concentration and carriers hopping mobility.

References

- [1] S.S. MCCLURE, L.D. EDMONDS, R. MICHAILOVICH, A.H. JOHNSTON, P. ALONZO, J. DeNATALE, J. LEHMAN and C. YUI, IEEE Trans. in Nuclear Science, **49**, p. 3197, 2002.
- [2] T. LISEC, C. HUTH AND B. WAGNER, Proceedings of 34th European Microwave Conf, IEEE CNF, **1**, p. 73, 2004.
- [3] X. ROTTENBERG, B. NAUWELAERS, W. De RAEDT and H.A.C TILMANS, Proceedings of the 34th European Microwave Conference, IEEE CNF, **1**, p. 77, 2004.
- [4] M. EXARCHOS, V. THEONAS, P. PONS, G.J. PAPAIOANNOU, S. MELLE, D. DUBUC, F. COCETTI, and R. PLANA, Journal of Microelectronics Reliability, **45**, p. 1782, 2005.
- [5] G.J. PAPAIOANNOU, M. EXARCHOS, V. THEONAS, G. WANG and J. PAPAPOLYMEROU, IEEE M.T.Ts, **53**, p. 3467, 2005.
- [6] V. THEONAS, M. EXARCHOS, G.J. PAPAIOANNOU and G. KONSTANTINIDIS, Sensors and Actuators, **132**, p. 25, 2006.
- [7] J. CAZAUX, Journal of Microscopy, **188**, p. 106, 1997.
- [8] J. CAZAUX, Journal of Appl. Physics, **89**, p. 8265, 2001.
- [9] US Los Alamos National Laboratory, <http://www.xdiv.lanl.gov/x5/MCNP/index.html>.
- [10] R.A. BARAGIOLA, M. SHI, R.A. VIDAL and C.A DUKES, Physical Review B, **58**, p. 13212, 1998.
- [11] M.D. VIOLET and A.R. FREDERICKSON, IEEE Transactions in Nuclear Science, 1993.
- [12] G.L. WRENN, J. on Spacecraft & Rocket, **32**, p. 514, 1995.
- [13] [13] S.T. Lai, Proceedings of the 6th Spacecraft Charging Technology Conference, **1**, p. 49, 2000.
- [14] A.R. FREDRICKSON, Brazil J. of Phys, **29**, p. 241, 1999.
- [15] O.A. PLASKSIN, *et al*, Radiation-Induced Electrical and Optical Processes in Materials Based on Al₂O₃, Journal of Nuclear Materials, **271-272**, pp. 496–501, 1999.

Effect of Environment Humidity on the C-V Characteristics of RF-MEMS Capacitive switch

Zbigniew OLSZEWSKI, Russell DUANE, Conor O'MAHONY

Tyndall National Institute, Lee Maltings, Prospect Row, Cork, Ireland

Phone: +353 21 4904112

E-mail: zbigniew.olszewski@tyndall.ie

Abstract. Measurements of the C-V characteristics of oxide-based RF-MEMS switches in humid-air and dry-air environment, before and after dc bias stress, are reported. It is shown that humidity affects the device behaviour and can determine the direction of the C-V characteristic drift. We report for the first time that the entire C-V curve “shifts” when the device operates in a humid environment and “narrows” when the environment is dry.

1. INTRODUCTION

Radio-frequency microelectromechanical capacitive switches (RF-MEMS) are high performance devices with applications in telecommunication systems [1]. The capacitance-voltage (C-V) characteristic of these devices shows threshold voltages at both forward and reverse bias as the switch is turned ON and then OFF at the pull-in (V_{PI}) and pull-out (V_{PO}) voltages, respectively. The C-V curve changes during the switch operation and this has received much attention in the literature.

Early work showed that the forward and reverse thresholds shift in the same direction [2]-[3]-[4]; this is referred to as the C-V shift effect. Recent work [5]-[6]-[7] showed another instability effect, namely, a C-V curve narrowing that occurs when the thresholds decrease in magnitude. Although both effects were attributed to dielectric charging, it is uncertain why different authors observe different effects. To explain these results various interpretations of the dielectric charging phenomenon in RF-MEMS were proposed. Moreover, published data usually relies on different test structures and measurement conditions which is a further cause of discrepancies.

Even though it was shown in [8] that humidity may shorten the lifetime of the switch, its influence on the C-V curve drift was not shown. For this reason we provide a simple experiment to show that humidity significantly affects the C-V performance of the switch.

2. CAPACITIVE SWITCH BACKGROUND

In their most basic form, MEMS capacitive switches consists of a movable top electrode (bridge or membrane) suspended above a dielectric-coated CPW (coplanar waveguide) transmission line (see Fig. 1a). The design of the switch involves balancing of the electrostatic force (F_{el}) and the mechanical restoring force (F_k) used to close and open the switch, respectively. If the magnitude of the applied voltage (V) exceeds pull-in (V_{PI}), an electrostatic force (F_{el}) induced on the top electrode is greater than the mechanical force (F_k) and the electrode collapses onto the dielectric. Then, the capacitance of the device rises sharply. To open the switch and decrease the capacitance, the applied voltage must be reduced until the pull-out is reached (V_{PO}). In the high capacitance state (switch closed) the RF signal is coupled to the ground, while in the low capacitance state (switch open) the RF signal passes through the device.

The capacitance and threshold voltages of the switch are defined by a common area between the top electrode and the signal line, air-gap height and the dielectric thickness and its permittivity. Since, the electrostatic force is proportional to the square of voltage ($F_{el} \propto V^2$) the ideal operation characteristic of the switch is symmetrical about 0V as shown in Fig. 1b). However, RF-MEMS reliability studies have shown that during switch operation the electrical properties of the dielectric change due to the dielectric charging phenomenon [2]-[8].

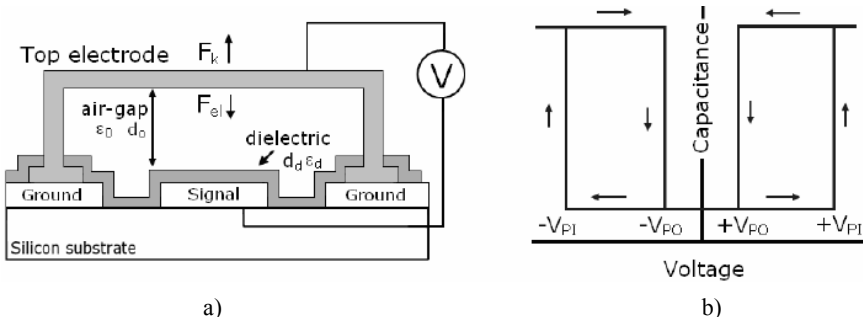


Fig. 1. (a) Schematic of MEMS capacitive switch, (b) ideal C-V operation characteristic for forward and reverse bias voltage.

The presence of parasitic charge (σ_p) in the dielectric appears as an additional voltage source (V_p) that distorts the electrostatic force in the air-gap of the device (F_{el}), which then is proportional to $(V-V_p)^2$. As a result, the threshold voltages (pull-in and pull-out) drift, this ultimately leads to device failure by stiction or

screening. In the first case, the switch fails in the closed position; the membrane stays in the down state even if the applied voltage is reduced to zero. In the second case, the switch fails in the open position; the membrane remains in the up state after bias voltage application. The direction of the threshold voltage change depends on the sign of V_p that is determined by the net polarity of parasitic charge (σ_p) and how the bias voltage polarity is defined with respect to the switch electrodes.

3. EXPERIMENT AND RESULTS

In our experiment we measure the C-V of the switch before and after dc bias stress was applied. However, in contrast to previous work which reports on measurements in either dry or humid ambient, we show results for both environments and at similar bias stress conditions. Therefore, we can directly observe the effect of humidity on C-V variation. The switch used in this work was built using a surface micromachining process and consists of a $100 \times 100 \mu\text{m}^2$ membrane suspended by four springs above a CPW transmission line (see Fig. 2).

The CPW is coated with 130 nm-thick PECVD (Chemical Vapor Deposition) SiO_2 . The membrane and CPW material are aluminium and aluminium/1%-silicon, respectively. The air-gap in the open state is around $1.5 \mu\text{m}$. Due to process variation (i.e. variation of material residual stress and sacrificial layer thickness) the pull-in voltage varies across the wafer with a standard deviation of 1.2 V measured over ten random devices.

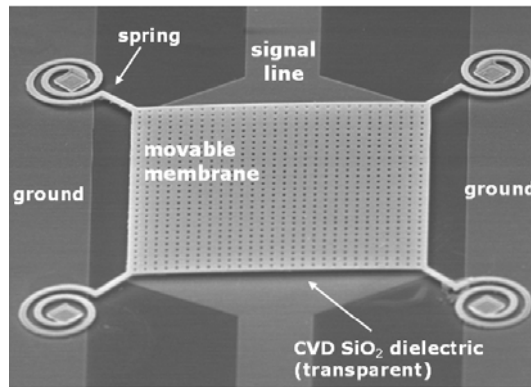


Fig. 2. SEM image of typical RF-MEMS capacitive switch used in this work.

The measurements were performed in room temperature by wafer probing on a Cascade Summit-1200 station with the wafer placed in the environment chamber. The system is equipped with an air-dryer that is capable of reducing the relative humidity of air to a dew point of -70°C ($\text{RH}=0.01\%$). The mean humidity of the lab

environment was 60% and when the air-dryer was turned off this level was measured inside the chamber. These conditions are later referred as dry-air and humid-air, respectively. The C-V measurements were performed with an Agilent-B1500A using a test signal of 100 kHz and 50 mV. A bias is applied between the membrane and the signal line and at the reverse bias the voltage at the membrane is negative and vice versa for the forward bias. The voltage sweep rate was 5 V/s with a step of 0.1V.

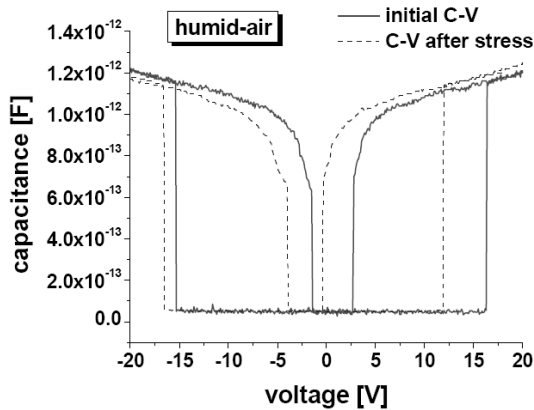


Fig. 3. C-V curves of the switch before and after a bias stress (-20V) applied for 60 seconds and performed in humid-air environment.

C-V characteristics of two similar switches measured in humid and dry environment are shown in Fig. 3 and 4, respectively. Each figure includes two C-V measurements taken by a voltage sweep from -20V to +20V and back to -20V. After the initial C-V measurement the device was stressed with a bias of -20V for a period of 60 seconds, then the second C-V was taken.

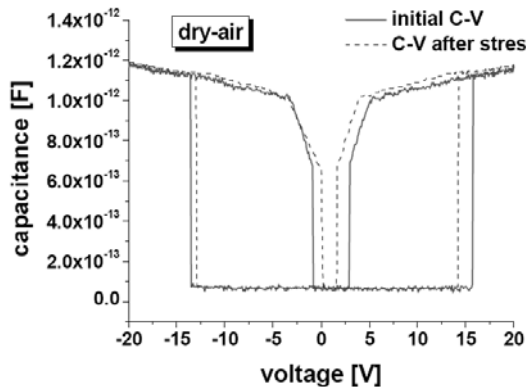


Fig. 4. C-V curves of the switch before and after a bias stress (-20V) applied for 60 seconds and performed in dry-air environment.

Figure 3 and 4 show that the operating characteristic of the switch behaves differently after the same bias stress condition and measurement sweep but in different test environment. After the stress applied in humid-air the characteristic has “shifted” (four thresholds moved in the same direction), while after the stress in dry-air the characteristic has “narrowed” (four thresholds moved towards the center of the plot). Although the device behaviour is different in both environments the failure mechanism due to stiction is common in each case. In Fig. 3 the positive pull-out voltage ($+V_{PO}$) moves slightly to below 0V, whereas, in case of results from Fig. 4 the negative pull-out ($-V_{PO}$) moves to above 0V.

From electrostatic theory, it is known that parasitic charge can shift the threshold voltage of the switch laterally, and that the direction of this shift depends on the net polarity of the charge and how the bias voltage polarity is defined with respect to the electrodes. In general, the electrostatic force required to pull-in or pullout the membrane decreases (absolute value of V_{PI} or V_{PO} decreases) when the dielectric charge is of opposite polarity to the polarity of the membrane and increases when these polarities are the same. This corresponds to a shift of the entire C-V curve laterally to the left and to the right by negative and positive fixed parasitic charge (not changing with time), respectively. This regularity has been experimentally confirmed in [9] for both polarities of charge which was fixed at the dielectric surface. Therefore, we can deduce that the shift of the C-V curve seen in Fig. 3 is induced by the negative fixed parasitic charge (not changing within time of the C-V measurement) which was injected into the dielectric from the membrane during the stress time. Note that the polarity of parasitic charge is the same as the stress voltage (or charge on the membrane). Nevertheless, the narrowing effect seen in Fig. 4, obtained in a dry-air environment but after the same bias stress condition, can not be explained in a similar way. A theoretical explanation of this effect was proposed by Rottenberg [6]-[10] based on the assumption of non-uniformities of the dielectric charging and air-gap distribution. Another study presented experimentally that besides dielectric charging, mechanical degradation known as fatigue [11] and creep [12] can also cause the narrowing effect, depending on the type of applied stress. An investigation of the physics of the narrowing effect is currently being undertaken by the authors.

Figure 5 shows absolute value of the negative pull-in voltage during the lifetime test of 110 successive voltage sweeps from 0V to -25V. The environment humidity during this test varies as indicated in the figure. It can be observed that the pull-in change corresponds to the behaviour observed in Fig. 3 and 4 and depends on the environment condition.

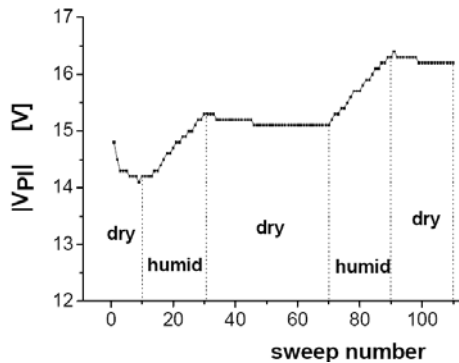


Fig. 5. Absolute value of negative pull-in during the lifetime test of 110 successive voltage sweeps from 0 to -25V.

4. CONCLUSION

In conclusion, we have shown that humidity significantly affects the C-V performance of an RFMEMS capacitive switch. It can be observed that after identical bias stress conditions the C-V curve “shifts” in humid environment while it “narrows” when the environment is dry. The results also demonstrate that although both effects raise similar reliability concerns due to device stiction, the root physical degradation mechanism can be different depending on test environment. Moreover, it is important to note that both polarity thresholds should be taken into account when physical interpretation of the C-V degradation mechanism is undertaken.

Acknowledgement. This study was supported by Intel Ireland and Enterprise Ireland through the Innovations Partnership Programme.

References

- [1] H.J. De Los SANTOS, G. FISCHER, H.A.C. TILMANS, and J.T.M. van BEEK, *RF MEMS for Ubiquitous Wireless Connectivity: Part 1 and 2*, IEEE Microwave Magazine, **1527-3342**, pp. 36–65, December 2004.
- [2] J.R. REID, *Simulation and Measurement of Dielectric Charging in Electrostatically Actuated Capacitive Microwave Switches*, Proc. Modeling and simulation of Microsystems, San Juan, Puerto Rico, pp. 250–253, April 2002.
- [3] X. YUAN, S. CHEREPKO, J. HWANG, C. L. GOLDSMITH, C. NORDQUIST, and C. DYCK, *Initial Observation and Analysis of Dielectric-Charging Effect on RF MEMS Capacitive Switches*, IEEE MTT-S Dig., pp. 1943–1946, 2004.
- [4] J.F. KUCKO, J.C. PETROSKY, J.R. REID, and Y.K. YEO, *Non-Charge Related Mechanism Affecting Capacitive MEMS Switch Lifetime*, IEEE Microwave and Wireless Components Letter, **16**(3), pp. 140–142, March 2006.
- [5] J.R. REID, and R.T. WEBSTER, *Measurements of Charging in Capacitive Microelectromechanical Switches*, Electronic Letters, **38**(24), pp. 1544–1545, November 2002.

- [6] X. ROTTENBERG, B. NAUWELARES, W. De RAEDT, AND H.A.C. TILMANS, *Distributed Dielectric Charging and its Impact on RF MEMS Devices*, IEEE European Microwave Conference, Amstardam, pp. 77–80, 2004.
- [7] R.W. HERFST, P.G. STEENEKEN, and J. SCHMITZ, *Time and Voltage Dependence Dielectric Charging in RF MEMS Capacitive Switches*, IEEE Annual International Reliability Physics Symposium, Phoenix, US, pp. 417–421, 2007.
- [8] W.M. Van SPENGEN, P. CZARNECKI, R. PUERS, J.T.M. Van BEEK, and I. De WOLF, *The Influence of the Package Environment on the Functioning and Reliability of RFMEMS Switches*, IEEE Annual International Reliability Physics Symposium, pp. 337–341, San Jose, US, 2005.
- [9] D. MOLINERO, R. COMULADA, and L. CASTANER, *Dielectric Charge Measurements in Capacitive Microelectromechanical Switches*, Applied Physics Letters, **89**, 103506, 2006.
- [10] X. ROTTENBERG, I. De WOLF, B. NAUWELARES, W. De RAEDT, and H.A.C. TILMANS, *Analytical Model of the DC Actuation of Electrostatic Charging and Nonplanar Electrodes*”, Journal of Micromechanical Systems, **16**(5), pp. 1243–1253, October 2007.
- [11] R.W. HERFST, P.G. STEENEKEN, and J. SCHMITZ, *Identifying Degradation Mechanisms in RF MEMS Capacitive Switches*, IEEE International Conference on Micro Electro Mechanical Systems, pp. 168–171, Tucson, US, 2008.
- [12] M. Van GILS, J. BIELEN, G. McDONALD, *Evaluation of Creep in RF MEMS Devices*, EuroSimE, IEEE International conference on Thermal, Mechanical and Multi-Physics simulation Experiments in Micromechanics and Micro-Systems, pp. 1–6, London, UK, 2007.

Fabrication of RF MEMS Components on CMOS Circuits

A.G. MUKHERJEE*, M.E. KIZIROGLOU, S. VATTI,
C. PAPAVALASSILIOU, A.S. HOLMES, E.M. YEATMAN

Department of Electrical and Electronic Engineering Imperial College London
Exhibition Road, London, SW7 2AZ, United Kingdom

*E-mail: a.mukherjee@imperial.ac.uk,
Telephone: +44 20 7594 6216

Abstract. Recently deep submicron and SiGe (silicongermanium) bipolar CMOS technologies have enhanced the performance of Si-based radio frequency (RF) integrated circuits up to microwave frequencies. The integration of RF MEMS components, such as inductors and capacitors, could further improve the performance of key RF circuit blocks such as voltage controlled oscillators (VCO), low-noise amplifiers, filters, mixers, and power amplifiers. We have developed a process to integrate RF MEMS inductors with standard commercial CMOS dies. The purpose of this work is to present the integration of MEMS inductors with VCOs fabricated in a 0.18 μm standard CMOS technology.

1. INTRODUCTION

WIRELESS systems today typically require a number of off-chip electronic devices in addition to the integrated circuits that carry most of the circuitry. External LC (inductor-capacitor) tanks and quartz reference oscillators are examples of common elements in transceiver architectures that are implemented off-chip. However, with the ongoing need for further miniaturization and higher performance, the replacement of these off-chip parts by monolithically integrated devices based on micromachining and microelectromechanical systems (MEMS) technology represents an increasingly attractive prospect, and there are many efforts in this direction [1-3]. Integrated MEMS components, such as high-Q inductors, have the potential to increase significantly the performance of key RF (radio-frequency) circuit blocks such as voltage controlled oscillators (VCO), low-noise amplifiers, filters, mixers, and power amplifiers. The performance of these

blocks at high frequency is limited by resistive and dielectric losses, resonant effects, dispersion, and parasitic radiation of the inductors. Key performance parameters for integrated reactive components are the quality factor (Q) and resonant frequency. Higher Q components help minimize RF power loss, reduce noise, and lower dc power consumption of RF integrated circuits.

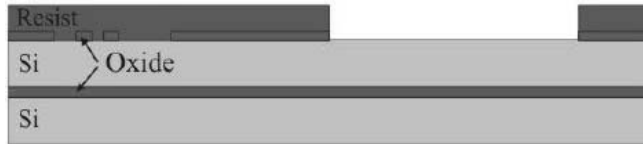
We have developed a process to integrate RF MEMS inductors with standard commercial CMOS dies. In this paper we demonstrate the integration of MEMS inductors with VCOs fabricated in a 0.18 μm standard CMOS technology [4]. The dies are embedded in device-layer cavities defined in a 100 mm-dia. BSOI (Bonded Silicon On Insulator) carrier wafer by deep reactive ion etching (DRIE). The device layer thickness is chosen to match the nominal die thickness, and the cavity depth is finely adjusted by thinning the device layer so that top surface of each die lies within $\pm 2 \mu\text{m}$ of the surface of the carrier. Once the dies have been placed, a layer of photoresist is spin-coated over the carrier [5] to fix the dies in place and planarize the top surface. Windows are opened in this layer to allow electrical and mechanical contact to the underlying dies carrying VCO circuitry. In this way, fabrication of MEMS inductors by patterned electroplating can be achieved on pre fabricated VCOs as on a bare silicon wafer. A self-assembly MEMS method for the fabrication of inductors in the vertical orientation has been used [6]. Self-assembled inductors of this type have higher Q [7] which is expected to result in lower VCO phase noise. This technology has the advantage of providing monolithic integration of state-of-the-art RF MEMS inductors with any standard CMOS technology without being constrained to particular silicon or compound-semiconductor platforms and also irrespective of wafer size.

2. DIE CARRIER PROCESS

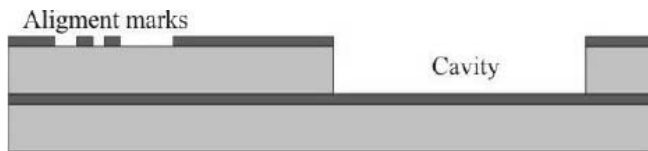
Use of a die carrier allows simultaneous processing of multiple dies, and better compatibility with process equipment and wafer handling techniques. It also has the potential to embed different types of CMOS dies, and is compatible with any wafer size. The process in this case used 100 mm-diameter BSOI starting wafers, comprising 300 μm -thick device layers and 380 μm -thick handle layers, separated by 1 μm of buried SiO_2 . The key steps in the die carrier process are illustrated in Fig. 1.

Firstly, alignment marks are formed, either in a thermally grown oxide layer on the top surface of the BSOI wafer, or by shallow etching of the silicon. Deep reactive ion etching (DRIE) with an STS Multiplex ICP etcher is then used to form cavities in the device layer. By adjusting the passivation and etching cycles, the DRIE process has been optimized to produce near-vertical sidewalls when stopping on the buried oxide layer. The cavity sizes are closely matched to the die dimensions to ensure placement of the dies to within $\pm 15 \mu\text{m}$.

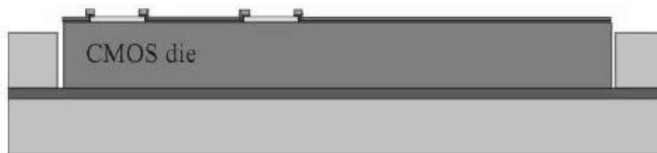
Following the cavity DRIE, the dies are placed, and a thin layer of photoresist is deposited by spin-coating to fix them in place and planarize the top surface.



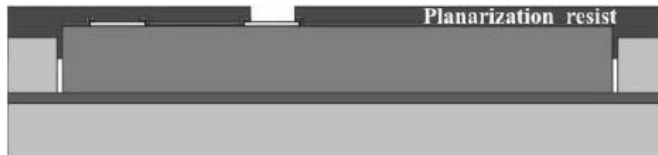
a) Pattern oxide; spin and pattern resist



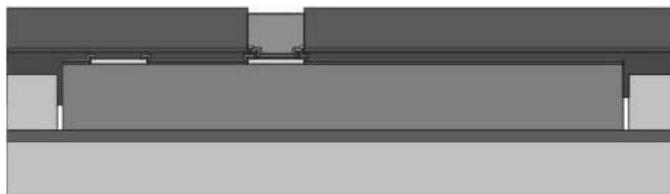
b) Si DRIE to form cavities



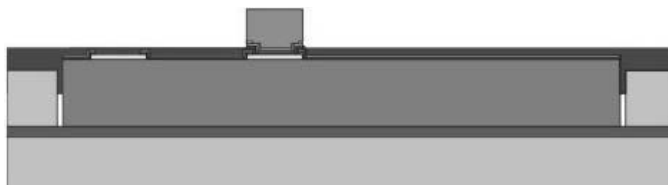
c) Place dies



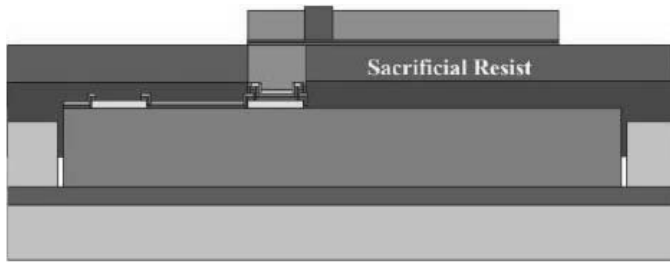
d) Spin & pattern planarization resist



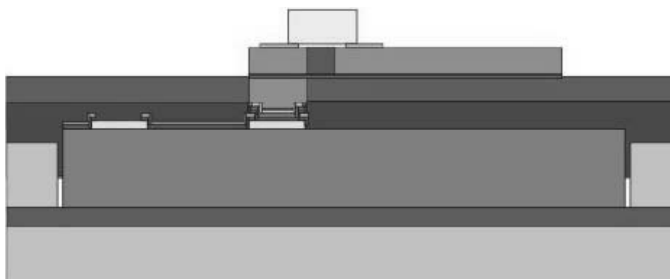
e) Electroplate gold interface pads



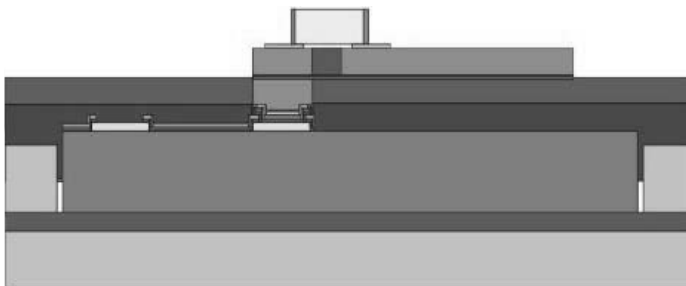
f) Strip mould; etch seed layer



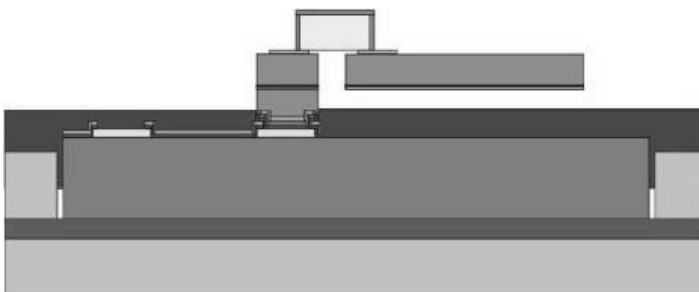
g) Deposit sacrificial layer; electroplate inductors



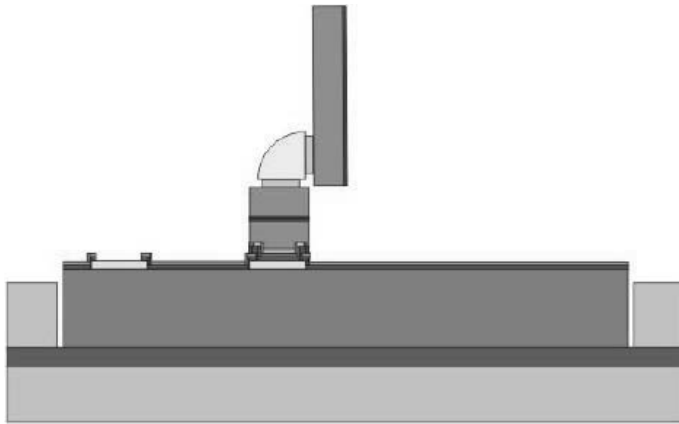
h) Deposit hinge



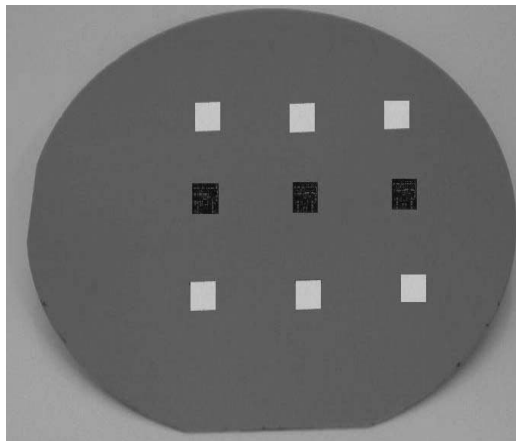
i) Overcoat hinges with gold



j) Release structures



k) Reflow hinges to self-assemble inductors

Fig. 1. Fabrication process flow for inductors on CMOS dies.**Fig. 2.** BSOI carrier with embedded CMOS dies.

In this research the UMC foundry service was used for CMOS die fabrication. A 0.18 micron silicided CMOS process was chosen, with up to 6 metal layers, 1 poly layer, and a high resistance layer. Stacked contacts are supported, as are MIM capacitors (metal 5 to metal 6, 3 pF total capacitance, $55 \times 55 \mu\text{m}^2$ area). The process is for 1.8 volt bias applications, although 2.5 volt thick transistors are also available. The dies fabricated were $5200 \times 5200 \times 284 \mu\text{m}^3$ in size, and carried a number of different voltage controlled oscillators for operation up to 5 GHz [4]. These were designed specifically for operation with our self-assembled MEMS inductors. Fig. 3 shows low- and high-magnification images of CMOS dies containing VCO circuits.

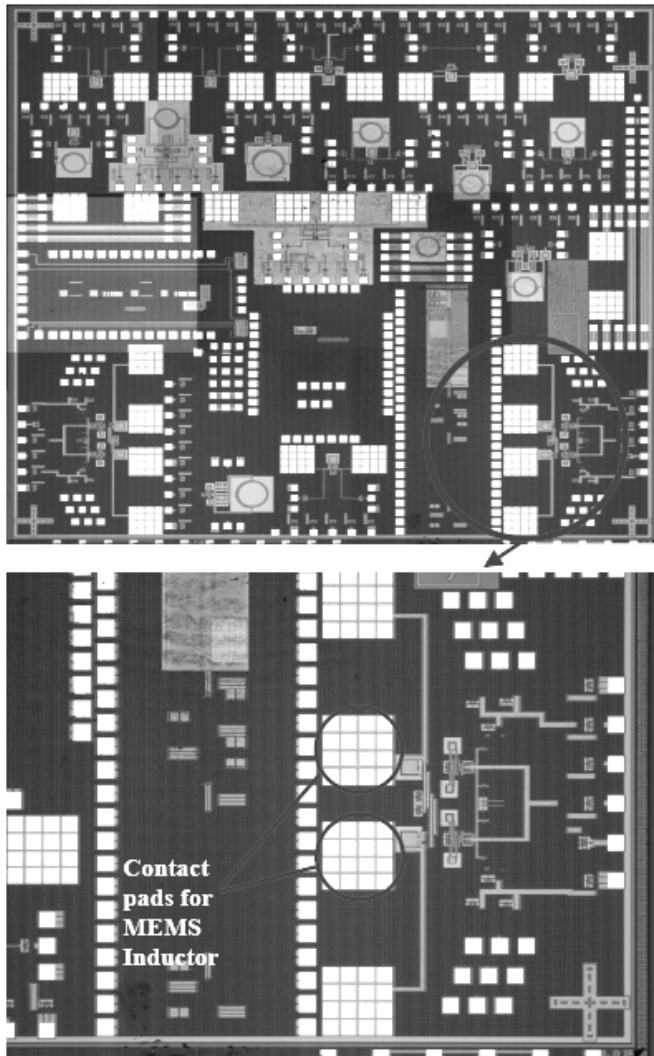


Fig. 3. CMOS die with VCO circuit.

In steps e and f of the process flow in Fig. 1, metal pads are deposited on the CMOS which will form the mechanical and electrical interface to the MEMS structures. In this work gold was chosen as the material for these interface pads because the aim was to realize low-loss RF MEMS components over CMOS. The mask used to define the mould was the same as that used to open the windows in the planarization layer, so that the plated pads were formed over the CMOS contact pads. Fig. 4 shows a CMOS die following these process steps.

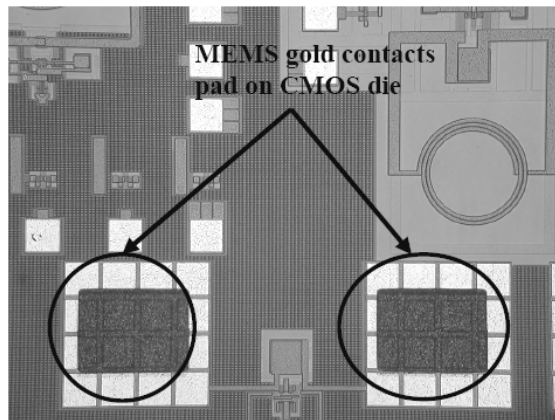


Fig. 4. Gold pads on CMOS die.

3. INTEGRATION OF SELF-ASSEMBLED INDUCTORS

Self-assembled inductors were fabricated using process steps g to k in Fig. 1. First, a sacrificial resist layer was deposited and patterned using the interface pad mask. The resist height was chosen to be around $0.5\ \mu\text{m}$ greater than that of the gold pads. A sputtered Ti/Cu (titanium/copper) seed layer was then deposited, and the inductors formed by gold electroplating into a mould formed in Shipley S1828 photoresist (step g). Fig. 5 shows a $4\ \mu\text{m}$ -thick gold electroplated inductor on a CMOS die.

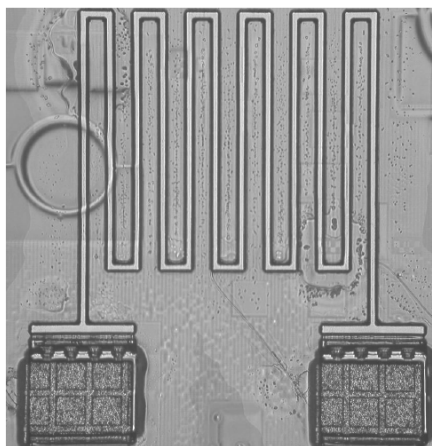


Fig. 5. MEMS inductor prior to deposition of hinge.

The meltable hinges required for the self-assembly process were formed by electrodeposition of pure tin into a new photoresist mould (step h). Prior to this

step a thin nickel barrier layer or “pedestal” was deposited in the hinge region to ensure lateral containment of the Sn during reflow, and to prevent interdiffusion between the Sn and the underlying gold. The Ti/Cu seed layer was also removed from the hinge region at this stage. After plating of the hinges, a 200 nm-thick gold layer was deposited over them to protect the tin from oxidation before and during reflow (step i). Figure 6 shows low and high-magnification images of 6 μm -thick tin hinge which is protected by a very thin layer of gold.

A shielding resist layer was deposited over the entire wafer, and the carrier wafer was diced to separate out the processed dies. Release of the inductor structures (step j) was carried out on individual dies by dry or wet etching of the photoresist layers, and wet etching of the seed Ti/Cu layer. Finally, the dies were placed in a chamber and the tin hinges were reflowed to self-assemble the inductors (step k).

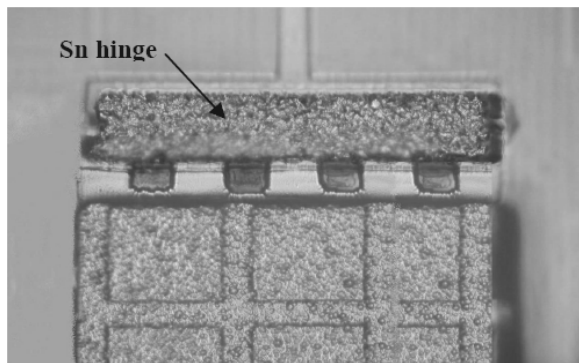


Fig. 6. Electroplated hinge for self assembled inductor.

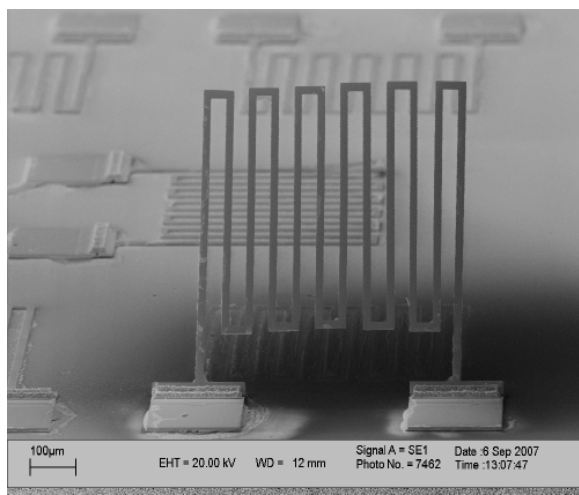


Fig. 7. Self-assembled inductor after solder reflow.

References

- [1] C.T.-C. NGUYEN, *Vibrating RF MEMS for Next Generation Wireless Applications*, Proc. IEEE Custom Integr. Circuits Conf., pp. 257–264, 2004.
- [2] G.K. FEDDER and T. MUKHERJEE, *Tunable RF and Analog Circuits Using Onchip MEMS Passive Components*, Proc. Int. Solid-State Circuits Conf., pp. 390–39, 2005.
- [3] A. DEC and K. SUYAMA, *A 1.9 GHz CMOS VCO With Micromachined Electromechanically Tunable Capacitors*, IEEE J. Solid-State Circuits, **35**(8), pp. 1231–1237, August 2000.
- [4] S. VATTI, C. PAPAVALASSILIOU, *A Capacitively-Coupled 5GHz CMOS LC Oscillator with Bias Tuning Capability*, Proc. 50th IEEE International Midwest Symposium on Circuits and Systems, Montreal, Canada, August, 2007.
- [5] A. GOSWAMI MUKHERJEE, M.E. KIZIROGLOU, A.S. HOLMES and E.M. YEATMAN, *MEMS Post-Processing of MPW Dies using BSOI Carrier Wafers*, Proc. of SPIE Micromachining and Microfabrication Process Technology XIII, **6882**, pp. 68820E-1, San José CA, Jan 2008.
- [6] M.E. KIZIROGLOU, A. GOSWAMI MUKHERJEE, R.W. MOSELEY, P. TAYLOR, S. PRANONSATIT, A.S. HOLMES, and E.M. YEATMAN, *Electrodeposition of Au for Self-Assembling 3D Micro-Structures*, Proc. of SPIE Micromachining and Microfabrication Process Technology XIII, **68826**, pp. 8820B-2, San José CA, Jan 2008.
- [7] G.W. DAHLMANN, E.M. YEATMAN, P. YOUNG, I.D. ROBERTSON and S. LUCYSZYN, *Fabrication, RF Characteristics and Mechanical Stability of Selfassembled 3D Microwave Inductors*, Sens. Actuators A, **97-98**, pp. 215–220, 2002.

On-Wafer Method for Experimental Characterization of Mems Matrix, Using a Two-Port Vector Network Analyzer

S. SIMION¹, R. MARCELLI², G. BARLOLUCCI³,
G. SAJIN¹, F. CRACIUNOIU¹

¹National Institute for Research and Development in Microtechnologies,
Erou Iancu Nicolae 126A, Bucharest, 077190, Romania
E-mail: tefan.simion@yahoo.com, gheorghe.sajin@imt.ro,
florea.craciunoiu@imt.ro

²CNR – Institute for Microelectronics and Microsystems, Microwave Microsystems Group,
Via del Fosso del Cavaliere 100, Rome, 00133, Italy
E-mail: omolo.Marcelli@imm.cnr.it,

³University of Rome “Tor Vergata”, Department of Electronics Engineering,
Via del Politecnico 1, Rome, 00133, Italy
E-mail: bartolucci@eln.uniroma2.it,

Abstract. The paper presents an experimental method useful to characterize a multiport circuit, in particular a MEMS (Micro-Electro-Mechanical System) matrix, using a two-port VNA (Vector Network Analyzer). As example, the method is applied for a four-port circuit (a coupler). The results obtained by using this method and the expected results obtained by simulation are in good agreement.

1. INTRODUCTION

Due to the increasing of circuit complexity for the communication technology, more and more switches are integrated, for reconfiguration as well as for the system redundancy. In this context, during the last years, a few configurations of MEMS (Micro-Electro-Mechanical System) matrices have been reported [1]-[4].

The experimental characterization of microwave multiport circuits, like MEMS matrix, could be made by using a two-port VNA (Vector Network Analyzer) based connectors, by matching the other $n - 2$ ports to 50Ω , where n is the number of ports. This solution may be easily applied for hybrid circuits.

For MMICs (Monolithic Microwave Integrated Circuits), a characterization method using two-port VNA based connectors is not longer a comfortable solution. This is because mechanical test fixtures must be realized, useful for experimental characterization only. Therefore, other solutions involving on-wafer characterization methods are necessary to be developed. One way is to realize a set of circuits, each one having $n - 2$ ports ended on 50Ω thin-film resistors. Unfortunately, this technique is not more accurately because for these loads connected to the $n - 2$ ports, the frequency behaviour, but also the impedance value to a particular frequency, cannot be known accurately.

In this paper, it is proposed an experimental characterization method for a multiport circuit, using a two-port VNA, when the other ports are let open. For this method, successive re-normalization of the circuit scattering parameters matrix is performed, computing also the load impedances for the open-ended ports. A similar method may be found in [5] (see also [6]), but here the load impedances connected to the ports (different from 50Ω) must be known. The proposed method is applied for a four-port circuit (a coupler), showing a good agreement between the results obtained by applying the proposed technique and the expected ones obtained by simulation.

2. METHOD DESCRIPTION

The proposed method to characterize a circuit having n ports consists of $m = C_n^2 = \frac{n!}{2!(n-2)!}$ set of measurements, performed for each frequency. Each set of measurements is a two-port measurement, obtaining m scattering matrixes, \mathbf{S}_{i-j} , where i and j are the port number. The scattering matrices \mathbf{S}_{i-j} must be renormalized to the impedance corresponding to the loads connecting to the each port (the ports are open-ended in this method), obtaining m scattering parameter matrices, \mathbf{S}'_{i-j} , accordingly to the formula:

$$\mathbf{S}'_{i-j} = (\mathbf{I}_2 - \Gamma_{i-j})^{-1} \cdot (\mathbf{S}_{i-j} - \Gamma_{i-j}) \cdot (\mathbf{I}_2 - \Gamma_{i-j} \cdot \mathbf{S}_{i-j})^{-1} \cdot (\mathbf{I}_2 - \Gamma_{i-j}) \quad (1)$$

where

$$\Gamma_{i-j} = \begin{bmatrix} \Gamma_i & 0 \\ 0 & \Gamma_j \end{bmatrix}$$

and Γ_i, Γ_j are the reflection coefficients to the ports i and j , computed for the case when these ports are openended (the reference impedance being 50Ω), while \mathbf{I}_2 is the unity matrix of order two.

Because each port is open, then, the load impedances, or the reflection coefficients to the each port are not known before. Therefore, first of all, the reflection coefficients to the all n ports, $\Gamma_1, \dots, \Gamma_n$ must be computed (theoretically

these reflection coefficients are equal to 1, but these values must be known more accurately). These reflection coefficients may be computed, minimizing the following functions:

$$\begin{aligned}
 f_k^{(1)} &= \mathbf{S}'_{l-2} [1,1] - \mathbf{S}'_{l-k} [1,1], \quad k = 3, \dots, n \\
 f_k^{(2)} &= \mathbf{S}'_{l-2} [2,2] - \mathbf{S}'_{2-k} [1,1], \quad k = 3, \dots, n \\
 f_k^{(3)} &= \mathbf{S}'_{l-3} [2,2] - \mathbf{S}'_{3-k} [1,1], \quad k = 4, \dots, n \\
 &\dots\dots\dots \\
 f^{(n-1)} &= \mathbf{S}'_{l-(n-1)} [2,2] - \mathbf{S}'_{(n-1)-(n)} [1,1]
 \end{aligned}
 \tag{2}$$

where $\mathbf{S}'_{i-j} [1,1]$ is the element of the \mathbf{S}'_{i-j} matrix from the first row and the first column, while $\mathbf{S}'_{i-j} [2,2]$ is the element of the \mathbf{S}'_{i-j} matrix from the second row and the second column.

In (2), the following analytical expression for $\mathbf{S}'_{i-j} [1,1]$ and $\mathbf{S}'_{i-j} [2,2]$ may be used (which were developed from (1)):

$$\mathbf{S}'_{i-j} [1,1] = \frac{A}{B}
 \tag{3a}$$

and

$$\mathbf{S}'_{i-j} [2,2] = \frac{C}{B}
 \tag{3b}$$

where:

$$A = (\mathbf{S}_{i,j} [1,1] - \Gamma_i) \cdot (1 - \mathbf{S}_{i,j} [2,2] \cdot \Gamma_j) + \mathbf{S}_{i,j} [1,2] \cdot \mathbf{S}_{i,j} [2,1] \cdot \Gamma_j$$

$$C = (\mathbf{S}_{i,j} [2,2] - \Gamma_i) \cdot (1 - \mathbf{S}_{i,j} [1,1] \cdot \Gamma_j) + \mathbf{S}_{i,j} [1,2] \cdot \mathbf{S}_{i,j} [2,1] \cdot \Gamma_j$$

and

$$B = (1 - \mathbf{S}_{i,j} [1,1] - \Gamma_i) \cdot (1 - \mathbf{S}_{i,j} [2,2] \cdot \Gamma_j) - \mathbf{S}_{i,j} [1,2] \cdot \mathbf{S}_{i,j} [2,1] \cdot \Gamma_i \cdot \Gamma_j$$

Using (3) in (2) the reflection coefficients, $\Gamma_1, \dots, \Gamma_n$, may be obtained.

Therefore, the all n matrixes \mathbf{S}_{i-j} have been obtained numerically with (1), so, the matrix for the n -port circuit having the all ports open-ended has been constructed as follows:

$$\mathbf{S}' = \begin{bmatrix} \mathbf{S}'_{l-2} [1,1] & \mathbf{S}'_{l-2} [1,2] \dots \mathbf{S}'_{l-n} [1,2] \\ \mathbf{S}'_{l-2} [2,1] & \mathbf{S}'_{l-2} [2,2] \dots \mathbf{S}'_{2-4} [1,2] \\ \dots & \dots \dots \dots \\ \mathbf{S}'_{l-n} [2,1] & \mathbf{S}'_{2-4} [2,1] \dots \mathbf{S}'_{l-n} [2,2] \end{bmatrix}
 \tag{4}$$

Finally, the scattering matrix of the circuit is renormalized from the load impedances corresponding to the open ports, to 50Ω , using the formula:

$$\mathbf{S} = (\mathbf{I}_n - \mathbf{\Gamma})^{-1} \cdot (\mathbf{S}' - \mathbf{\Gamma}) \cdot (\mathbf{I}_n - \mathbf{\Gamma S}')^{-1} \cdot (\mathbf{I}_n - \mathbf{\Gamma}) \tag{5}$$

where \mathbf{I}_n is the unity matrix of order n and

$$\mathbf{\Gamma} = \begin{bmatrix} -\mathbf{\Gamma}_1 & 0 & \dots & 0 \\ 0 & -\mathbf{\Gamma}_2 & \dots & 0 \\ \dots & \dots & \dots & \dots \\ 0 & 0 & \dots & -\mathbf{\Gamma}_n \end{bmatrix}$$

3. EXAMPLE FOR $n = 4$

The characterization method presented in the previous section has been applied for a test four-port circuit, in particular for a coupler.

In this case, 6 sets of measurements have been performed on the coupler, for each frequency into the analysis frequency bandwidth. Each set of measurements is a two-port measurement, obtaining the following 6 scattering matrices $\mathbf{S}_{i-j} : \mathbf{S}_{1-2}, \mathbf{S}_{1-3}, \mathbf{S}_{1-4}, \mathbf{S}_{2-3}, \mathbf{S}_{2-4}$ and \mathbf{S}_{3-4} .

Knowing the scattering matrices \mathbf{S}_{i-j} , the six scattering parameter matrices, \mathbf{S}'_{i-j} , normalized to the impedance corresponding to the case when the ports are open, may be computed accordingly to the formula (1), if $\mathbf{\Gamma}_1, \dots, \mathbf{\Gamma}_4$ are known.

The reflection coefficients to the all four ports, $\mathbf{\Gamma}_1, \dots, \mathbf{\Gamma}_4$ has been computed, by solving the following equation system (obtained from (2), for $n = 4$):

$$\begin{aligned} \mathbf{S}'_{1-2} [1,1] &= \mathbf{S}'_{1-3} [1,1] \\ \mathbf{S}'_{1-2} [1,1] &= \mathbf{S}'_{1-4} [1,1] \\ \mathbf{S}'_{1-2} [2,2] &= \mathbf{S}'_{2-3} [1,1] \\ \mathbf{S}'_{1-2} [2,2] &= \mathbf{S}'_{2-4} [1,1] \end{aligned} \tag{6}$$

where, the signification of $\mathbf{S}'_{i-j} [1,1]$ and $\mathbf{S}'_{i-j} [1,1]$ has been explained in section 2. It may be shown that imposing (6), the conditions:

$$\begin{aligned} \mathbf{S}'_{1-4} [2,2] &= \mathbf{S}'_{3-4} [2,2], \quad \mathbf{S}'_{2-4} [2,2] = \mathbf{S}'_{3-4} [2,2], \\ \mathbf{S}'_{3-4} [1,1] &= \mathbf{S}'_{2-4} [2,2], \quad \text{and } \mathbf{S}'_{3-4} [1,1] = \mathbf{S}'_{1-3} [2,2], \end{aligned}$$

are also fulfilled. In (6), the analytical expression for $\mathbf{S}'_{i-j} [1,1]$ and $\mathbf{S}'_{i-j} [2,2]$ have been obtained by using (3).

The equation system (6) has been solved in MATHCAD software, obtaining the reflection coefficients $\mathbf{\Gamma}_1, \dots, \mathbf{\Gamma}_4$.

Then, the all 6 scattering matrixes S'_{i-j} have been obtained numerically with (1), such as the four-port matrix of the circuit having the all ports open-ended has been constructed, accordingly to (4), for $n=4$, as follows:

$$S' = \begin{bmatrix} S'_{1-2} [1,1] & S'_{1-2} [1,2] & S'_{1-3} [1,2] & S'_{1-4} [1,2] \\ S'_{1-2} [2,1] & S'_{1-2} [2,2] & S'_{2-3} [1,2] & S'_{2-4} [1,2] \\ S'_{1-3} [2,1] & S'_{2-3} [2,1] & S'_{3-4} [2,1] & S'_{3-4} [1,2] \\ S'_{1-4} [2,1] & S'_{2-4} [2,1] & S'_{3-4} [2,1] & S'_{1-4} [2,2] \end{bmatrix}$$

The scattering matrix of the circuit was finally obtained using (5).

4. NUMERICAL AND EXPERIMENTAL RESULTS

For the measurements performed on the test circuit, a network analyzer (HP 8510C) and an on-wafer probe heads station (Karl Süss PM5) have been used. The simulated magnitudes of the scattering parameters S_{11} , S_{21} , S_{31} and S_{41} for the test circuit (a coupler) are shown in Fig. 1 (obtained by using IE3D-Zeland software).

The experimental results of the coupler were obtained by following the algorithm presented in sections 3, for each frequency.

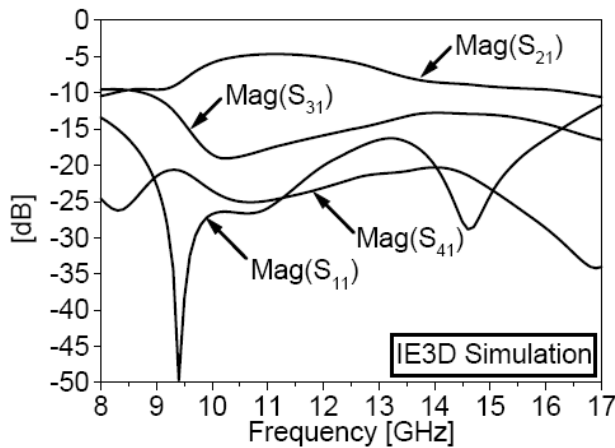


Fig. 1. Simulated scattering parameters, for the four-port test circuit (a coupler).

These results are presented in Fig. 2 for the magnitude of the scattering parameters S_{11} , S_{21} , S_{31} and S_{41} .

Fig. 3 shows the simulated and the experimental results for the phase difference between the coupled port and the through port.

By analyzing Figs. 1 and 2, for the frequency bandwidth of 10–12 GHz, the experimental coupling is 5 dB +/- 1dB, being in good agreement with the simulated results. The experimental input return-loss and isolation are better than 20dB for the same frequency bandwidth, a good agreement between simulated and experimental results being also observed. From Fig. 3, the experimental phase is 80 - 100 deg. for frequencies between 10.25–11.5 GHz, the simulated results being closed to them.

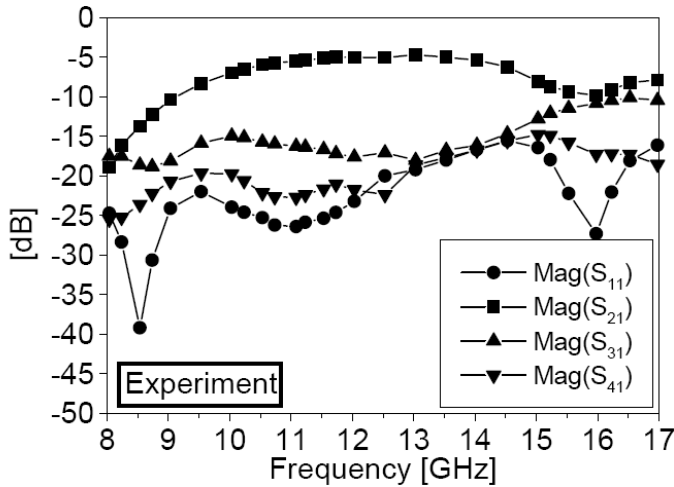


Fig. 2. Experimental scattering parameters, for the four-port test circuit (a coupler).

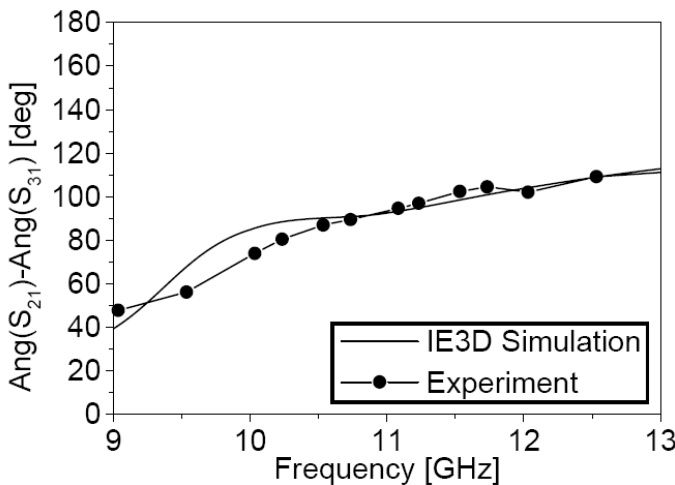


Fig. 3. Simulated and experimental phase difference between the coupled port and the through port of the coupler considered as a test four-port circuit.

5. CONCLUSION

An experimental technique to characterize a multiport has been proposed, using a two-port VNA. For this method $\frac{n!}{2!(n-2)!}$ sets of two-port measurements must be performed, while the other ports may be let open. The method is applied for a four-port test circuit (a coupler), showing a good agreement between the experimental results and the expected ones obtained by simulation. For a number of ports greater than 4, the difficulties of applying this method is expected to grow substantially.

References

- [1] M. DANESHMAND, R. R. MANSOUR, *Redundancy RF MEMS Multiport Switches and Switch Matrices*, Journal of Microelectronics System, **16**, pp. 296–303, April 2007.
- [2] M. DANESHMAND, R.R. MANSOUR, *Monolithic RF MEMS Switch Matrix Integration*, IEEE MTT-S Int. Microwave Symposium Dig., 2006.
- [3] B. YASSINI, S. CHOI, A. ZYBURA, M. YU, R.E. MIHAILOVICH, J.F. DeNATALE, *A Novel MEMS LTCC Switch Matrix*, IEEE MTT-S Int. Microwave Symposium Dig., pp. 721–724, 2004.
- [4] E.P. Mc. ERLEAN, J.S. HPNG, S.G. TAN, L. WANG, Z. CUI, R.B. GREED, D.C. VOYCE, *2x2 RF MEMS Switch Matrix*, IEEE Proc. of Microwave Antennas and Propagation, pp. 449–454, December 2005.
- [5] J.C. TIPPET and R.A. SPECIALE, *A Rigorous Technique for Measuring the Scattering Matrix of a Multiport Device With a 2-Port Network Analyzer*, IEEE Trans. on Microwave Theory and Techniques, **30**(5), pp.661–666, May 1982.
- [6] T.G. RUTTAN, B. GROSSMAN, A. FERRERO, V. TEPATTI, J. MARTENS, *Multiport VNA Measurements*, IEEE Microwave Magazine, **9**(3), pp. 56–69, June 2008.

Dynamics of Micromechanical Capacitive Shunt Switches

Romolo MARCELLI, Andrea LUCIBELLO, Giorgio De ANGELIS,
Emanuela PROIETTI, Daniele COMASTRI

CNR-IMM Roma, Via del Fosso del Cavaliere 100, 00133 Roma, Italy

Phone +39 06 4993 4536

Abstract. An analytical approach based on unidimensional equations has been settled up for studying the dynamics of RF MEMS switches. The model has been developed until now especially for shunt capacitive configurations, to predict the capacitance change and actuation times during the actuation and de-actuation mechanisms, and it has been implemented by means of a MATHCAD program.

Successively, two- and three-dimensional models based on a commercial software package, namely COMSOL Multiphysics, using equations about energy conservation and boundary conditions, has been used to validate the analytical one and to clearly identify the limits and advantages of a fully analytical formulation. The dynamical response of a capacitive shunt switch has been considered, but the approach is generally valid for resistive series as well as for capacitive shunt devices, because they refer to a double clamped beam, independently of the electrical configuration.

1. SUMMARY

RF MEMS switches [1], [2], [3], [4] can be actuated in several ways but, generally, the electrostatic actuation is preferred because no current is flowing in the device nor power absorption has to be involved in the process.

The equation which accounts for the most part of the physical mechanisms governing the dynamics of a RF MEMS switch can be written as:

$$m\ddot{z} = F_e + F_p + F_d + F_c \quad (1)$$

where: $m = \rho At$ is the bridge mass in the actuation region, computed by means of the density ρ , the area A and the thickness t ; $F_e = \frac{1}{2} \frac{\partial C}{\partial z} V^2$ is the electric force due

to the applied voltage V and to the change of the capacitance along the direction of the motion z ; $F_p = -k[z - (d + g)]$ is the force due to the equivalent spring with its constant k , acting against the electrical force to carry back the bridge to the equilibrium position; $F_d = -\alpha \dot{z}$ is the damping of the fluid, dependent on the bridge velocity \dot{z} and on the damping parameter α , which, in turns, is related to the geometry of the bridge and to the viscosity of the medium, d is the dielectric thickness and g the gap between bridge and substrate.

F_c is the contact contribution, which can be divided in the Van Der Waals and surface forces, the first acting as attracting and the second one as repulsive, with a possible equilibrium position at a given distance from the bottom electrode of the switch [5]. Currently, many papers about the dynamics of the switch are available in literature (see, for instance, [10] and related references, or [3]), including also possible collateral effects due to the Casimir force [11], [12] or self-actuation mechanisms due to the RF power [13]. The capacitance of a shunt capacitive MEMS switch can be described in terms of two series capacitors, each of them having its own dielectric constant. This is only a formal way to approach the problem, because the intermediate plate is a dielectric interface and not a metal one. On the other hand, the dielectric does not appear in the expressions describing the voltage change passing from one medium to another one, thus allowing the utilization of this approach. From the above considerations, the total capacitance will be:

$$C(z) = \frac{\epsilon_0 \epsilon_r A}{d + \epsilon_r (z - d)}; \quad z \in [d, d + g] \quad (1)$$

where $\epsilon_0 = 8.85 \times 10^{-12}$ is the vacuum dielectric constant in MKS units and ϵ_r is the relative dielectric constant of the material covering the bottom electrode. The derivative of $C(z)$, to be used in the definition of the electric force $F_e = \frac{1}{2} \frac{\partial C}{\partial z} V^2$ is given by:

$$\frac{\partial C}{\partial z} = \frac{\epsilon_0 \epsilon_r^2}{[d + \epsilon_r (z - d)]^2} A \quad (3)$$

and Eq. (1) can be rewritten as:

$$m\ddot{z} = k[z - (d + g)] + \alpha \dot{z} = -\frac{1}{2} \frac{\epsilon_0 \epsilon_r^2}{[d + \epsilon_r (z - d)]^2} V^2 \quad (4)$$

which can be transformed in:

$$\ddot{\xi} + \beta \dot{\xi} + \omega^2 \xi = B(\xi) V^2 \quad (5)$$

where:

$$\begin{aligned}\xi &= z - (d + g) \\ \beta &= \frac{\alpha}{m} \\ \omega &= \sqrt{\frac{k}{m}} \\ B(\xi) &= -\frac{1}{2m} \frac{\varepsilon_0 \varepsilon_r^0}{[d + \varepsilon_r \xi]^2}\end{aligned}\tag{6}$$

The voltage difference V is imposed between the metal bridge, connected to the ground plane of a coplanar waveguide (CPW) structure, and the central conductor of the CPW, which also carries the high frequency signal. Under these circumstances, the switch will experience an electrostatic force for the actuation which is balanced by its mechanical stiffness, measured in terms of a spring constant k . The balance is theoretically obtained until the bridge is going down approximately (1/3) of its initial height. After that, the bridge is fully actuated, and it needs a value of V less than the initial one to remain in the OFF (actuated) position, because contact forces help in maintaining it in the down position.

The actuation as well as the de-actuation are affected also by the presence of a medium (typically air, or preferably nitrogen for eliminating humidity residual contributions in a packaged device) which contributes with its own friction, introducing a damping, and changing the speed of the switch [5], [6], [7]. Moreover, the damping modifies the natural frequency of oscillation for the bridge. In particular, the actuation and deactuation mechanisms will be modified, thus leading to *simple oscillations* (no fluid damping contribution) or *damped oscillations* (fluid contribution) to *over-damping* for particular values of the bridge dimensions. Other contributions to the motion of the switch are given by the "contact force" of the bridge with respect to the plane, when it is actuated or very close to the plane of the CPW, i.e. close to the substrate. They are due to the interaction between the two surfaces. The Van Der Waals force, having an attractive effect, has to be also included [5], [7]. Both last contributions are, of course, very important when the bridge is close to the bottom electrode, in contact with the dielectric used for obtaining the high value of the capacitance needed to get the best isolation. It is difficult to manage all of these contributions, and usually a phenomenological approach is followed, trying to individuate the most important parameters useful for the required response. For instance, higher is the ratio between bridge thickness and bridge length, higher will be the spring constant value and, consequently, the robustness of the switch. It is common practice that a good value for k is in the order of tens of N/m.

All of the above contributions and solutions of the mechanics equation for the bridge motion have been considered and discussed in detail for actual configurations, setting up the method for the capacitance dynamics and for the actuation and de-actuation times.

Typical responses for the de-actuation are given in the following Fig. 1, where the contributions of the restoring mechanical force and of the damping have been clearly evidenced.

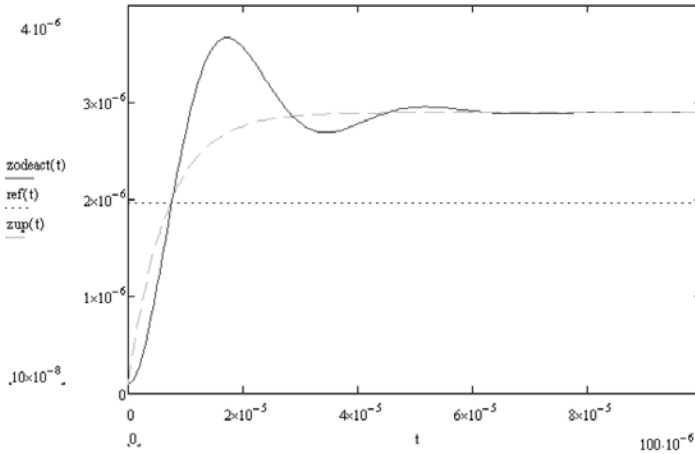


Fig. 1. De-actuation vs time for the shunt switch used as an example. The green curve accounts only for the exponential restoring mechanism, while the red one accounts also for the air damping.

From capacitance dynamics considerations at the threshold voltage, and by assuming that the de-actuation time is defined as the time at which the capacitance reaches the 90% of the final one, we can get:

$$\tau_{deact} = -\frac{2}{\beta} \ln \left[\frac{1}{9} \left(1 - \frac{d}{\varepsilon g} \right) \right] \tag{7}$$

By using an analogous analytical treatment, the actuation time will be given by:

$$\tau_{act} = -\frac{2}{\beta} \ln \left(\frac{1}{9} \frac{d}{\varepsilon g} \right) \tag{8}$$

Times in the order of tens, up to one hundred of μs are obtained for typical geometries of the MEMS switches.

By including the dependence on the applied voltage and energy considerations about the energy spent for the actuation, Eq. (8) is transformed in:

$$\tau_{act} = -\frac{2}{\beta} \ln \left(\frac{4}{\beta^2 g^2} \frac{C_{OFF} V_a^2 - h g^2}{m + 2 \frac{\beta}{\omega}} \right) \tag{9}$$

where C_{OFF} is the capacitance in the down state and it has been also given the explicit dependence on the applied voltage V_a .

In Fig. 2 the actuation time Vs the applied voltage is shown for a bridge 4 μm thick. Moreover, two- and three-dimensional approaches have been used for the same structure, based on the possibilities given by the commercial software package COMSOL Multi-physics.

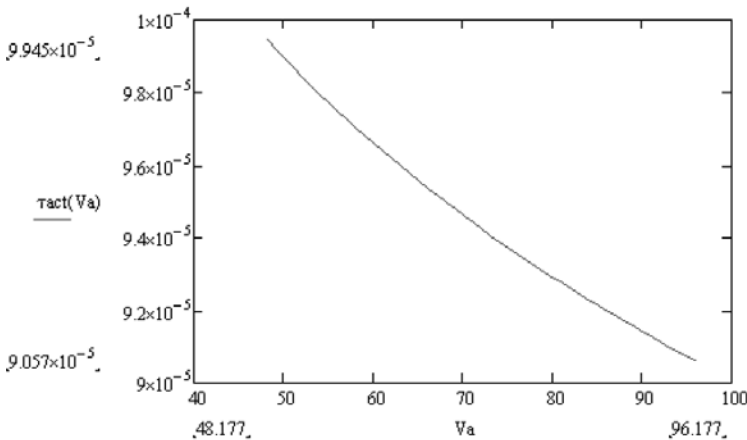


Fig. 2. Actuation time in sec of an RF MEMS capacitive shunt switch Vs the applied voltage V_a in volt.

In fact, simple geometries can be efficiently simulated by using an uni-dimensional approach, as also stated in [3], and actuation times can be estimated without using long and complicated simulations with finite elements. On the other hand, a full simulation is very important especially when the shape of the bridge is tailored in a not simple way. This happens when the cross section has not a constant width, or specific technological solutions, like multi-layers for the bridge and dimples in the actuation area to help the electrical contact are realized, or holes are present on the beam for improving the sacrificial layer removal and for lowering the spring constant. Moreover, a software able to treat combined solicitations involving the mechanical, thermal and electrical response of the MEMS device has to be considered if the goal is the definition of a figure of merit for such a technology. For this purpose, 2D and 3D mechanical simulations have been performed to clearly state the advantages of such an approach with respect to the uni-dimensional one. Some 2D results are presented in Fig. 3 and in Fig. 4,

where the OFF state of the switch is shown by using a central actuation (DC signal along the central conductor of the CPW) or a lateral one by means of symmetrical pads.

The proper shape of the actuated bridge, also in the case of simple geometries, is particularly useful for the prediction of the electrical properties of the device. In fact, the real deformed shape of the bridge can be used as the input for high frequency simulations, and parasitic contributions could be predicted in an easier way, especially when the millimetre wave range is considered.

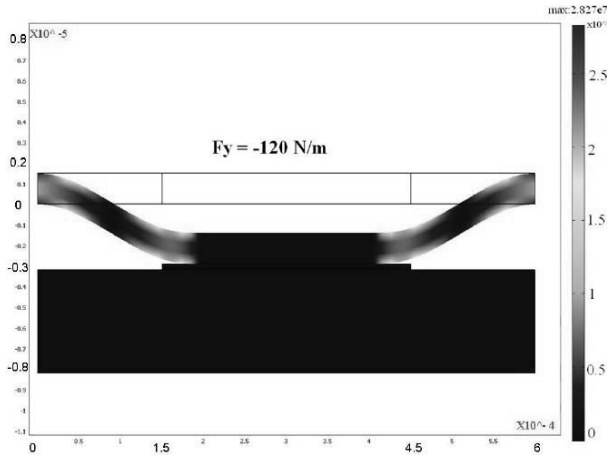


Fig. 3. Central actuation of the MEMS switch. A mechanical force on the central conductor of the CPW has been applied as high as 120 N/m.

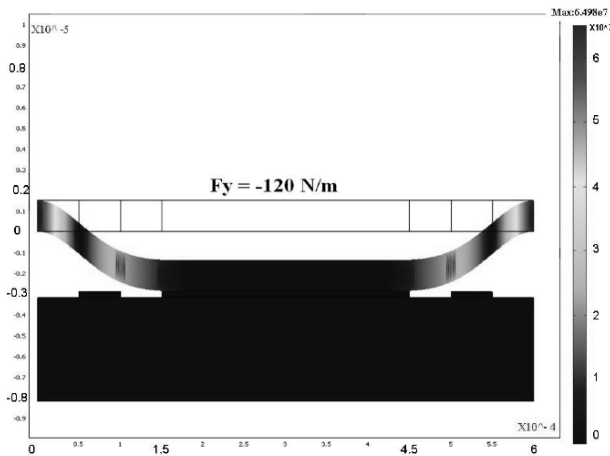


Fig. 4. Lateral actuation of the 2D structure. The same force was necessary for having a full collapse of the bridge, but applied on smaller pads.

From the result in Fig. 4, it turns out that by properly choosing the shape and the dimensions of the structure, the actuation occurs without having the bridge touching the lateral pads. This could help in decreasing the charging effects for these devices.

An example of the 3D response is given in the following Fig. 5 and Fig. 6, where the electrostatic actuation has been performed by means of a 20 volt DC signal along the central conductor of the CPW. In this case, additional details have been included, like the small lateral teeth useful for chemical removal of the sacrificial layer, and the holes used for both an easier cleaning of the area under the bridge and a lowering in the bridge stiffness.

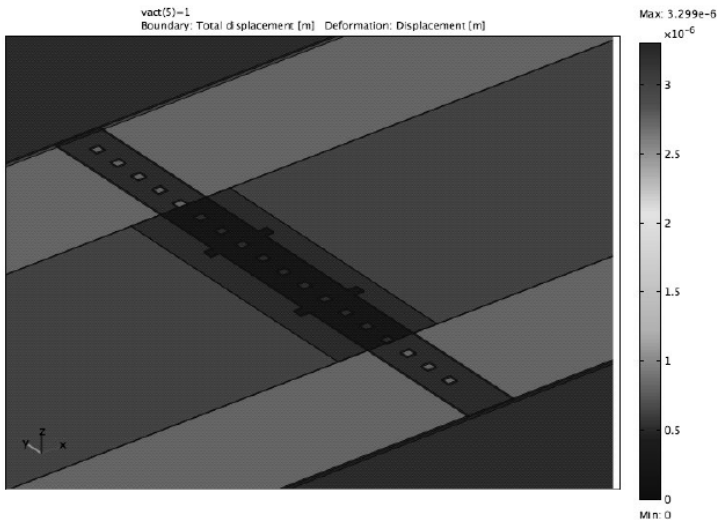


Fig. 5. 3D simulation by COMSOL Multi-Physics of an RF MEMS shunt capacitive switch in the ON state (bridge in the up position). The bridge is 50 μm wide, 600 μm long, 1 μm thick and distant from the substrate 2.8 μm . Holes having the diameter of 10 μm have been considered along the beam.

The result in Fig. 6 is coherent with the prediction performed by using an analytical approach for evaluating the threshold voltage for such a structure. In fact, $V_a=22$ volt if the uni-dimensional approach is used. Actually, in the most part of the investigated cases, the general response of the bridge can be easily predicted by using an uni-dimensional approach, and the presence of holes can be approximated by defining an effective stiffness for the metal beam. For the above reason, the 3D simulation is really useful, as already stressed, only in the case of configurations which have a very peculiar shape. Also in the case of a moving mesh, to be used for the dynamical response of the device, many informations can be already obtained from evaluations based on Eq.(7)-(9), by using a fully analytical model, without involving cumbersome simulations with a computer. The real advantage in having a full modelling of the device is in the combination of

mechanical and RF predictions, being based on the same geometry construction. Specifically, as it is the case of the COMSOL software package, thermal, power and charging effects can be considered in the same simulation environment. For the above reasons, this will be very useful to get a figure of merit for the RF MEMS technology based on different input conditions.

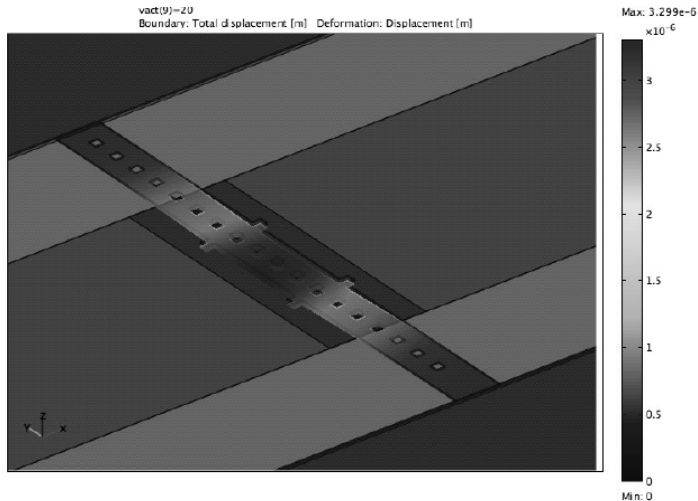


Fig. 6. 3D simulation of the RF MEMS switch in the OFF state (bridge in the down position). An actuation voltage around 20 volt has been necessary. The deformation of the bridge is represented by the change in the colours, from the blue (at rest) to the red (fully actuated).

Acknowledgement. The authors wish to acknowledge the funding from the Contract ESA/ESTEC AO 1-5288/06/NL/GLC: High Reliability MEMS Redundancy Switch.

References

- [1] G.M. REBEIZ, J.P. MULDAVIN, *RF MEMS Switches and Switch Circuits*, IEEE Microwave Magazine, **2**(4), pp. 59–71, 2001.
- [2] G.M. REBEIZ, Guan-Leng TAN, J.S. HAYDEN, *RF MEMS Phase Shifters, Design and Applications*, IEEE Microwave Magazine, **3**(2), pp. 72–81 2002.
- [3] G.M. REBEIZ, *RF MEMS, Theory, Design and Technology*, John Wiley and Sons, Hoboken, 2003.
- [4] Harrie A.C. TILMANS, *MEMS Components for Wireless Communication*, XVI Conference on Solid State Transducers, Prague, Czech Republic, Sept. 15-18, 2002.
- [5] E.K. CHAN, E.C. KAN, R.W. DUTTON, *Nonlinear Dynamic Modeling of Micromachined Switches*, Proceedings of IEEE MTT-Symposium, pp. 1511–1514, 1997.
- [6] E.K. CHAN, R.W. DUTTON, *Effect of Capacitors, Resistors and Residual Charge on the static and dynamic Performance of Electrostatically Actuated Devices*, SPIE Symposium on Design and Test of MEMS/MOEMS -March 1999.
- [7] D. MERCIER, P. BLONDY, D. CROS, P. GUILLON, *An Electromechanical Model for MEMS Switches*, Proceedings of IEEE MTT-Symposium, pp. 2123–2126, 2001.

- [8] J.B. MULDAVIN, G.M. REBEIZ, *Nonlinear Electro-Mechanical Modeling of MEMS Switches*, Proceedings of IEEE MTT Symposium, pp. 21119–2122, 2001.
- [9] Fuqian YANG, *Electromechanical Instability of Microscale Structures*, J. Appl. Phys, **92**(2), pp. 2789–2794, 2002.
- [10] Z.J. GUO, N.E. Mc GRUER, G.G. ADAMS, *Modeling, Simulation and Measurement of the Dynamic Performance of an Ohmic Contact, Electrostatically Actuated RF MEMS Switch*, J. Micromech Microeng., **17**, pp. 1899–1909, 2007.
- [11] F. MICHAEL SERRY, DIRK WALLISER, G.J. MACLAY, *The Role of the Casimir Effect in the Static Deflection and Stiction of Membrane Strips in Microelectromechanical Systems (MEMS)*”, J. Appl. Phys., **84**(5) pp. 2501–2506, 1998).
- [12] Steve K. LAMOREAUX, *Casimir Forces: Still Surprising After 60 Years*, Physics Today, pp. 40–45, February 2007.
- [13] Karl M. STROHM, *et al*, *RF-MEMS Switching Concepts for High Power Applications*, Proceedings IMS, pp. 42–46, 2001.

Electromagnetic and Electromechanical Study of a H-Shaped Millimeter MEMS Shunt Switch

Federico CASINI¹, Romain CRUNELLE², Michel FRYZIEL²,
Natalie ROLLAND², Paul Alain ROLLAND²,
Paola FARINELLI¹, Roberto SORRENTINO¹

¹University of Perugia, DIEI, Via G. Duranti 93, 06125 Perugia, ITALY,
Phone: +39-075-585-3658; Fax: +39-075-585-3654

²Université des Sciences et Technologies de Lille, IEMN, Avenue Poincaré,
B.P. 69, 59652 Villeneuve d'Ascq, France
Phone: +33.3.20.19.79.79

Abstract. This paper presents the electromagnetic and electromechanical design of a new H-shaped millimeter RF MEMS switch for high frequency applications. The switch is a fixed-fixed metal beam placed in a shunt configuration over a coplanar waveguide transmission line. A numerical model of the switch has been developed in order to analyze the influence of its parameters on both the electromagnetic and electro-mechanical domains. Measurements of fabricated prototypes have been performed in order to compare simulated and experimental results, showing very good agreement.

1. INTRODUCTION

RF-MEMS switches are the key element for innovative reconfigurable low loss circuits, such as impedancematching networks, tunable phase shifter and filters. Low loss, low power consumption, high bandwidth and very compact size and weight are some of the advantages that make this technology a possible leading solution in the years to come for a lot of TLC applications. On the other hand, high actuation voltage, switching time and above all dielectric charging are the main critical aspect that so far prevented its complete success, even if a lot of progress has been done in the recent years.

In this paper, an H-shaped RF-MEMS capacitive shunt switch working at a center frequency of 60 GHz is presented. The switch is realized on a 200 μm GaAs substrate through a cold manufacturing process ($T_{\text{max}} = 250^\circ\text{C}$), whose main

advantage is the post process compatibility that allows MEMS integration with active devices.

The shunt-capacitive switch here presented consists of a thin metal membrane, suspended over the center conductor of a coplanar waveguide (Fig. 1). The bridge is fixed at both ends to the ground conductors by means of four torsion bars and is electro-statically actuated using two electrodes placed at two sides of the signal line. A 200 nm layer of Silicon Nitride is used to DC isolate the CPW central conductor to the membrane in the actuated state, realizing a parallel plate shunt capacitor.

Such a structure is the result of an articulated study whose purpose was to conceive an RF-MEMS switch with high reliability and very high RF performance. For that reason, both the electromagnetic and the electromechanical domain of the device have been accurately studied, conceiving two separate models. This way, a deep analysis on the effects of the switch parameters on its performance on both aspects has been realized and is here presented.

The simulated results given by the model have been compared with measurements of fabricated prototypes. Experimental data and observations by optical profilometer confirm the accuracy of the proposed multiphysics models.

2. ELECTROMAGNETIC MODEL

The developed switch topology is presented in Fig. 1, along with the lumped element model showing the equivalent components used to represent each portion of the membrane.

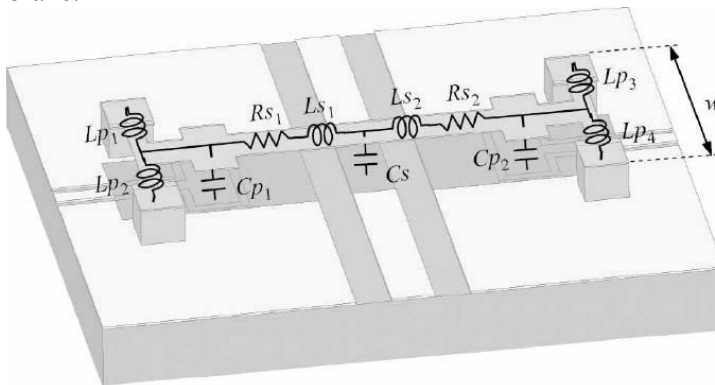


Fig. 1. Developed RF-MEMS switch structure and equivalent circuit.

As said in the previous chapter, the shape of the membrane, the actuating mechanism and the anchoring system, along with all the structural parameters of the device, are the result of an accurate study aimed to conceive a high reliability component. As it has been shown by many authors in fact, reliability is the most

critical issue of the RF-MEMS technology and one of the factors preventing its large diffusion [1-4]. Among the different phenomena involved in that aspect, dielectric charging is maybe the most significant one, since it is responsible of various failure mechanisms, like membrane sticking or auto-actuation.

One of the best ways to reduce dielectric charging is to avoid direct contact between the membrane and the dielectric covering the control electrodes, ensuring the presence of a little air gap even in the actuated state. For this reason, instead of using the signal line to actuate the bridge, two separated electrodes are introduced, placed one at each side of the line. The control voltage, the shape, Young modulus and other characteristic of the membrane have also been chosen so that in the actuated state it presents a curved profile, touching the dielectric film only the over signal line, whereas a small air gap is ensured over the areas where the two electrodes are placed.

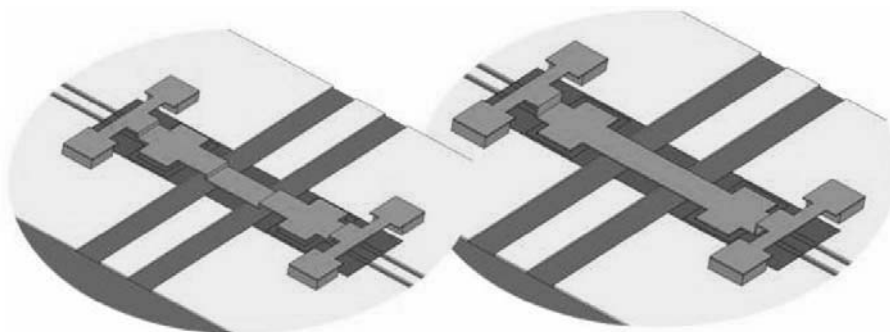


Fig. 2. Comparison between the curved profile that allows the membrane to touch the dielectric only over the signal line and the flat profile that causes the membrane to touch also the electrode area.

The RF equivalent circuit (Fig. 1) of such structure consists mainly of a variable capacitance C_s , modeling the parallel plate capacitor formed by the beam and the signal line in the interfacing area. The non idealities of the metallic membrane introduce series resistance and inductance, whereas the presence of the actuation electrodes introduces two other parasite capacitors. [5].

Each dimension of the membrane has been chosen in order to set its working frequency at 60 GHz. Given the dielectric film thickness of 200 nm and the signal line width, fixed to have a desired line impedance of 50 Ω , the parallel plate capacitance C_s is controlled by varying the membrane width, whereas parasite resistance and inductance depend on the membrane length.

Anyway, full-wave simulations on Ansoft HFSS proved that a very important role is also played by the position of actuating electrode. As a matter of fact, it has been observed that all the parasite elements introduced by the extra-electrodes

portions of the membrane have a slight or negligible effect on the RF performance of the switch.

This way, it has been possible to design and realize four different versions of the presented switch, each one having a chosen value of length, in order to study the influence of this parameter on the electro-mechanical performance without affecting the RF one.

The simulated performance of the four different switches in the UP state are presented in Fig. 3

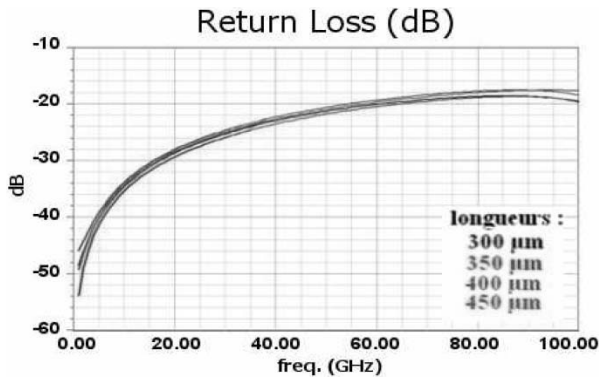


Fig. 3. Simulated performance of the switch in the UP state.

As it can be seen, at the operating frequency of 60 GHz the Return Loss is about -20dB for all the four different lengths of the switch, whereas the Insertion Loss is about 0.2 dB. The presence of the bridge in the UP state has thus a negligible effect on the propagation of the signal, thanks to the 2.7 mm air gap between the bridge and substrate which assures a very low UP-state capacitance.

As said, in the actuated state the profile of the membrane has a curvature that makes it touch the dielectric film only over the signal line. For that reason, this condition has been simulated in Ansoft HFSS simplifying the real profile with a three stepped one, as depicted in Fig. 4, that allows to take into account the air gap over the electrodes.

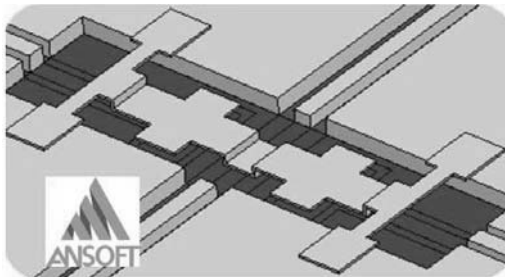


Fig. 4. Ansoft HFSS full-wave model of the switch in the actuated state simulating the real curved profile of the bridge.

Fig. 5 shows the compared performance of the four designed versions of the switch in terms of Insertion Loss. First of all it can be observed that the maximum shift in terms of resonant frequency from the desired value of 60 GHz is only 3 GHz for all the curves. As said before, fullwave simulations show that the extra-electrode portions of the bridge have little effect on the RF behaviour and also, at the centre frequency Insertion Loss is only -40dB, meaning very low resistive loss.

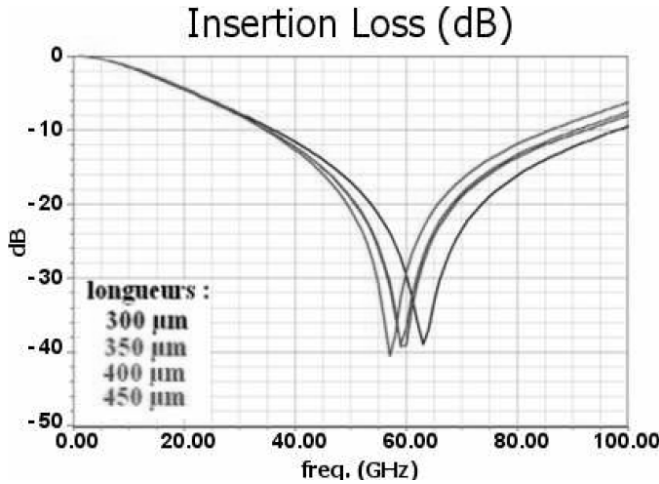


Fig. 5. Simulated performance of the switch in the DOWN state given by the three-step profile bridge.

The conclusions drawn by the analysis of the Insertion Loss graph are confirmed by the data reported on Table 1, where the values of each component of the lumped element circuit modelling this state are reported. As it can be seen, the parallel plate capacitor has a value of 0.33 pF, which is consistent with theoretical computations. On the contrary, the variation of the inductance associated to the extra-electrode portions of the membrane L_p is much lower than what theoretically computed, justifying the restrained frequency shift shown on Fig. 4.

Table 1. Values of the lumped element circuit modelling the shunt switch in the DOWN state

C_s (pF)	L_s (pH)	C_p (pF)	L_p (pH)	R (Ω)
0.33 pF	9-9.6	0.1-0.11	9.8-11.3	0.4

Although conceived as a solution to improve the reliability of the device, the air gap over the electrodes ensured by the curved profile in the DOWN state is also crucial for its RF performance. Full wave simulations in HFSS have been used to analyze the switch behaviour in the case when that condition is not satisfied. Results reported on Fig. 6 show that when there is a direct contact between the

membrane and the dielectric film over the electrodes, the frequency response is totally different. As it can be seen, the centre frequency is strongly shifted toward the lower frequencies and also a second resonance appear.

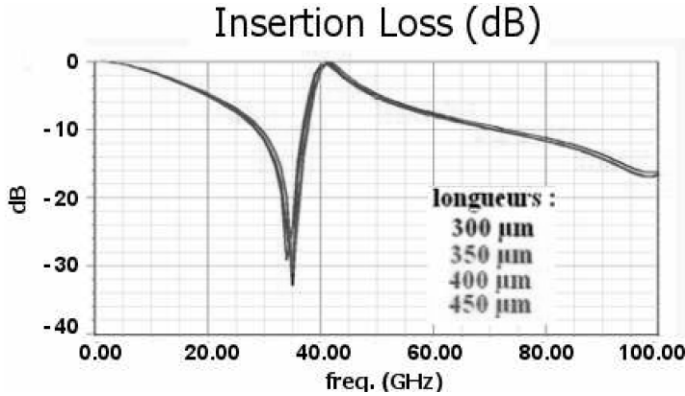


Fig. 6. Simulated performance of the switch in the DOWN state with the membrane touching the electrodes.

The reason for such a different behaviour can be found analyzing the values of the components of the equivalent circuit modelling the switch in this condition, reported on Table 2. As a result of the absence of the air gap, the parasite capacitance associated to the electrodes is ten times higher than in the previous case. This capacitance is responsible of both the frequency shift and the second resonance that make the switch unusable in the V-band.

Table 2. Values of the lumped element circuit modelling the shunt switch contacting the actuation electrodes

C_s (pF)	L_s (pH)	C_p (pF)	L_p (pH)	R (Ω)
0.33 pF	0.2-1.1	0.9-1	13-16	0.4

3. TECHNICAL ISSUES

It has been demonstrated how the key point for the device to work properly on both the mechanical and high frequency domain is the membrane configuration in the actuated state. It is easy to understand then how the mechanical aspect of the switch plays a critical role.

The original mechanical design of the device was focused to conceive a structure with the lowest actuation voltage possible. The reason for such a choice is due to the direct relationship between the dielectric charging phenomenon and the control voltage. Experience [3] has shown in fact that the higher is the actuation voltage of an RF-MEMS switch, the faster electric charges are injected into the dielectric from the bottom electrode, thus shortening the life-time and the maximum number of cycles of the device.

With the aim to reduce the actuation voltage, it has been decided to lower the elastic constant of the membrane by adopting two main technical solutions. The first one is the bridge anchorage to the substrate by means of four lateral torsion bars. With this solution the mechanical stress generated during actuation is distributed along almost all the surface of the bridge, resulting in a lower elastic force. The second solution is instead the choice of a very low value of membrane thickness (1.2 μm), a parameter to which the elastic constant is directly related.

The cold manufacturing process that allows post process compatibility ($T_{\text{max}} = 250^\circ\text{C}^\circ$) developed at IEMN has been used to fabricate prototypes. The realized devices shown actuation voltages ranging from a maximum of 25 V for the 300 μm prototypes down to only 10V for the 450 μm ones. These very low measured values of actuation voltage confirm the effect of the mechanical solutions explained above.

Anyway, fabricated prototypes also showed an undesired consequence of that obtained low value of elastic force which strongly affects the bridge reliability. On a high percentage of tested samples it has indeed been observed that the membrane remains stuck to the substrate just after the first deactuation. Such behaviour is due to the contact force which arises between the bridge and the substrate when the first touches the second during actuation. That force, which tends to keep the membrane stuck to dielectric film, is normally counterbalanced by the elastic force, but in this case the last one is not sufficient to bring the bridge back to the UP position.

4. ELECTROMECHANICAL MODEL

In order to analyze the electromechanical behaviour of the designed switches and find a solution to the encountered problems, also an electromechanical model of the device has been developed by means of Ansys multi-physics simulator.

The Ansys model has been realized using the direct electromechanical coupling elements TRANS126. In order to get a reliable tool, the prototypes realized in the first fabrication run have been replicated in the simulation environment, optimizing the model parameters to fit experimental data.

The comparison between measured actuation voltage and the corresponding simulated results are shown on Table 3. A very good correspondence for all the different instances of the switch has been achieved.

Table 3. Comparison between simulated and measured pull-in voltage of 1.2 μm thick prototypes of different lengths

Length	Simulated	Measured
300 μm	24 V	22-25 V
350 μm	17 V	17-20 V
400 μm	14 V	13-16 V
450 μm	11.5V	10-12 V

The developed model has been used to analyze the dependence between the membrane thickness and the relative spring constant of the switch for the different instances. This parameter is in fact one the key factors for the solution of the sticking problem. Also, the incidence of process parameters, such as Young Modulus and residual stress has been taken into account in order to foresee possible deviation of measured data from the simulated ones.

The comparison between simulated data and measures from the working samples allowed us to identify the minimum value of bridge spring constant necessary to overcome the sticking issue.

Anyway, it has already been explained how increasing the spring constant of the switch affects the actuation voltage and thus its long-term reliability. It is for this reason that a more accurate study has been developed in order to optimize the mechanical performance.

Going deeper into details, the elastic behaviour of the membrane has been distinct in the two cases of actuation and deactuation. As a matter of fact, the electrostatic force practised by electrodes acts in correspondence of their position along the membrane, whereas the sticking force acts in its middle. The spring constant values modelling the two different situation has proven to be different, with the first being always higher than the second. This fact explains how the membrane tends to remain actuated even though it opposes a high elastic force during actuation.

Table 4 analyzes the relationship between the membrane thickness and the two elastic constant for the 350 μm long switch. As it can be seen, both constants increase by thickening the membrane. Anyway, since their ratio decreases, the simple growth in thickness of the entire membrane is not advantageous because the greater elastic force is counterbalanced by an even greater V_{PI} .

Table 4. Mechanical performance of the 350 μm switch for different values of membrane thickness

t	$K1$	$K2$	$K2/K1$	V_{PI}
1.2	0.63	0.43	0.675	17
1.5	1.17	0.76	0.647	23
1.8	1.99	1.28	0.641	31
2.1	3.14	2.01	0.640	38

An accurate study has thus been conducted on the profile of the membrane in order to optimize the mechanical performance. Ansys simulations proved that if the membrane is locally thickened only in its centre the spring constant ratio increases considerably. Fig. 7 shows the original switch with an 80 μm long brick of increased thickness, while Table 5 illustrates the relationship between the brick thickness and mechanical performance.

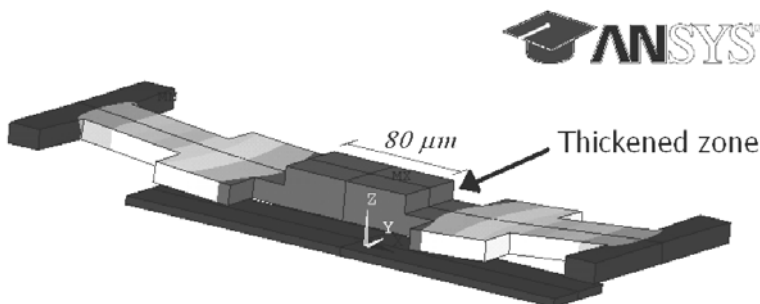


Fig. 7. Shunt switch locally thickened in the membrane centre.

Table 5. Mechanical performance of the 350 μm switch with localized thickening

t_{inc}	$K1$	$K2$	$K2/K1$	V_{PI}
1.2+0	0.63	0.43	0.675	17
1.2+0.8	0.68	0.63	0.752	20
1.2+1.1	0.87	0.67	0.771	22
1.2+1.4	0.90	0.70	0.784	24

In this case the spring constant ratio increases with higher values of thickness of central brick, which means a much better mechanical behaviour. The drawback associated to this solution is the reduction of the air gap over the electrode that can anyway be easily controlled.

5. CONCLUSIONS

A high frequency MEMS shunt switch has been presented. Simulated results on HFSS full wave simulator of the developed electromagnetic model show remarkable RF performance. Because of the need of controlling the membrane profile in the actuated state and the technical issues shown by fabricated prototypes, also an electromechanical model has been developed. The developed multi physics approach allowed us to design an optimized H-shaped RF-MEMS switch for high frequency applications.

References

- [1] W.M. van SPENGEN, R. PUERS, R. MERTENS, I. De WOLF, *A Comprehensive Model to Predict the Charging and Reliability of Capacitive RF MEMS Switches*, J. Micromech. Microeng. **14**, pp. 514–521, 2004.
- [2] C.L. GOLDSMITH, J. EHMKE, A. MALCZEWSKI, B. PILLANS, S. ESHELMAN, Z. YAO, J. BRANK, M. EBERLY, *Lifetime Characterization of Capacitive RF MEMS Switches*, IEEE MTT-S Int. Microwave Symp. Digest, pp. 227–230, 2001.

- [3] R.W. HERFST, P.G. STEENEKEN, J. SCHMITZ, *Time and Voltage Dependence of Dielectric Charging in RF MEMS Capacitive Switches*”, Reliability physics symposium, 2007. proceedings. 45th annual. IEEE international, April 2007.
- [4] G.J. PAPAIOANNOU, J. PAPAPOLYMEROU, *Dielectric Charging Mechanisms in RF-MEMS Capacitive Switches*, Microwave Conference, European, 9-12 October 2007.
- [5] M. FRYZIEL, *et al*, *New H-Shape RF Microswitch Design for Microwave and Millimeter-Wave Applications*, Workshop on MEMS for Millimeter Wave Communication, MEMSWAVE, Uppsala, Sweden, June 30-july 2, 2004.

This volume is promoted by the Commission: “Science and Technology of microsystems” of the Romanian Academy with the technical and financial support of the National Institute for Research and Development in Microtechnologies (IMT-Bucharest, <http://www.imt.ro>). The volume is part of the “Micro and Nanoengineering series (coordinator – Professor Dan Dascalu, member of the Romanian Academy).

